SEARCH FOR BC+ -> BS0 PI+, BS0 -> J/PSI PHI DECAYS AT THE CDF II DETECTOR

BY

EDWIN LLOYD ROGERS

DISSERTATION

Submitted in partial fulfillment of the requirements
for the degree of Doctor of Philosophy in Physics
in the Graduate College of the
University of Illinois at Urbana-Champaign, 2010

Urbana, Illinois

Doctoral Committee:

Professor Steven Errede, Chair
Professor Kevin Pitts, Director of Research
Professor Aida El-Khadra
Professor Russell Giannetta

Abstract

This analysis details the search for $B_c^+ \rightarrow B_s^0\ \pi^+, B_s^0 \rightarrow J/\psi\ \phi$ decays, and the charge conjugate mode, using the CDF II detector at the Fermi National Accelerator Laboratory. The search is derived from a sample of 5.84 fb^{-1} of data from $p\bar{p}$ collisions of $\sqrt{s} = 1.96$ TeV collected via J/ψ trigger paths. Selection of candidate events within the Di-Muon trigger dataset is performed in two stages, both using artificial neural networks trained to select signal over combinatoric backgrounds. A 95% confidence upper limit is set on the number of $B_c^+ \rightarrow B_s^0\ \pi^+$ events within our sample, $n_{signal} \leq 4.15$, for B_s^0 candidate events of $p_T \geq 4.0$ GeV/c and $|\eta| \leq 1.0$. Using this to compute the ratio $\frac{\sigma_{B_c \rightarrow B_s \pi}}{\sigma_{B_s}}$, a 95% confidence limit is set on the quantity $\frac{f_{B_c^+}}{f_{B_s^0}} \cdot \mathcal{B}(B_c^+ \rightarrow B_s^0\ \pi^+) \leq 0.00683$, where $f_{B_c^+}$ is the fragmentation fraction of $\bar{b}$ quarks to B_c^+ mesons and $f_{B_s^0}$ is the fragmentation fraction of $\bar{b}$ quarks to B_s^0 mesons. Assuming a ratio of fragmentation fractions $\frac{f_{B_c^+}}{f_{B_s^0}} = 0.014$, as estimated from yields in related experiments, a limit is placed on the branching fraction, $\mathcal{B}(B_c^+ \rightarrow B_s^0\ \pi^+) \leq 48.8\%$.

For my parents and my wife, whose encouragements and assurances made this work possible.

Acknowledgments

I would like to thank the many people whose support has helped me create this document. My advisor, Kevin Pitts, has been an outstanding teacher, providing guidance and instruction with incredible patience. Throughout my graduate career, his tutelage, more than any other, has advanced my understanding of physics and experimental science. For this, I am most grateful.

In addition, the High Energy Physics Group at the University of Illinois at Urbana-Champaign has provided critical assistance through the many challenges of this analysis. Heather Gerberich, Greg Veramendi, Ben Carls, Olga Norniella, and Greg Thompson have all been tremendously helpful in tackling the many challenges that arose. Further, this thesis would not be possible if not for the work of the entire CDF collaboration. In particular, I have received valuable, personal assistance from Ray Culbertson, Nils Krumnack, Guillelmo Ceballos, Elisa Pueschel, and Michal Kreps.

I thank my many friends, both here in Champaign-Urbana, and those more distant, for inspiring me to persevere.

Last, I could not have made it this far without the love and support of my family. My gratitude goes to my parents, who have been tireless advocates of and believers in my work, and to my wife, Sarah, whose faith in my ability has often exceeded my own, and who has provided encouragement the many times it was needed.

Contents

1 Introduction

Elementary particle physics has focused on the study of the smallest elements of matter and their interactions. In the modern-day field, experimental devices to perform measurements on the tiniest scales have, themselves, become colossal, sophisticated instruments. The Fermi National Accelerator Laboratory (Fermilab) has, for over three decades, generated advanced experimental results in the field, including the discovery of the b quark in 1977 [1]. Today, Fermilab is home to the Tevatron and the Collider-Detector at Fermilab (CDF), where, along with other research, our knowledge of the b quark has made some of its greatest advancements to date. Currently, measurements from CDF are among the most precise in all of b physics.

For the time being, the Standard Model provides the most accurate description of observed phenomena in the field of elementary particle physics. Since its first observation in 1977, the b quark and its study have played a strong role in helping develop, test, and challenge the Standard Model. The measurement described in this paper, made at CDF, attempts to extend that field of work and to add to the extensive collection of results from experiments at Fermilab. The measurement of the branching fractions of the $B_c^+ \to B_s^0\ \pi^+$ mesons is the first of its kind and adds to our understanding of heavy flavor production and decay.

This analysis is divided into thirteen chapters, four appendices, and a references list. In the second chapter, the theoretical framework and experimental history that describes the B_c^+ meson is discussed. Chapters three through five discuss the CDF II detector, with a particular focus on the three level trigger system. The recent upgrade of the Level 1 tracking trigger upgrade – advanced with the help of researchers at the University of Illinois at Urbana-Champaign, including the author – is also delineated. In chapter six, monte carlo simluations used in the analysis are examined. The seventh chapter focuses on details of this analysis specific to the CDF II data set. Chapters eight through twelve discuss the techniques used in and results of the search for $B_c^+ \to B_s^0\ \pi^+$ decays in this analysis. The thirteenth and final chapter describes possible opportunities for future research along these lines.

Within appendix A is a more detailed review of the theoretical basis for the use of artificial neural networks in this analysis. Appendix B reports the exact TCL settings used to produce

the custom ntuples used for this analysis. Appendix C is a tutorial document explaining the diagnostic techniques for Level 1 trigger hardware. Lastly, appendix D is a thorough diagnostic from the B_c^+ neural network training broken down according to the input variables, ordered by variable significance in selection.

2 Theoretical Framework

2.1 Matter and its Interactions in the Standard Model

To our current understanding, matter is made up of a limited variety of particles which serve as building blocks. These particles interact with one another, and it is by the nature of these interactions that we classify these particles. Currently, the best description of the properties of particles and their interactions is found in the Standard Model, which is defined as the directly factorizable gauge group, SU(3)⊗ SU(2)⊗U(1) [2]. Interactions in the Standard Model are mediated by gauge bosons associated with the local symmetries of the model. Matter is divided into two classes, quarks and leptons, as described below.

Quarks are classified in three families, which each include a left-handed doublet and two right-handed singlets, where handedness refers to weak isospin chiralities, labeled below with the subscripts "L" and "R", respectively. As the $W^{\pm}$ boson does not interact with right-handed fermions (or left-handed anti-fermions), right-handed neutrinos have no gauge interactions, and are thus not included in the listings below.

$$Q_L = \begin{pmatrix} u_L \\ d_L \end{pmatrix}, \begin{pmatrix} c_L \\ s_L \end{pmatrix}, \begin{pmatrix} t_L \\ b_L \end{pmatrix} \quad (1)$$

$$Q_R = u_R, d_R, c_R, s_R, t_R, b_R \quad (2)$$

$$L_L = \begin{pmatrix} \nu_L^e \\ e_L \end{pmatrix}, \begin{pmatrix} \nu_L^\mu \\ \mu_L \end{pmatrix}, \begin{pmatrix} \nu_L^\tau \\ \tau_L \end{pmatrix} \quad (3)$$

$$L_R = e_R, \mu_R, \tau_R \quad (4)$$

All quarks and leptons are fermions, with an intrinsic spin quantum number of $\frac{1}{2}$. The "up-type" quarks, represented by u, c, and t in equation 1, all have charge $+\frac{2}{3}$, while their doublet counterparts, the "down-type" quarks (d, s, and b in equation 1) each have charge $-\frac{1}{3}$. Each of the neutrinos, (ν^e, ν^μ, and ν^τ) are charge neutral, while their counterparts, (e, μ, τ) all have charge -1.

All fundamental particles, fermions and bosons, have corresponding antiparticles within the

Standard Model that have equal mass, lifetime, and intrinsic angular momentum, but an equal and opposite charge. The Standard Model does not make predictions of the masses of the fermions. The values of these masses, as they have been determined in experiments are shown in Table 1 [3].

		Mass [GeV/c^2]	Charge
Quarks	u	$(1.5 \text{ to } 3.3)\cdot 10^{-3}$	$\frac{2}{3}$
	d	$(3.5 \text{ to } 6.0)\cdot 10^{-3}$	$-\frac{1}{3}$
	c	$1.27^{+0.07}_{-0.11}$	$\frac{2}{3}$
	s	$105^{+25}_{-35} \cdot 10^{-3}$	$-\frac{1}{3}$
	t	$171.3 \pm 1.1 \pm 1.2$	$\frac{2}{3}$
	b	$4.20^{+0.17}_{-0.07}$	$-\frac{1}{3}$
Leptons	ν_e	$< 225 \cdot 10^{-9}$ CL 95%	0
	e	$(0.510998910 \pm 0.000000013)\cdot 10^{-3}$	-1
	ν_μ	$< 0.19 \cdot 10^{-3}$ CL 90%	0
	μ	$(105.658367 \pm 0.000004)\cdot 10^{-3}$	-1
	ν_τ	$< 18.2 \cdot 10^{-3}$ CL 95%	0
	τ	$1776.84 \pm 0.17 \cdot 10^{-3}$	-1

Table 1: Experimental determinations of fermion masses [3].

In the Standard Model, all fermions couple to bosons ($W^\pm$ and Z^0) that mediate the weak force. Also, all charged fermions couple to photons (γ), the bosons that mediate the electromagnetic force. Further, each of the quarks, due to an additional quantum number they possess called "color," also couple to a collection of gauge bosons called gluons (g).

2.1.1 QCD in the Standard Model

The strength of the color force is sufficiently great that quarks are not observed in the laboratory in isolation. Instead, particles may be produced by vacuum fluctuations in order to balance the color to a neutral (or "white") state, overall. This color confinement causes the high energy collisions of particles to have a complicated dynamics involving "hadronization," wherein quarks produced in collision with high transverse momentum produce new bound states with particles generated in vacuum fluctuations.

It is worth noting that, in contrast to quantum electrodynamics, quantum chromodynamics (QCD) is a non-perturbative theory. As a result, the fragmentation and hadronization processes

in physics cannot be determined from first principles. In high energy scenarios, however, the coupling constant in QCD decreases logarithmically, and the dynamics become amenable to perturbation theory. Further, this running coupling constant allows for an asymptotic freedom, where at sufficiently short length scales, the color force becomes arbitrarily weak.

2.1.2 The Cabibbo-Kobayashi-Maskawa Matrix

While all fermions couple to the weak force, interactions between generations are mediated exclusively by $W^{\pm}$ bosons. Via radiation of a $W^{\pm}$, each quark may couple with any of three other possible quarks – any "up-type" quark may couple with any "down-type" quark and vice-versa. The Standard Model permits an interpretation that generational mixing via the weak force is the result of differences in the mass eigenstates and flavor eigenstates. The transformation between the flavor basis and the mass basis can thus be represented as a 3×3 matrix, $\mathbf{V}_{\mathrm{CKM}}$, (named the Cabibbo-Kobayashi-Maskawa matrix, for scientists Nicola Cabibbo, Makoto Kobayashi, and Toshihide Maskawa) as shown in Equation 5 [4, 5].

$$\mathbf{V}_{\mathrm{CKM}} = \begin{pmatrix} V_{ud} & V_{us} & V_{ub} \\ V_{cd} & V_{cs} & V_{cb} \\ V_{td} & V_{ts} & V_{tb} \end{pmatrix} \tag{5}$$

The eighteen parameters corresponding to the nine complex elements of this array are constrained within the standard model. The matrix is constrained to be unitary, meaning $\mathbf{V}_{\mathrm{CKM}}\mathbf{V}_{\mathrm{CKM}}^{\dagger} = \mathbb{1}$. This requirement, given that there are only three generations of quarks, implies that there are only nine free parameters. In addition, the complex phase of each element does not have a physical meaning. Thus, a global phase can be set to unity for the matrix, while the remaining four relative phases will have no physical meaning.

Unitarity, as defined in equation 6, generates a system of equations from the elements of the matrix (and their complex conjugates) as shown in equation 7.

$$\mathbf{V}_{\mathrm{CKM}}\mathbf{V}_{\mathrm{CKM}}^{\dagger} = \mathbb{1} \tag{6}$$

$$\sum_{k} V_{ki}V_{kj}^{*} = \delta_{ij},\ k \in \{u,c,t\},\ i,j \in \{d,s,b\} \tag{7}$$

$$\therefore V_{ud}V_{ub}^{*} + V_{cd}V_{cb}^{*} + V_{td}V_{tb}^{*} = 0 \tag{8}$$

By selecting the case $i = d$ and $j = b$, equation 7 generates equation 8 to explicitly show the relationship among 6 particular elements of the CKM matrix.

Through experiment, it is determined that the matrix is nearly diagonal. This fact provides an opportunity to approximate the elements. After selecting a global phase, an approximation is expressed in equation 9 [6].

$$\mathbf{V}_{\mathrm{CKM}} = \begin{pmatrix} \mathrm{c}_{13} & \mathrm{s}_{12}\mathrm{c}_{13} & \mathrm{s}_{13}e^{-i\delta_{13}} \\ -\mathrm{s}_{12}\mathrm{c}_{23} - \mathrm{c}_{12}\mathrm{s}_{23}\mathrm{s}_{13}e^{-i\delta_{13}} & \mathrm{c}_{12}\mathrm{c}_{23} - \mathrm{s}_{12}\mathrm{s}_{23}\mathrm{s}_{13}e^{-i\delta_{13}} & \mathrm{s}_{23}\mathrm{c}_{13} \\ \mathrm{s}_{12}\mathrm{c}_{23} - \mathrm{c}_{12}\mathrm{s}_{23}\mathrm{s}_{13}e^{-i\delta_{13}} & -\mathrm{c}_{12}\mathrm{c}_{23} - \mathrm{s}_{12}\mathrm{s}_{23}\mathrm{s}_{13}e^{-i\delta_{13}} & \mathrm{c}_{23}\mathrm{c}_{13} \end{pmatrix} \tag{9}$$

Here, s_{ij} and c_{ij} represent the operations sin θ_{ij} and cos θ_{ij} respectively, acting on a rotational angle θ_{ij}; δ_{13} is the phase corresponding the components of the matrix with complex value. While this is the standard representation of the CKM matrix, we are able to create another, equivalent representation using four new parameters, from functions of s_{ij}, c_{ij}, θ_{ij}, and δ_{13}. These four new parameters are defined in equation 10 [7].

$$\begin{aligned} \lambda &\stackrel{\mathrm{def}}{=} \mathrm{s}_{12} \\ \mathrm{A}\lambda^2 &\stackrel{\mathrm{def}}{=} \mathrm{s}_{23} \\ \mathrm{A}\lambda^3(\rho - i\eta) &\stackrel{\mathrm{def}}{=} \mathrm{s}_{13}e^{-i\delta_{13}} \\ \eta/\rho &\stackrel{\mathrm{def}}{=} \mathrm{s}_{13}/\mathrm{c}_{13} \end{aligned} \tag{10}$$

In using these four new parameters, we create a new representation of the CKM matrix

that relies on the diagonal nature of the elements. That is, a polynomial expansion in powers of λ (which is less than one), becomes increasingly accurate. This approach is termed the Wolfenstein parameterization, and is shown (to order $\mathcal{O}(\lambda^3)$) in equation 11.

$$\mathbf{V}_{\mathrm{CKM}} \approx \begin{pmatrix} 1-\frac{\lambda^2}{2} & \lambda & \mathrm{A}\lambda^3(\rho - i\eta) \\ -\lambda & 1-\frac{\lambda^2}{2} & \mathrm{A}\lambda^2 \\ \mathrm{A}\lambda^3(1-\rho-i\eta) & -\mathrm{A}\lambda^2 & 1 \end{pmatrix} \tag{11}$$

If equation 8 is expressed using the Wolfenstein parameterization, each term is of order $\mathcal{O}(\lambda^3)$ in the expression, making the variables in this equation more readily studied by experimental means. Rewriting and rearranging this equation using Wolfenstein parameters is shown in equation 12.

$$\begin{aligned} \frac{V_{ud}V_{ub}^*}{V_{cd}V_{cb}^*} + \frac{V_{td}V_{tb}^*}{V_{cd}V_{cb}^*} &= -1 \\ -\frac{V_{ud}V_{ub}^*}{V_{cd}V_{cb}^*} + \left(-\frac{V_{td}V_{tb}^*}{V_{cd}V_{cb}^*}\right) &= 1 \\ \left(1-\frac{\lambda^2}{2}\right)(\rho+i\eta) + \left(-\frac{V_{td}V_{tb}^*}{V_{cd}V_{cb}^*}\right) &= 1 \\ \bar{\rho} &\stackrel{\mathrm{def}}{=} \rho\left(1-\frac{\lambda^2}{2}\right) \\ \bar{\eta} &\stackrel{\mathrm{def}}{=} \eta\left(1-\frac{\lambda^2}{2}\right) \\ (\bar{\rho}+i\bar{\eta}) + \left(-\frac{V_{td}V_{tb}^*}{V_{cd}V_{cb}^*}\right) &= 1 \end{aligned} \tag{12}$$

In this presentation, the two, newly-defined parameters, $\bar{\rho}$ and $\bar{\eta}$ can be thought of as co-ordinates on the complex plane, $\bar{\rho}$ defining a distance along the real axis, $\bar{\eta}$ defining a distance along the imaginary axis. In describing the variables in this way, we can use equation 12 to draw a triangle with a base normalized in length to unity. The other legs of the triangles connect at the point $(\bar{\rho}, \bar{\eta})$ in the complex plane. A diagram showing this construction is shown in Figure 1.

The angles shown in the Unitarity Triangle of Figure 1 are of direct physical significance.

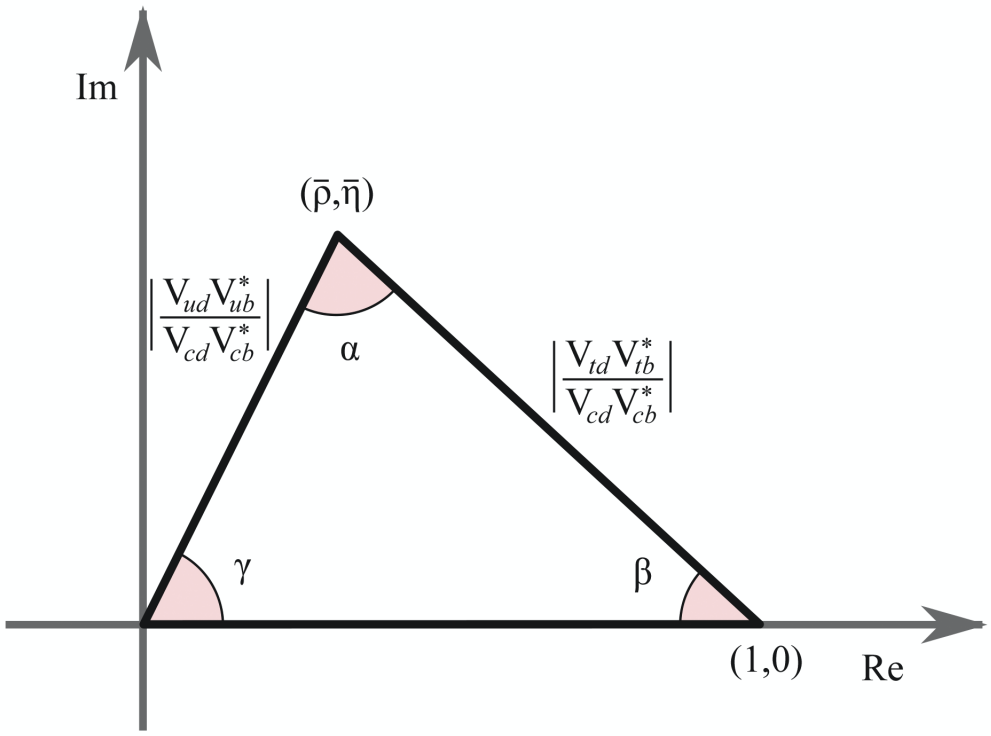

Figure 1: The Unitarity Triangle. A representation of the values $\bar{\rho}$ and $i\bar{\eta}$ in the complex plane.

For example, were β measured to be zero, CP violation would not be present in the Standard Model. However, CP violation has been observed, and β has been measured to be significantly above zero. The most recent measures of each of these angles are shown in Table 2 [3]. Measures of the Wolfenstein parameters are listed in Table 3 [3].

$$\begin{array}{ccc|ccc} \alpha & \stackrel{\text{def}}{=} & \arg\left(-\frac{V_{td}V_{tb}^*}{V_{ud}V_{ub}^*}\right) & \alpha & = & \left(88^{+6}_{-5}\right)^\circ \\ \beta & \stackrel{\text{def}}{=} & \arg\left(-\frac{V_{cd}V_{cb}^*}{V_{td}V_{tb}^*}\right) & \sin 2\beta & = & 0.681 \pm 0.025 \\ \gamma & \stackrel{\text{def}}{=} & \arg\left(-\frac{V_{ud}V_{ub}^*}{V_{cd}V_{cb}^*}\right) & \gamma & = & \left(77^{+30}_{-32}\right)^\circ \end{array}$$

Table 2: Experimental measures of the Interior Angles of the Unitarity Triangle [3].

Parameter	Value
λ	$0.2257^{+0.0009}_{-0.0010}$
A	$0.814^{+0.021}_{-0.022}$
$\bar{\rho}$	$0.135^{+0.031}_{-0.016}$
$\bar{\eta}$	$0.349^{+0.015}_{-0.017}$

Table 3: Experimental determinations of the Wolfenstein Parameters [3].

The different experimental measures of the coordinates of $\bar{\rho}$ and $\bar{\eta}$ have been fairly consistent. The overlap of these measurements has been plotted in Figure 2 [3]. This analysis provides an opportunity to directly study the competing tree-level decay modes of the B_c^+, which is probative to the values of V_{cb}, and V_{cs}.

2.2 Lifetimes of B Mesons

As a result of color confinement, quarks are not seen in isolation in nature. Thus, any measure of the lifetime associated with b quarks comes from a measure of the lifetime of B hadrons. Because weak force mediated decays of b quarks are constrained within the Standard Model to change generations, they are said to be "Cabibbo-suppressed." As a result, B mesons (other than the Υ, the unflavored $b\bar{b}$ meson) are relatively long-lived compared to other particles that may decay by strong or electromagnetic interactions. The decays of these flavored B mesons are often described in a "spectator model," where the decay of the b quark drives the overall decay rate, while the lighter quark does not directly participate in the process.

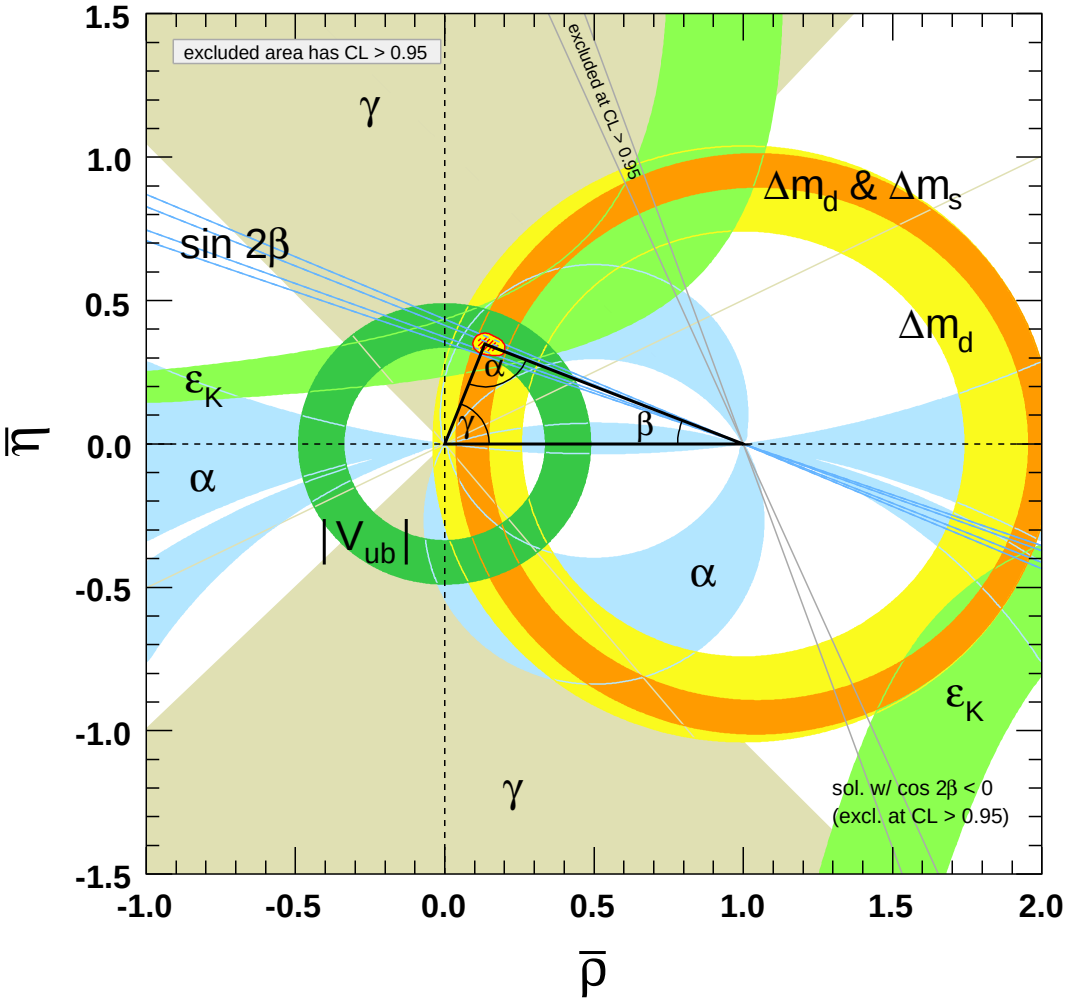

Figure 2: The overlap of various experimental measures of $\bar{\rho}$ and $\bar{\eta}$. The shaded regions have 95% CL [3].

Meson	Measured Mass [3]	Measured Lifetime [3]
B_c^+	6.277 ± 0.006 GeV/c^2	$(0.453 \pm 0.041) \times 10^{-12}$ s
B_s^0	5366.3 ± 0.6 MeV/c^2	$(1.472^{+0.024}_{-0.026}) \times 10^{-12}$ s
B^+	5279.17 ± 0.29 MeV/c^2	$(1.638 \pm 0.011) \times 10^{-12}$ s
B^0	5279.50 ± 0.30 MeV/c^2	$(1.525 \pm 0.009) \times 10^{-12}$ s

Table 4: Weakly decaying B mesons show similar lifetimes and masses, as the b quark is dominantly responsible for both properties. It is evident, however, that the heavy c quark plays a role in decreasing the lifetime of the B_c^+ with respect to the other, lighter B mesons [3].

Indeed, this spectator model is fairly acccurate in predicting the lifetime of the light B mesons. However, the mass of the c quark in a B_c^+ meson implies that this model is inappropriate for making a lifetime estimation. There exist other tree-level decays for the B_c^+ mesons beyond b quark decay. The possible tree-level decays of the B_c^+ are shown in Figure 3.

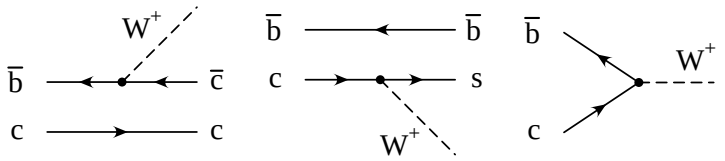

Figure 3: Three categories of B_c^+ decays: b decay, c decay, and annihilation to $W^{\pm}$.

Because of the possibility of contribution of the heavy c quark in B_c^+ decays, Heavy Quark Effective Theory, a powerful tool in predicting the lifetimes of B mesons in the spectator model, is not useful in analyzing the overall B_c^+ lifetime. Instead, the B_c^+ is better understood as two heavy quarks, similar to a $c\bar{c}$ or $b\bar{b}$ bound state. All of this is in line with current experimental determinations of B meson lifetimes, which show the shorter lifetime of the B_c^+ compared to those mesons where the b quark is bound with a lighter, spectator quark. The specific lifetimes are shown in Table 4 [3].

2.3 The B_c^+ Meson

2.3.1 Theoretical Significance of B_c^+

The B_c^+ meson is the heaviest flavored ground-state meson. In Section 2.2, the relatively short lifetime of the B_c^+ meson (compared to other, lighter B mesons) is attributed to the combination

of two massive quarks to form a bound state, where both quarks contribute to the decay rate.

As an *ab initio* theory, lattice QCD has proven capable of predicting B_c^+ mass [13]. By nature of the composition of the B_c^+, a mass measurement can experimentally test the heavy-quark methods of lattice QCD. Previous lattice QCD models for the mass splittings of $b\bar{b}$ and $c\bar{c}$ pairs substantiate the expectation that light mass quarks (sea-quarks) should have a modest contribution to computations related to the B_c^+ [13]. Examining new, fully reconstructed decays of the B_c^+ meson in a new decay channel could refine this kind of measurement.

Perturbative QCD also provides testable predictions concerning the B_c^+, including its mass and the spectroscopy of $b\bar{c}$ bound states (including the 1^1S_0 ground state, constrained to decay weakly, as well as other, excited bound states). An experimental comparison of these predictions could clarify the importance of non-zero charm-quark mass loops in these perturbative calculations [14].

In addition, a nonrelativistic potential model can provide strong predictions concerning the B_c^+ and its excited states [15]. Further, the spectral lines, as computed in this model, are extraordinarily narrow, allowing for radiative decays (hadronic and electromagnetic) with potentially observable peaks in the mass distribution of particles generated near the B_c^+ [16].

All B_c^+ mesons observed thus far have been produced at the Tevatron and have decayed via b decay to $J/\psi\ell X$ or $J/\psi\pi$ [3]. Existing theory, however, indicates that the dominant decay channel is c decay, due to CKM suppression of b decay and annihilation [17]. This decay is of particular interest, as it produces another bottom-flavored, weakly-decaying meson, the B_s^0. Thus, the full decay of $B_c^+ \to B_s^0 X$ is an opportunity to observe a "double-weak double-B decay" for the first time.

2.3.2 Experimental History of B_c^+

As mentioned in Section 2.3.1, previous observations of B_c^+ have occurred only in the $J/\psi X$ channels, where the b quark directly radiates a virtual $W^\pm$ boson. These observations were first reported in a search over 110 pb^{-1} of data taken from high energy $p\bar{p}$ collisions in the CDF detector [21]. The decay channel in this observation was $B_c^+ \to J/\psi\ell^\pm X$, and the mass plot is shown in Figure 4 [21]. Later searches were able to uncover the B_c^+ in a related decay,

Year	Measured B_c^+ Mass [3]	Measured B_c^+ Lifetime [3]
1998	$6.4 \pm 0.39 \pm 0.13$ GeV/c^2	$(0.46^{+0.18}_{-0.16} \pm 0.03) \times 10^{-12}$ s
2006	$6.2857 \pm 0.0053 \pm 0.0012$ GeV/c^2	$(0.463^{+0.073}_{-0.065} \pm 0.036) \times 10^{-12}$ s
2008	$6.2756 \pm 0.0029 \pm 0.0025$ GeV/c^2	—

Table 5: A history of B_c^+ mass and lifetime measurements performed at CDF II [3].

$B_c^+ \to J/\psi\pi^+$ [22]. The most recent mass measurement from this observed decay is shown in Figure 5. A history of B_c^+ mass and lifetime measurements made at CDF II is shown in Table 5 [3].

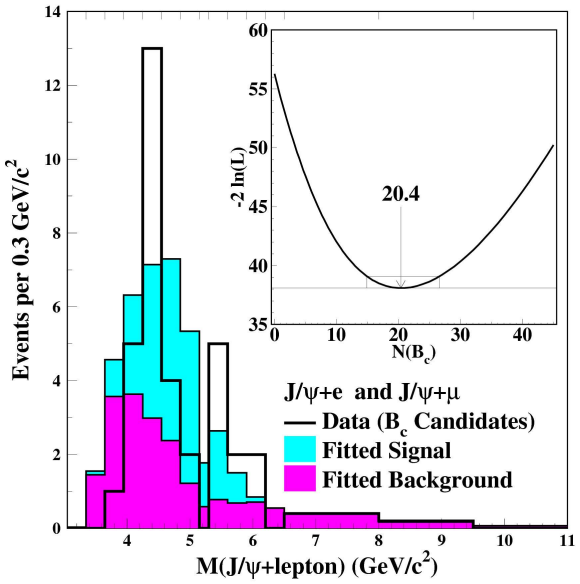

Figure 4: Histogram of the $J/\psi\ell$ mass that compares the signal and background contributions determined in the likelihood fit to the combined data for $J/\psi e$ and $J/\psi\mu$. The total B_c contribution is $20.4^{+6.2}_{-5.5}$ events. The inset shows the behavior of the loglikelihood function $-2\ln(L)$ vs. the number of B_c mesons [21].

To date, the B_c^+ has been observed exclusively at the Tevatron, though not for lack of effort. Before the observation of B_c^+ at the Tevatron, researchers at LEP searched for B_c^+ production within a sample of more than 3 million Z^0 hadronic decays produced by e^+e^- collisions and collected by the DELPHI Collaboration [23]. The OPAL Collaboration and ALEPH Collaboration also searched for B_c^+ decays from the Z^0 resonance [24, 25].

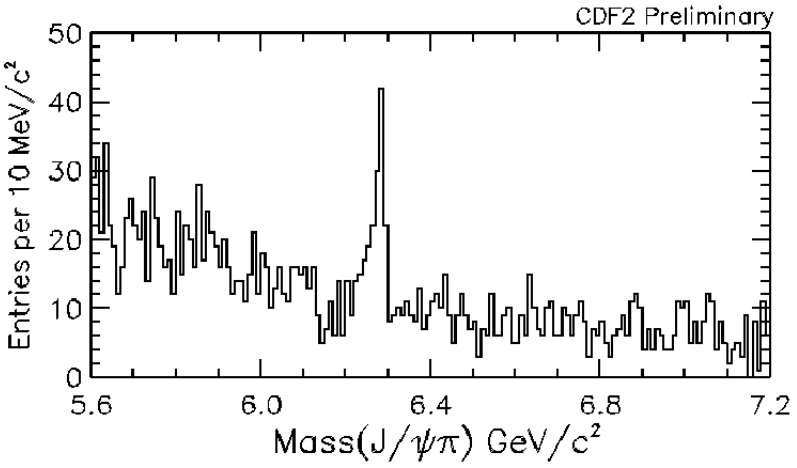

Figure 5: Histogram of the most recent measurement of $J/\psi\pi^{\pm}$ mass, performed at CDF II [22].

This analysis is the first published attempt to search for B_c^+ through a c decay channel, as described in Section 2.3.1. Because theory indicates that this decay mode will be preferred, evidence of a signal seems possible, while a lack evidence could generate considerable interest, depending on the strength of the limit that could be set by the large sample of data recorded at CDF.

2.3.3 B_c^+ Search Strategy

This analysis details, in particular, the search for $B_c^+ \to B_s^0\ \pi^+$, $B_s^0 \to J/\psi\ \phi$, $J/\psi \to \mu^+\mu^-$, $\phi \to K^+K^-$. This is a final state of five charged particles, to be selected within a Di-Muon Trigger sample as described in Section 4.4.1, with precise momentum and decay length quantities are provided by the tracking system of the detector. In this section, details of the strategy for this analysis will be reviewed.

Primary Challenges of the $B_c^+ \to B_s^0\ \pi^+$ Search The strategy used in this analysis is designed to overcome two major challenges: the minimization of uncertainties that affect the final measurement; and the selection of B_c^+ candidates over a significant prompt B_s^0+track background, where the extra track is the result of fragmentation at the interaction point.

To overcome the first challenge, the selection techniques used in previous searches for $B_s^0 \rightarrow J/\psi\ \phi$ are employed to create a sample, within which $B_c^+ \rightarrow B_s^0\ \pi^+$ candidates are evaluated. The resulting limit on the yield of $B_c^+ \rightarrow B_s^0 \pi^+$ candidates is then computed relative to the B_s^0 yield. In doing so, uncertainties associated with acceptance and efficiency are limited to the identification of a single track. Other uncertainties, such as luminosity, are completely canceled by the technique. The details of this cancelation are shown in Chapter 12.

In order to overcome the second challenge, that of selecting B_c^+ signal candidates within a large B_s^0+track background, an artificial neural network is trained to select likely candidates using a knowledge of simulated B_c^+ signal events as well as a sample of prompt B_s^0 background. Details of the training of this neural network are discussed in Chapter 11.

Estimating the $B_c^+ \rightarrow B_s^0\pi^+$ Branching Fraction The relative yield, $\frac{N_{B_c}(observed)}{N_{B_s}(observed)}$, is directly related to the branching fraction of $B_c^+ \rightarrow B_s^0\pi^+$, by equation 13.

$$\frac{N_{B_c}(obs)}{N_{B_s}(obs)} = \frac{f_c}{f_s} \cdot \mathcal{B}(B_c^+ \rightarrow B_s^0\ \pi^+) \cdot \left(\frac{\mathcal{A}_{B_c} \cdot \epsilon_{B_c}}{\mathcal{A}_{B_s} \cdot \epsilon_{B_s}}\right) \tag{13}$$

Here, $\mathcal{A}\cdot\epsilon$ represents the acceptance times efficiency of a decay – a product ranging between zero and one, representing the sensitivity of the experiment to signal. The values f_c and f_s correspond to the fragmentation fractions to B_c^+ and B_s^0, respectively. The probability that a given $\bar{b}$ quark produced by the $p\bar{p}$ collision will hadronize to a B_c^+ is represented as f_c. Likewise, f_s is the likelihood that a B_s^0 will be produced in the hadronization of a $\bar{b}$ quark.

An estimate of these two values can be extracted from experiments in other modes. By comparing the $B_c^+ \rightarrow J/\psi\ \pi^+$ decay, which has been observed, to the $B^- \rightarrow J/\psi\ K^-$ yield in data, the value of f_c can be extracted, as shown in equation 14 [26, 27]. That these decays are topologically quite similar allows for a useful comparison. In order to make an estimate of f_c, it is assumed that efficiencies and acceptances for the two modes will roughly cancel.

$$
\begin{aligned}
\frac{N(B_c^+ \to J/\psi\ \pi^+)}{N(B^+ \to J/\psi\ K^+)} &= \frac{f_{B_c^+} \cdot \epsilon_{B_c^+} \cdot \mathcal{B}(B_c^+ \to J/\psi\ \pi^+)}{f_{B^+} \cdot \epsilon_{B^+} \cdot \mathcal{B}(B^+ \to J/\psi\ K^+)} \\
&\approx \frac{f_{B_c^+} \cdot \mathcal{B}(B_c^+ \to J/\psi\ \pi^+)}{f_{B^+} \cdot \mathcal{B}(B^+ \to J/\psi\ K^+)} \\
\therefore f_c \stackrel{\text{def}}{=} f_{B_c^+} &\approx f_{B^+} \cdot \frac{N(B_c^+ \to J/\psi\ \pi^+)}{N(B^+ \to J/\psi\ K^+)} \cdot \frac{\mathcal{B}(B^+ \to J/\psi\ K^+)}{\mathcal{B}(B_c^+ \to J/\psi\ \pi^+)} \\
&= 39.9\% \cdot \frac{108}{21,100} \cdot \frac{1.0 \times 10^{-3}}{1.3 \times 10^{-3}} \\
&\approx 0.16\% \qquad (14)
\end{aligned}
$$

Values for number of observed events are taken from previous experiments at CDF [22], while the B^+ fragmentation fraction and branching ratio are drawn from the PDG [3], and the B_c^+ branching ratio is taken from theoretical models [17]. With this estimate of f_c, along with the PDG value of f_s, (11.0% [3]), the ratio of fragmentation fractions is estimated to be $\frac{f_c}{f_s} = 0.014$. This value is used, in combination with measurements of the number of $B_c^+ \to B_s^0\ \pi^+$ events observed in this analysis, to estimate the branching fraction, $\mathcal{B}(B_c^+ \to B_s^0\ \pi^+)$. Because this technique of estimating $\frac{f_c}{f_s} = 0.014$ relies on the theoretical value of $\mathcal{B}(B_c^+ \to J/\psi\ \pi^+)$, which is not known precisely, an alternative value for the $J/\psi\ \pi^+$ branching fraction (and, thus, the fragmentation fraction and $B_s^0\ \pi^+$ branching fraction) is examined. The resulting estimate of the ratio of cross-sections under both estimates is shown in Section 12.6.

Using Δm as a Discriminating Variable Both the B_s^0 and the B_c^+ mesons have been observed at the Tevatron, and rather precise mass measurements have been made. The total mass of the combination of the B_s^0 and the extra track from a $B_c^+ \to B_s^0\pi^+$ decay should equal the B_c^+ mass, as this is a fully reconstructed decay. Therefore, the difference between the mass in this combination and the mass of the B_s^0 meson should be constant for $B_c^+ \to B_s^0\pi^+$ decays, and have better resolution as uncertainties in the B_s^0 reconstruction are not incorporated in the result. This quantity, $\mathrm{m}(B_s^0 + \pi^+) - \mathrm{m}(B_s^0)$, also termed Δm in this analysis, is estimated (using PDG values of B_s^0 and B_c^+ mass) to be 0.91 GeV/c^2 for all $B_c^+ \to B_s^0\pi^+$ decays.

Other, partially reconstructed $B_c^+ \to B_s^0 X$ decays can occur, such as the $B_c^+ \to B_s^0\mu\nu_\mu$.

These alternate decay modes always have a lower value of Δm, due to the non-zero mass of the undetected particle. A topologically similar decay to the $B_c^+ \to B_s^0\pi^+$ decay is the $B_c^+ \to B_s^*\pi^+$, $B_s^* \to B_s^0\gamma$ decay. The Δm for this decay is slightly lower, offset by the 49 MeV/c^2 associated with the spectroscopic transition of the B_s^* decay to B_s^0, the electromagnetic ground state.

A Monte Carlo simulation of B_c^+ decays (without any background) shows the distribution of Δm as described above in Figure 6 [26]. The primary peak, to the right, is composed of fully reconstructed $B_c^+ \to B_s^0\pi^+$ candidates for which this analysis will search. Immediately to its left is a secondary peak with the collection of events of $B_s^* \to B_s^0\gamma$. Events below that are broadened by the larger phase space available to the neutral particles not detected in the decays. No events are expected above the fully reconstructed peak in Δm, as this region is kinematically forbidden. Therefore, this region is useful as a sideband for understanding background contributions in data.

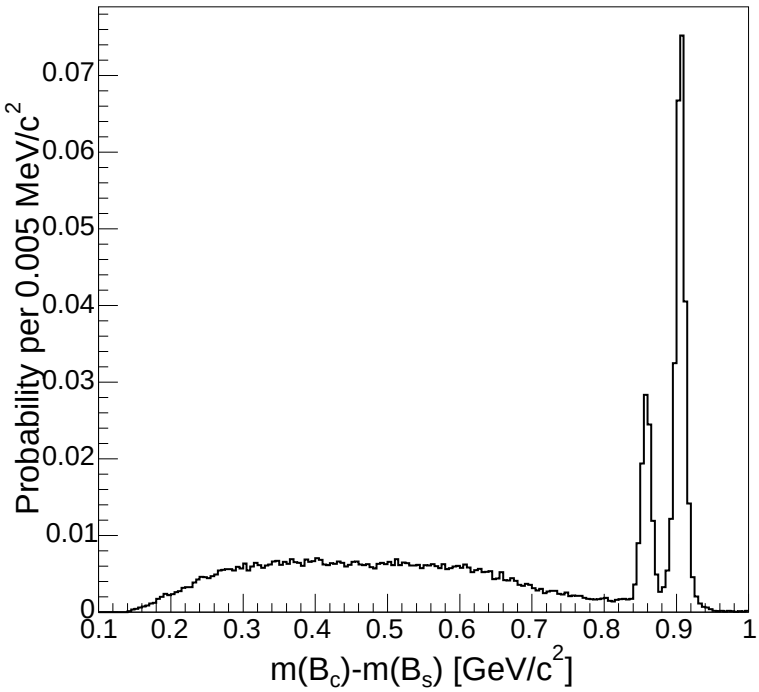

Figure 6: Monte Carlo simulation of Δm from $B_c^+ \to B_s^{(*)0}X$ decays. The primary peak, located at Δm=0.91 GeV/c^2 corresponds to the fully reconstructed $B_c^+ \to B_s^0\pi^+$ decays sought in this analysis [26].

2.3.4 The B_c^+ Meson p_T Spectrum

Compared to other B mesons, little is known about the B_c^+ production spectrum at the Tevatron. However, a proper estimate of the anticipated momentum of the B_c^+ candidates is important to building a selection algorithm. Monte carlo simulations suggest that B_s^0 candidates resulting from $B_c^+ \to B_s^0\ \pi^+$ decays will be softer than their prompt counterparts.

This can be understood intuitively by considering the role of the hadronization responsible for creating B_c^+ and prompt B_s^0 particles. In the vast majority of cases, both of these species are produced by the creation of a b quark at the interaction point, caused by the energy of collision. The second quark, c in the case of B_c^+ and s in the case of B_s^0, is created by hadronization – a form of quantum vacuum fluctuation brought about by the energy associated with the color-confinement of the scattered b quark. It is known that the energy required in a given event to pull a c quark out of the vacuum will be greater than that required to produce an s quark. As a result, B_c^+ mesons will tend to be lower in p_T than prompt B_s^0 candidates. This means that B_c^+ mesons, having a softer spectrum than prompt B_s^0, should have lower acceptance by the B_s^0 neural network.

2.3.5 Future Research Opportunities for B_c^+

As described above, the spectroscopy of B_c^+ is of considerable interest to theorists. Direct measurments of the branching ratios for $B_c^+ \to B_s^0 X$ can allow for a better understanding of non-"spectator" effects in B_c^+ decay. A large collection of likely B_c^+ candidate events would allow for a search for the radiative decay products of an excitation in the $b\bar{c}$ bound state, as well as for a precise measure of lifetime and mass of the B_c^+ meson. These searches could be performed simultaneously within the previously observed $J/\psi X$ modes as well as candidates from $B_s^0 X$ decays.

Further, it has been speculated that B_s^0 mesons, which have a high mixing frequency, could be flavor tagged at their creation using the associated track from the $B_c^+ \to B_s^0 \pi^+$ decay vertex [16]. This would boost the already powerful B_s^0 mixing studies that could be performed at LHCb, and further the understanding of CP violation in the B_s^0 system.

3 The CDF II Experiment at the Tevatron

Since 1967, the Fermi National Accelerator Laboratory, located 32 miles west of Chicago, has hosted advanced research in high-energy physics. The Tevatron, a circular proton-antiproton accelerator and collider, is home to highest center-of-mass energy $p\bar{p}$ collisions ever studied, currently operating at $\sqrt{s} = 1.96$ TeV. Collisions are studied directly at two collision points along the beamline. The Collider-Detector at Fermilab (CDF) and D$\emptyset$, located at these two collision points, have the unique opportunity to gather data at the forefront of high energy physics.

In the first eleven years of operation, CDF accumulated 110 pb^{-1} of data at $\sqrt{s} = 1.8$ TeV. In 2001, the Tevatron was temporarily shutdown for upgrades. After this shutdown, the Tevatron operated at its higher center-of-mass energy, and data-taking henceforth was dubbed "Run II." During the shutdown, CDF was upgraded to meet the new data-taking demands, and was renamed "CDF II." This thesis uses 5.84 fb^{-1} of data collected at CDF II.

3.1 The Accelerator

3.1.1 Proton Production

Before proton-antiproton collisions within the Tevatron can occur, protons and antiprotons need to be created and accelerated to the required energy. To begin this process, protons are accelerated to 980 GeV, using the devices shown in Figure 7 [28].

Cockroft-Walton Accelerator To begin with, hydrogen gas (H_2) is converted into negatively charged hydrogen ions, using molybdenum electrodes. These negatively charged ions are then separated from other particles and accelerated through a 750 keV electrostatic field generated by the Cockroft-Walton accelerator, shown in Figure 8 [29].

The LINAC The "LINAC," a linear accelerator, receives negatively charged hydrogen ions from the Cockroft-Walton accelerator at an energy of approximately 750 keV. The LINAC is shown in Figure 9 [29]. Using oscillating RF (radio frequency) electromagnetic pulses, the

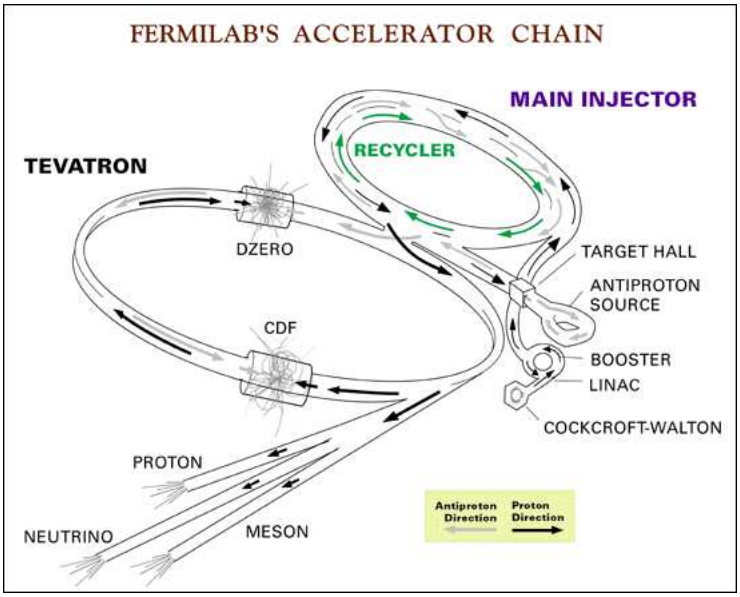

Figure 7: Multiple stages of acceleration for protons and antiprotons are performed by different components at Fermilab [28].

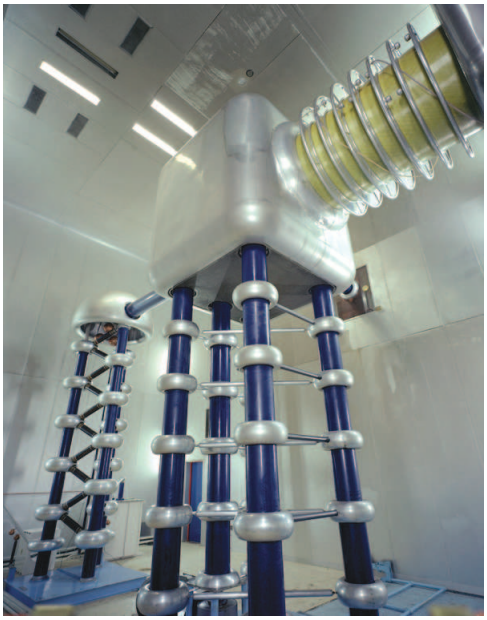

Figure 8: The first stage of acceleration is performed by Fermilab's Cockroft-Walton acclerator [29].

.

Figure 9: Acceleration up to 400 MeV is accomplished by RF pulsing in the LINAC [29].

LINAC accelerates the ions over the course of 150 m to an energy of 400 MeV – an energy of the same order as the hydrogen ion's rest energy. By the LINAC's design using RF pulses, the ionized Hydrogen output is bunched into pulses. At the far end of the LINAC, the hydrogen ions enter the Booster.

The Booster Negatively charged hydrogen ions enter the Booster (shown in Figure 10 [29]) at an energy of 400 MeV. Upon entering the Booster, these particles pass through a carbon foil which strips each hydrogen ion of both electrons. The resulting bare protons enter the Booster, a synchrotron and circular accelerator of radius 75 m. The Booster then collects these protons into 84 bunches, each bunch containing $6 \cdot 10^6$ protons. Each of these bunches is then accelerated during its passage around the Booster ring, increasing in energy by 500 keV per proton for each revolution. By the end of acceleration within the Booster, the protons achieve 8.9 GeV, before they are passed into the Main Injector.

The Main Injector The Main Injector (shown in Figure 11 [29]) plays a role in the production and acceleration of antiprotons, as well as the acceleration of protons. Before Run II

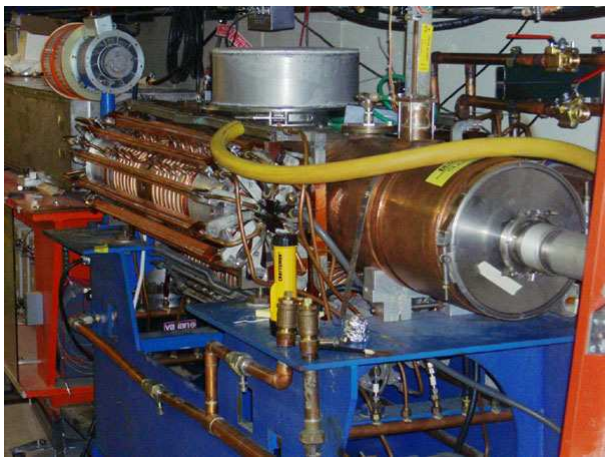

Figure 10: An RF Cavity and Alternate Gradient Magnet in the Booster Accelerator

.

Figure 11: The Main Injector Tunnel showing the Main Injector (blue magnets on bottom) and the Recycler (green magnets on top).

began, protons from the Booster were sent directly to the Main Ring for acceleration to colliding energy. Currently, protons leaving the Booster are sent to the Main Injector for that purpose. The Main Injector can receive protons or antiprotons from the Recycler and Accumulator. Either protons or antiprotons can be accelerated in the Main Injector to an energy of 150 GeV before being injected into the Tevatron for further acceleration and collision.

3.1.2 Antiproton Production and Accumulation

The Antiproton Source In order to produce antiprotons, a high energy collision of a proton beam on a fixed target of nickel is created. The protons are produced in the same accelerator setup as described above, and are diverted from the Main Injector. The Main Injector then fires the protons at an energy of 120 GeV at the target. A lithium lens is set up to direct the resulting antiprotons, which are produced, along with many other species of particle, in a wide angular distribution. At this stage, the antiprotons have an average momentum of 8 GeV, and are produced in bunches, due to the bunching of the beam from the Main Injector. After their creation, these antiprotons are collected into the Debuncher, where the beam loses its bunch structure. The Debuncher transforms the bunched beam of antiprotons with a wide distribution of energies into an unbunched, monochromatic beam. This beam can be stochastically cooled to 8 GeV before being injected into the final stage of the antiproton source, the Accumulator Ring. At the Accumulator Ring, the bunch structure of the antiproton beam is restored. At this point, the 8 GeV bunched beam of antiprotons leave the antiproton source and are sent to the Main Injector.

The Recycler Ring In 2004, a secondary storage ring for antiprotons, called the Recycler Ring, was added in the same tunnel as the Accumulator Ring. The rate of antiproton production is inversely related to the quantity of antiprotons stored in the Accumulator Ring. The Recycler Ring improves the antiproton production rate by keeping the quantity of antiprotons in the Accumulator Ring low. Since the rate limiting factor for luminosity in the Tevatron is the production and accumulation of antiprotons, the addition of the Recycler Ring improves the overall performance and running luminosity of the Tevatron.

3.2 The Tevatron

3.2.1 Collisions and Luminosity

After creation and acceleration, protons and antiprotons are injected into the Tevatron in preparation for acceleration to maximum energy and collision. Protons are injected first, as they are easier to reproduce in the case of an unexpected abort. The Main Injector adds 150 GeV protons in 36 bunches to the Tevatron. These bunches are divided in the three sets of twelve bunches, called trains. Each train is separated by 139 RF buckets. The twelve individual bunches within each train are separated by 21 RF buckets, which corresponds to a separation of 396 ns for particle energies approaching the speed of light. The additional space between trains allows for the stable injection of antiprotons and creates "abort gaps" which are necessary for the activation of magnets in the event that the beam needs to be terminated. Antiprotons are injected in a similar pattern of trains and bunches, heading in the opposite direction from the protons (counter-clockwise as viewed from above).

Once injected into the Tevatron, protons and antiprotons are rapidly accelerated to their final, collision energy of 980 GeV. This corresponds to a relativistic γ of over 1,000, or a velocity greater than 99.9999% of c. Because, at this stage, there are two beams of 36 bunches traveling in opposite directions, there exist many different points in the Tevatron where a collision is theoretically possible. Electrostatic separators are used to prevent these collisions during and after acceleration to final collision energy. Once the collision energy has been reached, some checks of beam quality are made and the beam is "scraped" or collimated to remove poorly bunched particles in a process called "halo removal." After this scraping, quadrapole magnets are used to steer the two beams into collisions at two points within the Tevatron. These two points are the locations of the collider detectors, CDF II and D$\emptyset$.

Instantaneous luminosity ($\mathcal{L}$) is used to quantitatively measure the cross-sectional size of the beams along with the frequency of beam crossings. This quantity is directly proportional to the likelihood of inelastic scattering on a given crossing. In this sense, the instantaneous luminosity and the time-integrated luminosity are direct measures of Tevatron performance. To compute instantaneous luminosity, Equation 15 is used.

$$\begin{aligned} \mathcal{L} &= \frac{n \cdot f \cdot N_p N_{\bar{p}}}{A} \cdot F(\frac{\sigma_l}{\beta^*}) \\ &= \frac{n \cdot f \cdot N_p N_{\bar{p}}}{2\pi(\sigma_p^2 + \sigma_{\bar{p}}^2)} \cdot F(\frac{\sigma_l}{\beta^*}) \end{aligned} \tag{15}$$

Here, f is the frequency of revolution for any bunch in the Tevatron; n is the number of bunches in the Tevatron; A is the cross-sectional area of the interaction region, which can be further broken down to the transverse widths of each beam, σ_p and $\sigma_{\bar{p}}$; N_p and $N_{\bar{p}}$ are the numbers of protons and antiprotons in a given bunch, respectively; and, lastly, $F(\frac{\sigma_l}{\beta^*})$ is a form factor that depends on the ratio of longitudinal bunch RMS (σ_l) and the beta function (β^*) at the interaction point. Typical numbers for N_p and $N_{\bar{p}}$ at the beginning of a store have reached as high as 2.2×10^{10}, and 1.0×10^{10}, respectively. Typical values for σ_p and $\sigma_{\bar{p}}$, the transverse width of the beam, are approximately 30 μm.

Further, a calculation of theoretical cross-section for a given physics interaction may be used, along with instantaneous luminosity, to predict the statistical rate at which that interaction will proceed. The typical unit for instantaneous luminosity is the inverse microbarn per second (which is equivalent to 10^{30} cm^{-2}/sec). Thus, it is common to measure cross sections in picobarns (or, similarly, in nanobarns).

3.3 Accelerator Performance

Since the beginning of Run II, the Tevatron has increased its instantaneous luminosity with numerous upgrades. This increase is plotted as a function of time in Figure 12 [31]. Because of this increasing peak instantaneous luminosity, the total integrated luminosity has grown rapidly, and the challenge of collecting data efficiently at the collider detectors has grown. The total integrated luminosity delivered by the Tevatron, along with the total integrated luminosity recorded to tape by CDF II, is plotted in Figure 13 [32].

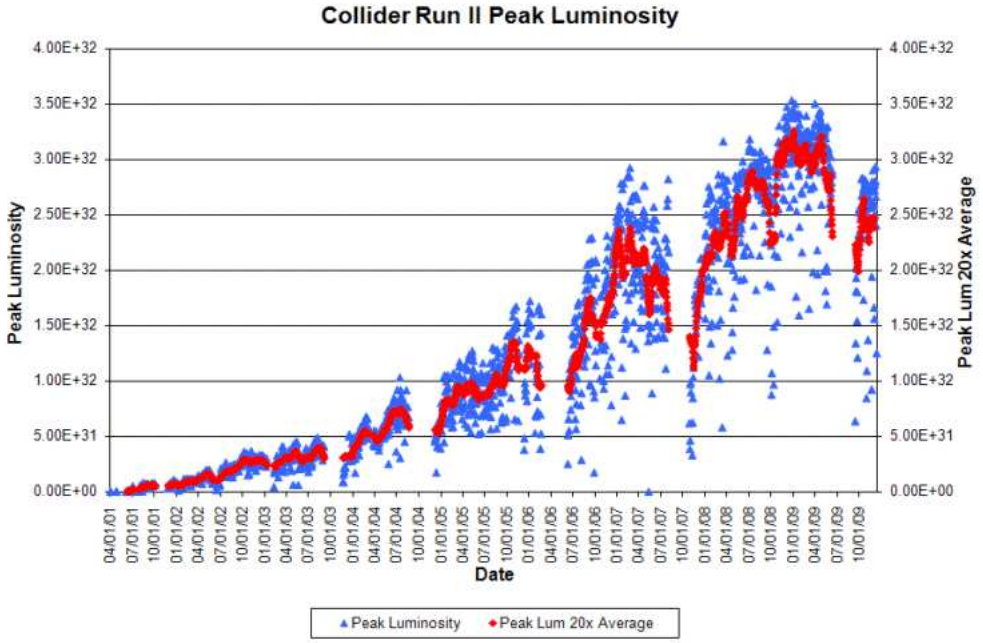

Figure 12: Peak Luminosity and Peak Luminosity 20X Average The blue triangles show the peak luminosity at the beginning of each store. The red diamond displays a point representing the last 20 peak values averaged together [31].

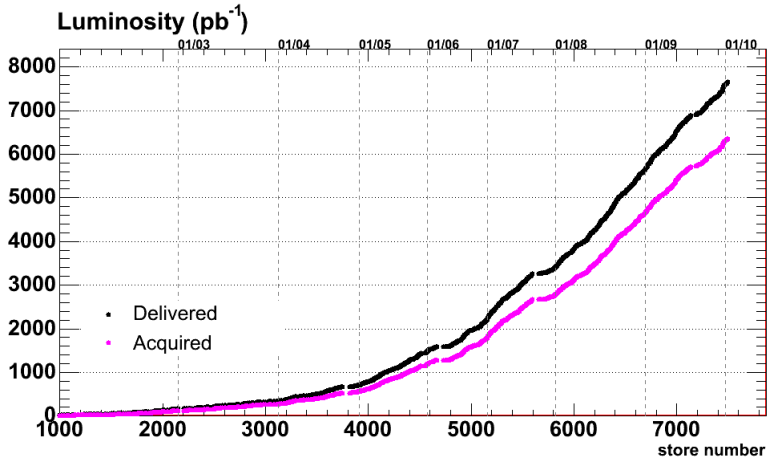

Figure 13: Integrated Luminosity Delivered and To Tape at CDF II [32].

3.4 CDF II

Located at the B0 interaction point on the beamline of the Tevatron, CDF II is a multipurpose solenoidal detector. Its design allows for a broad range of physics programs, spanning from bottom and charm studies to searches for the Higgs boson and physics beyond the Standard Model.

The structure of the detector is shown in Figure 14. A cylindrical coordinate system has been defined to describe the detector. The beamline as it passes through the detector is defined as the z-axis, with the trajectory of the protons defined as the positive direction in z. The distance perpendicular to the beamline is, naturally, defined as r, while ϕ is the angular measure around the beamline. The value of ϕ is defined as zero in the half-plane parallel to the horizon and on the geographic north side of the detector. (The coordinate system is also right-handed.)

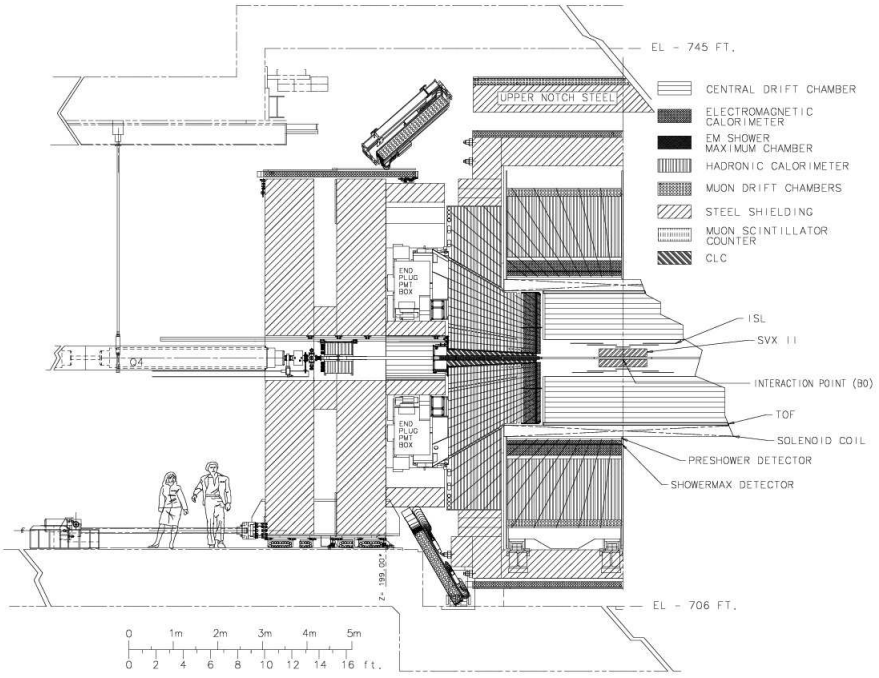

Figure 14: Elevation view of one half of the CDF II detector [33].

While the polar angle, θ, is also defined, its value (which ranges from 0 to π) is usually trans-

formed into the more useful, Lorentz-Invariant quantity, η, (also known as "pseudorapidity") defined in Equation 16. Occasionally, the quantity of rapidity, y is used, as defined in Equation 17, particularly when computing acceptance calculations for the detector. It is relevant that, as a particle's total energy rises, and its fraction of energy found in rest mass falls, the two quantities converge to the same value.

$$\eta \stackrel{\text{def}}{=} -\ln\left(\tan\left(\frac{\theta}{2}\right)\right) \tag{16}$$

$$y \stackrel{\text{def}}{=} \frac{1}{2}\ln\left(\frac{E+p_T}{E-p_T}\right) \tag{17}$$

A magnetic field, parallel to the beamline and pointing in the positive z direction, is produced by a solenoid. Tracking systems reside within the the solenoid and the 1.4 Tesla magnetic field it produces, while calorimetry and muon detection systems surround the solenoid. The various subsystems will be described briefly in the following sections.

3.4.1 Charged Particle Tracking Systems

Tracking of charged particles for CDF II is divided into four main systems: L00, SVX II, the ISL, and the COT.

Layer 00, "L00" Measurements of a displaced vertex are central to all analyses that detect B mesons, including this analysis. The typical lab-frame decay length of a B meson is approximately 1 mm. To maximize sensitivity to these small displaced vertices, the closest tracking devices, silicon micro strip detectors, are mounted directly to the beampipe. This leading tracking element, depicted in Figure 15(a), is named Layer 00.

As shown in Figure 15(a), Layer 00 consists of overlapping sections of radiation-hard, oxygenated, silicon micro strip detectors, one at a radius of 1.35 cm and another at 1.62 cm. With a length of 94 cm, it covers the range $|\eta| < 4$. Layer 00 is single-sided to allow large bias voltages to ensure depletion even after extensive radiation damage, as well as for capacitance and space reasons.

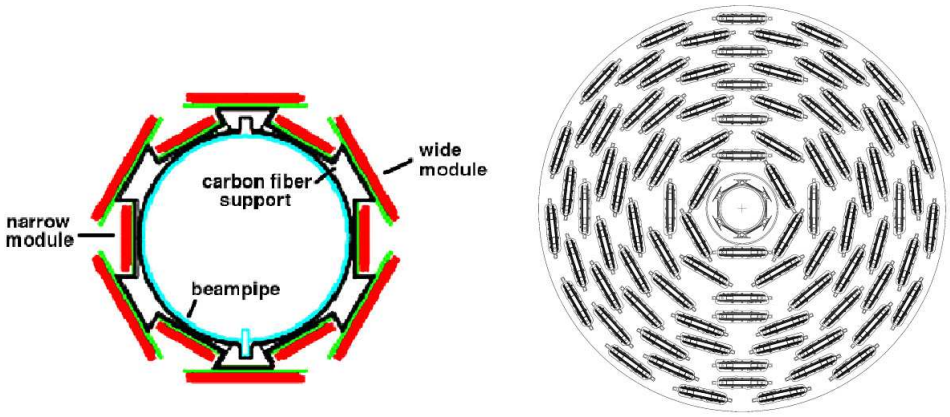

(a) L00 (b) SVX II

Figure 15: (a): L00, the closest detector element to the interaction point [34]. **(b):** Arrangement of silicon layers around the beampipe in SVX II [33].

Silicon Vertex Detector, "SVX II" Immediately surrounding Layer 00 is the SVX II, which also measures track trajectories and vertex displacements with high precision. The SVX II is composed of five double-sided layers of silicon arranged cylindrically around the beampipe, as shown in Figure 15(b). Numbered from zero to four, the layer closet to the interaction point ("Layer 0") sits at radius r=2.1cm, while the farthest layer sits at r=17.3 cm. These five layers are segmented in the z-direction in three distinct barrels that span the region of $|\eta| < 2$.

Each layer of silicon is double-sided in the SVX II. One side of every layer is oriented to make axial tracking measurements. Axial measurements directly measure the $r - \phi$ coordinate, leaving the z coordinate to be inferred from timing information. The improve resolution, the second side of each silicon layer is oriented in a non-axial, or "stereo" alignment to triangulate a given track's position. Layers 0, 1, and 3 are oriented with the silicon strips rotated by 90°, effectively exchanging the ability to make a measurement of the ϕ coordinate for the ability to measure the z coordinate. Layers 2 and 4 are small-angle stereo, and are rotated from axial by only 1.2°.

Intermediate Silicon Layers, "ISL" The ISL consists of a double-sided single strip silicon detector in the central region of the detector ($|\eta| < 1$), and two double-sided layers of silicon in the forward/backward region of the detector ($1 < |\eta| < 2$). It is depicted in Figure 16. Each layer (in both the central and non-central strips) has one side devoted to axial detection, while the other side is small angle stereo (reoriented by 1.2°). The central region is fixed at $r = 22$ cm, while the non-central sections of the ISL are located at $r = 20$ cm and $r = 29$ cm. The primary role of the ISL is to link tracks found by the SVX II to those found by the COT by adding information about the trajectory of each track as it passes between those two systems.

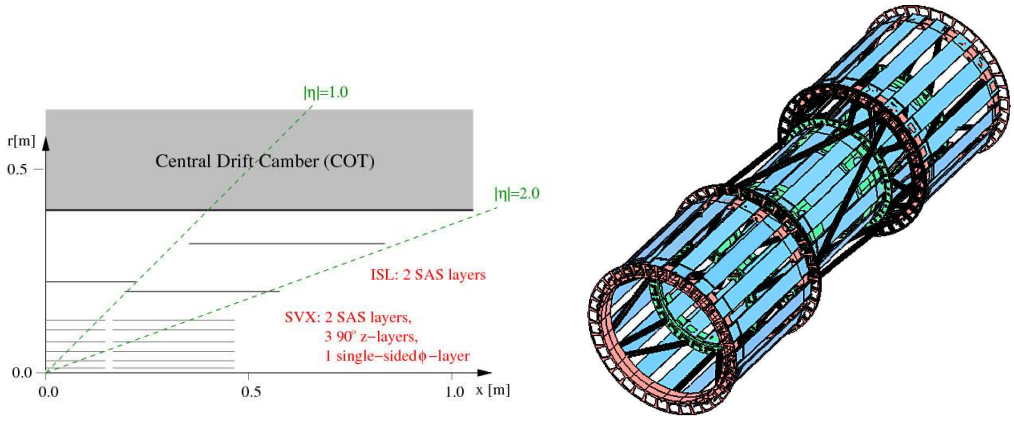

(a) ISL

(b) 3D view of ISL

Figure 16: (a): Arrangement of silicon layers in the ISL [34]. **(b):** A 3D view of the ISL structure [37].

Central Outer Tracker, "COT" The largest single device inside the solenoid of CDF II is the COT, a large drift chamber covering 40 cm $< r <$ 137 cm, and $|z| < 155$ cm (which translates to $|\eta| \leq 1$). Sense wires run the length of the cylinder and are used to detect the flight of charged particles through the gas filling the drift chamber. The gas used is a mixture of argon and ethane, with a small addition of tetrafluoromethane used to prevent aging. The exact mixture is tuned to optimize the resolution of tracks generated by an event rate of 2.5 MHz (corresponding to a time between collisions of 396 ns).

Layers of wires running the length of the chamber, which include sense wires, potential wires,

and shaper wires, are themselves divided into eight "super-layers," as shown in Figure 17. The orientation of wires in these layers alternate between axial (super-layers 2, 4, 6, and 8), and small angle stereo ±3° (super-layers 1, 3, 5, and 7) – super-layers 1 and 5 are rotated by +3°, while super-layers 3 and 7 are rotated by −3°. While the COT is not capable of providing the position resolution of the silicon strip detectors by its design, its large size, particularly in the radial direction, allows for very precise momentum measurements.

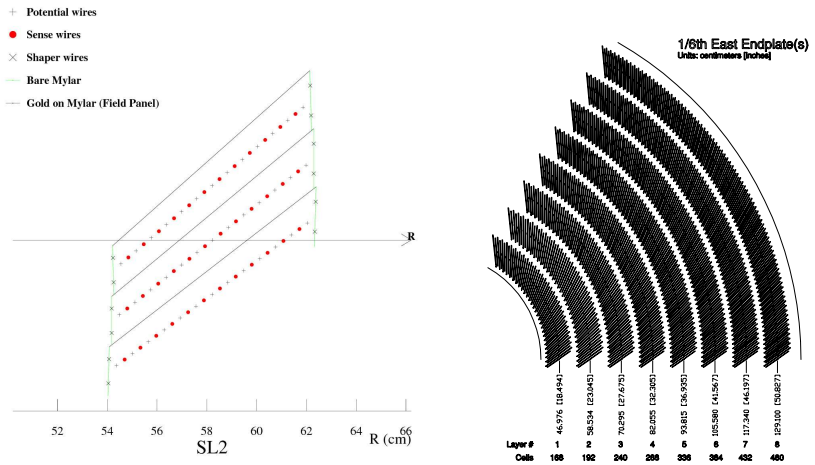

(a) COT Wire Arrangement (b) COT East End Plate

Figure 17: (a): A axial cross-section schematic of three layers in super-layer 2 [38]. **(b):** A schematic view of 1/6 of the COT endplate on the east end of the detector which shows the 8 super-layers in the COT [38].

3.4.2 Particle Identification

Numerous species of charged particles have a lifetime large enough to pass completely through the detector before decaying. These species include the electron, the muon, most pions, most kaons, the proton, and each of their antimatter counterparts. Immediately between the COT and the solenoid, there exists a time-of-flight detector, the "TOF," to measure timing of tracks leaving the tracking region, as shown in Figure 18(a). This information is one of two parts of a particle identification ("PID") system used to differentiate the varied species of charged particles that can be tracked through our detector. The TOF uses the timing of a track's exit

from the tracking region, in conjunction with information from the COT to compute the track's velocity. Using curvature information from the COT, momentum, and therefore mass, can be estimated as a means of distinguishing between the various possible species of the particle. The TOF maintains discriminating power for tracks with $p_T \lesssim 1.5$ GeV/c, above which timing differences become too small, as the velocity of stable tracks begins approaching the speed of light. The TOF is a collection of 216 scintillating bars at $r = 140$ cm, spanning the full range of ϕ. Each bar is connected to a photomultiplier to detect the passage of the charged particles through the scintillating material.

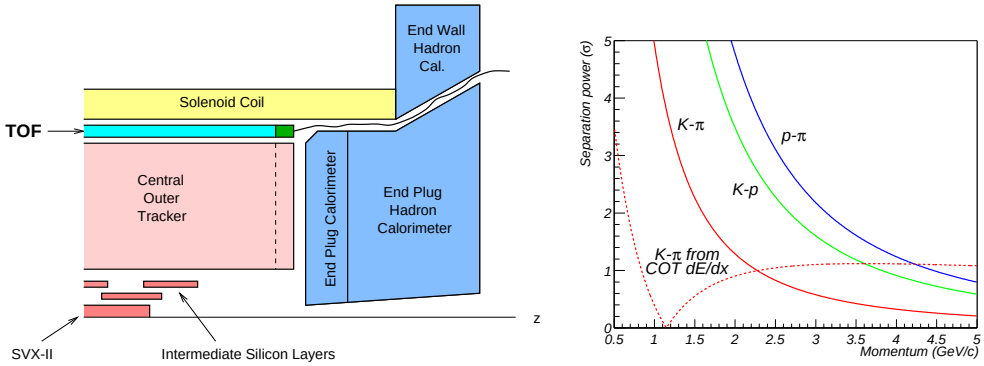

(a) CDF II Side View

(b) TOF Separation Power

Figure 18: (a): A side view of CDF II with the location of TOF shown [35]. **(b):** A plot of the separation power of the TOF between different species of charged tracks as a function of their transverse momentum. The dashed line reports the separation power for kaons and pions using dE/dx [35].

There is a second method of performing particle identification, that of measuring the rate of energy loss of a particle during its passage through the drift chamber. It is well-understood that different species of charged particles will deposit energy during flight at different rates. Since this rate of energy loss is directly proportional to the logarithm of the charge deposited, the quantity log Q is encoded by the electronics into the width of the pulses measured by the COT. In this way, the width of pulses measured by the COT serves as an indirect measure of dE/dx, the rate of energy deposition of the track during flight. The ability of these two methods to distinguish between any two species of particles is plotted as a function of track momentum in Figure 18(b). Notably, the ability for dE/dx to discriminate between species

persists at high momentum, where the power of TOF is diminished. In this way, these two particle identification methods complement one another.

3.4.3 Calorimetry

Beyond the solenoid and to the sides of the tracking chamber, calorimeters provide the ability to measure the energy of photons, electrons, and jets. Knowledge of the energy of these decay products can, indirectly, provide an estimate of the missing energy due to neutrinos generated during the interaction. Calorimetry measurements are not critical to this analysis, so a concise outline of the calorimeter subsystems will be provided. The coverage of the calorimeters is complete in the azimuthal angle, ϕ, and within the range of $|\eta| < 3.6$. The calorimeter subsystems are divided between "central" and "plug" calorimeters according to their position in η.

Calorimetry itself is performed in two different ways – electromagnetic and hadronic. Electromagnetic calorimeters use lead as the absorbing material, while hadronic calorimeters use iron or steel. Both use layers of plastic scintillating material within the absorbing material in order to perform the measurement. The electromagnetic calorimeters are placed closer to the interaction point, as they are sensitive to particle with shorter shower lengths, such as electrons and photons. Hadronic calorimeters surround the outside of electromagnetic calorimeters.

Central Calorimeters Within the range of $\eta < 1.1$, the central calorimeters provide coverage using towers subtending a solid angle $\Delta\eta \times \Delta\phi = 0.1 \times 15^\circ$. The Central Electromagnetic calorimeter is assisted in making measurements by two devices, the Central Preshower Radiator (CPR) and the Central Electromagnetic Shower Max (CES) detectors. Located at six radiation lengths into the CEM, the CES is designed to measure the size of a developed shower caused by electromagnetic particles depositing energy in the detector. The CPR lies inside of the CEM, detecting showers that are triggered by the solenoid or cryostat systems as opposed to the absorbing materials of the CEM itself.

Outside of the CEM, the Central Hadronic calorimeters (CHA) and the Wall Hadronic Calorimeters (WHA) detect showers caused by the passage of hadronic tracks which tend to have larger interaction lengths. Layers of steel absorbing material 2.54 cm thick alternate with

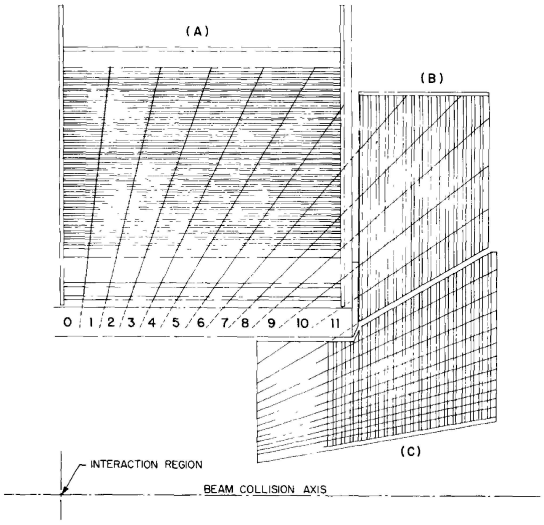

Figure 19: Central, wall, and plug calorimeters are shown as A, B, and C, respectively. Towers of central and endwall calorimeters are numbered 0 through 11 as shown. Hadronic towers 6, 7, and 8 are shared between the CHA and WHA [36].

10 mm thick layers of scintillator. As shown in Figure 19, the WHA extends the coverage of calorimetry to $|\eta| < 1.3$. One wedge tower of the CHA and of the WHA are each shown in Figure 20.

Plug Calorimeters The technology behind the plug calorimetry systems is analogous in many ways to that of the central calorimeters. The plug calorimeters provide coverage in the range of $1.1 < |\eta| < 3.6$, and is thus the closest calorimetry system to the beampipe. Electromagnetic calorimetry is performed by the Plug Electromagnetic calorimeter (PEM), which, like the CEM, is aided by two subsystems for monitoring preshower radiation and shower max radiation – the Plug Preshower Radiator (PPR) and the Plug Shower Max Detector (PSM). The PSM, like the CES, lies six radiation lengths deep into the electromagnetic calorimeter.

The Plug Hadronic calorimeter (PHA) uses 23 layers of iron absorbers 5 cm thick alternated with 6 mm thick scintillator layers. Along its length in the z direction, the outer edge of the hadronic calorimeter maintains a constant η of 1.3, giving the plug its distinctive shape, as shown in Figure 19.

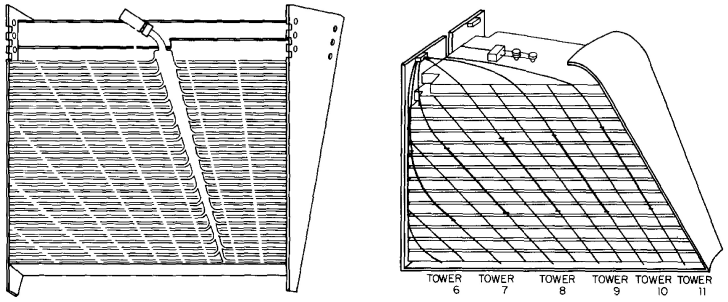

(a) Central Calorimeter Wedge (b) Wall Hadron Calorimeter Wedge

Figure 20: (a): A schematic view of one wedge of the central calorimeters. Layers of absorbing material and scintillator alternate through the body of the calorimeter. One of the many sets of light guides and phototubes is shown. [36]. **(b):** The endwall hadronic calorimeter is shown with a calibration source that is capable of traversing the all towers, allowing a measure of scintillator response and phototube gain [36].

3.4.4 Muon Chambers

The outermost detector systems are the muon chambers, a collection of scintillators and drift chambers installed outside the calorimeters. At that distance from the interaction point, the only interacting particles that reach that distance are, by vast majority muons. Drift chambers used for muon detection are filled with a 50:50 mixture of Argon and Ethane, and contain a single sense wire. Scintillators are used to provide timing information about the muons, suppressing backgrounds due to cosmic rays and other sources. The fake rate of muons – the number of muon identifications that are false positives – is at the level of a few percent. Each muon chamber subsystem is composed of layers of drift chambers. Any collection of three matching hits is classified as a "muon stub." There are four separate muon detection systems to be outlined below. Coverage for each of these systems is represented in table form in Table 6 and in graphical form in Figure 21.

The Central Muon Detector – CMU The Central Muon Detector (CMU) sits directly outside the central calorimeters at a radius of 3.47 m, providing coverage in the range of $|\eta| < 0.6$. Coverage in ϕ is broken into 24 segments, each covering 12.6°, leaving a 2.4° gap in coverage between the wedges. Resolution in the $r - \phi$ plane is at the level of 250 μm, as drift

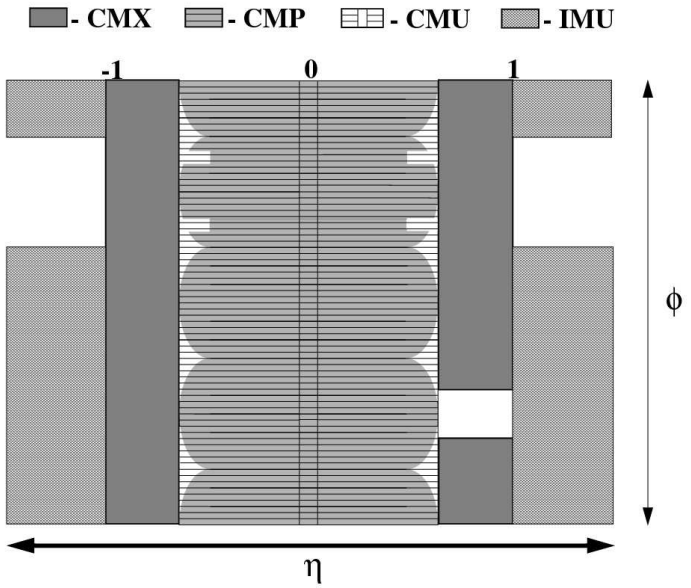

Figure 21: A projection of the coverage of muon chamber systems in the plane of azimuth, ϕ, and pseudorapidity, η [38].

chambers are stacked in alternating layers. Resolution in z reaches approximately 1 mm.

The Central Muon Upgrade – CMP Covering an area in the $\eta - \phi$ plane that overlaps the CMU, (see Figure 21), the Central Muon Upgrade (CMP) is a box of drift chambers surrounding the detector. The presence of this extra detector provides coverage for the gaps of the CMU. Also, because the CMP sits behind an extra 60 cm of steel, the probability of fake muon detection due to hadronic punch-through is reduced. While the CMP provides extra coverage in ϕ for the central region, its azimuthal asymmetry gives rise to gaps of its own in η. A layer of scintillation counters, the CSP, sits immediately outside the CMP. The location of the CMP and CSP are shown, along with the steel absorber between these devices and the CMU, in Figure 22.

The Central Muon Extension – CMX/CSX The Central Muon Extension (CMX) is a collection of drift tubes arrayed as a logical extension of the CMU system. Along with the Central Muon Scintillation Counters (CSX), the CMX provides coverage for the range of

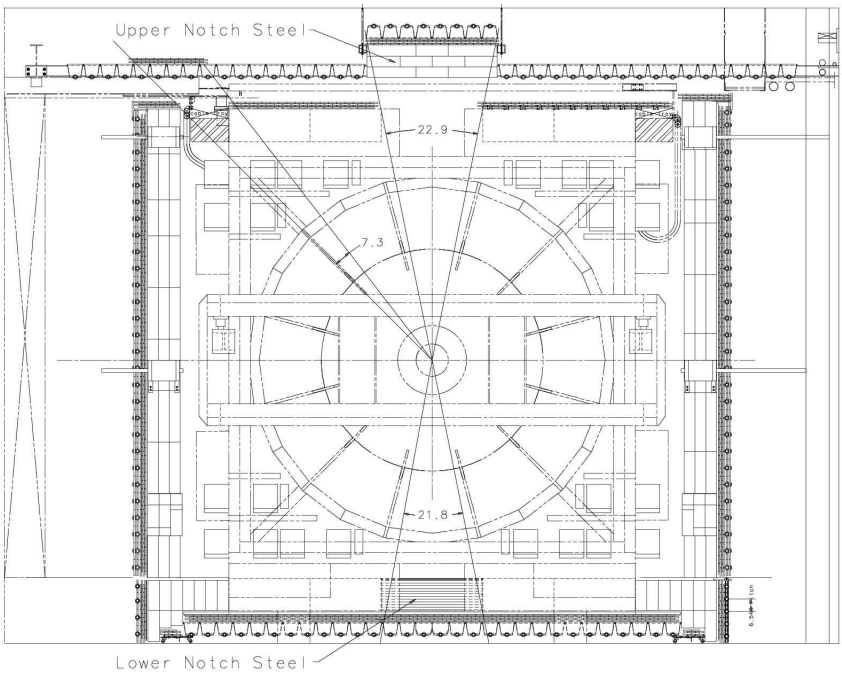

Figure 22: Configuration of the Central Muon Upgrade detector (CMP), Upgrade Scintillator (CSP) and steel absorber in Run II. On the walls the circles are the ends of PMTs. On the top and bottom the trapezoids are the lightguides viewed endon. [38].

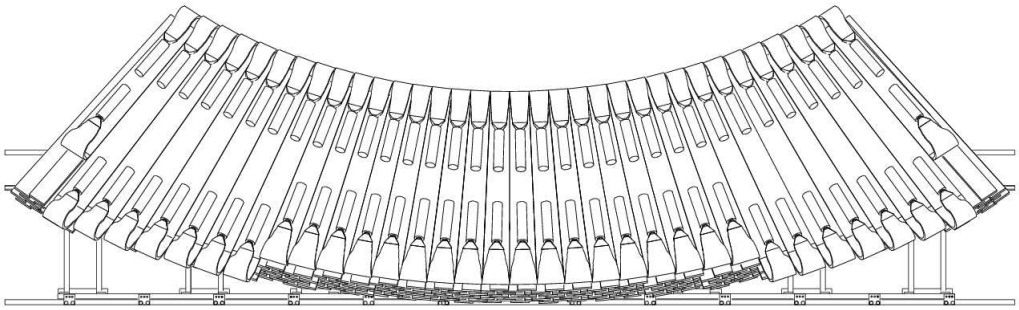

Figure 23: Lower chambers for the CMX and CSX [38].

$0.6 \lesssim |\eta| \lesssim 1.0$. The CMX is segmented into 24 sections in ϕ, each covering 15°. The structure of the arches that compose the CMX is shown in Figure 23. The azimuthal coverage of the CMX is interrupted for a 30° gap in ϕ near the top of the detector to allow room for the solenoid refrigerator and the Tevatron Main Ring [38].

The Intermediate Muon System – IMU Mounted around the outer radius of two steel toroids, the Intermediate Muon System (IMU) extends the muon coverage out to $1.0 \lesssim |\eta| \lesssim 1.5$. As with the other muon detection systems, the IMU relies on layers of drift chambers surrounded by a scintillator. Due to the positioning of the IMU around the toroids, the distance to the IMU, in interaction lengths, varies in η from 6.2 up to 20.

	CMU	CMP/CSP	CMX/CSX	IMU
Pseudo-rapidity coverage	$\lvert\eta\rvert \lesssim 0.6$	$\lvert\eta\rvert \lesssim 0.6$	$0.6 \lesssim \lvert\eta\rvert \lesssim 1.0$	$1.0 \lesssim \lvert\eta\rvert \lesssim 1.5$
Drift tube cross-section	2.68×6.35 cm	2.5×15 cm	2.5×15 cm	2.5×8.4 cm
Drift tube length	226 cm	640 cm	180 cm	363 cm
Max drift time	800 ns	1.4 μs	1.4 μs	800 ns
Total drift tubes	2304	1076	2208	1728
Scintillation counter thickness		2.5 cm	1.5 cm	2.5 cm
Scintillation counter width		30 cm	30-40 cm	17 cm
Scintillation counter length		320 cm	180 cm	180 cm
Total counters		269	324	864
Pion interaction lengths	5.5	7.8	6.2	6.2-20
Minimum detectable muon p_T	1.4 GeV/c	2.2 GeV/c	1.4 GeV/c	1.4-2.0 GeV/c
Multiple scattering resolution	12 cm/p (GeV/p)	15 cm/p	13 cm/p	13-25 cm/p

Table 6: Design Parameters of the CDF II Muon Detectors. Pion interaction lengths and multiple scattering are computed at a reference angle of $\theta = 90^\circ$ in CMU and CMP/CSP, at an angle of $\theta = 55^\circ$ in CMX/CSX, and show the range of values for the IMU.

4 The Trigger

Typical events at the CDF II detector produce 200 kB of data [38]. Because the overall crossing rate during Tevatron operation is 1.7 MHz, far more data is produced than can be recorded. Instead, pre-selection must be performed at the hardware and software levels before recording events to disk. Most events are inelastic $p\bar{p}$ collisions which are generally uninteresting, lending the output of the detector to a trigger system that can select more interesting events. An understanding of the specific design and implementation of this trigger is critical to the development of any analysis, as its selection criteria determine in large part what physics can be found in the data.

The CDF II trigger system is divided into three levels. Each level considers an event for further evaluation (at the subsequent level) or for veto. Levels 1 and 2 use hardware to directly analyze front-end output of the detector. Level 3 relies on a farm of hundreds of machines performing a software based analysis of nearly all the detector information. Particular physics parameters motivate the trigger decisions at each level. The overall structure of the trigger system is shown in Figure 24 [39, 40], and will be discussed in some detail in this chapter. Particular focus is given to the Level 1 trigger, including its recent upgrade in 2006 to incorporate stereo tracking information in an effort to meet the challenge of increasing luminosity provided to CDF by the Tevatron. Details about this upgrade are included in Chapter 5.

4.1 Level 1

The first pass over front-end readout electronics on the detector is performed by the Level 1 trigger. Level 1 is a synchronous pipeline, 42 clock cycles (or 14 events) deep [38]. This pipeline of events serves a buffer of time, during which the Level 1 can choose whether or not to pass the event forward for consideration by Level 2. Events that are not passed forward by Level 1 are vetoed, and thus permanently dropped from consideration for future recording. By nature of having no deadtime, each event is considered by the trigger at Level 1, the time between the occurrence of any event and its possible Level 1 accept remains a constant 5,544 nanoseconds.

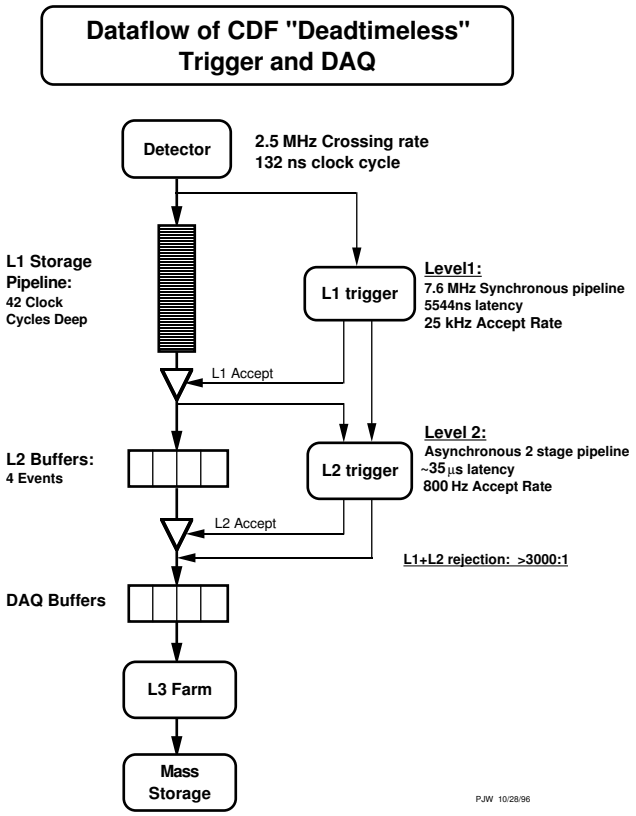

Figure 24: An overview of the three level trigger used in data acquisition at CDF II [39, 40].

To accommodate the timing requirements of the Level 2 trigger, the Level 1 trigger paths must be stringent enough to keep the Level 1 accept rate at or below 28 kHz.

At Level 1, the trigger reads out only from select elements of CDF II. Information from the silicon tracking devices, for example, is not used at Level 1. Instead, information from the COT is used to perform a low-level form of tracking. Specifically, a Level 1 trigger subsystem, the XFT (eXtremely Fast Tracker), uses readout from the COT, along with look-up tables, to identify so-called "XFT tracks." XFT tracks are a course-grained estimate of the kinematic parameters of tracks — p_T and ϕ — left by charged particles passing through the chamber. As mentioned previously, stereo information for these tracks, as derived from the oblique sense wires in the COT, has been incorporated into the Level 1 trigger as of the XFT upgrade in 2006. This adds η as a potential variable for estimation before making a decision at Level 1. More details about the XFT upgrade can be found in Chapter 5.

Before any Level 1 decision is made, XFT tracks are matched to muon chamber and/or calorimeter clusters to increase information available about the track. The calorimeters provide the total energy deposited in a tower to Level 1. Muon chamber information comes from the CMU, CMP, and CMX subsystems. Information from all of these systems is combined with output from the XTRP, a hardware device responsible for extrapolating tracks and feeding the three Level 1 subprocesses: L1 CAL, L1 TRACK, and L1 MUON. These three subprocesses then report to the Global Level 1 system which makes a final decision to either reject or announce a Level 1 Accept. This structure is shown as a diagram in Figure 25 [39].

4.2 Level 2

At Level 2, there is more time and data to make decisions. Information from SVX is included, allowing better vertexing and tracking information to be available for the Level 2 decision. The SVT (Silicon Vertex Trigger) has a resolution of approximately 50 μm.

The Level 2 buffer can hold up to four incoming events for consideration. This decision is made by an asynchronous combination of hardware and software triggers. Any Level 1 accepts that occur while the buffer is full will be vetoed. This becomes a possibility as the Level 1 accepts

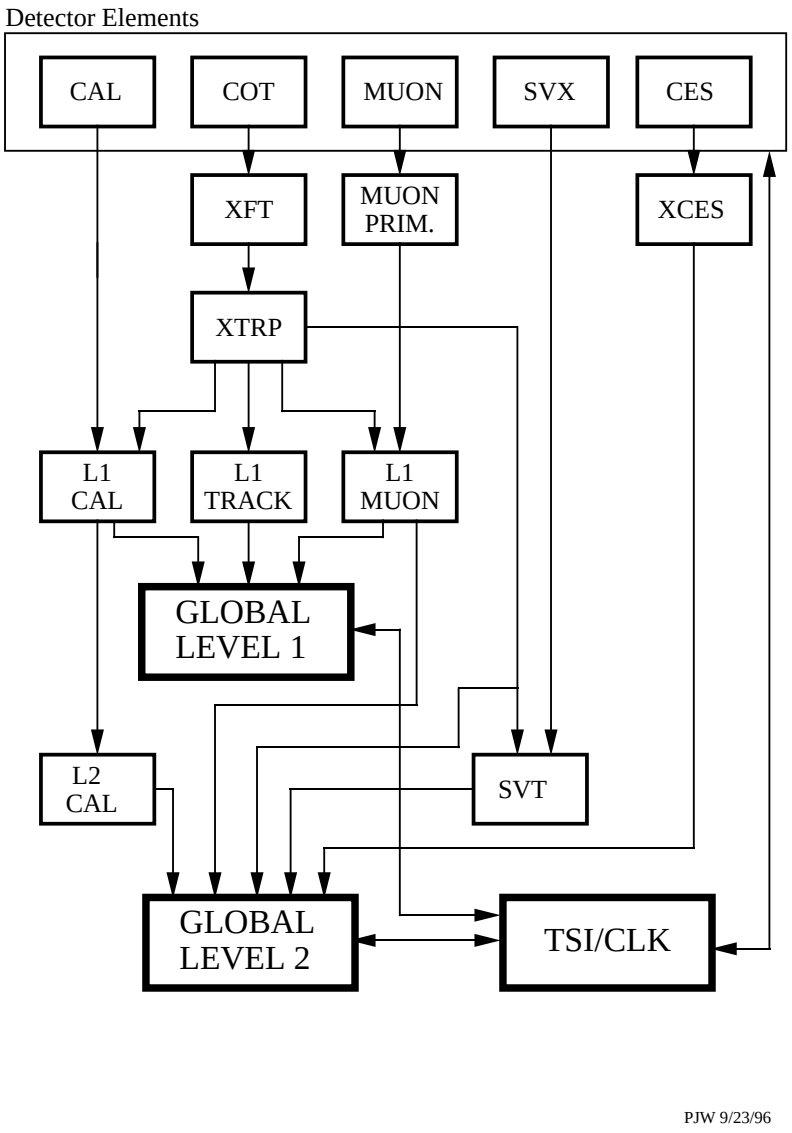

Figure 25: Detector elements, at top, and their connections to the Level 1 and Level 2 decision making subsystems [39].

can be irregular in their frequency. This undesirable situation is declared as deadtime in the detector. Properly designed trigger paths (tailored to the instantaneous luminosity provided by the Tevatron) can prevent this deadtime at all but the highest instantaneous luminosities.

Typical Level 2 accept rates are are approximately 800 Hz [40]. Overall, of all the events in the detector, less than one in 3,000 will receive a L2 accept. These events are then stored in the DAQ buffers and provided to Level 3, which is described in the next section.

4.3 Level 3

The final level of the CDF II trigger system, Level 3, is capable of making decisions using more advanced software techniques. The goal is to reduce the number of events by another order of magnitude before recording to disk. To do this, the event in the detector is read out directly to one of a farm of computers via optical fibers. Thus, the information available to the trigger at Level 3 is, for the first time, complete. (Levels 1 and 2 each receive coarse-grained information from many detector components.) Each computer then uses a set of criteria similar to the Level 2 trigger requirements to make a decision. At this point, many of the Level 1 front-end readout components can be cross-checked against their Level 3 counterparts to monitor for errors.

4.4 Trigger Paths Used In This Analysis

This analysis in particular uses one major trigger path to collect data. This path is selected for the yield and purity of B_s^0 candidates, which in turn lends itself to a search for $B_c^+ \to B_s^0\ \pi^+$.

4.4.1 Di-Muon (J/ψ) Trigger

The $B_s^0 \to J/\psi\ \phi$ decays selected in this analysis are found within the Di-Muon Trigger dataset. The specific requirements of the Di-Muon Trigger have evolved over time. In general, though, the Di-Muon Trigger attempts to select events with a pair of muons produced by the occurrence of a J/ψ in the event. The trigger decision is made by incorporating information from XFT and the CMU and CMX. Within the Di-Muon Trigger, there are two basic trigger paths: the CMU-CMU trigger path, selecting events with two distinct muons identified in the muon chambers in

the central detector region; and the CMU-CMX trigger path, selecting events with one muon in the region covered by the CMX. The fundamental requirements of the Di-Muon Trigger have the following characteristics [46]:

- The transverse momentum and ϕ information is taken from the XFT tracks matched to hits in the muon chambers. This is extrapolated to the inner radius of the muon system. Due to the uncertainty of the extrapolation coming from multiple scattering, a window covering the 3σ area in ϕ is determined and called the footprint.

- A tower in the muon system has to agree with at least one footprint. If there is agreement, the tower is called a muon tower. A tower requires at least one of its stacks to have a Level-1 muon track segment. A "stack" is four cells of scintillator stacked on top of each other. It is required that at least cells 1 and 3 or 2 and 4 have hits which coincide during the stub gate width of 396 ns.

- For the Di-Muon trigger, two muon towers are needed, which are either at different sides (east and west) of the detector, or at least separated by two muon towers, where the gap between two wedges is treated as a tower, as well.

4.5 Dynamic Prescales

With each beam crossing in a run of data-taking, there is a reduction in the instantaneous luminosity delivered by the Tevatron. Indeed, many runs are terminated not due to any problems at the Tevatron or at CDF or DØ, but simply because the Tevatron is capable of beginning a fresh run with a higher delivered luminosity. As luminosity and detector occupancy fall, there is an opportunity to tune the use of triggers to optimize the data-taking performed. CDF II directly addresses that opportunity using different forms of dynamic prescales.

If a trigger is more time-intensive than would be feasible during the highest luminosity acheived, it may be prescaled early in the run. This means that it may not be implemented as a trigger until the luminosity falls below a certain level. Dynamic prescaling is a more clever variant of this approach, where the trigger in question is used with increasingly frequency as

the instantaneous luminosity falls. This effectively levels off the usage of the trigger system, so that a low luminosity does not leave the trigger system idle. This leveling is shown in a plot of Level 1 Accepts as a function of instantaneous luminosity delivered by the Tevatron, seen in Figure 26 [41]. Further improvements, including fractional prescaling, (a more precise implementation of dynamic prescaling), and "uber prescaling" have been implemented. The later, the "uber prescale", incorporates both information of the instantaneous luminosity and of the number of slots available at Level 2. Both the fractional prescale and the uber prescale allow for a dramatic increase in the Level 1 Accept rate on average, as shown in Figure 27 [41].

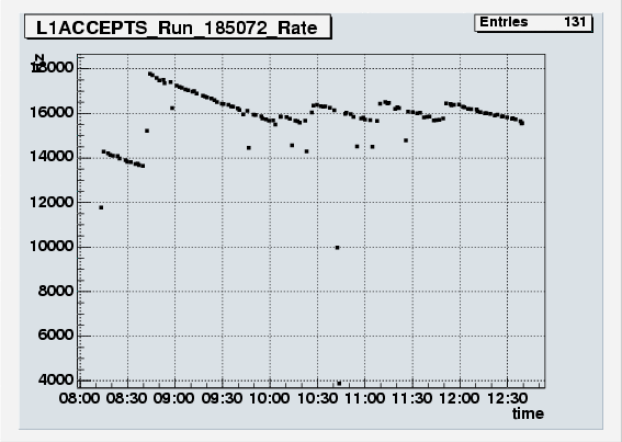

Figure 26: Dynamic prescales applied to the trigger system allow the detector to continue recording events at or near its maximum rate while the physics inside the detector, (to wit, the occupancy) is constantly falling with decreasing instantaneous luminosity. Shown here, the dynamic prescales update over time, bringing the rate of Level 1 Accepts in the trigger system back up near its maximum value [41].

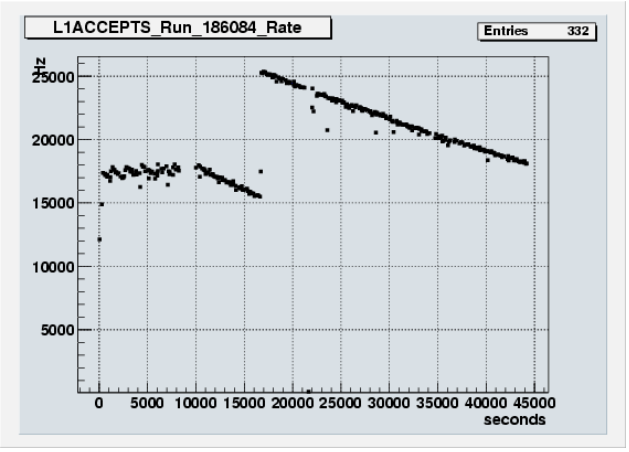

Figure 27: Fractional prescaling is a finer tuned version of the dynamic prescales shown in Figure 26, allowing for a more precise leveling of the usage of detector over time. The effect of fractional prescales is shown at the left of this plot. Later in the run, the so-called "uber prescales" allow the trigger system to perform dynamic prescaling action both as a function of instantaneous luminosity and of current trigger system available capacity. This dramatically increases the maximum permissible Level 1 Accept rate without incurring a significant hit to deadtime, as seen at the right on this plot [41].

5 The XFT Upgrade

The increasing instantaneous luminosity delivered by the Tevatron poses a challenge for CDF. In order to maintain acceptable trigger rates while also reducing the rate of false positives — the so-called "fake rate" — the Level 1 trigger required an upgrade. Planning for the upgrade began in 2004, and the final installation occurred in 2006. Since then, fake rates have been reduced dramatically at given instantaneous luminosities, resulting in improving data taking at CDF [42]. This section will discuss some elements of the upgrade, with a specific, detailed focus on the XTC2 — its design, implementation, and the diagnostic tools used to evaluate its performance.

Multiple interactions per crossing is one of many challenges to CDF imposed by increasing instantaneous luminosity. As luminosity delivered by the Tevatron rises, the statistical likelihood of more than one $p\bar{p}$ pair being involved in an inelastic collision becomes greater [38]. (For all luminosities, the statistical distribution closely follows a Poisson curve.) Studies performed before the Run II upgrade indicated a likely average interaction per beam crossing rate signif-

icantly above 1 as instantaneous luminosity rose above 10^{32} cm^{-2} s^{-1}. Figure 28 shows the projected average interactions per crossing as a function of instantaneous luminosity. Three dimensional information about tracks during low level triggering becomes an important tool, as separate interactions (and the tracks they produce) can be differentiated using z information. The XFT upgrade improved the Level 1 trigger in many ways, including the extraction of z information from the stereo layers of the COT.

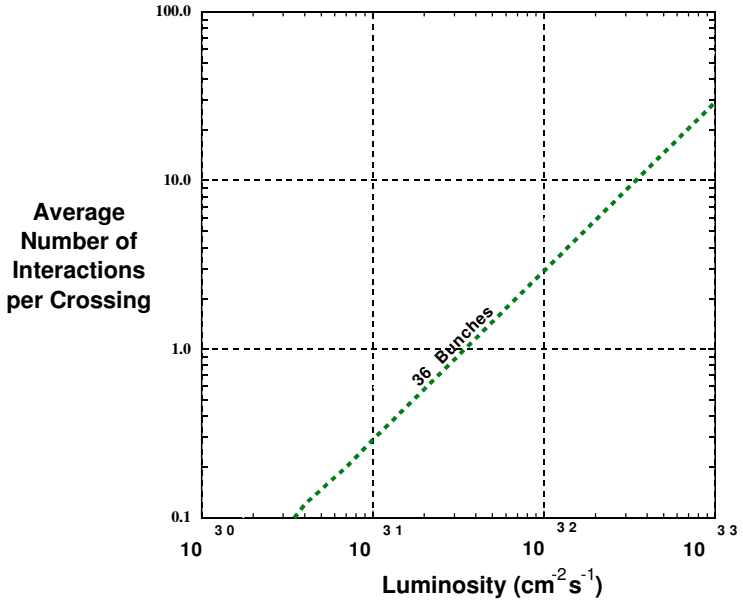

Figure 28: Projected average number of interactions per crossing as a function of rising instantaneous luminosity. Current instantaneous luminosities during data-taking allow for multiple interactions in a typical crossing [38].

In Figure 29 [43], the structure of the XFT is shown after the upgrade was performed. New components did not replace older devices, but instead were installed alongside the original equipment [43]. The axial XFT components, shown in the top row of Figure 29, were not changed, so as to ensure the upgrade could be reverted in case of failure. Hardware to perform the stereo tracking at Level 1, the heart of the XFT upgrade, is shown in the bottom row of Figure 29. The systems installed perform the analogous role to those already present in the axial tracking trigger system: XTC2s are mezzanine cards on-board the TDC; Stereo Finders collect information from the XTC2s via a transmission cable connected to an output module;

the SLAM system, replacing the Linker Output Module performs the task of combining the two data paths. Subsequently, the combined data is sent to the XTRP, as well as to a new Tracklist board which can provide information for use in a Level 2 Trigger decision.

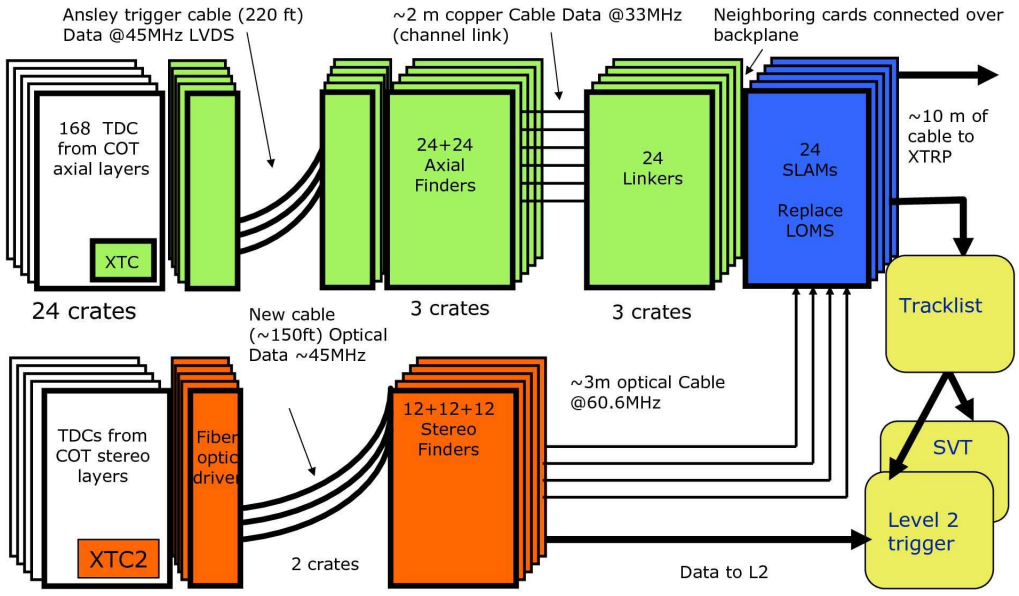

Figure 29: Schematic of XFT hardware after the XFT upgrade in 2006. The new hardware to perform tracking at Level 1 trigger rates for stereo layers is shown on bottom left, with the older, axial devices above. The two systems are merged at the SLAM boards, shown in blue [43].

5.1 The Function of the XTC2 (XFT TDC Card 2)

Tracking in the drift chamber is performed by timing the pulses measured on the sense wires strewn throughout the chamber. This technique is used both for the ultimate measurement of tracking parameters in the XFT as well as for the estimation of those parameters for trigger decisions. With the more powerful technology available during the XFT upgrade, the newer, stereo components could provide greater resolution than their axial counterparts. This is particularly true for the XTC2, which will be discussed at length in this section.

The XTC2 (XFT TDC Card 2) is, as its name implies, a low resolution version of the TDCs (Time to Digital Converters) used to measure pulse timing from the COT. It is mounted on

the TDC, clipped in as a mezzanine board or "daughter card", and given access to the same input data (from the COT ASDQs – Amplifier Shaper Discriminator $\frac{dE}{dx}$) as the TDC. Thus the output provided by the XTC2s can be cross-checked against the later TDC output, which should be the same, albeit with a finer resolution.

Eleven windows of time are evaluated when the XTC2 makes its decision. However, only six bits of data will eventually be output by the XTC2. Thus, there is a logical mapping between the eleven input timing windows (which allow for $2^{11} = 2048$ possible input sequences) and the six output timing bins (which allow for $2^6 = 64$ possible output sequences). The heuristic for this mapping can be described as follows:

While a hit (a pulse rising above threshold voltage) should signify that a corresponding output bin should be set to 1, this should not be the case if this voltage is merely a lingering pulse from the previous window. It is possible, for example, to imagine a hit appearing on a sense wire shortly before the end of a timing window. In this event, voltage will be above threshold for both the timing window in question, as well as for the next window, which is merely detecting the delayed after-effects of the hit.

To distinguish between these "delayed after-effects" and valid, second pulses in the neighboring time bin, a "not-sure" window is defined for each output window, excepting the first in an event. Thus, for six output windows, there are 5 not-sure windows used in the XTC2 decision algorithm. If a hit shows up in a particular input window, it will turn on the corresponding output window in all cases excepting one: if the previous window also had a hit, and only the not-sure window of the current window has a hit (and not the rest of the window). In that case, the "hit" is considered lingering voltage from a previous window and ignored. This functionality precisely mimics the original XTC design, which had only two output windows, but three input timing windows. This functionality is also described in Figure 30 [44].

5.2 Diagnostic Procedures for the XTC2

A suite of testing and diagnostic software tools were developed to ensure the functionality of the XTC2. These tests involve a complete teststand for the XTC2 which simulate hits on the

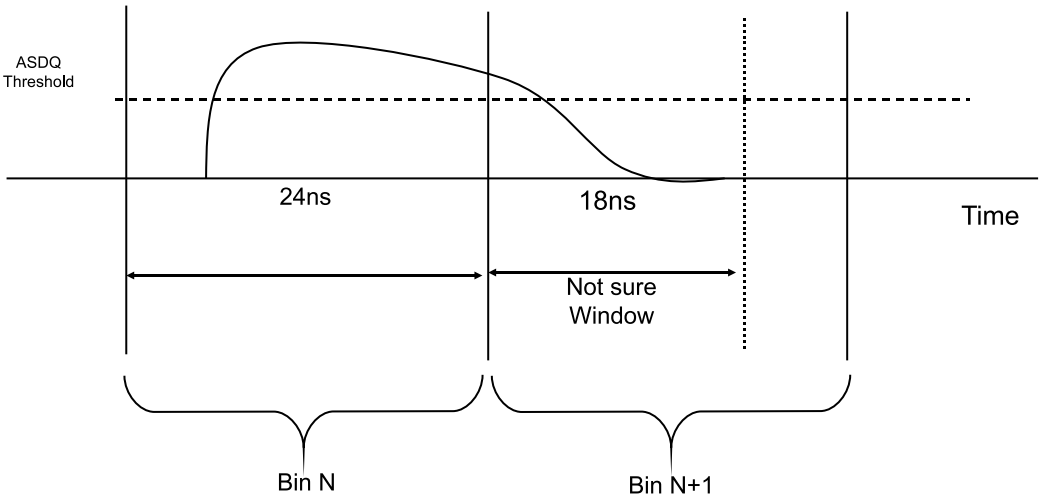

Figure 30: Single pulses can rise above ASDQ threshold for longer than the typical timing window, as shown in this figure. To improve the functional resolution (and thus decrease fake rates in tracking), a "not-sure window" algorithm is implemented to identify pulses that appear in two bins, but are due to only one track. According to the XTC and XTC2 functionality, only Bin N will turn on in the above situation as depicted [44].

detector as well as all the timing and control signals that would be found for a board *in situ*. This section will discuss how these tests are used and how their results are interpreted.

Logging into a crate using SSH The teststand crate is designed to be accessible by remote login though a hardwired ethernet connection to a local network. To join that network (thereby getting access to the crate) requires SSH access to another machine on that network. This secondary machine serves as a middle man for all interactions with the crate controller. In this example, the crate is connected to the Illinois HEP network, accessible by SSH via the LX machines.

The following commands are useful to put into a startup script for C-shell users on the LX machines, so as to alias commonly used programs:

```
alias cdfsoft source ~/docdfsoft2.csh
alias crate "rlogin -l vxcdf mvme2300d.hep.uiuc.edu"
alias key "kinit ${USER}"
alias sb0 "ssh -XA ${USER}@b0doorway.fnal.gov"
```

```
set autologout = 9999
```

Incorporated by reference in the above script, there is a secondary script, `docdfsoft2.csh` that needs to be available in the home area if the command `cdfsoft` is to properly function. The contents of that script are listed below, verbatim:

```
#!/bin/csh f
setenv USESHLIBS 1
source ~cdfsoft/cdf2.cshrc
setup cdfsoft2 6.1.4mc.m
#setup kai v4_0f
#setup -f Linux+2.2 -q KCC_4_0 root v2_26_01a
#srt_setup STR_QUAL=default SRT_CXX=KCC_4_0
setenv LD_LIBRARY_PATH "../shlib/Linux2-KCC_4_0:/usr/lib:$LD_LIBRARY_PATH"
setup kerberos
setup ssh
# to tell what releases are available, type
# ups list -a cdfsoft2
```

With these two scripts in the home area, logging in to the crate is performed with the command `crate`. The login and password for the HEP Illinois crate are `vxcdf` and `cdf347vx`, respectively.

Using pre-compiled code After logging in to the crate, the user has access to a directory visible to the crate controller, and all the files within that directory (and its subdirectories). This directory is also available on the Illinois windows network as `\\Hep-ntweb\VxUsers\VxCDF`. Pre-compiled code exists in this directory as well as some subdirectories. In particular, the subdirectory `xtctest` has programs for testing the XTC2s. Backup copies of source code are stored in its subdirectory, `code`. It is important to note that to change directories on the crate controller requires quotation marks to be specially placed around the directory name used as an argument. For example, to change directories to find XTC2 code, a user would enter the following command:

```
cd "~/xtctest/"
```

Pre-compiled executables must be loaded into memory, then run using the function name (and any relevant arguments) defined in the source code. For example, to run the diagnostic program `xtc_comp` (explained later in this section), the commands entered into the crate controller would be the following:

```
ld < xtc_comp
run
```

In this instance, `run` is the function name as defined in the source code for `xtc_comp`, which can be found in the subdirectory, `code`, under the filename, `xtc_comp.c`.

Memory management As programs are loaded into memory by the crate controller CPU, the remaining memory can diminish, causing poor performance. To see what programs are consuming memory at any given time on the crate, the following command is issued:

```
moduleShow()
```

Memory can be freed by unloading the program (or "module") by issuing the command `unld()`, with the specific module ID within the parentheses.

Compiling code The software libraries used to convert source code in `C++` to crate controller CPU run executables are called the VISION libraries. (Some documentation occasionally mentions the FISION libraries, which is a mistranslation by the developers.) These libraries allow for the use of the VISION commands which are used to read and write to devices on the crate at specific register addresses. A typical VISION command looks like the following:

```
VISIONwrite(boardHandle[tdc_slot], VMEADDRESSPREFIX + i,
            sizeof(my_byte), &bytes, &my_byte);
```

Here, `boardHandle` is an array of addresses (called `VISION_SLAVE` objects), indexed by slot number in the crate. The argument `VMEADDRESSPREFIX+i` identifies the location of the register to be written, and the remaining arguments describe the data to be written. Compiling code that includes these commands requires the following pre-processor directive for library inclusion:

```
#include <vxWorks.h>
#include "VISION.h"
```

To compile source code, it must be copied to a machine (such as `b0doorway` at fermilab) that has permission to use the VISION preprocessor libraries. The previously aliased command `sb0` is ideal for this purpose. On this authorized machine, the following aliasing commands should be included in the start-up shell script to facilitate compilation:

```
alias cpc1 "setup fision"
alias cpc2 "setup -q ppc vxworks"
alias cpc3 '$VXCC -I${FISION_DIR}/include \!^.c'
alias cpc4 '$VXLD -g -o \!* \!*.o'
alias cpc "cpc1; cpc2; cpc3 \!*; cpc4 \!*"
```

Code, such as `xtc_comp.c`, can be compiled into an executable, such as `xtc_comp`, as simply as entering the following command on `b0doorway` (after copying the necessary files over).

```
cpc xtc_comp
```

XTC2 Tests In this section, the suite of diagnostic tests currently developed and used for pre-deployment check-out of XTC2s is described [47]. Each test can be loaded and executed as pre-compiled code using the steps detailed above.

`regtest` is a simple test of the ability to read and write to the available registers on the XTC2. These registers are written to numerous times with varying sequences of ones and zeros and subsequently read back. This test, along with the tests below, (within `xtc_comp`) are considered part of the XTC2 checkout suite. These tests should be performed first, as `xtc_comp` will return the XTC2 registers to a useable state.

`xtc_comp` is the most comprehensive XTC2 testing program. The basic suite of tests used to check out an XTC2 is available entirely in `xtc_comp`. The normal routine to "checkout" an XTC2 is to run the following subprocesses, listed with their Menu Option number:

- `15) 6-Bin: Program Registers Production XTC, Standard Values...` This option configures each of the write accessible registers with their default values. An explanation of each register is given in Section 5.3.
- `17) 6-Bin: Connectivity Test` The connectivity test instructs the TDC and XTC2 to begin sending an event of all zeros. After a few such events have been sent, it inspects the Finders RAM, and compares it to its expectation. The Finder expects to find all zeros, along with the correct formatting of B0 and Word0 signals. The test repeats using all ones, all zeros, and all ones again, for a total of 4 events worth of information being read out.

  This is essentially a test of equipment between the TDC output module and the Finder input module. No XTC2 logic is used here.
- `18) 6-Bin: Finder Capture Functionality Test` The Finder Capture test is nearly identical to the connectivity test. The most notable difference is that random words are created in a couple of XTC2 timing windows, and the Finder RAMs are checked to insure that those words are properly formatted. This is a good test of XTC2 logic functionality, and channel-by-channel accuracy.

  This test starts with a quick scan to determine approximately where the XTC2 timing windows are. Also, 100 events are tested, compared to only 4 events in the connectivity test.
- `19) 6-Bin: Extended Finder Capture Functionality Test` This test is exactly the same as the previous, with 100 times as many events tested.
- `21) 6-Bin: L2 Buffer Test New Way ...` The L2 Buffer is a memory device on the output end of the XTC2. It stores, for testing purposes, the output of the XTC2 before it is sent on toward the Finder. If the XTC2 has shown correct functionality in the Finder Capture tests above, this can subsequently check the functionality of the L2 Buffer by comparing what it records to what the Finder receives.

  The test is run in the same way as the Finder Capture functionality tests, except the inputs and outputs it compares are different. Instead of comparing XTC2 input

to Finder output, it compares Finder output to XTC2 output (in the L2 buffer).

- `27) Edgetest` Edgetest uses pulses from the Tracer to search, channel-by-channel, for the timing of each edge of the XTC2 logical windows. On the input side of the XTC2, there are 11 windows (6 output + 5 not-sure). This test scans with variable sized pulses to find each windows beginning and end.

  At the end of the test, a 12 by 96 table of timing values is displayed. Currently, there is no failure mode of this test, but it can be used to search for anomalous behavior on a specific channel.

ODLD (Output Data Looping Design) loads an alternate FPGA configuration into the FlashRAM. The different configuration does not perform XTC2 functionality; instead, it loops an output pattern. This is very useful for testing of downstream components, such as the stereo finder or the transition boards on the backplane.

`xtc_kill` is now, essentially, an obsolete diagnostic tool. In a previous CPLD design, there were rare cases where an XTC2 would "die" while the FPGAs were being configured. The only remedy at the time was to reprogram the CPLDs. To help diagnose this problem, `xtc_kill` was built to repeatedly configure the FPGAs 5000 times an hour. The most recent version of the CPLD software ("v16") does not exhibit this issue.

5.3 Memory Map of the XTC2

An understanding of the functionality of each of the registers, as well as the general outline of the register space, on-board the XTC2 is critical for diagnosing issues on an individual board. To this end, a complete mapping of the registers on the XTC2 is given in Table 7 [48].

Table 7: XTC 2 Production Board Register Space Summary: Covering the CPLD registers (XTC2: x38-x3F) and the FPGA registers on the XTC2 [48].

Address		R/W	First Version			Init. Value		Function
VME	XTC		2-Bin	6-Bin	CPLD	2-Bin	6-Bin	
xFC	(x3F)	R/W	—	—	16	x00		Addr2 (flash address bits 18:16; only bits 2:0 of register are used)
xF8	(x3E)	R/W	—	—	16	x00		Addr1 (flash address bits 15:8)
xF4	(x3D)	R/W	—	—	16	x00		Addr0 (flash address bits 7:0)
xF0	(x3C)	R/W	—	—	16	x00		Flash Data Byte (data = byte to write when writing; data = byte read from flash when reading)
xEC	(x3B)	W	—	—	16	N/A		Command Register.
xE8	(x3A)	R	—	—	16	Varies		Read CPLD/Flash Status
xE4	(x39)	W	—	—	1	N/A		Reset FPGA_Prog CPLD logic (any data value may be written)
xE0	(x38)	R	—	—	1	Ver. #		FPGA_Prog CPLD Firmwave Version Number

Table 7: (cont.)

xDC – xB0	(x37 – x2C)	—	—	—	—	—	—	UNUSED
xAC	(x2B)	W	—	32	—	N/A	x00	Write Byte to ODLD Buffer (data = byte to be written)
xA8	(x2A)	R	—	32	—	N/A	x00	ODLD Buffer Byte
xA4	(x29)	R/W	—	32	—	N/A	x00	ODLD Memory Address Bits 9:8 (in bits 1:0 of register)
xA0	(x28)	R/W	—	32	—	N/A	x00	ODLD Memory Address Bits 7:0 (in bits 7:0 of register)
x9C	(x27)	R/W	—	32	—	N/A	x03	Clk132 Shift/Shift_In_Bit Clock Count (Range: x00-x0E)
x98	(x26)	R/W	—	32	—	N/A	x07	ODLD Clk22 Delay (Range: x00-x1F)
x94	(x25)	R/W	—	32	—	N/A	x05	BRAM Clk22 Delay (Range: x00-x1F)
x90	(x24)	R/W	—	32	—	N/A	x15	BRAM Clk132 Delay (Range: x00-x1F)

Table 7: (cont.)

x8C	(x23)	R/W	—	32	—	N/A	x00	Clock Delay Register Lock (xFE = not locked, Else = locked)
x88	(x22)	R/W	—	32	—	N/A	x00	KS Test Mode (x00 = alternating ones and zeros, Else = ODLD)
x84	(x21)	R/W	—	23	—	N/A	x00	Transition Board Mode (Range: 0-3)
x80	(x20)	R/W	—	16	—	N/A	xFF	Not-Sure Window Enable (x00 = disable, Else = enable)
x7C	(x1F)	R/W	17	17	—	xFF	xFF	Shift_In_Bit Enable (x00 = disable [enable test mode], Else = enable)
x78	(x1E)	R/W	16	16	—	x00	x00	Transition Board FPGA Reprogram Signal (x00 = high, Else = low)
x74	(x1D)	R	16	16	—	x02	x06	Number of Time Bins in Design (= 2 or 6)
x70	(x1C)	R	16	16	—	Ser. #	Ser. #	Board Serial Number (high serial number bit in the lsb of the register)

Table 7: (cont.)

x6C	(x1B)	R	16	16	—	Ser. #	Ser. #	Board Serial Number (low 8 bits)
x68	(x1A)	R/W	—	16	—	N/A	x0A	Not-Sure Window 5 Width (Range: x00-x0F)
x64	(x19)	R/W	—	16	—	N/A	x0A	Not-Sure Window 4 Width (Range: x00-x0F)
x60	(x18)	R/W	—	16	—	N/A	x0C	Not-Sure Window 3 Width (Range: x00-x0F)
x5C	(x17)	R/W	—	16	—	N/A	x0A	Not-Sure Window 2 Width (Range: x00-x0F)
x58	(x16)	R/W	—	16	—	N/A	x0C	Not-Sure Window 1 Width (Range: x00-x0F)
x54	(x15)	R	16	16	—	Ver. #	Ver. #	Kitchen Sink FPGA Firmware Version Number
x50	(x14)	R	16	16	—	Ver. #	Ver. #	Data FPGA Firmware Version Number
x4C	(x13)	R	19	19	—	x00	x00	Buffer 3 Content Bits (bits 5:0)
x48	(x12)	R	19	19	—	x00	x00	Buffer 2 Content Bits (bits 5:0)
x44	(x11)	R	19	19	—	x00	x00	Buffer 1 Content Bits (bits 5:0)
x40	(x10)	R	19	19	—	x00	x00	Buffer 0 Content Bits (bits 5:0)

Table 7: (cont.)

x3C	(x0F)	R	16	16	—	x00	x00	Read Buffer Byte (Automatically triggers read of next address)
x38	(x0E)	W	16	16	—	x00	x00	Buffer Byte Address (Range: 0-72) (Automatically triggers read)
x34	(x0D)	W	16	16	—	x00	x00	Buffer Number (Range: 0-3)
x30	(x0C)	W	16	16	—	x03	x29	Level 1 Accept Delay Value (in CDFCLK periods)
x2C	(x0B)	R/W	16	16	—	x00	x14	Clock 5 Delay (DELCLK[5]) (U13) (0.5ns/step) (LE_L)
x28	(x0A)	R/W	16	16	—	x00	x15	Clock 4 Delay (DELCLK[4]) (U12) (0.5ns/step) (LE_K)
x24	(x09)	R/W	16	16	—	x00	x12	Clock 3 Delay (DELCLK[3]) (U17) (0.5ns/step) (LE_J)
x20	(x08)	R/W	16	16	—	x7F	x87	Delayed Set/Clear Delay (U15) **(2ns/step) (LE_I)

Table 7: (cont.)

x1C	(x07)	R/W	16	16	—	xBC	x00	Prompt Set/Clear Delay (U16) (0.5ns/step) (LE_H)
x18	(x06)	R/W	16	16	—	x70	x10	Clock 2 Delay (DELCLK[2]) (U14) (0.5ns/step) (LE_G)
x14	(x05)	R/W	16	16	—	x62	x58	Clock 1 Delay (DELCLK[1]) (U19) (0.5ns/step) (LE_F)
x10	(x04)	R/W	16	16	—	x06	x03	CDFB0 Delay (U18) **(5ns/step) (LE_E)
x0C	(x03)	R	—	25	—	N/A	xF1	Board ID Register
x08	(x02)	R/W	16	16	—	xC8	xC8	PLL Input Delay (U11) (0.5ns/step) (LE_C)
x04	(x01)	R/W	16	16	—	x06	x03	CDFBC Delay (U20) **(5ns/step) (LE_B)
x00	(x00)	R/W	16	16	—	x5C	x4A	Initial CDFCLK Delay (U21) (0.5ns/step) (LE_A)

5.4 Stereo Finders

The role of the Finder, simply stated, is to identify valid track segments in a given COT super-layer. The Stereo Finders, installed during the XFT Upgrade, perform this same function in connection with the stereo super-layers of the COT. After the XTC2 has completed its digitization of the time information for pulses in the COT, the information is given to TDC Transition Modules which performs multiplexing and transmission via optical fiber. Passed forward via the optical fibers, the Stereo Finders receive this information and begin their own track segment identification.

Because the Stereo Finders are instrumented upon stereo super-layers, the track paths they find will necessarily appear displaced in ϕ from their actual location. This displacement will be a function approximately linear in the z value of the track. The SLAM (discussed below) can capitalize upon that correlation. A diagram showing how pixels from a track passing through a stereo super-layer can appear displaced in ϕ due to their location in z is shown in Figure 31 [44].

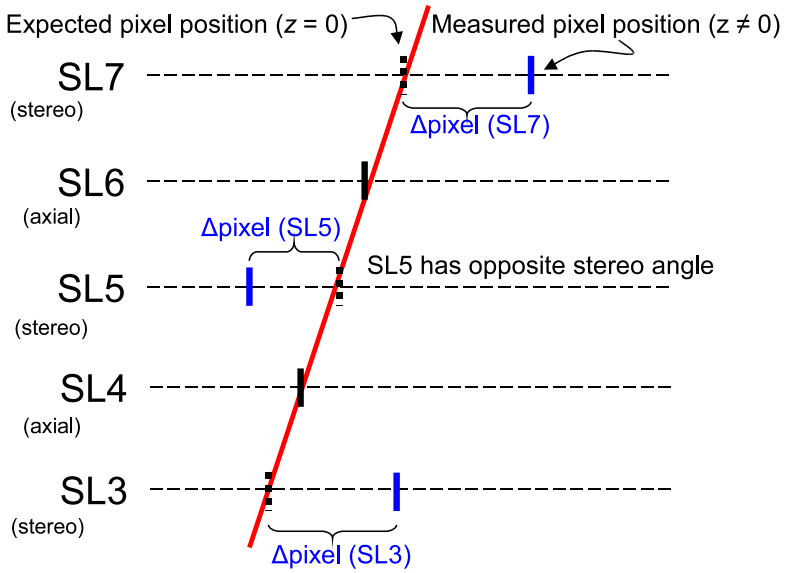

Figure 31: Pixel Displacement of Hits on Stereo COT Super-layers: A diagram representing the pixel displacement that will occur for tracks passing through stereo super-layers with non-zero z values. Importantly, the pixel displacement alternates directions from one stereo super-layer to the next [44].

5.5 SLAM

The Stereo Linker Association Module (SLAM) is capable of capitalizing upon the correlation between COT pixel displacement in ϕ with the associated track displacement in z (which is due to stereo super-layer sense wires not being precisely parallel to the collision axis). Notably, stereo super-layers alternate their direction of rotation away from the beamline axis (as described in more detail in Section 3.4.1). Thus, pixel displacement between adjacent stereo super-layers, such as SL5 and SL7, should be anti-correlated for real tracks. A simulation of real tracks shows this in the upper plot of Figure 32 [44]. Simulations of fake tracks show a complete lack of this correlation, providing a handle to the SLAM for fake rejection by comparing the pixel displacement for these tracks in the stereo super-layers.

Within the original, axial-based Level 1 XFT Trigger system, individual Finders have access to only local information in a geometric sense. That is to say, information corresponding to pixels on one side of the detector is not provided to Finders instrumented on the other side. While this holds true for the Stereo Finders installed in the XFT Upgrade, the domain of Finders which need to be linked in order to identify a full track is necessarily larger, due to the alternating direction of stereo rotation of the COT sense wires. Therefore, any individual SLAM board collects information from three different Stereo Finders in order to identify all possible tracks of interest [45].

Before the upgrade, information was sent from the Linker (part of the axial XFT Trigger path), to the XTRP, via a simple pass-through board, the Linker Output Module (LOM). The LOM was the only board replaced in the XFT system during the upgrade. The SLAM took its place, and thus has access to all the necessary stereo and axial information to perform fake track rejection. The upgraded system is represented in Figure 29 [43].

Since the upgrade, the Level 1 Trigger has been able to maintain a healthy accept rate despite growing instantaneous luminosity. Evidence of this is shown in Figure 33, where cross sections for a typical Level 2 Trigger path are shown before and after the XFT upgrade as a function of rising instantaneous luminosity [43]. As the higher luminosities, the inclusion of the stereo confirmation of tracks at Level 1 plays a vital role in maintaining trigger rates.

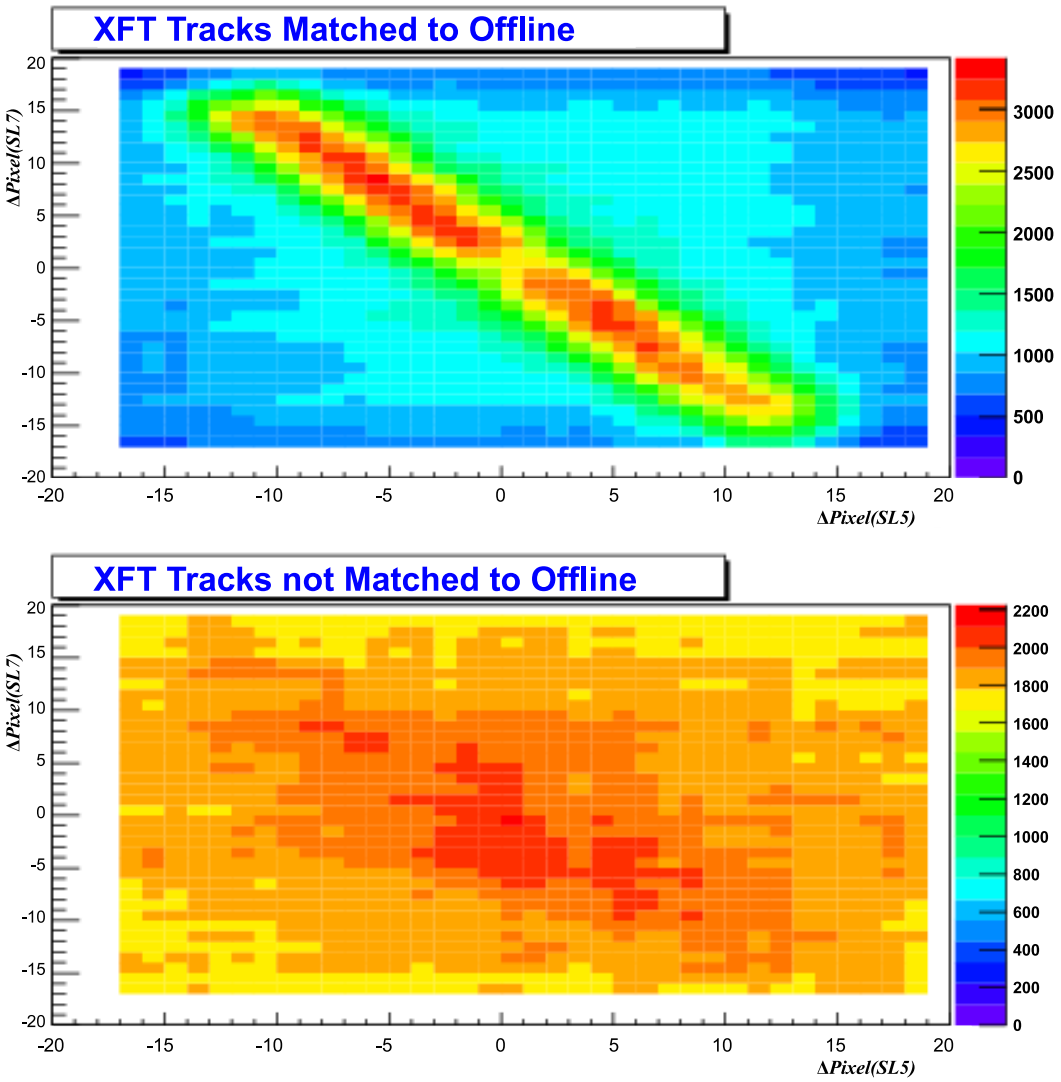

Figure 32: Anti-Correlation of Pixel Displacement Between Adjacent Stereo Super-layers (Simulation): Simulations show that real tracks will exhibit (negative) correlations of pixel displacement between stereo super-layers. This is represented in the above temperature histogram. Fake tracks, however, will show no such correlation, as is shown in the lower temperature histogram. Thus, Stereo Finders can capitalize on this expected correlation to improve fake track rejection at Level 1 [44].

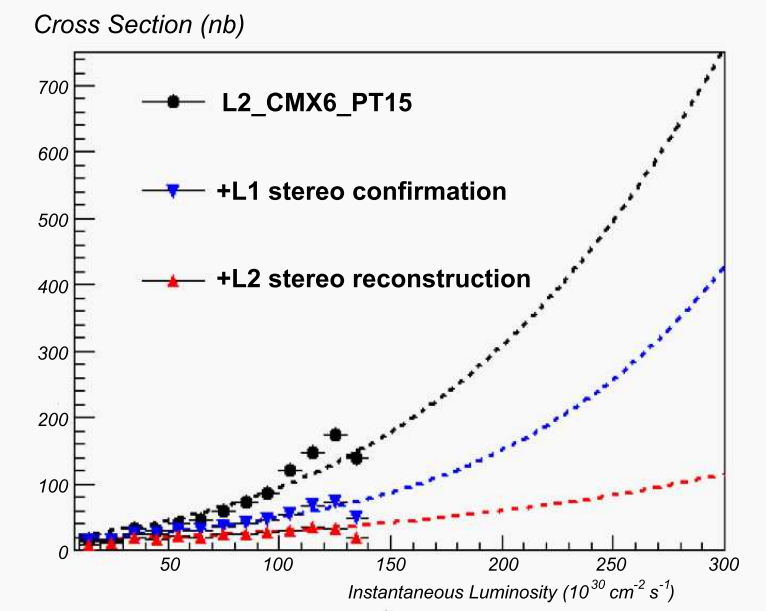

Figure 33: A typical Level 2 Trigger path has a cross section (black) that becomes unmanageable at higher instantaneous luminosities. After applying the XFT upgrade, bringing stereo confirmation to the Level 1 Trigger, the cross section (blue) continues to be manageable at very high luminosities [43].

6 Monte Carlo Used in This Analysis

The Monte Carlo samples generated for this analysis used software release `6.1.4` and `6.1.4mc.m`, the Scientific Linux 4 and Scientific Linux 5 versions of `cdfsoft` code, respectively. Simulations of $b\bar{b}$ production events, and the resulting decay of a B meson are performed using EvtGen. EvtGen is a Monte Carlo simulation specifically tuned to physics of B hadron decays, with a capability of handling CP violation in decays [50].

Detector effects are simulated in the Monte Carlo using standard CDF executables, including `cdfSim`, `TRGSim++`, and `ProductionExe`. The directory structure is further developed in accordance with the CDF B Group prescription [51]. Specifics of the three Monte Carlo sets used as part of this analysis are found in Table 8. To compare these Monte Carlo samples, plots are made using the selection criteria explained in Chapters 10 and 11. These plots, shown in Figures 34 through 40 demonstrate which aspects of the Monte Carlo samples vary, and the extent to which they accurately model data.

Monte Carlo Simulation	Description
Prompt B_s^0	$B_s^0 \to J/\psi\ \phi$ B_s^0 is prompt and constrained to decay directly to $J/\psi\ \phi$ Fragmentation tracks are excluded (B-Generator)
Scenario I B_c^+	$B_c^+ \to B_s^0\ \pi^+, B_s^0 \to J/\psi\ \phi$ B_c^+ is constrained to decay directly to $B_s^0\ \pi^+$. B_s^0 is constrained to decay directly to $J/\psi\ \phi$ Fragmentation tracks are excluded (B-Generator) B_c^+ is produced with a likely estimate of p_T spectrum
Scenario II B_c^+	$B_c^+ \to B_s^0\pi^+, B_s^0 \to J/\psi\ \phi$ B_c^+ is constrained to decay directly to $B_s^0\pi^+$. B_s^0 is constrained to decay directly to $J/\psi\ \phi$ Fragmentation tracks are excluded (B-Generator) B_c^+ is produced with p_T spectrum matching the Prompt B_s^0

Table 8: Descriptions of the three Monte Carlo samples developed for this analysis. The Scenario I B_c^+ and Scenario II B_c^+ differ, primarily, in the p_T spectrum of the B_c^+, as demonstrated in Figure 34. The Prompt B_s^0 sample accurately models the B_s^0+track background to this search, as shown in Figures 38 through 40.

In Figures 34 through 37, each of the three Monte Carlo samples described in Table 8 is compared. Figure 34 applies the pre-selections for the B_c^+ neural network to these samples (as

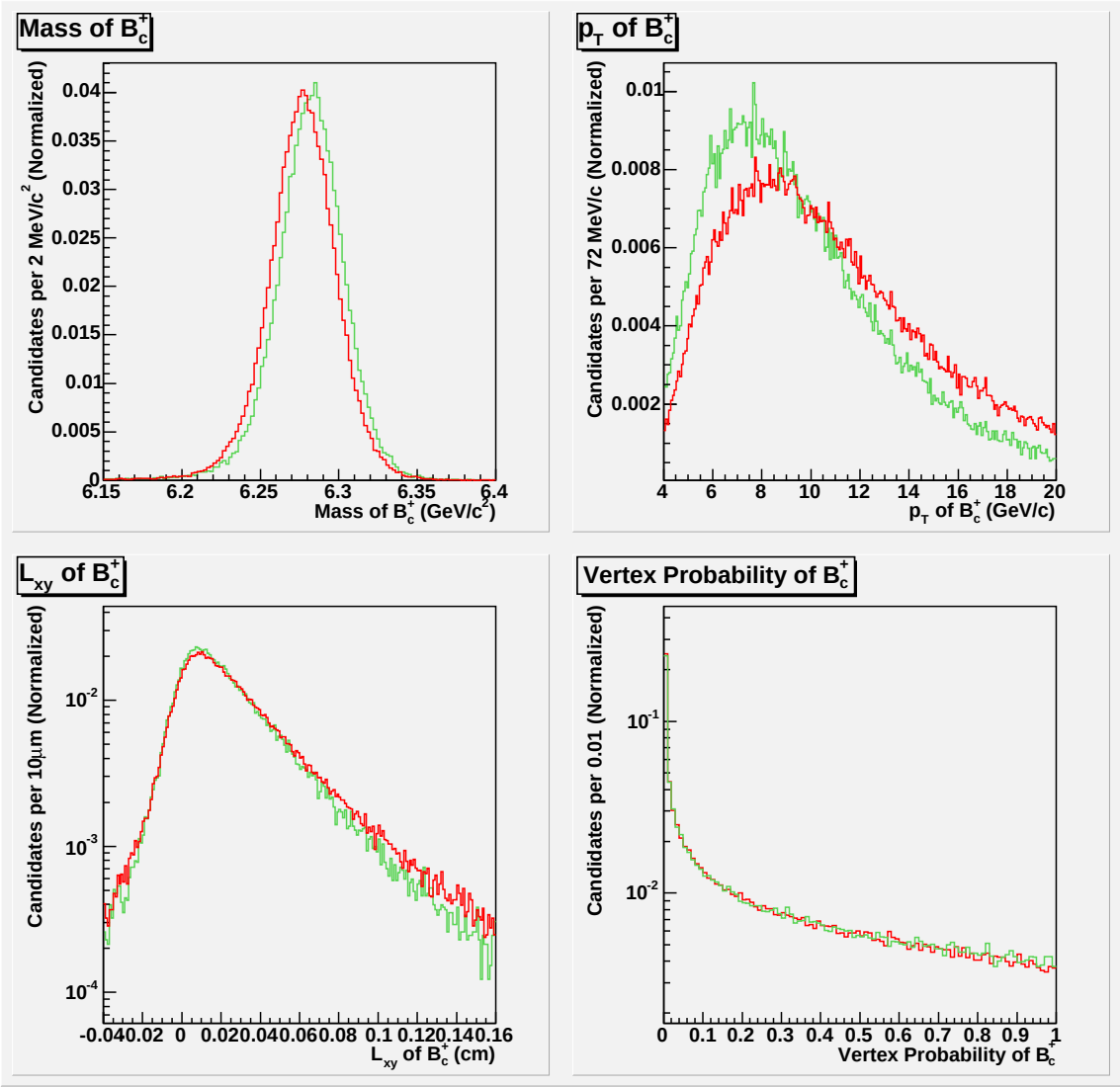

Figure 34: B_c^+ kinematic quantities as simulated for the CDF II detector, after applying B_c^+ neural network pre-selections as described in Chapter 11. The two Monte Carlo distributions shown are Scenario I B_c^+ (green) and Scenario II B_c^+ (red). Each distribution is normalized to unit area.

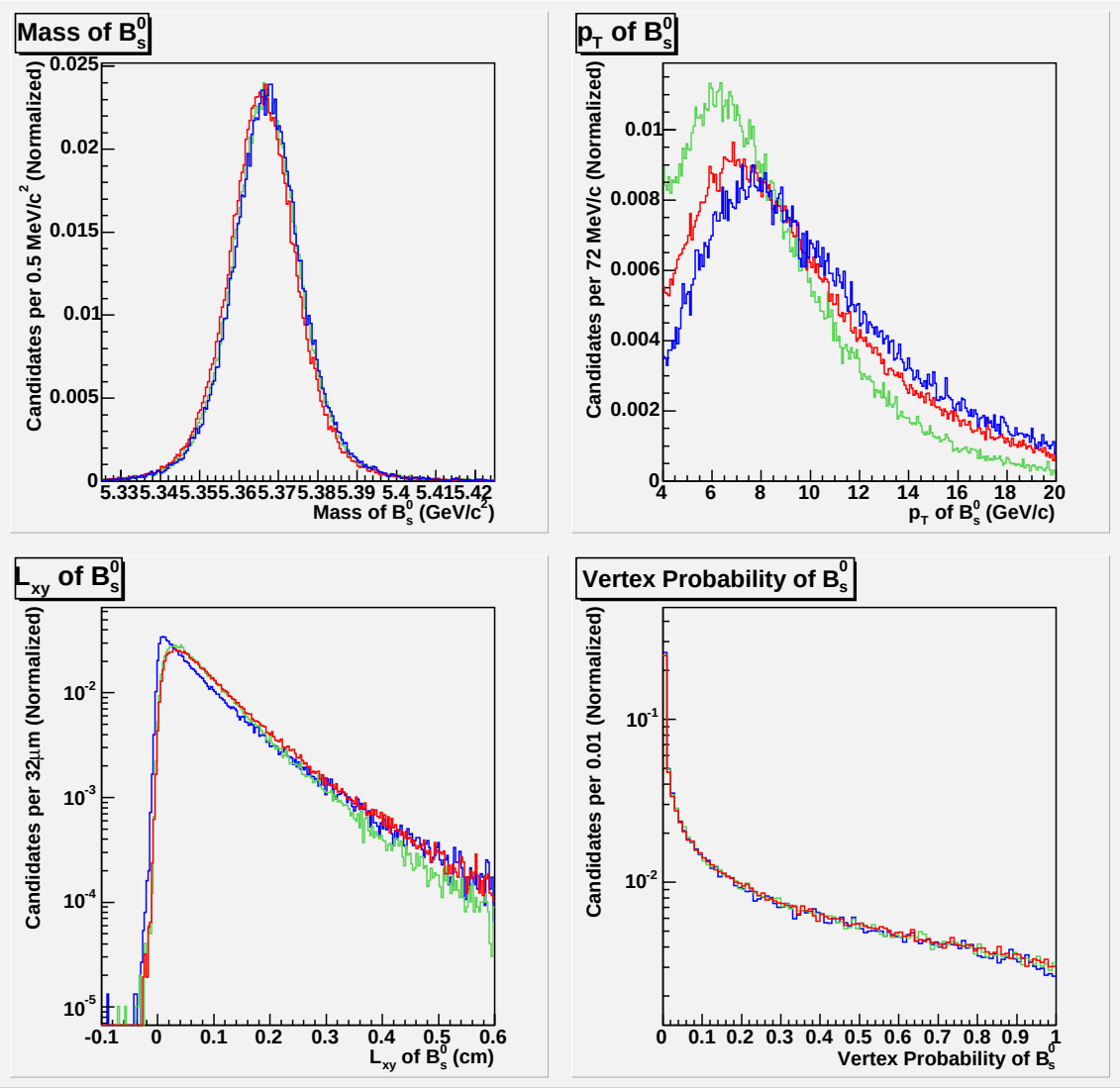

Figure 35: B_s^0 kinematic quantities as simulated for the CDF II detector, after applying B_s^0 neural network selection as described in Chapter 10. The three Monte Carlo distributions shown are Scenario I B_c^+ (green), Scenario II B_c^+ (red), and Prompt B_s^0 (blue). Each distribution is normalized to unit area.

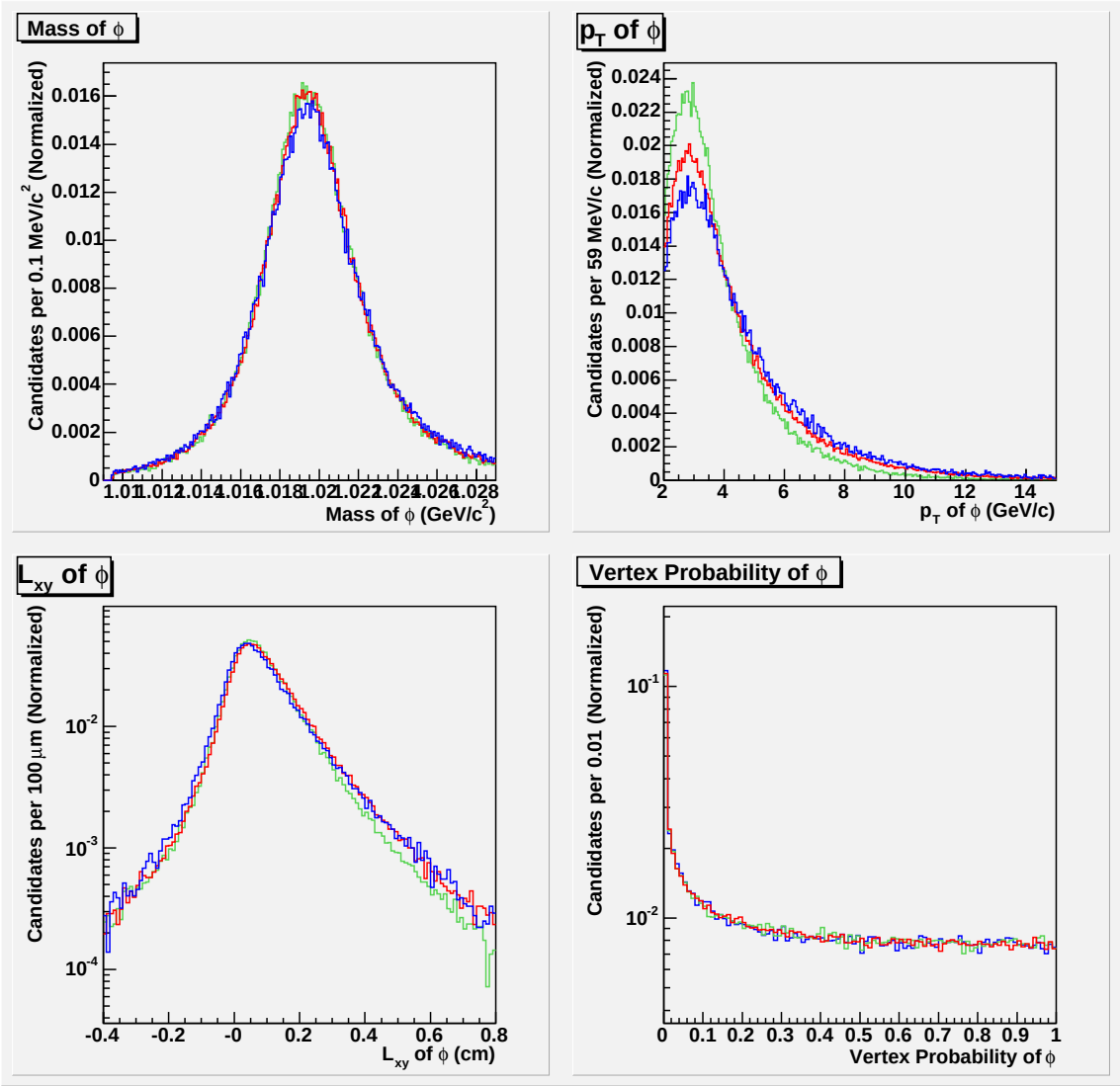

Figure 36: ϕ kinematic quantities as simulated for the CDF II detector, after applying B_s^0 neural network selection as described in Chapter 10. The three Monte Carlo distributions shown are Scenario I B_c^+ (green), Scenario II B_c^+ (red), and Prompt B_s^0 (blue). Each distribution is normalized to unit area.

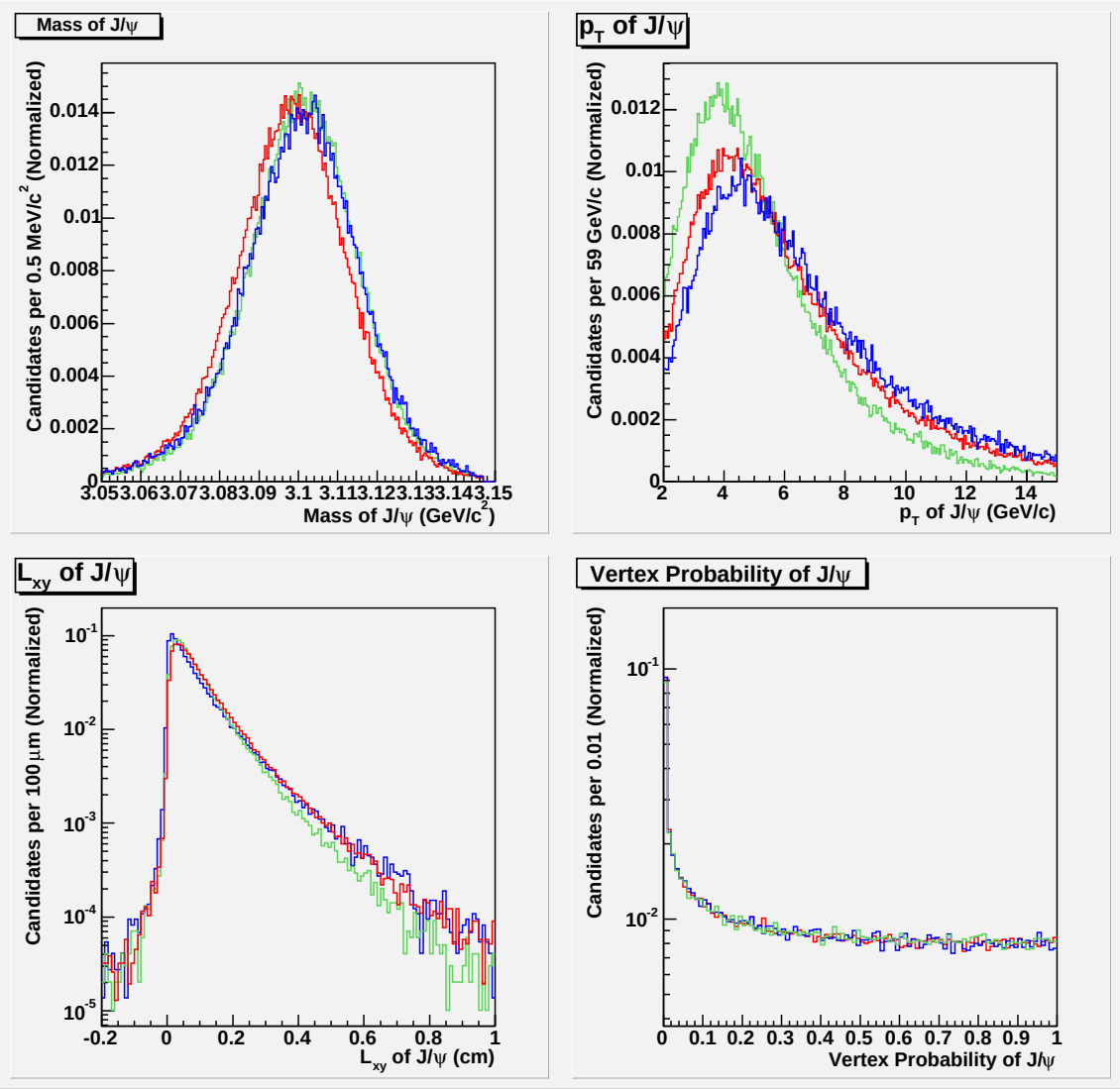

Figure 37: J/ψ kinematic quantities as simulated for the CDF II detector, after applying B_s^0 neural network selection as described in Chapter 10. The three Monte Carlo distributions shown are Scenario I B_c^+ (green), Scenario II B_c^+ (red), and Prompt B_s^0 (blue). Each distribution is normalized to unit area.

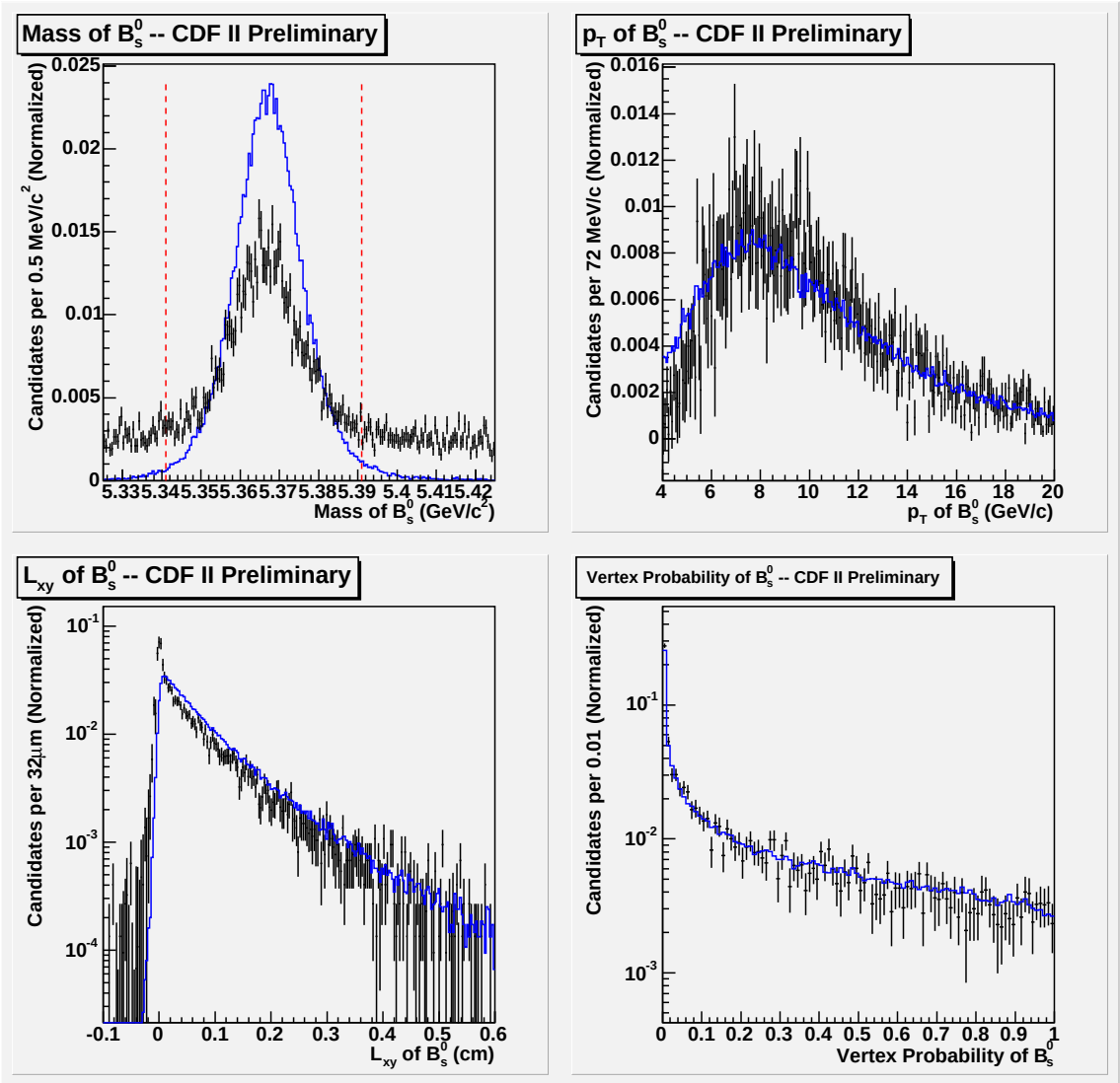

Figure 38: A comparison of kinematic quantities of the B_s^0 for Prompt B_s Monte Carlo (blue) versus sideband subtracted data (black) after applying B_s^0 neural network selection as described in Chapter 10. Data from the B_s^0 mass sideband (shown here with dashed red lines in the B_s^0 mass plot) is subtracted off from the other kinematic distributions to cancel the contribution from combinatoric background. All distributions are normalized to unit area.

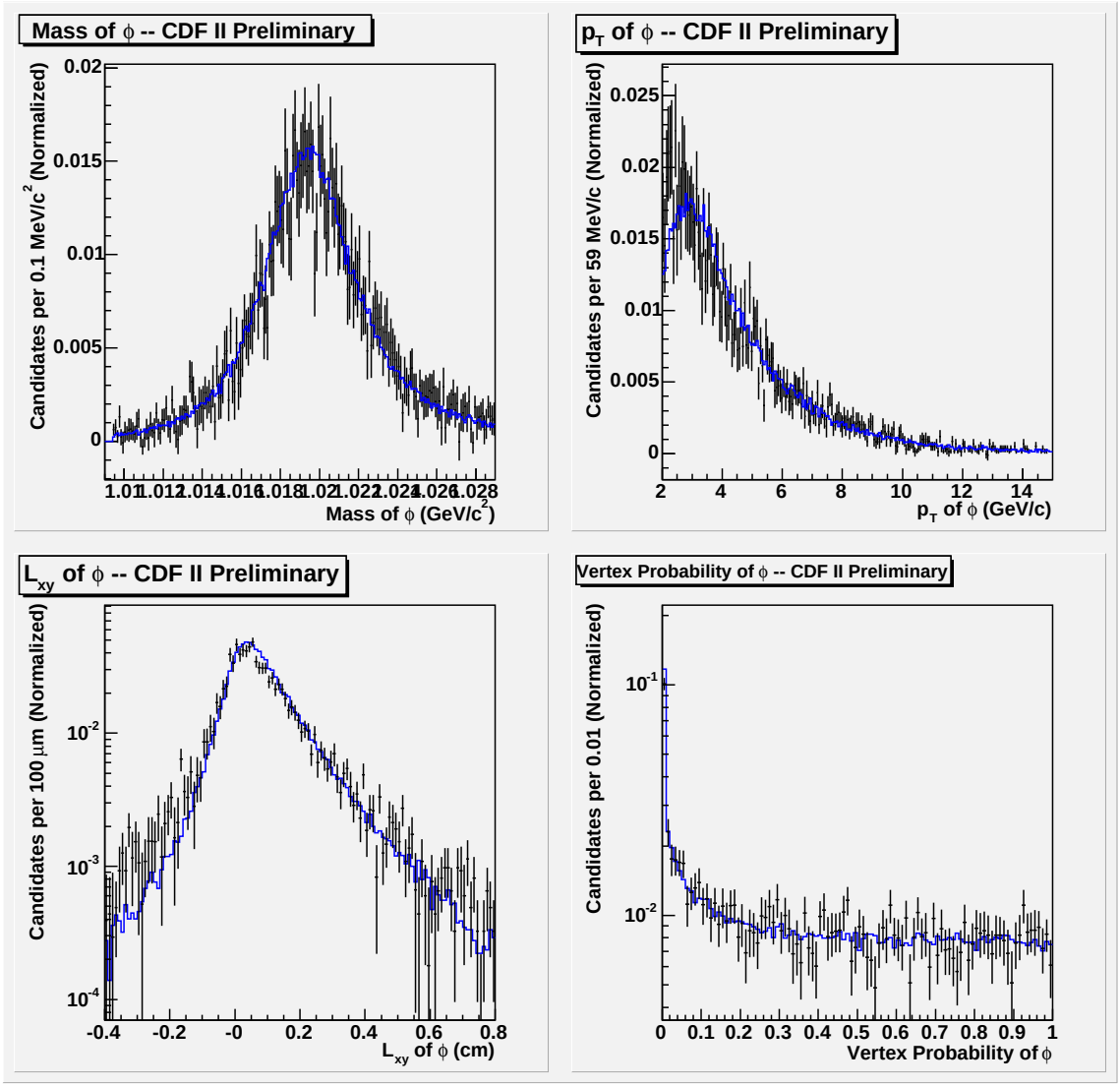

Figure 39: A comparison of kinematic quantities of the ϕ meson for Prompt B_s Monte Carlo (blue) versus sideband subtracted data (black) after applying B_s^0 neural network selection as described in Chapter 10. Data from the B_s^0 mass sideband (shown in Figure 38 with dashed red lines in the B_s^0 mass plot) is subtracted off from the other kinematic distributions to cancel the contribution from combinatoric background. All distributions are normalized to unit area.

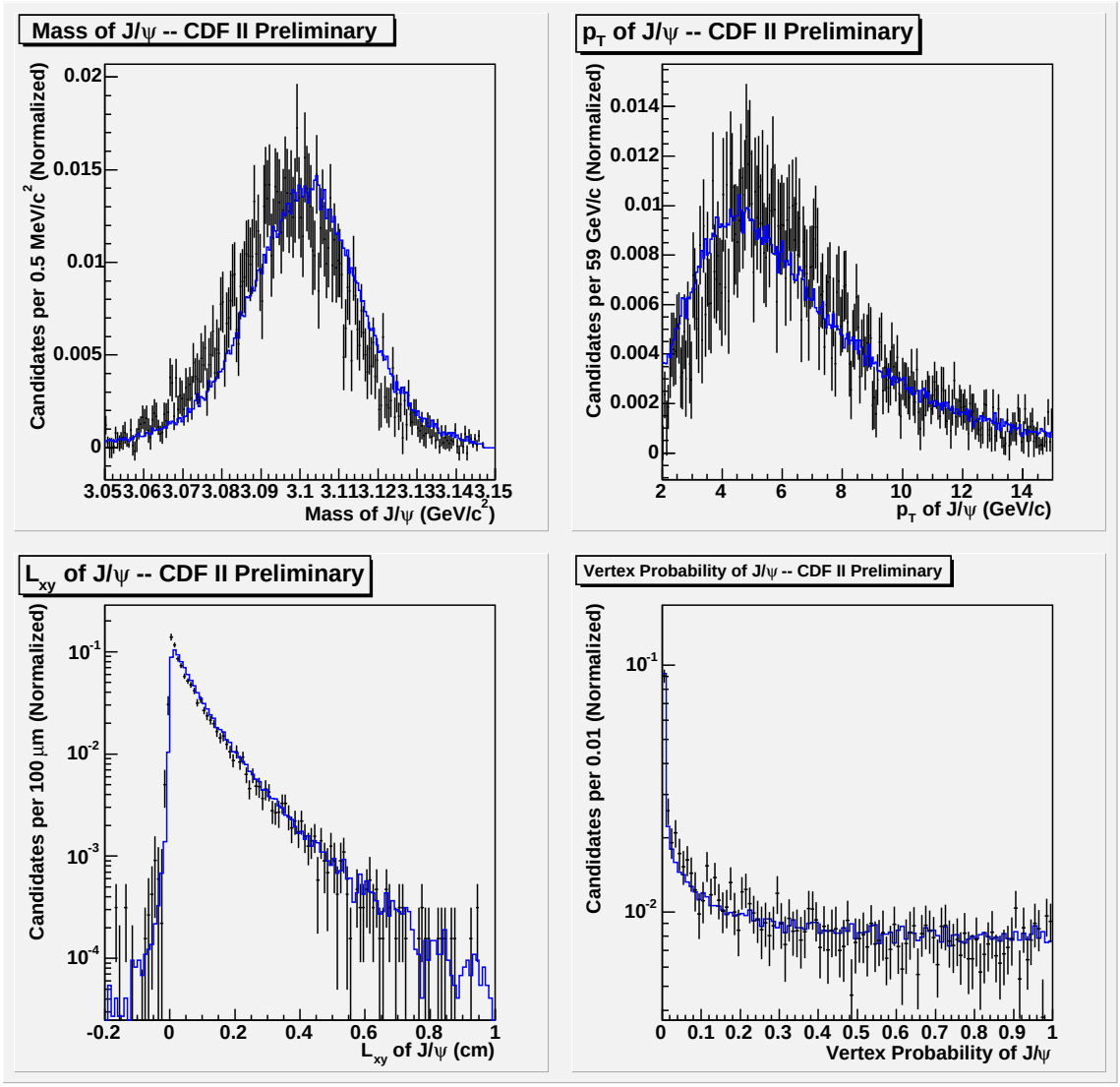

Figure 40: A comparison of kinematic quantities of the J/ψ meson for Prompt B_s Monte Carlo (blue) versus sideband subtracted data (black) after applying B_s^0 neural network selection as described in Chapter 10. Data from the B_s^0 mass sideband (shown in Figure 38 with dashed red lines in the B_s^0 mass plot) is subtracted off from the other kinematic distributions to cancel the contribution from combinatoric background. All distributions are normalized to unit area.

described later, in Chapter 11), and compares the resulting kinematics of the B_c^+. (Naturally, the Prompt B_s^0 sample is excluded from this collection of plots.) Similarly, Figures 35 through 37 show the various kinematics properties of the B_s^0, ϕ, and J/ψ mesons after applying the B_s^0 neural network selection criteria as described in Chapter 10.

Most notably, in Figure 34, the difference in the p_T spectrum of the B_c^+ between the Scenario I and Scenario II B_c^+ samples is evident. This is by construction, as the two samples are generated with differing hypotheses for the p_T spectrum of the B_c^+. The spectrum for Scenario I B_c^+ Monte Carlo is built using information from perturbative QCD models of B_c^+ production in hadron collisions [52, 53]. On the other hand, the spectrum for Scenario II B_c^+ Monte Carlo posits a B_c^+ with a harder spectrum, equivalent to that of the p_T spectrum of the B_s^0 in Prompt B_s^0 decays.

The harder p_T spectrum of B_s^0 candidates from Prompt B_s^0 decays is also evident in Figure 38. The softer B_s^0 spectrum for candidates produced by $B_c^+ \to B_s^0\ \pi^+$ decay is explained in Section 2.3.4.

Figures 38 through 40 demonstrate how data is well-modeled by the Prompt B_s^0 Monte Carlo sample. Both samples have the B_s^0 neural network selection cuts applied, as described in Chapter 10. To reduce the contribution from combinatoric B_s^0 background, sideband subtraction (using the B_s^0 mass sidebands) is applied to each plot (other than the B_s^0 mass plot itself). The sidebands to B_s^0, for the purposes of Figures 38 through 40, are the events with B_s^0 outside a 50 MeV/c^2 wide window. This window is shown in Figure 38 using dashed red lines. After applying this sideband subtraction, the kinematic distributions for every other variable in data is well-modeled by the Monte Carlo.

6.1 Polarization in B_s^0 Decays

Polarization of the B_s^0 is not expected to play a significant role in this analysis, as the method described in Section 2.3.3 allows for a cancelation of any effects confined to the B_s^0 decay. In light of this, each of the Monte Carlo samples produced has a roughly identical polarization spectrum for the B_s^0, which is based upon experimental results.

7 Technical Aspects of the Analysis Specific to CDF II

Some aspects of this analysis are designed around the particular methodologies of data-handling found at CDF II. Separate from the larger physics context of this analysis, these details are collected in this chapter. The particulars involved do not affect the final results, but play a critical role in accelerating the selection of candidates from large backgrounds.

7.1 Tools Available to Search for B_s^0 Events

The trigger system at CDF is a powerful tool in searching for B_s^0 events within our data. This analysis will capitalize on the success of the J/ψ Trigger in order search for the fully reconstructed $B_s^0 \to J/\psi\ \phi$ decay mode. Details of how the trigger selects events to be recorded are discussed in Chapter 4.

As a by-product of the B_s^0 mixing analysis, CDF has numerous other tools at its disposal to aid in a search for B_s^0 candidates within its data. The creation of the B-Stntuple has dramatically increased the speed of searching for B_s^0 meson by extracting only the relevant data from a a full event in data. In addition, the likelihood of error has been reduced by the implementation of B-Stntuple, as a standardized data format can be used across numerous analyses.

Since the first B_s^0 mixing analysis was published, measured yields have dramatically increased due to the development of artificial neural networks trained to search for B_s^0 decays. Details of the functioning of artificial neural networks are discussed generally in Appendix A, and briefly in Chapter 8. Specifics regarding the neural networks trained to search for B_s^0 decays are discussed in Chapter 9.

7.2 Overcoming the Limitations to a $B_c^+ \to B_s^0\ \pi^+$ Analysis

Though currently existing tools allow for a relatively straight-forward search for B_s^0 candidates in the data, there are limitations that hinder the search for $B_c^+ \to B_s^0\ \pi^+$ decays. First and foremost, the B-Stntuple structure, by default, does not have enough information to construct a $B_c^+ \to B_s^0\ \pi^+$ vertex. As a result, the pre-existing, cataloged B-Stntuples can only be used

in a limited way, and full events in data must be reprocessed to include a $B_c^+ \rightarrow B_s^0\ \pi^+$ vertex. By applying different settings in the TCL parameters of the B-Stntuple executable, the $B_c^+ \rightarrow B_s^0\ \pi^+$ vertex is generated while reprocessing full events in data. The specific TCL settings are detailed in Appendix B.

7.2.1 B_s^0 Skimming Requirements

Because the cataloged, standard B-Stntuples are not the primary source of data in this analysis; custom B-Stntuples that include a $B_c^+ \rightarrow B_s^0\ \pi^+$ vertex must be generated from the full events in compressed production output data. To expedite this process, however, the B_s^0 candidates of the cataloged B-Stntuples are reviewed to build a run and event list. This list is then used to skim over the compressed production output, building a vertex only in events in which quality B_s^0 candidates seem likely.

The cuts on neural network score of the B_s^0 applied before building the run and event list are shown in Table 9. In addition, these neural network score requirements imply the application of selection requirements described in Table 11. Each entry in Table 9 shows the minimum neural network score required by a candidate for the event to be included in the run and event list.

	$B_s^0 \rightarrow J/\psi\ \phi$
0d	≥ -0.999
0h	≥ -0.999
0i	≥ -0.999
0j	≥ -0.999
0k	≥ -0.999
0m	≥ -0.999

Table 9: Neural network score requirements imposed during run-event list skimming of cataloged B-Stntuples.

7.2.2 Prompt B_s^0 Bias in B_s^0 Neural Networks

A second limitation is that the neural networks currently trained to select B_s^0 candidates tend to be biased toward prompt B_s^0 candidates. To the extent that these neural networks are used

to eliminate combinatorial background during a $B_c^+ \to B_s^0\ \pi^+$ search, effort must be made to understand and, where possible, eliminate bias toward prompt B_s^0 candidates. Much of this effort is discussed in Chapter 9.

$B_s^0 \to J/\psi\ \phi$ neural network is used without PID. Because Monte Carlo simulation of particle identification is not well-modeled, this analysis will refrain from using particle identification as a means of validating candidates. To this end, the B_s^0 neural networks will not use particle ID information for kaons in $B_s^0 \to J/\psi\ \phi$ decays. This means that B_s^0 candidates will be scored using "version 2" of the neural network expert file for that mode. This does not dramatically affect the purity of the signal sample, which is shown in Chapter 10.

8 Artificial Neural Networks

From a mathematical standpoint, this analysis is a binary classification problem – deciding whether any given event in data, after some selection criteria are imposed, is a $B_c^+ \to B_s^0\ \pi^+$ decay. Artificial neural networks, and in particular, feed forward neural networks, are an effective technique in approaching this classification problem. This section will briefly describe their usage in this analysis. A more careful discussion of the theory of artificial neural networks is found in Appendix A.

8.1 Neural Network Input

8.1.1 Pre-selection cuts on variables

Any time a neural network is used to select signal candidates from a mixture of possible signal and background, carefully constructed training samples must be created. It is in the best interest of the analysis to perform a basic set of single variable selection cuts before creating these samples or scoring candidates. (These single variable cuts, which depend only on one parameter, and are thus 1-dimensional in their approach to selection, are named "rectangular" cuts, due to the shape these cuts impose when constraining the phase-space of variables.) As such, each neural network in this analysis is accompanied by an associated set of "rectangular" pre-selection cuts to speed training and improve scoring.

8.1.2 Training

The training of the neural network is at the heart of the neural network technique. For each variable provided during training, the distribution of signal and background is fitted with a spline fit. Certain pre-processing directives can be used to request special constraints, such as monotonic fits or Dirac δ functions. Any variable that cannot significantly contribute to the classification of candidates is eliminated from the decision process.

The remaining variables after the initial pruning may still have some correlations among them. The next step in the training is to decorrelate the variables by rotating the covariance matrix to the identity. The final step in training a neural network classifier (or "expert") is

to regularize the classification functions (reducing the effect of fluctuations within the training samples) and to reduce the number of free parameters as possible to improve the dilution.

All of this is training is performed using the Neurobayes® analysis software, which can take in structured collections of event information (called "flat ntuples") and perform the rotations, decorrelations, and spline fits on an arbitrary number of variables within the collection. This is discussed in more detail in Appendix A.

8.2 Neural Network Output

8.2.1 Interpretation of a neural network score

For binary classification problems, it is often the case (as in this analysis) that for each candidate evaluated a neural network, once trained, will output a score ranging between -1.0 and 1.0, inclusive. Higher scores indicate a higher probability of signal-like candidates over background-like candidates. Scores are distributed based on the monotonic sigmoid function, which is discussed in more depth in Appendix A. Suffice it to say that, once candidates are scored, a cut can be placed on the neural network score itself to select a group of likely signal candidates.

8.2.2 Auditing for bias in neural network score

Measurement of signal content within a sample of data that includes both signal and background is done by measuring yield in a discriminating variable. The discriminating variable, in this sense, is the key to the user's ability to optimize a cut on neural network score.

It is crucial, then, to avoid bias by insuring that any neural network used to distinguish signal from background not have information correlated to this discriminating variable. Otherwise, a cut on neural network score will introduce bias in the discriminating variable, invalidating any attempt to measure signal over background. It can be useful, then, to look in the sidebands of this parameter to check for any neural network score dependence. This technique is performed for the B_c^+ neural network used in this analysis, as can be seen in Section 11.5.

9 B_s^0 Neural Networks

This analysis searches within one fully reconstructed B_s^0 decay channel with no partially reconstructed modes of decay. The decay sequence, $B_s^0 \to J/\psi\ \phi$, $J/\psi \to \mu^+\mu^-$, $\phi \to K^+K^-$, includes four charged tracks in the final state of the B_s^0 decay. In previous analyses, selection of B_s^0 candidates against a combinatoric background has been optimized using neural networks. As a result, this analysis has a custom B_s^0 neural network that can be implemented to help in searching for B_s^0 decays. This section will discuss some of the details of this neural network, as it will be used to assist in the search for $B_c^+ \to B_s^0\ \pi^+$ decays.

9.1 Variable Definitions

Numerous variables are used to train and score the B_s^0 neural network in this analysis. In Table 10, each variable is defined.

9.2 Pre-Selection Variables

Section 8.1.1 noted that pre-selection requirements are necessary when training or implementing a neural network. Table 11 gives these requirements for the neural network expert that will evaluate the B_s^0 decay. The result of this evaluation, the B_s^0 neural network score, will be used later as an input to the B_c^+ neural network expert, which will have its own preselection requirements.

9.3 Selection Variables

Table 12 presents the variables used to train and score $B_s^0 \to J/\psi\ \phi$ decay candidates.

9.4 Avoiding Adverse Bias from B_s^0 Neural Networks

It is the sole aim of the B_s^0 neural network to select a maximal number of B_s^0 candidates in a sample while suppressing a combinatoric background. Thus, there is no assurance, *a priori*, that the output of the B_s^0 neural network will not be biased against $B_c^+ \to B_s^0\ \pi^+$ candidates (in favor of prompt B_s^0). For example, a $B_c^+ \to B_s^0\pi^+$ event may be scored poorly by the

Variable	Definition
$\chi^2_{r\phi}(B_s)$	The error (χ^2) found when fitting the B_s vertex from its collection of daughter tracks, using only information in the $r-\phi$ plane
$p_T(B_s)$	The transverse momentum of the B_s candidate
Prob(B_s)	The probability of the B_s vertex, as computed using the $\chi^2_{r\phi}(B_s)$
$p_T(\phi)$	The transverse momentum of the ϕ meson daughter
Prob(ϕ)	The probability of the ϕ meson vertex fit
$\lvert\Delta m(K^+K^-,\phi)\rvert$	The absolute difference in mass of the reconstructed (unconstrained) mass of the ϕ and the PDG value of the ϕ mass
$p_T(K_1)$	The transverse momentum of the first kaon daughter
$p_T(K_2)$	The transverse momentum of the second kaon daughter
$p_T(J/\psi)$	The transverse momentum of the J/ψ meson daughter
Prob(J/ψ)	The probability of the J/ψ meson vertex fit
$\lvert\Delta$m $(\mu^+\mu^-, J/\psi)\rvert$	The absolute difference in mass of the reconstructed (unconstrained) mass of the J/ψ and the PDG value of the J/ψ mass
μ likelihood	The output of the muon likelihood function, an estimate of the probability that a muon is real given track-stub matching quantities and calorimetry information, for the muon daughters [54]
$p_T(\mu)$	The transverse momentum of the muon daughters

Table 10: Variables used in B_s^0 selection and their definitions. Each variable listed used during selection or pre-selection is defined here. The distinction of when each variable is used is made in Tables 11 and 12.

Pre-Selection Requirement	$B_s \to J/\psi\,\phi$
$\chi^2_{r\phi}(B_s)$	< 50
$p_T(B_s)$ [GeV/c]	> 4.0
$p_T(\phi)$ [GeV/c]	> 1.0
$p_T(K)$ [GeV/c]	> 0.4
$\lvert\Delta m(K^+K^-,\phi)\rvert$ [GeV/c^2]	< 0.01
$\lvert\Delta m(\mu^+\mu^-,J/\psi)\rvert$ [GeV/c^2]	< 0.05

Table 11: Pre-Selection Requirements – $B_s^0 \to J/\psi\ \phi$ If a B_s^0 candidate fails to pass any of the above cuts, the B_s^0 neural network score will default to -1.0, the lowest possible value.

$B_s^0 \to J/\psi\ \phi,\ J/\psi \to \mu^+\mu^-,\ \phi \to K^+K^-$
$\chi^2_{r\phi}(B_s)$
$p_T(B_s)$
Prob(B_s)
$p_T(\phi)$
Prob(ϕ)
$\lvert\Delta m(K^+K^-,\phi)\rvert$
$p_T(K_1)$
$p_T(K_2)$
$p_T(J/\psi)$
Prob(J/ψ)
$\lvert\Delta$m $(\mu^+\mu^-,J/\psi)\rvert$
μ_1 likelihood
μ_2 likelihood
$p_T(\mu_1)$
$p_T(\mu_2)$

Table 12: Training and scoring variables for the $B_s^0 \to J/\psi\ \phi$ neural network expert. The definition of μ_1 and μ_2 is arbitrary.

B_s^0 neural network if the kinematic properties of the B_s^0 are statistically less attractive to the neural network than those properties of a B_s^0 produced promptly.

In particular, the role of $p_T(B_s^0)$ in pre-selection and scoring merits attention. While this variable will be used in the training and scoring of the B_c^+ neural network expert, the extent to which a negative correlation is found between B_s^0 neural network score and $p_T(B_s^0)$ itself should be understood from the outset.

9.4.1 $p_T(B_s^0)$ distribution for $B_c^+ \to B_s^0\ \pi^+$ vs. prompt B_s^0

A review of pre-selection criteria for the B_s^0 neural network (see Table 11) shows that selection criteria require $p_T \geq 4.0$ GeV/c – a reasonable cut considering the challenge of selecting against combinatoric candidates, that has also been shown in previous analyses to be efficient in discriminating signal and background.

p_T bias in B_s^0 neural networks is adverse. In order to improve their yield of B_s^0 candidates above combinatoric background, neural networks prefer selecting B_s^0 candidates with higher p_T. However, as described in Section 2.3.4, the B_c^+ is expected to have a softer production spectrum than prompt B_s^0 candidates. This leads to softer B_s^0 candidates in $B_c^+ \to B_s^0\ \pi^+$ signal events than in the prompt B_s^0 background, hurting the overall acceptance of $B_c^+ \to B_s^0\ \pi^+$ candidates when using the B_s^0 neural network.

Figure 41 shows direct evidence that the acceptance of a B_s^0 neural network increases as a function of p_T of the parent hadron in an event, using generator level (Scenario I B_c^+ and Prompt B_s^0) Monte Carlo. This adverse bias toward prompt B_s^0 candidates is unavoidable, though not necessarily problematic. Figure 42 shows that, for high values of parent hadron p_T, candidates are treated almost identically by the B_s^0 neural network cut, regardless of whether the event was prompt B_s^0 or a $B_c^+ \to B_s^0\ \pi^+$ decay. At low values of parent hadron p_T, the expected adverse bias that is demonstrated is shown to be acceptable, given the strength of the B_s^0 neural network in eliminating combinatoric candidates. In the end, the total effect of this bias shows up in the relative acceptance calculations used to quantify final measurement.

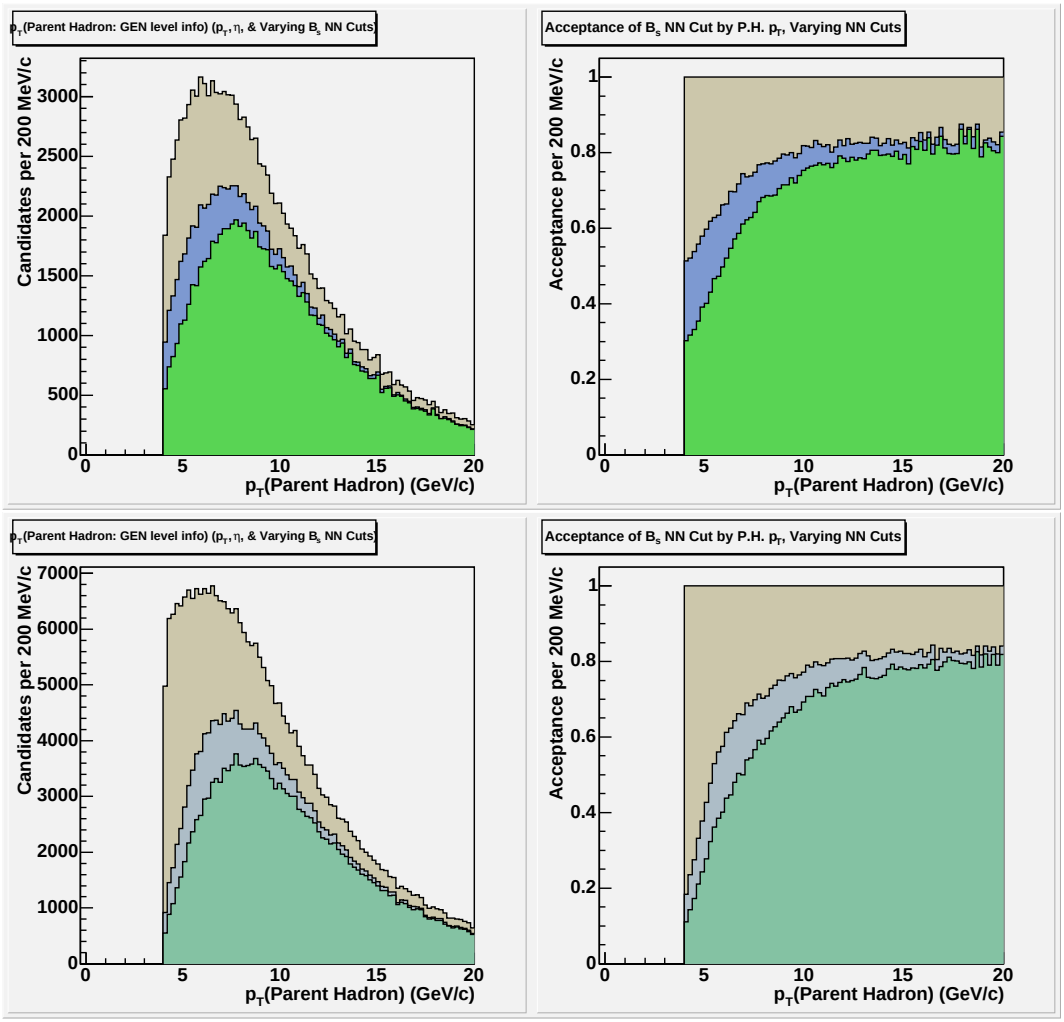

Figure 41: Monte carlo simulation of $B_c^+ \to B_s^0\,\pi^+$ candidates and prompt B_s^0 candidates are used to study the effect of B_s^0 neural network cuts on p_T distributions of the parent b-hadrons. **left:** p_T of parent hadron candidates (prompt B_s^0 above and Scenario I B_c^+ below – further description of these Monte Carlo simulations are found in Chapter 6) increases as increasing cuts on B_s^0 neural network score are applied. p_T value is as listed at Generator Level. Loose p_T and η requirements are applied to all candidates to simulate detector acceptance. **right:** Taking the ratios of the distributions at left (using the largest as the denominator), shows that acceptance for B_s^0 neural network score cut increases as a function of p_T for the parent hadron.

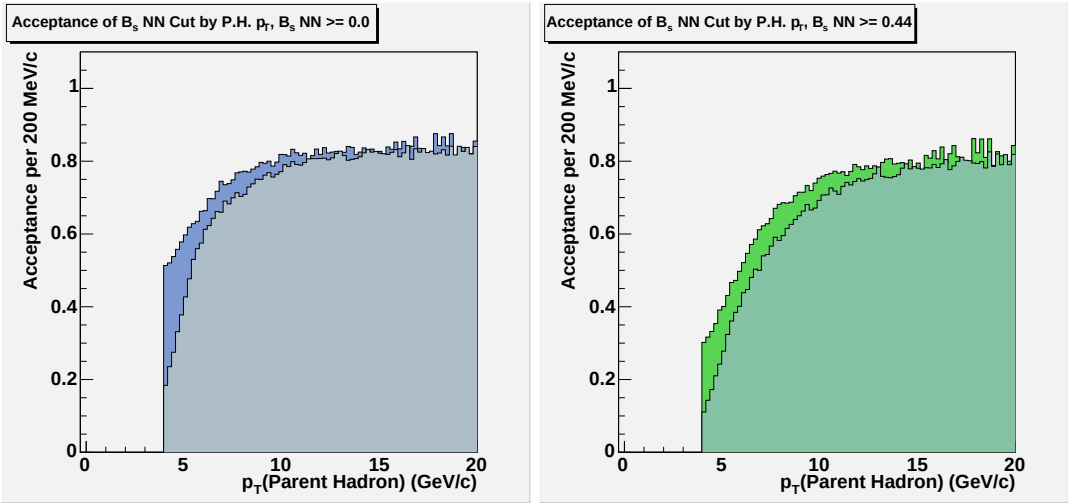

Figure 42: At high values of parent hadron p_T, B_s^0 neural network cuts have about equal acceptance values, regardless of whether the event was prompt B_s^0 or a $B_c^+ \rightarrow B_s^0\pi^+$ decay. This is demonstrated when overlaying the acceptance plots from Figure 41. For low values of parent hadron p_T, a bias toward prompt B_s^0 in acceptance is inevitable, but shown to be small enough to be considered acceptable.

10 B_s^0 Skims and Yields in Custom B-Stntuples

In this chapter, the B_s^0 yields within our custom B-Stntuples is computed. To maintain consistency with previous B_s^0 searches, we optimize our yield using the B_s^0 neural network score as the primary selection mechanism. In addition, the fitted value of $\frac{S}{\sqrt{S+B}}$ is optimized for each mode. This is a direct measure of the number of B_s^0 candidates used in the search for $B_c^+ \to B_s^0\ \pi^+$, as this will be used as a requirement in the final event selection.

Concerning the fitted value of $\frac{S}{\sqrt{S+B}}$ that is used to optimize the following yields, S and B are defined from a fit made to the mass distribution. S is defined as the integral of the gaussian of the fit, while B is the integral of the underlying exponential background in a range of $\pm 2\sigma$ of the gaussian peak.

	$B_s^0 \to J/\psi\ \phi$
NN Cut	0.44
B_s^0 yield	$5,574 \pm 97$

Table 13: Selection of the final collection of B_s^0 candidates is performed by optimizing the B_s^0 neural network score (as a function of $\frac{S}{\sqrt{S+B}}$). The yield (over 5.84 fb^{-1}) is listed here, along with the optimized B_s^0 neural network score cut. A plot of the fitted yield, as well as a break-down of yield by period, is found in Figures 43(a) & (b). The yields appear compatible to that achieved in other analyses.

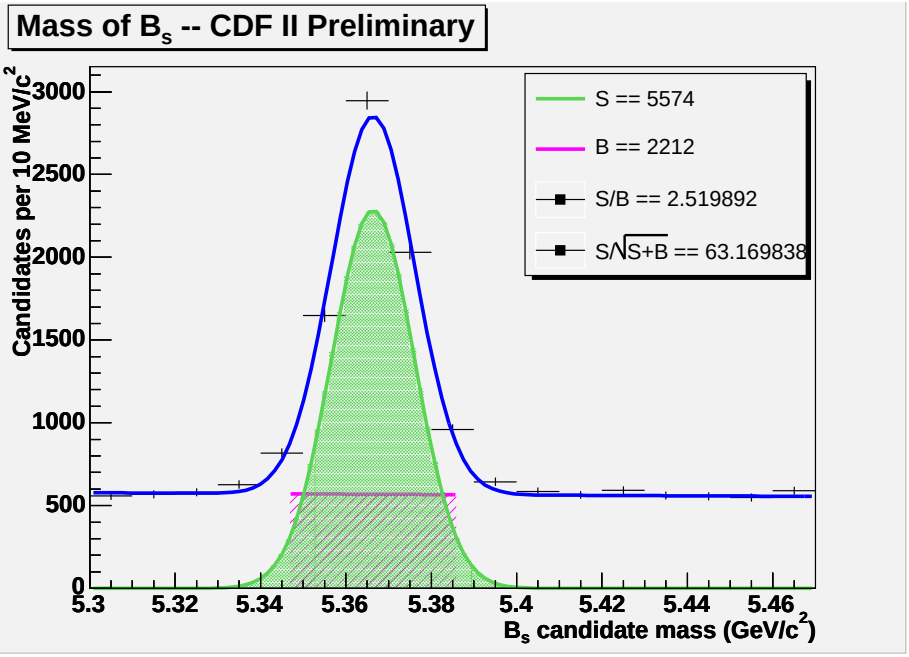

(a) B_s^0 yield through period 25

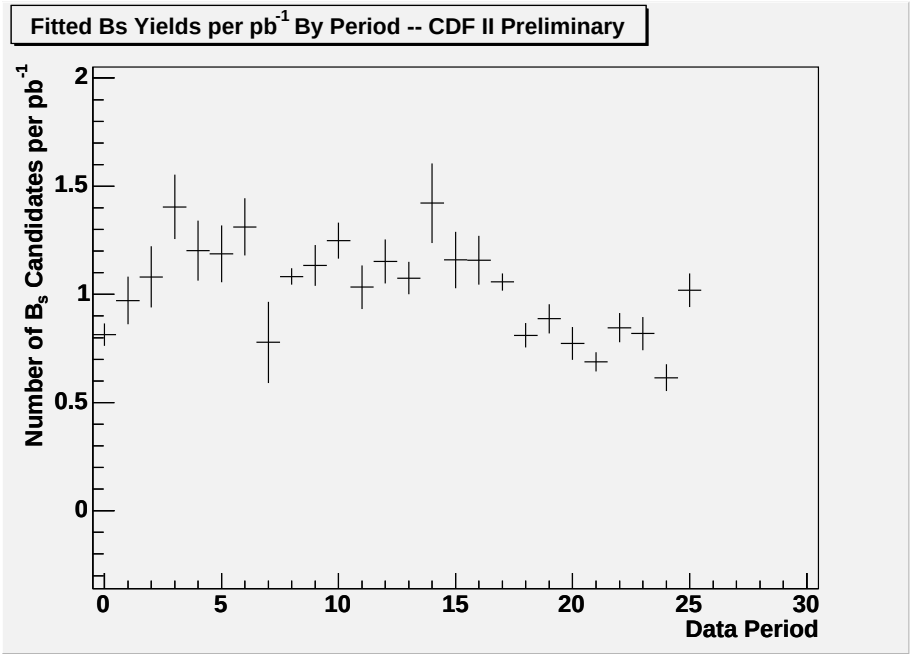

(b) B_s^0 cross-section by data period

Figure 43: After optimization on $\frac{S}{\sqrt{S+B}}$, the B_s^0 neural network cut is set at ≥ 0.44. The resulting yield is shown to be over 5500 B_s^0 candidates in the $B_s^0 \to J/\psi\ \phi$, $J/\psi \to \mu^+\mu^-$, $\phi \to K^+K^-$ mode. Estimated cross-section is shown on a period-by-period basis.

11 Training B_c^+ Neural Networks

11.1 Variable Definitions

Numerous variables are used to train and score the B_c^+ neural network in this analysis. In Table 14, each variable is defined. The definition provided for "d_0(Track) signed w.r.t B_s^0" is further clarified as a diagram in Figure 44.

Table 14: Variables used in B_c^0 selection and their definitions.

Variable	Definition
$p_T(B_c^+)$	The transverse momentum of the B_c^+ candidate
$L_{xy}(B_c^+)$	The displacement between the primary vertex and the decay point of the B_c^+, after projection onto the $r-\phi$ plane
$\sigma_{L_{xy}}(B_c^+)$	The error on the L_{xy} of the B_c^+
Prob(B_c^+)	The probability of the B_c^+ vertex, as computed using the $\chi^2_{r\phi}(B_c^+)$
$\chi^2_{r\phi}(B_c^+)$	The error (χ^2) found when fitting the B_c^+ vertex from its collection of daughter tracks, using only information in the $r-\phi$ plane
$\lvert d_0(B_c^+)\rvert$	The impact parameter (extrapolated distance of closest approach to the primary vertex) of the B_c^+ meson

Table 14: (cont.)

Prob(B_s^0)	The probability of the B_s vertex, as computed using the $\chi^2_{r\phi}(B_s)$
$\chi^2_{r\phi}(B_s^0)$	The error (χ^2) found when fitting the B_s vertex from its collection of daughter tracks, using only information in the $r-\phi$ plane
$\lvert d_0(B_s^0)\rvert$	The impact parameter (extrapolated distance of closest approach to the primary vertex) of the B_s meson
$\sigma_{d_0}(B_s^0)$	The error on the B_s impact parameter
NN Score(B_s^0)	The neural network score output by the B_s^0 neural network, as described in Chapter 9
$\lvert\text{mass}(B_s^0) - 5.366\ \text{GeV}/c^2\rvert$	The difference between the reconstructed (unconstrained) mass of the B_s and the PDG value
$L_{xy}(B_s^0)$	The displacement between the decay point of the B_c and the decay point of the B_s, after projection onto the $r-\phi$ plane
$\sigma_{L_{xy}}(B_s^0)$	The error on the L_{xy} of the B_s

Table 14: (cont.)

p_T(Track)	The transverse momentum of the B_c^+ daughter track
$\|d_0$(Track)$\|$	The impact parameter of the B_c^+ daughter track
d_0(Track) w.r.t B_s^0	The impact parameter of the B_c^+ daughter track, as measured with respect to the B_c^+ decay point, (*ie.* the B_s creation point)
σ_{d_0}(Track)	The error on the impact parameter of the B_c^+ daughter track
d_0(Track) signed w.r.t B_s^0	The impact parameter of the B_c^+ daughter track, signed according to the geometry of the decay. (See Figure 44)
Δz$_0$(Track,B_s^0)	The distance along the beamline axis between the origin of the B_c^+ daughter track and the B_s meson

11.2 Pre-selection of $B_c^+ \rightarrow B_s^0\ \pi^+$ Candidates

As described in Section 8.1.1, the pre-selection of candidates is necessary for the proper training of (and later scoring by) the B_c^+ neural network. Each of the training variables was examined for potential pre-selections that could expedite training of the B_c^+ neural networks. The selected cuts are shown in Table 15.

11.3 Training and Scoring Variables

Before training the B_c^+, it is worthwhile to examine the kinematic distributions of the input training variables, as well as of the Δm distribution (as defined in Section 2.3.3) of candidates from both signal and background. Though the B_c^+ neural network will certainly make use of

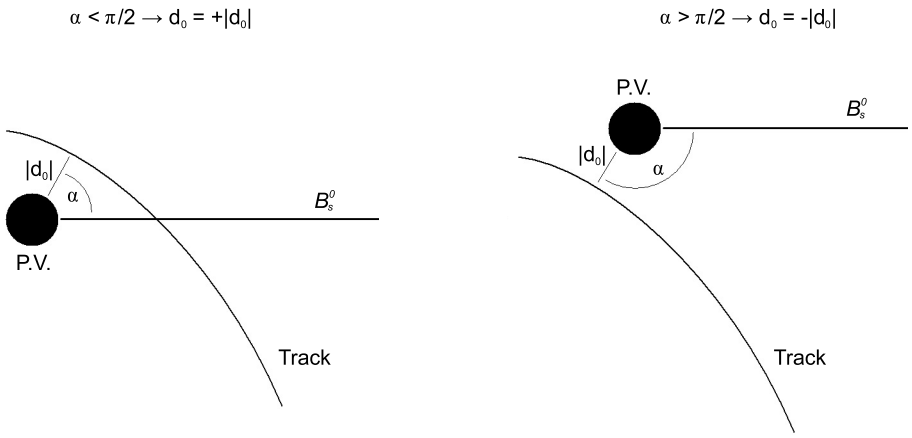

Figure 44: The variable d_0 when signed with respect to the B_s^0, remains a direct measure of the distance of closest approach to the primary vertex for a track. However, the sign is set to provide information about the angular configuration of the track with respect to the B_s^0 – tracks pointing in agreement with a B_c^+ hypothesis are signed positive, while others negative, as shown.

Variable	Pre-selection Requirement for J/ψ Trigger candidates
B_s^0 NN score	≥ 0.0
$L_{xy}(B_s^0)$	≥ 0.0005 cm
Prob(B_c^+)	$\geq 1 \times 10^{-5}$
$p_T(B_c^+)$	≥ 5.5 GeV/c
p_T(Track)	≥ 0.4 GeV/c
Δz_0(Track)	≤ 1.2 cm
d_0(Track) signed w.r.t B_s^0	≥ -0.01 cm
m(B_s^0) (upper-bound)	≤ 5.406 GeV/c^2
m(B_s^0) (lower-bound)	≥ 5.326 GeV/c^2
# silicon hits(B_s^0 tracks)	≥ 3
# axial COT hits (Kaons)	≥ 10
# stereo COT hits (Kaons)	≥ 10
# silicon hits(B_c^+ track)	≥ 3
# axial COT hits(B_c^+ track)	≥ 10
# stereo COT hits(B_c^+ track)	≥ 10

Table 15: Pre-selection requirements (imposed on top of skimming requirements) before training and scoring with the $B_c^+ \to B_s^0\ \pi^+$ neural network.

knowledge of the training variable distributions independent from one another (particularly when one variable has a distinct distribution between signal and background), variables with very similar distributions can also be considered valuable. Specifically, correlations can be discerned among multiple variables that might not be visible in a one dimensional histogram. Nevertheless, evaluating these one dimensional histograms can be a useful check on the health of the training data for the neural network. The one dimensional histograms are shown in Figures 45 through 50, and in Figure 51.

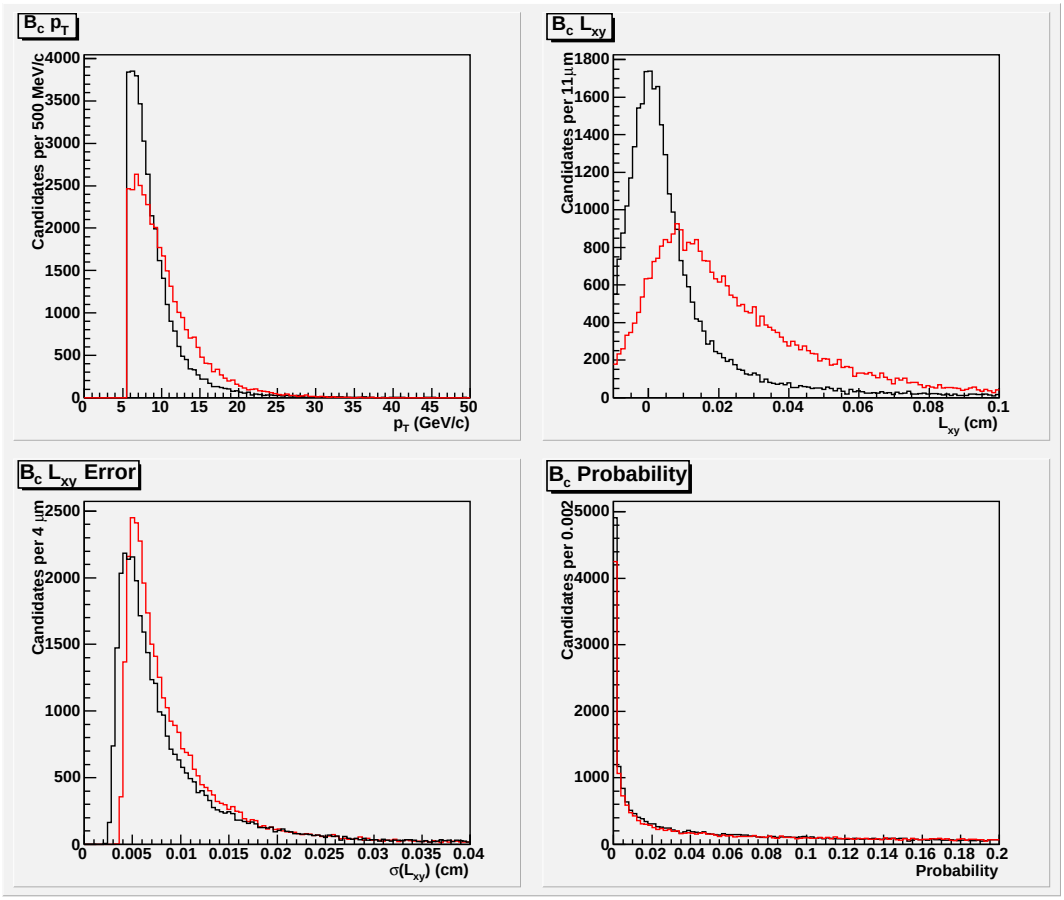

Figure 45: Variables, as described in Table 14, used in the training of the B_c^+ neural network. The distribution of the two training samples are shown – signal is red while background is black.

Upon training the B_c^+ neural network, the NeuroBayes® software package will create addi-

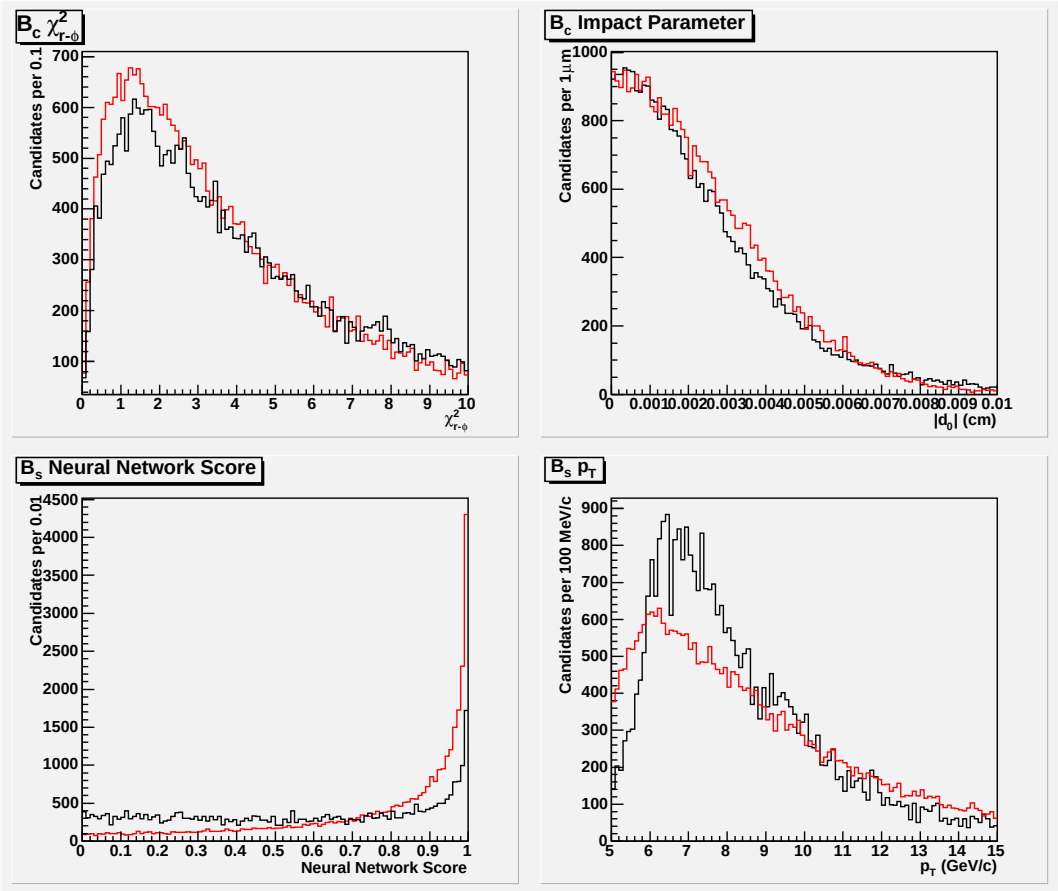

Figure 46: Variables, as described in Table 14, used in the training of the B_c^+ neural network. The distribution of the two training samples are shown – signal is red while background is black.

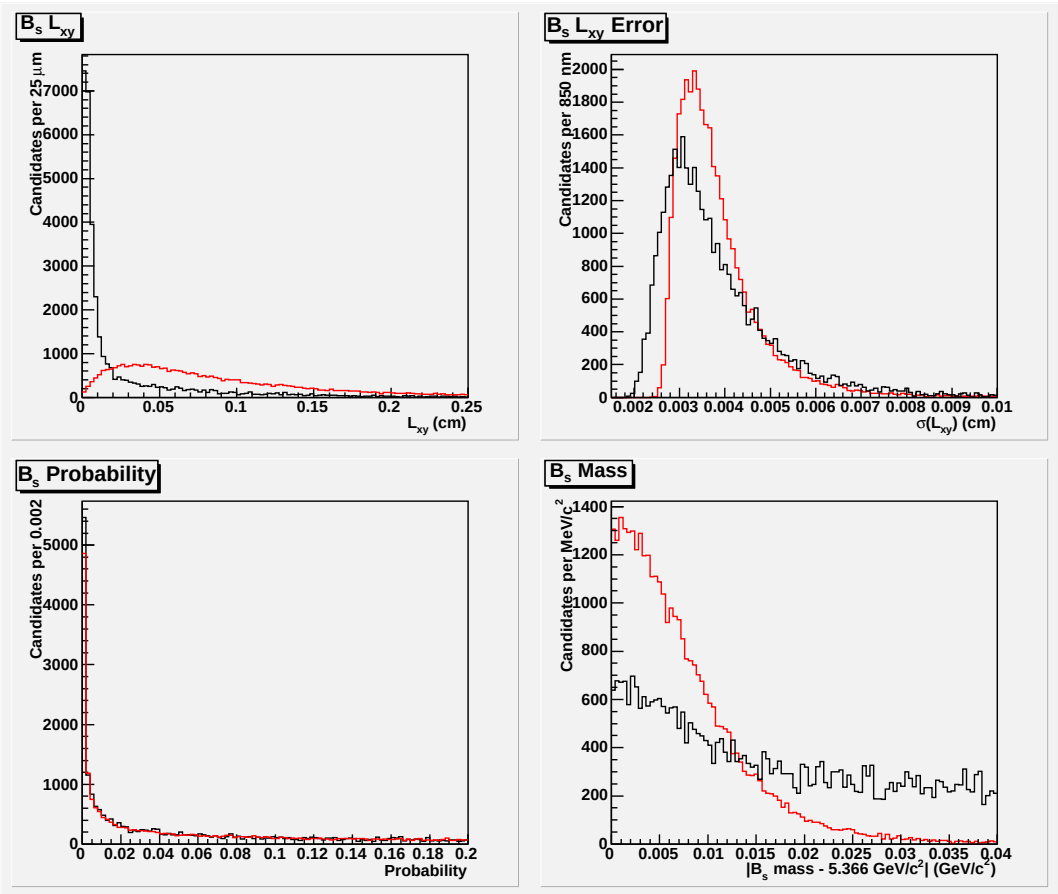

Figure 47: Variables, as described in Table 14, used in the training of the B_c^+ neural network. The distribution of the two training samples are shown – signal is red while background is black.

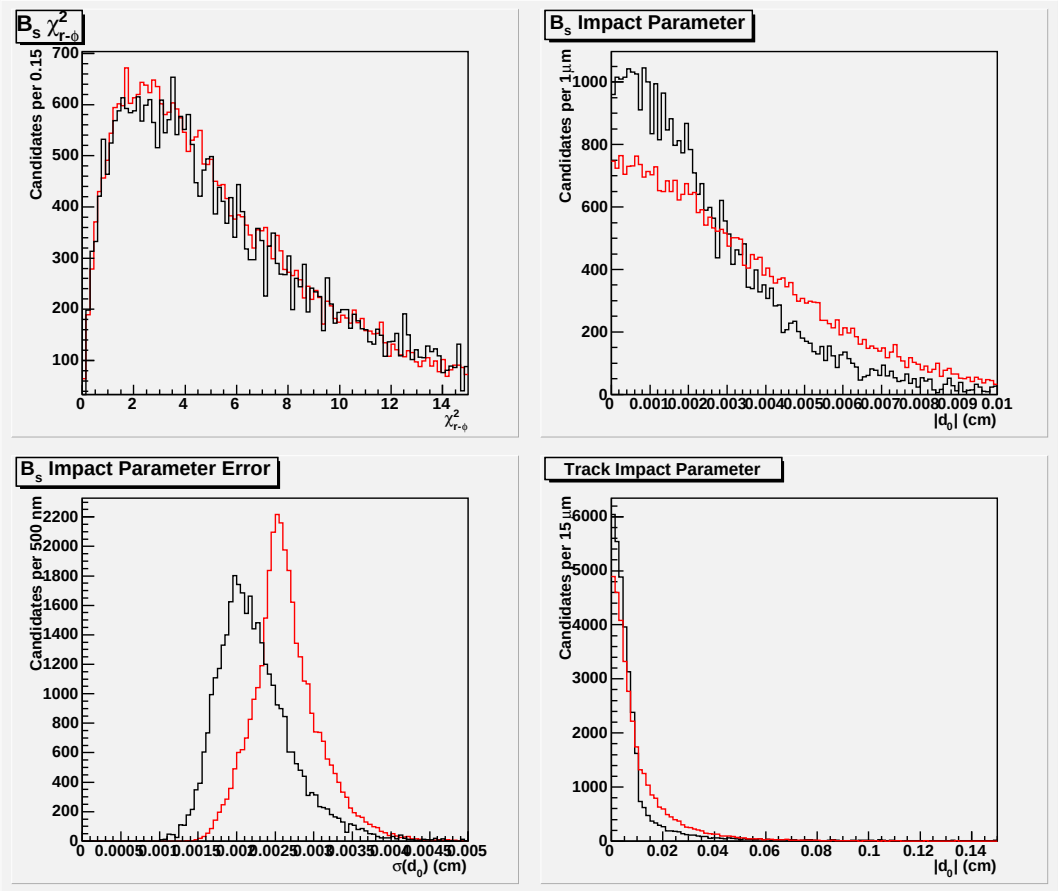

Figure 48: Variables, as described in Table 14, used in the training of the B_c^+ neural network. The distribution of the two training samples are shown – signal is red while background is black.

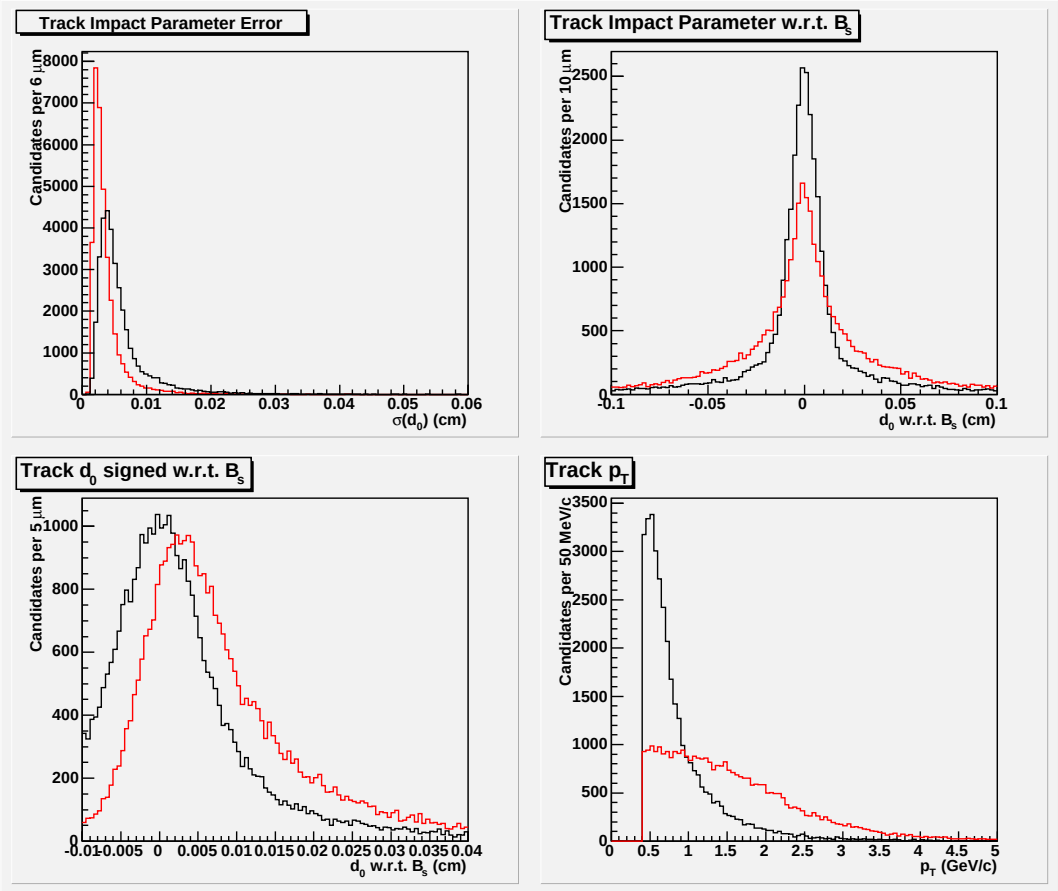

Figure 49: Variables, as described in Table 14, used in the training of the B_c^+ neural network. The distribution of the two training samples are shown – signal is red while background is black.

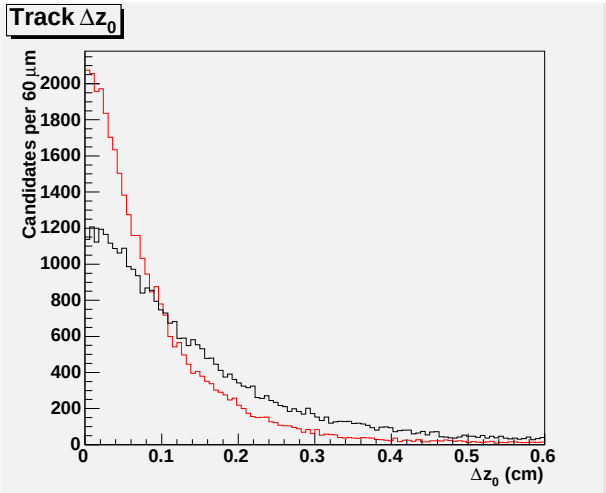

Figure 50: The last variable used in the training of the B_c^+ neural network. The distribution of the two training samples are shown – signal is red while background is black.

tional plots of signal and background efficiency for each training variable. In order that the sum of the two histograms remain constant, the plots are given variable bin widths. The resulting plots display the ratio of signal to background in the training samples as a function of the variable considered, albeit with varying bin widths. These plots can be found in Appendix D.

The variables used to train and score the $B_c^+ \rightarrow B_s^0\ \pi^+$ neural network are summarized in Table 16.

11.4 Signal and Background Samples Used in Training

Because it was found that isolation would not be a critical factor in differentiating signal from background (see Section 11.7), B-Gen Monte Carlo was used to simulate signal of $B_c^+ \rightarrow B_s^0\ \pi^+$ decays. For background, data in the range of $1.2\text{GeV}/c^2 \leq \Delta\text{m} \leq 2.0\text{GeV}/c^2$ – a kinematically forbidden, upper sideband to signal, as described in Section 2.3.3 – is used. The amount of background used in training was constrained such that the number of events would not be greater than the number of signal events. The samples for each of the modes are shown in Figure 51.

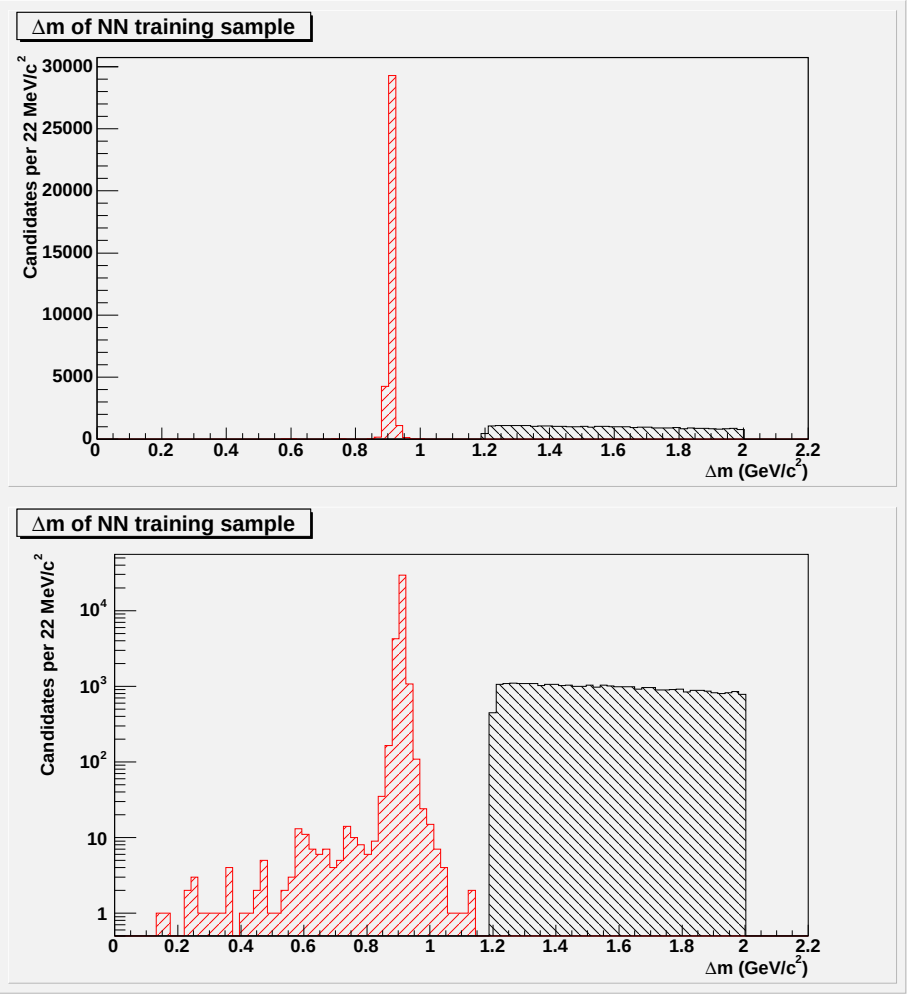

Figure 51: The upper sideband of Δm, from Δm=1.2 GeV/c^2 is used to select prompt B_s^0 candidates from the data sample as a $B_c^+ \to B_s^0\pi^+$ background, while signal is extracted from $B_c^+ \to B_s^0\pi^+$ Monte Carlo.

Training Variables for the $B_c^+ \to B_s^0\pi^+$, $B_s^0 \to J/\psi\ \phi$ Neural Network
$p_T(B_c^+)$
$L_{xy}(B_c^+)$
$\sigma_{L_{xy}}(B_c^+)$
Prob(B_c^+)
$\chi^2_{r\phi}(B_c^+)$
$\lvert d_0(B_c^+)\rvert$
Prob(B_s^0)
$\chi^2_{r\phi}(B_s^0)$
$\lvert d_0(B_s^0)\rvert$
$\sigma_{d_0}(B_s^0)$
NN Score(B_s^0)
$\lvert$mass$(B_s^0) - 5.366$ GeV$/c^2\rvert$
$L_{xy}(B_s^0)$
$\sigma_{L_{xy}}(B_s^0)$
p_T(Track)
$\lvert d_0$(Track)$\rvert$
d_0(Track) w.r.t B_s^0
σ_{d_0}(Track)
d_0(Track) signed w.r.t B_s^0
Δz$_0$(Track,B_s^0)

Table 16: Training variables for the B_c^+ neural network.

11.5 Checking for Δm Bias

Ultimately, Δm is used to identify $B_c^+ \rightarrow B_s^0\ \pi^+$ candidates after selection has been performed. As discussed in Section 2.3.3, Δm compares the mass of the B_s^0 alone to the combination of the B_s^0 with the daughter track of the B_c^+ candidate. This is an effective technique, as resolution effects for the B_s^0 are canceled, allowing signal events to occupy a narrow window in Δm, located at approximately 910 MeV/c^2 with a gaussian width of less than 10 MeV/c^2.

To ensure that each B_c^+ neural network trained in this analysis is not biased in Δm, increasing cuts on B_c^+ neural network score are applied, and the effect on the distribution of Δm in upper sideband data is examined. The result, as shown in Figure 52 is a flat efficiency as a function of Δm for each neural network, which indicates the neural networks are unbiased.

11.6 Optimizing the Final $B_c^+ \rightarrow B_s^0\ \pi^+$ Neural Network Cut

An optimal cut on B_c^+ neural network cut is selected by maximizing $\frac{S}{1.5+\sqrt{B}}$ while running over a mixture of signal Monte Carlo and background (upper sideband data). This figure of merit was chosen as it is mathematically appropriate to maximize the chance of finding a 3σ signal when a search is expected to have low signal to background ratios [55]. Signal Monte Carlo is not counted as contributing to S of the optimization unless the candidate is within a narrow window around the Δm signal peak, $|\Delta\text{m}-0.910\ \text{GeV}/c^2| \leq 0.018\ \text{GeV}/c^2$. The optimized cut value, which appears as the peak in the distribution of $\frac{S}{1.5+\sqrt{B}}$ over varying B_c^+ neural network score cuts, is shown in Figure 53.

After optimization, the B_c^+ neural network selects a cut at a score of 0.994. This score is driven to a high value, eliminating the vast majority of background, by nature of the figure of merit, $\frac{S}{1.5+\sqrt{B}}$. The result will be a highly purified sample, albeit with a sizable penalty to the efficiency of the analysis.

11.7 Consideration of Simultaneous Selection Cuts

In the interest of considering every tool in the toolbox, the effect of implementing multiple, simultaneous cuts to select B_c^+ candidates was evaluated. On top of the B_c^+ neural network

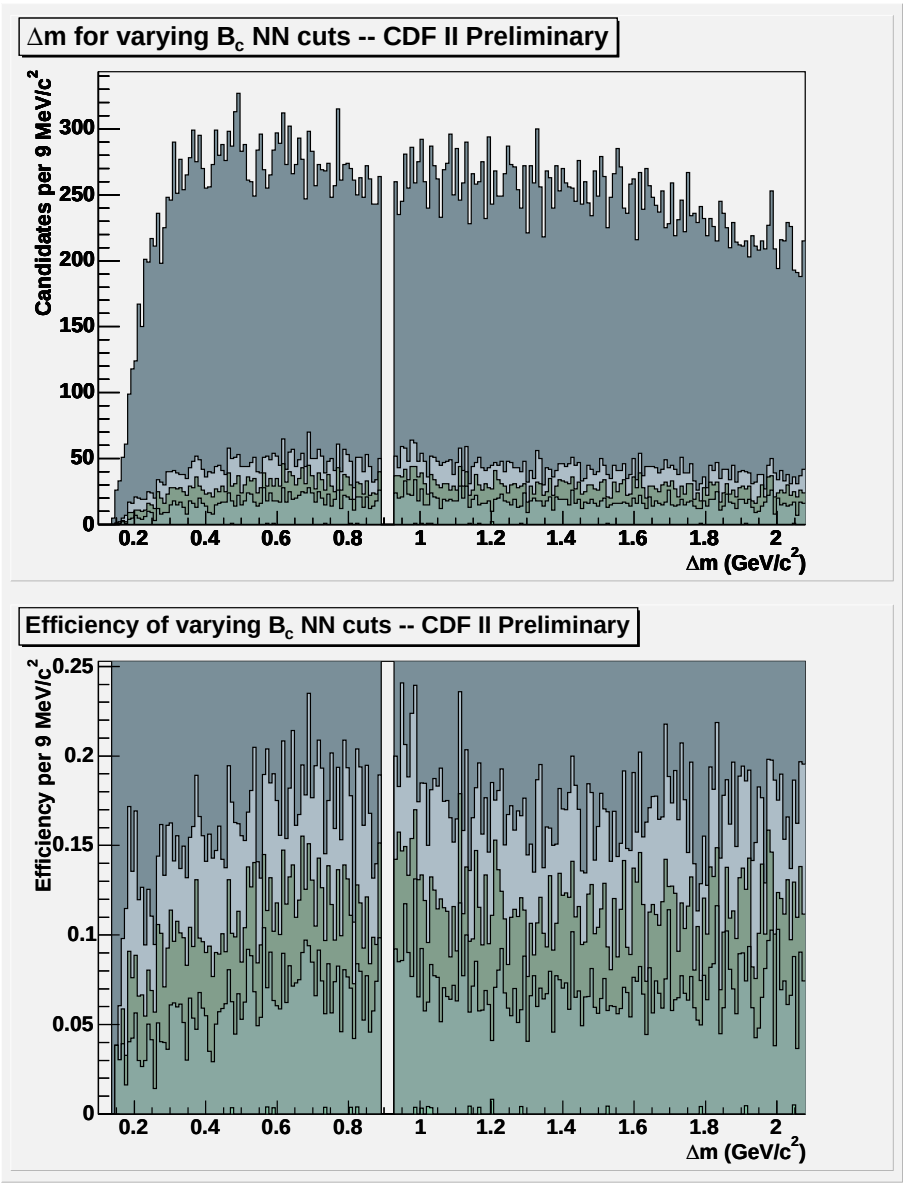

Figure 52: *Above:* The distribution of Δm (with the $B_c^+ \to B_s^0\pi^+$ signal window blinded) is shown for B_c^+ candidates in data as selected by varying B_c^+ neural network cuts. The tallest histogram has no B_c^+ neural network cut applied. *Below:* The acceptance of the B_c^+ neural network cuts shown in the above plot are shown by dividing each plot by the uncut histogram. Because the upper sideband remains flat and unsculpted, the neural networks can be considered unbiased.

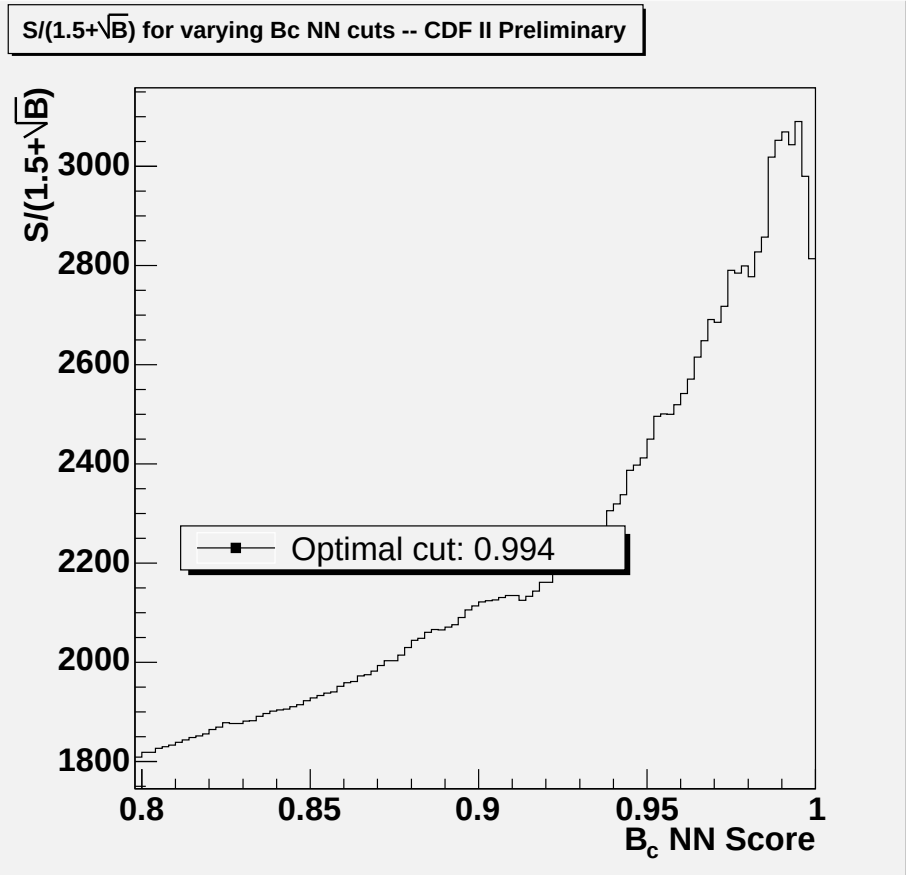

Figure 53: The B_c^+ neural network score is maximized as a function of $\frac{S}{1.5+\sqrt{B}}$. The peak in $\frac{S}{1.5+\sqrt{B}}$ found at 0.994 is visible.

cut, which is sure to be the vital selection tool of this analysis, eight additional kinematic cuts were considered: ΔR(B_s^0,π^+), B_c^+ track helicity angle, B_s^0 neural network score, probability of B_c^+ vertex, p_T of the B_c^+ daughter track, daughter track impact parameter signed with respect to the B_s^0, $\Delta z_0(B_s^0,\pi^+)$, and $p_T(B_c^+)$.

Using Scenario I B_c^+ Monte Carlo to simulate signal candidates and upper sideband data to model background, varying cuts for each of the nine parameters were considered. Optimizing the yield (by maximizing the quantity $\frac{S}{1.5+\sqrt{B}}$) showed that B_c^+ neural network score would indeed be the most stringently used parameter. The globally optimized cut throws away more candidates using the neural network score than any other single variable (by a factor of 4). Further, five of the variables were not used by the global optimization for selection in any way. The collection of these optimized cut values are shown in Figures 54 through 56.

Because background becomes sparse with these tight selection criteria, the benefit of applying the two selection cuts on top of a stringent B_c^+ neural network cut was compared to the effect of an optimized B_c^+ neural network cut alone. The result, shown in Figure 57, (which is in line with expectation from Figure 53) is that the B_c^+ neural network can perform quite well without the help of simultaneous optimization among eight other variables. That is to say, the B_c^+ neural network appears to be doing all the heavy lifting, so to speak. Further, the additional of other variables for a global optimization hurts signal yield dramatically. For this reason, only an optimized B_c^+ neural network score cut is applied to select B_c^+ candidates over background.

Another variable was also considered for optimization, but not used – the number of passing candidates per event. This cut was considered for its ability to serve as a measure of isolation. However, after applying basic selection cuts (including a very loose B_c^+ neural network cut), the number of passing candidates per event falls to exactly one for nearly every remaining event. Thus, this variable is not useful for pre-selection. (To study this particular parameter, PYTHIA Monte Carlo was compared with upper sideband data for the $B_s^0 \to J/\psi\ \phi$ mode.)

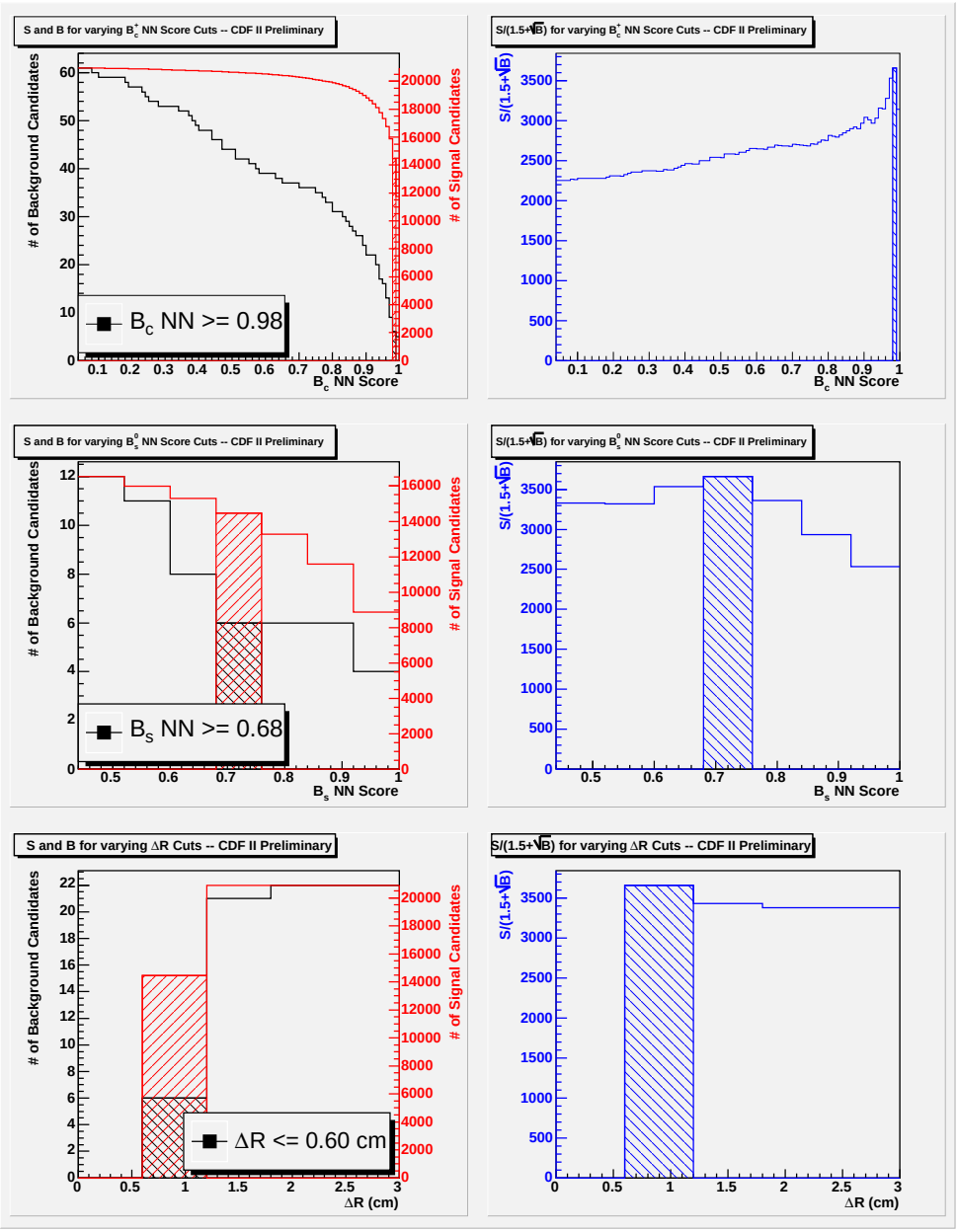

Figure 54: *Figures 54 through 56*: After simultaneous selection cuts on nine different variables are considered, the number of signal and background candidates passing a cut on each optimized variable is plotted for signal (red) and background (black). The cross-hatch shaded bin corresponds to the optimized cut.
Immediately to the right of each of these histograms, in blue, is a plot of the value of $\frac{S}{1.5+\sqrt{B}}$ as a function of the varying cut value. In all plots, S is the number of candidates in B-Gen Monte Carlo with Δm between 0.849 GeV/c^2 and 0.969 GeV/c^2, while B is measured as the number of upper sideband candidates from data with Δm between 1.2 GeV/c^2 and 2.0 GeV/c^2.
In this figure, B_c^+ neural network score, B_s^0 neural network score, and ΔR(track,B_s^0) are shown.

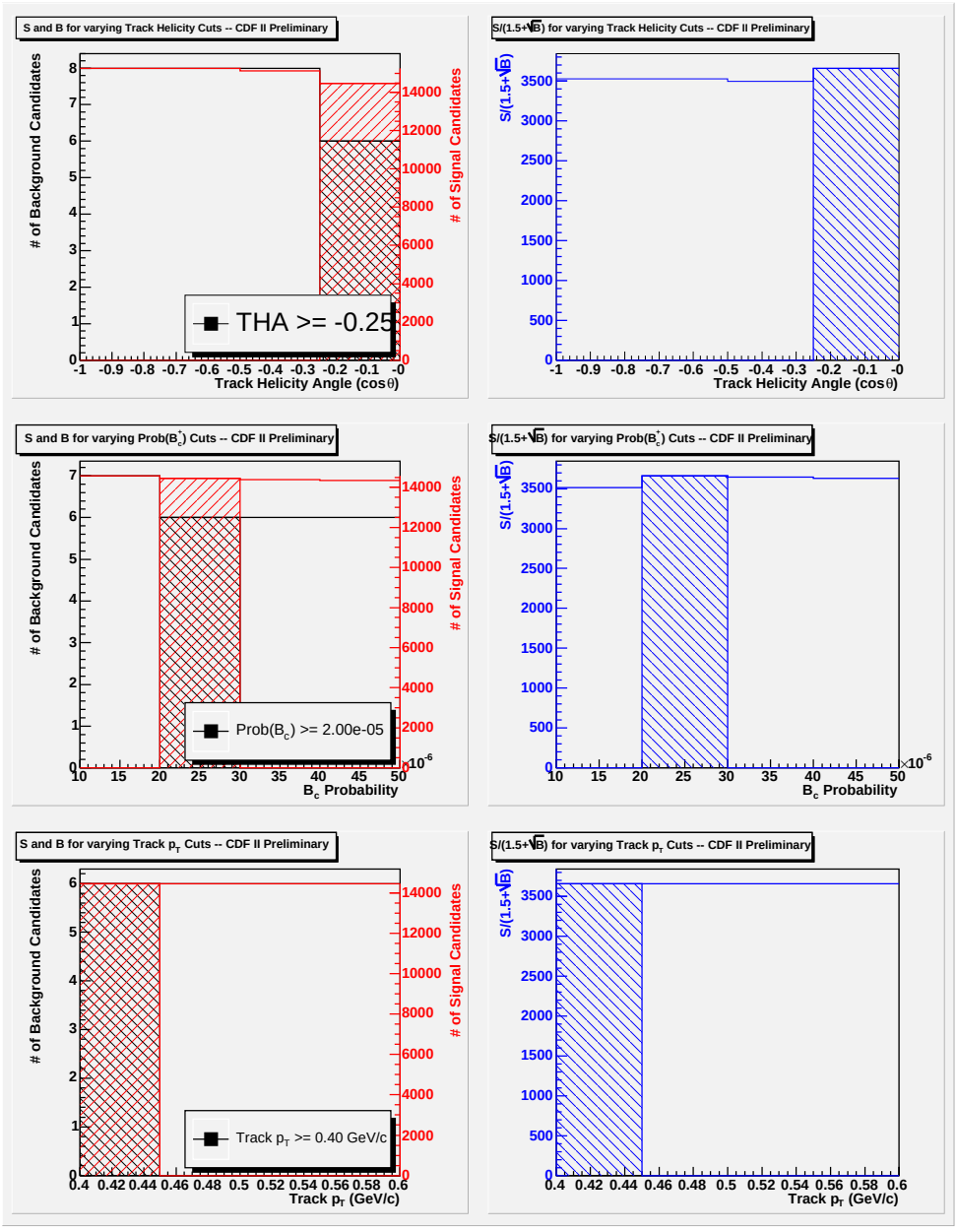

Figure 55: In this figure, Track Helicity Angle ($\cos\theta$), B_c^+ vertex probability, and track p_T are shown. An explanation of the figures is found in the caption of Figure 54 and in the text.

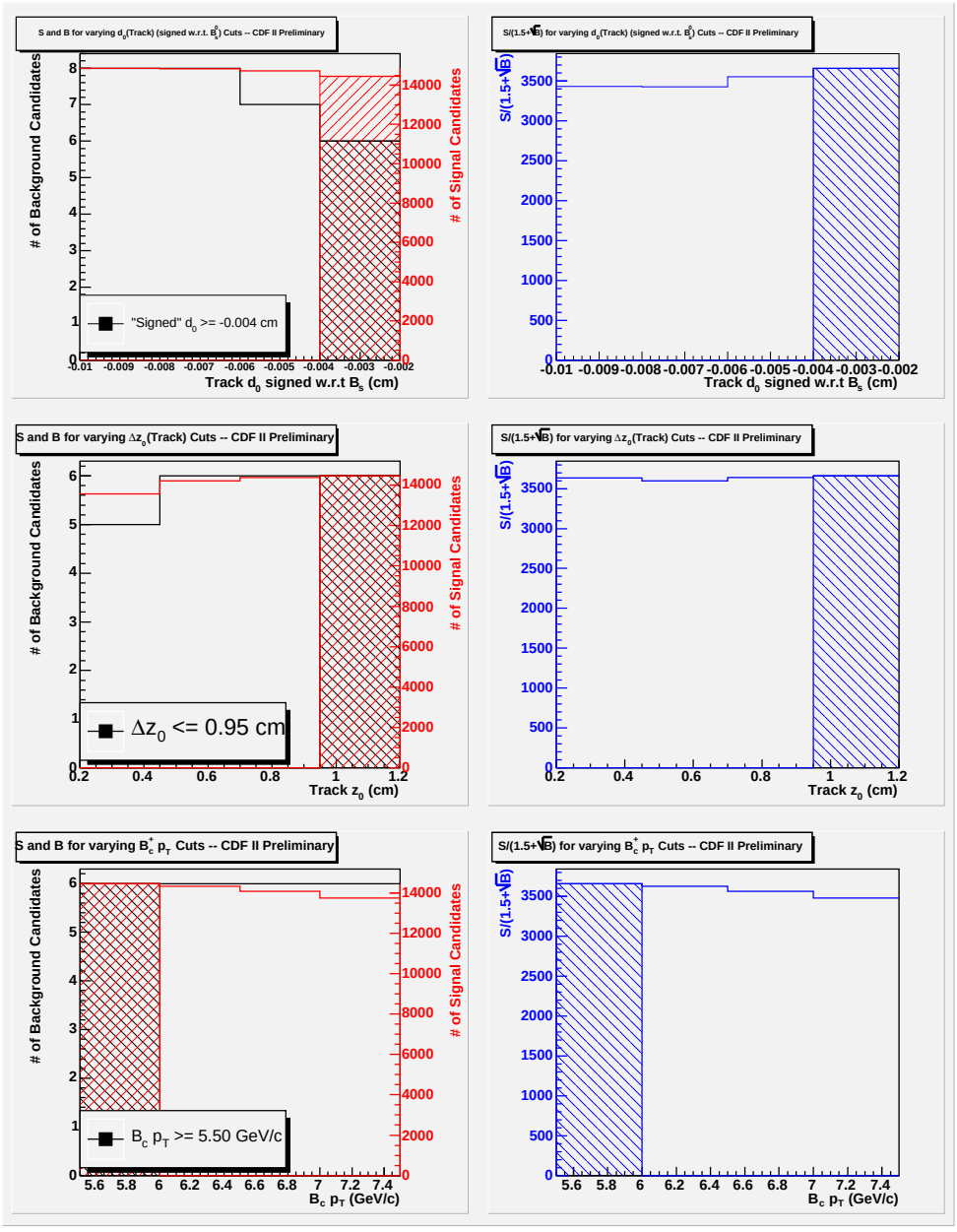

Figure 56: In this figure, track d_0 signed with respect to the B_s^0, Δz_0 between the track and the B_s^0, and B_c^+ p_T are shown. An explanation of the figures is found in the caption of Figure 54 and in the text.

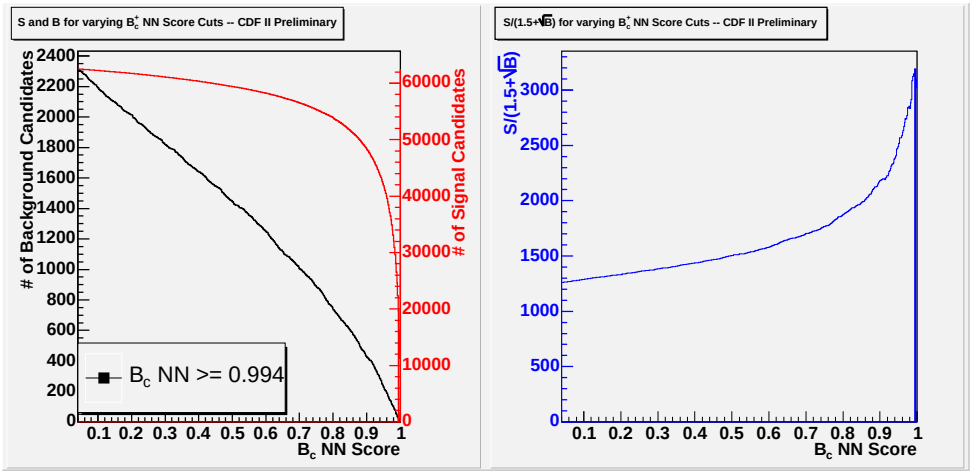

Figure 57: Using only B_c^+ neural network score to select $B_c^+ \to B_s^0\ \pi^+$ candidates, a minimum score cut, varying from 0.04 to 1.00, is applied to Monte Carlo simulation of signal and upper sideband data. The number of candidates passing each neural network cut are shown for signal (red) and background (black). The bin corresponding to the optimal cut in $\frac{S}{1.5+\sqrt{B}}$ is cross-hatch shaded. A plot of this figure of merit as a function of the varying cuts is shown in blue, also with the optimal bin shaded. Comparing this to Figures 54 through 56 shows that the B_c^+ neural network will be the primary tool for selection in this analysis, regardless of how many variables are employed in an optimization. This single variable optimization will thus be the preferred selection method.

11.8 Final Event Selection

Candidate events from data are selected using the optimized cut and plotted on top of the distribution of (Scenario I) B-Gen Monte Carlo candidates after the identical selection criteria are applied. Binning of the Δm plot is chosen to ensure that 95% of the Monte Carlo peak spans four bins. These four bins, ranging from $[0.892, 0.928]$ GeV/c^2, are considered the signal window. As shown in Figure 58, there are zero candidates in the signal window of data.

As a cross-check on the B_c^+ neural network, the cut is moved to a number of other, nearby values. By examining the yield within the signal window for alternative B_c^+ neural network cut values, it can be verified that the selection cut chosen is not excessively precise. Figure 59 shows that, for values below the optimized neural network cut, there is no evidence of any excess of events within the signal window.

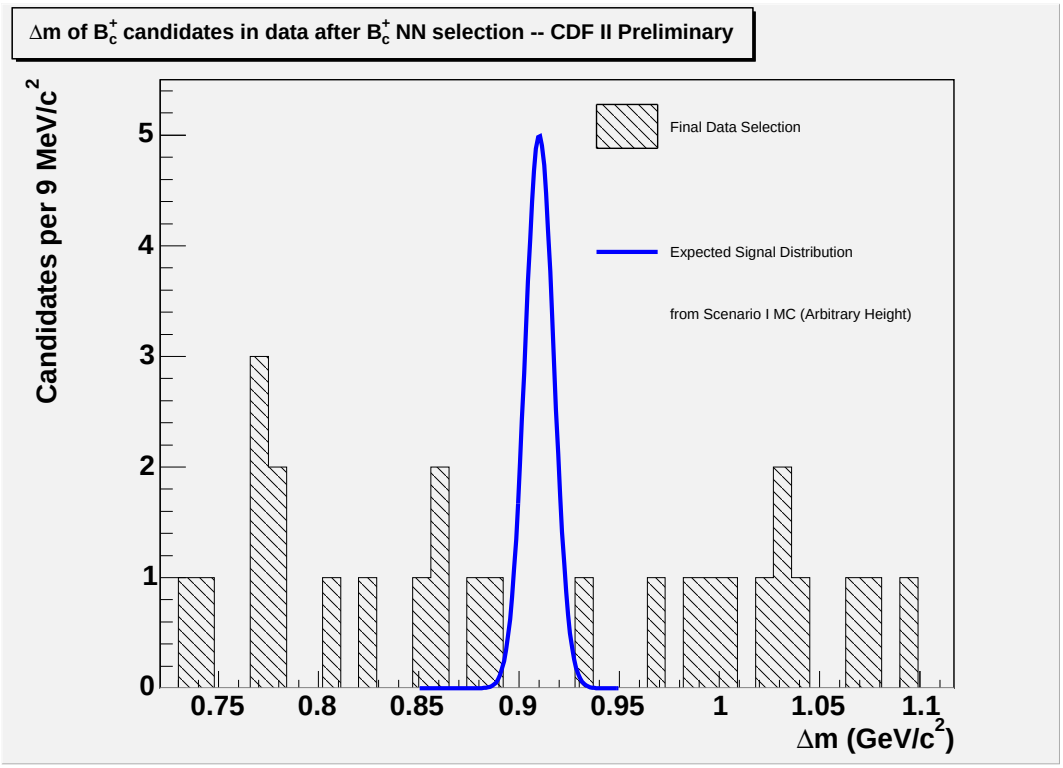

Figure 58: After applying the optimized B_c^+ neural network cut, the distribution of Δm for B_c^+ candidates in data is shown. The four bins covering 95% of the expected signal region for $B_c^+ \to B_s^0\ \pi^+$ have no events. The location of these bins is demonstrated by a gaussian (of arbitrary height) with a width and mean value determined by Scenario I B_c^+ Monte Carlo as selected by the B_c^+ neural network.

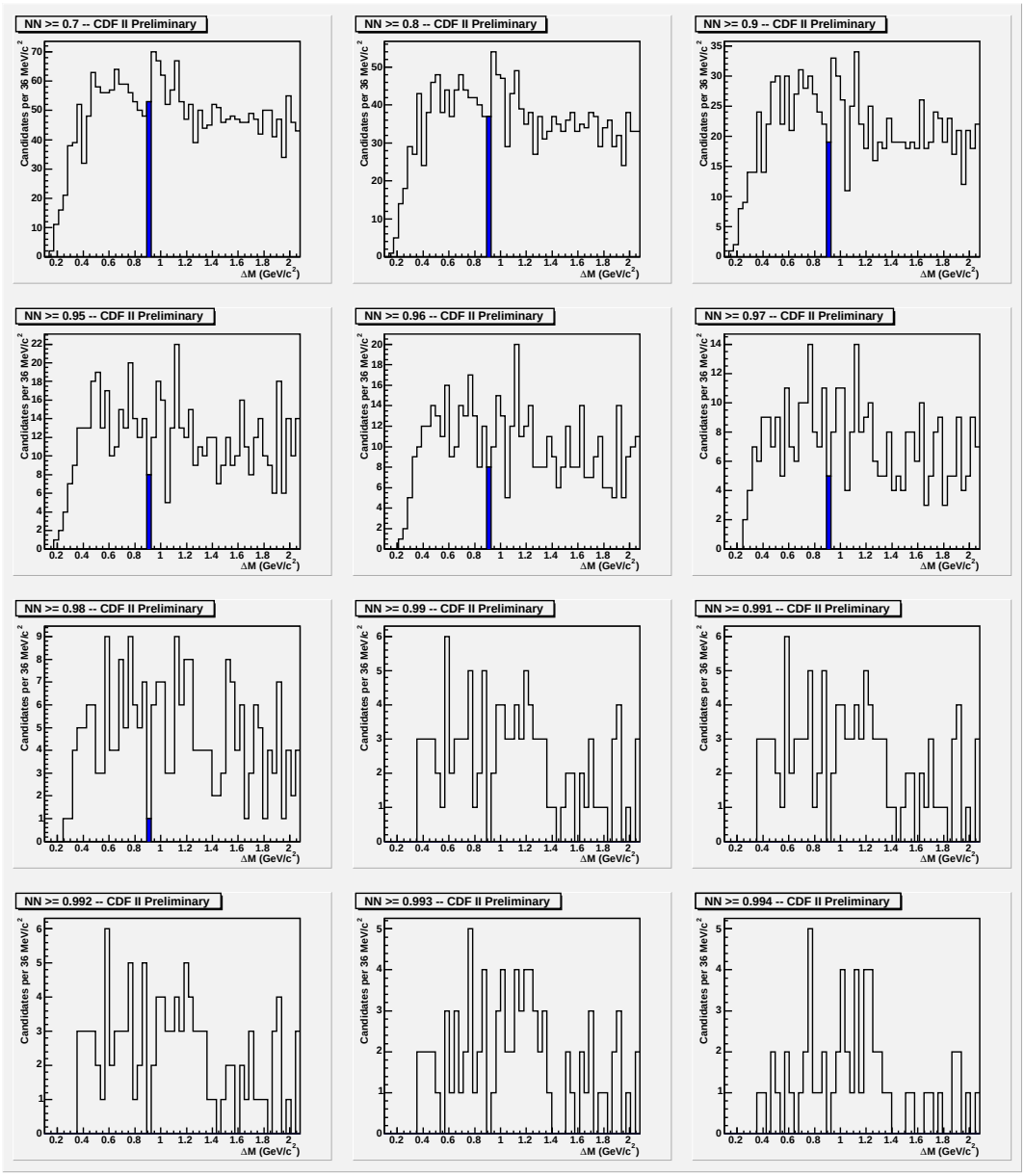

Figure 59: Varying the B_c^+ neural network cut to values below the optimized selection criteria shows that no excess of signal is found in the nearby, non-optimized selections. In each plot, the signal window is shaded and the binning changed such that the signal window occupies exactly one bin. From the ensemble of plots, it can be concluded that the selection criteria does not suffer from excessive precision in the optimization.

12 Extraction of the Ratio of Cross-Sections

The cross-section of the decay of $B_c^+ \to B_s^0\pi^+, B_s^0 \to J/\psi\ \phi, J/\psi \to \mu^+\mu^-, \phi \to K^+K^-$ can be compared directly to the $b\bar{b}$ cross-section as shown in equation 18.

$$\begin{aligned} \sigma_{B_c} &\stackrel{\text{def}}{=} \sigma(B_c^+ \to B_s^0\pi^+, B_s^0 \to J/\psi\ \phi, J/\psi \to \mu^+\mu^-, \phi \to K^+K^-) \\ \sigma_{B_c} &= \sigma(b\bar{b}) \cdot f_c \cdot \mathcal{B}(B_c^+ \to B_s^0\pi^+) \cdot \mathcal{B}(B_s^0 \to J/\psi\ \phi) \cdot \mathcal{B}(J/\psi \to \mu^+\mu^-) \cdot \mathcal{B}(\phi \to K^+K^-) \end{aligned} \tag{18}$$

$$\text{where } p_T(B_c^+) \geq 4.0 \text{ GeV}/c; |y(B_c^+)| \leq 1.0$$

In equation 18, $\sigma(b\bar{b})$ represents the cross-section of $b\bar{b}$ production at the Tevatron, f_c is the fragmentation function of c quarks (the frequency which with a b or $\bar{b}$ quark will hadronize with a $\bar{c}$ or c quark to form a B_c^+ or its charge conjugate), and $\mathcal{B}$(decay process) is the branching fraction of a particular decay. Basic kinematic cuts are applied to the parent hadron (in this case, the B_c^+) which thus become part of the definition of σ_{B_c}

The cross-section of the equivalent prompt B_s^0 decay, *i.e.*, the decay of $B_s^0 \to J/\psi\ \phi, J/\psi \to \mu^+\mu^-, \phi \to K^+K^-$, can be defined in an identical manner, as shown in equation 19.

$$\begin{aligned} \sigma_{B_s} &\stackrel{\text{def}}{=} \sigma(B_s^0 \to J/\psi\ \phi, J/\psi \to \mu^+\mu^-, \phi \to K^+K^-) \\ \sigma_{B_s} &= \sigma(b\bar{b}) \cdot f_s \cdot \mathcal{B}(B_s^0 \to J/\psi\ \phi) \cdot \mathcal{B}(J/\psi \to \mu^+\mu^-) \cdot \mathcal{B}(\phi \to K^+K^-) \end{aligned} \tag{19}$$

$$\text{where } p_T(B_s^+) \geq 4.0 \text{ GeV}/c; |y(B_s^+)| \leq 1.0$$

The number of B mesons created and observed in this experiment should follow the relations shown in equations 20 through 23. Because the branching fractions and kinematic quantities

have been incorporated into the definitions of σ_{B_c} and σ_{B_s}, these values only reflect the $J/\psi\ \phi$ search mode used in this analysis.

$$N_{B_c}(prod) = \sigma_{B_c} \cdot \mathcal{L} \quad (20)$$

$$N_{B_s}(prod) = \sigma_{B_s} \cdot \mathcal{L} \quad (21)$$

$$N_{B_c}(obs) = \sigma_{B_c} \cdot \mathcal{L} \cdot \mathcal{A} \cdot \epsilon \quad (22)$$

$$N_{B_s}(obs) = \sigma_{B_s} \cdot \mathcal{L} \cdot \mathcal{A} \cdot \epsilon \quad (23)$$

Here, $N_i(prod)$ is the number of particles of species i produced in $p\bar{p}$ collisions at the Tevatron. Meanwhile, σ_i is the cross-section of species i for the experiment, while $\mathcal{L}$ is the integrated luminosity of the experiment. Naturally, not all particles produced by nature will be observed in the experiment. This leads to the terms of acceptance, $\mathcal{A}$, and efficiency, ϵ, explained below.

Acceptance is a multiplicative factor, ranging between 0 and 1, intending to account for the inability of a detector to have complete fiducial coverage in tracking of the entire space into which a particle could decay. After multiplying in the acceptance factor, the number of expected particles no longer includes decays the detector could not possibly reconstruct. In this analysis, acceptance is defined as the frequency with which B meson parent hadrons (B_c^+ or prompt B_s^0) have $p_T \geq 4.0$ GeV/c and $|y| \leq 1.0$, where y is the rapidity, as defined in equation 17. The daughter tracks must also have $|y| \leq 1.0$ and $p_T \geq 400$ MeV/c^2.

Efficiency is a final multiplicative factor, also ranging between 0 and 1, which accounts for the number of particles the experiment and analysis do not identify as signal candidates. Causes can include (but are not limited to) failure to reconstruct the decay due to tracking errors, failure to correctly evaluate the mass of a particle, and failure of the neural network to score signal above the threshold cut. Both the acceptance and the efficiency are evaluated in this experiment using Monte Carlo and data. This is discussed in the next section.

The value of computing the ratio of cross-sections become clear as we take the ratio, and

find the majority of terms in the above cross-section evaluations can cancel. This is shown in equations 24 & 25. Equation 24 is drawn directly from equations 22 and 23, while equation 25 follows directly from equations 18 & 19.

$$\frac{\sigma_{B_c}}{\sigma_{B_s}} = \frac{N_{B_c}(obs)}{N_{B_s}(obs)} \cdot \left(\frac{\mathcal{A}_{B_c} \cdot \epsilon_{B_c}}{\mathcal{A}_{B_s} \cdot \epsilon_{B_s}}\right)^{-1} \quad (24)$$

$$= \frac{f_c}{f_s} \cdot \mathcal{B}(B_c^+ \to B_s^0 \pi^+) \quad (25)$$

$$\therefore \frac{N_{B_c}(obs)}{N_{B_s}(obs)} \cdot \left(\frac{\mathcal{A}_{B_c} \cdot \epsilon_{B_c}}{\mathcal{A}_{B_s} \cdot \epsilon_{B_s}}\right)^{-1} = \frac{f_c}{f_s} \cdot \mathcal{B}(B_c^+ \to B_s^0 \pi^+) \quad (26)$$

It is in this way that the number of $B_c^+ \to B_s^0\pi^+$, $B_s^0 \to J/\psi\ \phi$ decays observed in this analysis can directly indicate the limit on the cross-section ratio, and thus, the limit on $\mathcal{B}(B_c^+ \to B_s^0\pi^+)$. As discussed in Section 2.3.3, this technique greatly simplifies the computation of the branching fraction, by using the cancelation of many nuisance variables and their uncertainties.

12.1 $N_{B_s}(obs)$

As shown in Figure 43, the number of B_s^0 candidates observed is well-modeled by a gaussian fit to signal. The integral of the fitted gaussian, including the errors on the fit computed using the covariance matrix from the fit, is equal to $5,574 \pm 97$. This gives a relative error of 1.7%, which is assigned as a statistical error.

12.2 The Relative Acceptance Ratio

As shown in the equation 26, the relative acceptance ratio, $\frac{\mathcal{A}_{B_c} \cdot \epsilon_{B_c}}{\mathcal{A}_{B_s} \cdot \epsilon_{B_s}}$, plays an important role in computing the ratio of cross-sections. In specific, this factor directly indicates the fraction of $B_c^+ \to B_s^0\pi^+$ decays can be detected as B_s^0 candidates, without being identified correctly as the B_c^+ candidates they are. Its value, and the error on that value, are computed using Monte Carlo and data in the following way.

12.2.1 $\mathcal{A}_{B_s} \cdot \epsilon_{B_s}$

Using generator level Monte Carlo information, the prompt B_s^0 Monte Carlo sample (as described in Chapter 6) is used to to compute the denominator of the relative acceptance ratio. As prescribed in equation 19, the following kinematic cuts are placed upon the sample: $p_T(B_s^+) \geq 4.0$ GeV/c; $|y(B_s^+)| \leq 1.0$. (These cuts are placed on the generator level quantities, and not on the fitted values after detector simulation has been performed.) After the application of these cuts, there are $499,912$ events in the sample. Within that collection, B_s^0 candidates are selected using the optimized B_s^0 neural network, as optimized according to Section 10. This leaves a final collection of $69,279$ events, for an acceptance on B_s^0 (after kinematic constraints) of 13.9%.

While this value is here termed an acceptance, it is, in fact a combination of both acceptance and efficiency, as indicated by its representation in equation 26. By nature of using the analysis cuts to select B_s^0 candidates, the efficiencies of these analysis cuts are combined with the acceptance of the detector, which is introduced in large part by the Monte Carlo simulation software.

12.2.2 $\mathcal{A}_{B_c} \cdot \epsilon_{B_c}$

In an analogous method to Section 12.2.1, the acceptance is computed on B_c^+ candidates as generated in Scenario I $B_c^+ \to B_s^0 \pi^+$ Monte Carlo – see Chapter 6 for details on this sample. As in Section 12.2.1, kinematic constraints are imposed according to equation 18. After these constraints alone, the sample contains $1,234,868$ events. Applying the analysis cuts described in previous chapters, including the optimized B_c^+ neural network cut, the remaining collection of $18,954$ candidates implies an acceptance of 1.53%.

12.2.3 $\frac{\mathcal{A}_{B_c} \cdot \epsilon_{B_c}}{\mathcal{A}_{B_s} \cdot \epsilon_{B_s}}$

The relative acceptance ratio value is the quotient of the two acceptances computed in Sections 12.2.1 and 12.2.2. The result is $\frac{1.53\%}{13.9\%} = 0.11$. Systematic uncertainties on this quantity will be discussed later in this Chapter. Statistical error on the relative acceptance ratio is considered

negligible given the size of the Monte Carlo samples used in this calculation.

12.2.4 Correction to ϵ Using Track Embedding Studies

The relative acceptance ratio, as computed in this Section, has thus far relied heavily on B Generator Monte Carlo. While this Monte Carlo is considered quite reliable for many applications, it is worthwhile to consider the loss of charged particle tracking efficiency that may occur in data, which is sure to have a higher detector occupancy during $B_c^+ \to B_s^0\pi^+$ events than does a simulated B_c^+ decay in the Monte Carlo. To correct for this efficiency, it is appropriate to express the term we have considered thus far as a relative acceptance using Monte Carlo to compute efficiency, then multiply that term by a correction factor. This is shown in equation 27.

$$\left(\frac{\mathcal{A}_{B_c}\cdot\epsilon_{B_c}}{\mathcal{A}_{B_s}\cdot\epsilon_{B_s}}\right)^{-1} = \left(\frac{\mathcal{A}_{B_c}\cdot\epsilon_{B_c}(\mathrm{MC})\cdot\left(\frac{\epsilon_{B_c}(\mathrm{data+MC})}{\epsilon_{B_c}(\mathrm{MC})}\right)}{\mathcal{A}_{B_s}\cdot\epsilon_{B_s}(\mathrm{MC})\cdot\left(\frac{\epsilon_{B_s}(\mathrm{data+MC})}{\epsilon_{B_s}(\mathrm{MC})}\right)}\right)^{-1} \tag{27}$$

While the acceptance and efficiency of this B_c^+ analysis is not readily separable into quantities for the B_s^0 and the extra track, such a separation can be safely approximated for the correction factor on efficiency (within some small systematic uncertainty due to Monte Carlo modeling). This separability simplifies equation 27, as shown in equation 28.

$$\begin{aligned}\left(\frac{\mathcal{A}_{B_c}\cdot\epsilon_{B_c}(\mathrm{MC})\cdot\left(\frac{\epsilon_{B_c}(\mathrm{data+MC})}{\epsilon_{B_c}(\mathrm{MC})}\right)}{\mathcal{A}_{B_s}\cdot\epsilon_{B_s}(\mathrm{MC})\cdot\left(\frac{\epsilon_{B_s}(\mathrm{data+MC})}{\epsilon_{B_s}(\mathrm{MC})}\right)}\right)^{-1} &\approx \left(\frac{\mathcal{A}_{B_c}\cdot\epsilon_{B_c}(\mathrm{MC})\cdot\left(\frac{\epsilon_{B_s}(\mathrm{data+MC})\cdot\epsilon_{\pi}(\mathrm{data+MC})}{\epsilon_{B_s}(\mathrm{MC})\cdot\epsilon_{\pi}(\mathrm{MC})}\right)}{\mathcal{A}_{B_s}\cdot\epsilon_{B_s}(\mathrm{MC})\cdot\left(\frac{\epsilon_{B_s}(\mathrm{data+MC})}{\epsilon_{B_s}(\mathrm{MC})}\right)}\right)^{-1} \\ &= \left(\frac{\mathcal{A}_{B_c}\cdot\epsilon_{B_c}(\mathrm{MC})\cdot\left(\frac{\epsilon_{\pi}(\mathrm{data+MC})}{\epsilon_{\pi}(\mathrm{MC})}\right)}{\mathcal{A}_{B_s}\cdot\epsilon_{B_s}(\mathrm{MC})}\right)^{-1}\end{aligned} \tag{28}$$

In this approximation, a proper correction to the above estimation of the relative acceptance ratio need only be applied with regard to the tracking efficiencies of a single track in Monte Carlo versus data. That is, the quantity $\frac{\epsilon_{\pi}(\mathrm{data+MC})}{\epsilon_{\pi}(\mathrm{MC})}$ needs to be computed.

ϵ_π(**MC**) In order to properly compute the efficiency of selection of the single extra track in Monte Carlo, a study is performed on B_s^0 candidates identified (applying the relevant kinematic constraints) within the Scenario I B_c^+ Monte Carlo. Within this collection of identified B_s^0 candidates, the relevant efficiency is the fraction of pion B_c^+ daughter tracks (applying the relevant kinematic constraints) that are identified by the simulation as tracks. Thus, inefficiency of the Monte Carlo is described by this parameter only in cases where the B_s^0 from a $B_c^+ \to B_s^0\pi^+$ decay is found, but the extra track is not identified as such. This fraction is shown as a function of inverse p_T of the track in Figure 60.

To compute an overall value of ϵ_π(MC), a weighted average of entries in the plot of tracking efficiency in Monte Carlo as a function of inverse p_T (Figure 60) is performed. The weighting is drawn directly from the spectrum of tracks in events passing the B_c^+ analysis cuts from a sample of Scenario I B_c^+ Monte Carlo. This weighting spectrum is shown in Figure 61. The result is an overall value of $\epsilon_\pi(\text{MC}) = 0.907$

ϵ_π(**data+MC**) To estimate the efficiency on the B_c^+ track in data, the track embedding study on a single track, performed in a recent B production cross-section is used [20]. In this study, events in data are taken at the detector level, and an extra track is added as generated by Monte Carlo. The frequency with which this extra track is identified by the detector simulation is then considered the embedded track efficiency. The result is not precisely a measure of tracking efficiency in data – indeed, it is a mixture of data and Monte Carlo – but the approximation is considered quite realistic, within systematic error, as described later.

The tracking efficiency in data, as studied by the track embedding study decreases markedly for low momentum (high inverse p_T) pions. Despite this, the average tracking efficiency is still nearly as high as that for the Monte Carlo alone. Figure 62 shows the efficiency as a function of inverse p_T. Using the same weighting from Figure 61, the average tracking efficiency from the study is $\epsilon_\pi(\text{data+MC}) = 0.895$.

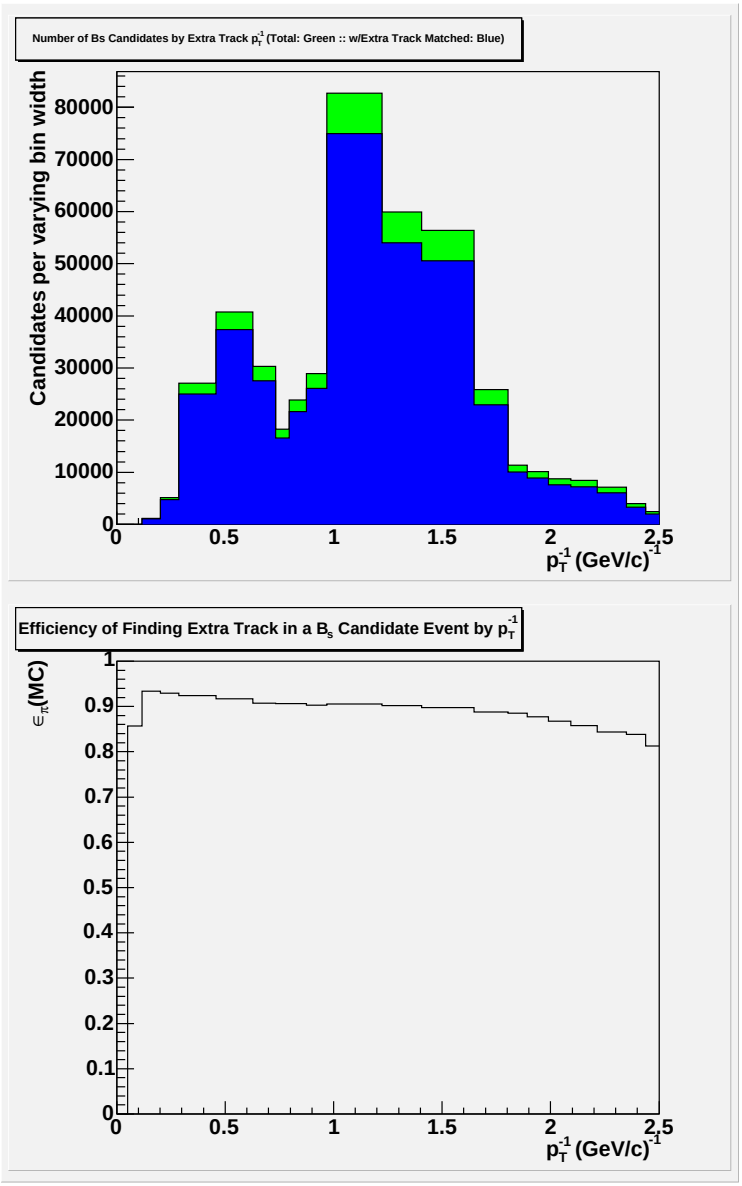

Figure 60: *Above*: In green, the number of B_s^0 candidates reconstructed within a B_c^+ Monte Carlo sample (given some kinematic constraints), as a function of inverse p_T of the track with varying bin widths. In blue, the number of B_c^+ daughter track candidates identified as tracks by the detector simulation within this sample. The structure seen in this plot is derived from the variable bin width, and is not directly indicative of physics effects.*Below*: The fraction of B_c^+ daughter tracks correctly reconstructed given the identification of the B_s^0 candidate and relevant kinematic constraints. Overall, the efficiency is very steady over a wide range of track momenta.

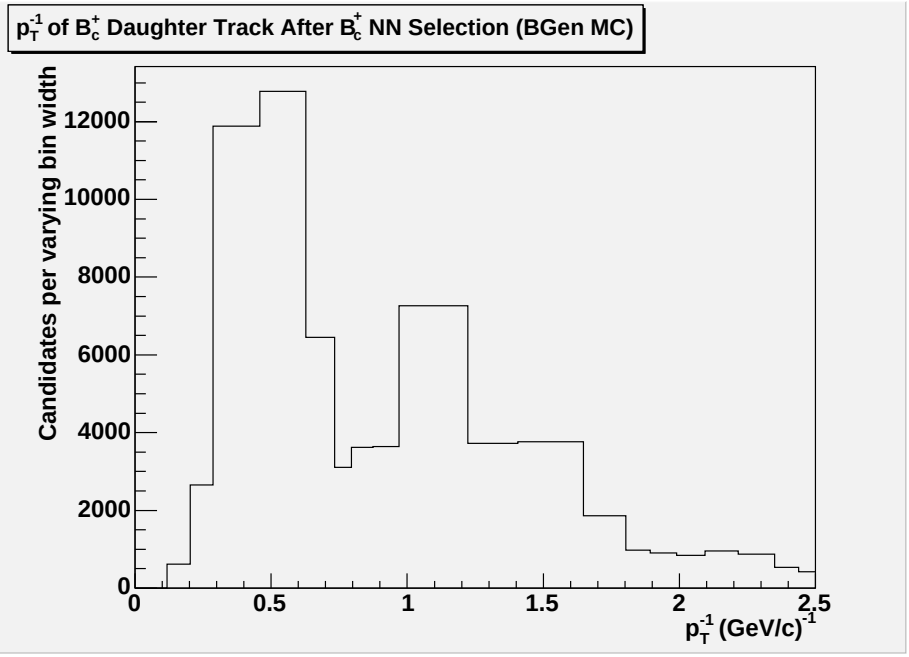

Figure 61: The number of B_c^+ candidates found as a function of inverse p_T of the B_c^+ track with varying bin widths. As in Figure 60, the structure seen in this plot is derived from the variable bin width, and is not directly indicative of physics effects.

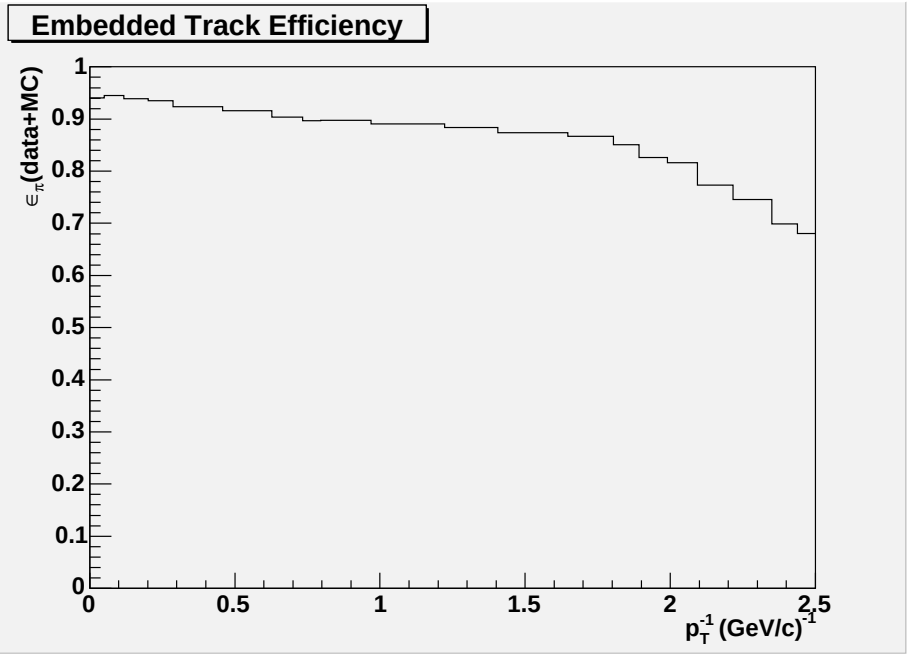

Figure 62: The fraction of pions correctly reconstructed in a track embedding study as a function of inverse p_T with varying bin width.

12.2.5 The final estimate on relative acceptance ratio

Combining the measurements from Monte Carlo and data explained in this section, the overall value of the relative acceptance ratio, given the kinematic constraints described in equations 18 and 19, is computed in equation 29.

$$\begin{aligned}\left(\frac{\mathcal{A}_{B_c}\cdot\epsilon_{B_c}}{\mathcal{A}_{B_s}\cdot\epsilon_{B_s}}\right)^{-1} &\approx \left(\frac{\mathcal{A}_{B_c}\cdot\epsilon_{B_c}(\mathrm{MC})\cdot\left(\frac{\epsilon_\pi(\mathrm{data+MC})}{\epsilon_\pi(\mathrm{MC})}\right)}{\mathcal{A}_{B_s}\cdot\epsilon_{B_s}(\mathrm{MC})}\right)^{-1} \\ &= \left(\frac{1.53\%\cdot\left(\frac{0.895}{0.907}\right)}{13.9\%}\right)^{-1} \\ &= (0.109)^{-1} = 9.21 \end{aligned} \quad (29)$$

12.3 Systematic Error

Systematic errors originate from numerous sources in this analysis. To properly estimate the ratio of cross-sections, these systematic errors will be reviewed. A listing of each systematic error individually, as well as the total combined error is found in Table 17.

12.3.1 Error on Acceptance and Efficiency

The computation of the acceptance and efficiency in Section 12.2 relies heavily on simulation of the B_c^+ meson by B Generator Monte Carlo. Because of the relatively low number of B_c^+ meson decays that have been measured in all modes, the p_T spectrum of the B_c^+ cannot be assumed to be perfectly modeled by Monte Carlo. In light of this, the Scenario II $B_c^+ \to B_s^0\pi^+$ sample can be used to approximate a very different, hypothetical $B_c^+ p_T$ spectrum.

Using Scenario II B_c^+ Monte Carlo (see Chapter 6), the resulting value of $\mathcal{A}_{B_c} \cdot \epsilon_{B_c}$ was $\frac{37{,}576}{1{,}579{,}910} = 2.38\%$. Here, the same kinematic requirements have been applied as in the original calculation. This value is significantly higher than the original result of 1.53% from Scenario I B_c^+ Monte Carlo. Because this value will be inverted in the final computation of the ratio of cross-sections, and because Scenario II B_c^+ Monte Carlo is considered exceedingly optimistic, the systematic error assigned to this acceptance and efficiency value is set to 20%, as $\frac{1}{2} \cdot \left(\frac{2.38\% - 1.53\%}{2.38\%}\right) = 17.9\%$.

12.3.2 Error on Correction to ϵ Using Track Embedding Studies

The use of track embedding studies to correct for the use of B Generator Monte Carlo in modeling background presents two sources of error. The larger of the two is due to the approximation performed in equation 28, which presumes a separability of B_s^0 efficiency correction and B_c^+ daughter track efficiency correction. Because this is not a proven assumption *a priori*, a systematic of 10% is assigned to the resulting correction.

A second, smaller source of error comes from the track embedding study itself [56]. This error itself is a mixture of uncertainties on low p_T efficiency measurement, as well as uncertainty on the amount of material within the inner detector region, both of which affect absolute track-

finding efficiency. Its value is computed to be 2.6%.

12.3.3 Error on B_s^0 Signal Modeling and B_s^0 Polarization

Because the B_s^0 has been well-studied in data, allowing for Monte Carlo parameters related to its kinematics to be cross-checked and tuned, the systematic error due to B_s^0 signal modeling in the Monte Carlo is considered to be negligible. Similarly, the error due to B_s^0 polarization, which is varied slightly between Scenario I and Scenario II B_c^+ Monte Carlo sets is also presumed to be negligible. This is likely a safe assumption, as the B_s^0 is a spin zero (pseudo-scalar) meson. Thus, the B_s^0 is unable to carry polarization information from the B_c^+ forward into the kinematics of the final decay products.

Systematic uncertainties on the trigger efficiency do not contribute to the systematics of this analysis, due to the cancelation that is performed in computing the relative acceptance ratio.

12.3.4 Total Systematic Error

The total systematic error due to each factor described in this section, after adding in quadrature, sums to 20.5%. Each factor, as described above, is listed in Table 17.

Source	Value (in percent)
Relative Acceptance Ratio	20.0
Monte Carlo Modeling	10.0
Track Embedding	2.6
B_s^0 Signal Modeling	negligible
B_c^+ Polarization	negligible
Total (added in quadrature)	22.5

Table 17: Sources of systematic error in this analysis are listed, and summed in quadrature. Detailed descriptions of each of these sources of error can be found in Section 12.3.

12.4 Statistical Error

The primary source of statistical error in this analysis is the size of the B_s^0 sample. As mentioned in Section 12.1, the statistical error on the B_s^0 sample is 1.7%. Other sources of statistical error,

such as the size of the Monte Carlo samples used to compute the relative acceptance ratio, are considered negligible.

12.5 $N_{B_c}(obs)$

The number of B_c^+ candidates appearing in the predefined signal window after final selection is performed is zero. This can be seen in Figure 58, where no candidates appear in the range $0.892\ \text{GeV}/c^2 \leq \Delta m \leq 0.928\ \text{GeV}/c^2$. A limit is thus computed with a 95% confidence interval to estimate the number of B_c^+ candidates produced. To properly compute this limit requires the incorporation of uncertainties in acceptance in background. This is done following the standard technique adopted by the CDF Collaboration of computing upper limits on such Poisson processes with uncertainties on acceptance and expected background, which is hybrid frequentist/Bayesian approach [57].

Computing an exact limit in closed form, while incorporating the uncertainties in acceptance and background is out of the reach of this analysis. Indeed, this would require a normalized integral of the probability density function associated with the observation of more than n_0 events in the signal window, where n_0 is the exact number of observed events. To compute a 95% confidence interval limit, the integral shown in equation 30 would need to be computed for N such that ϵ would equal 5% [57].

$$\epsilon = \frac{\sum_{n=0}^{n_0} \frac{1}{\sqrt{2\pi\sigma_N^2}} \int_0^\infty \int_0^\infty P(n; \mu'_B + \mu'_S) e^{-\frac{(\mu_B - \mu'_B)^2}{2\sigma_B^2}} e^{-\frac{(N - \mu'_S)^2}{2\sigma_N^2}} d\mu'_B d\mu'_S}{\sum_{n=0}^{n_0} \int_0^\infty P(n; \mu_B) e^{-\frac{(\mu_B - \mu'_B)^2}{2\sigma_B^2}} d\mu'_B} \tag{30}$$

Here, μ_B is the average number of background events among the n_0 observed; σ_B is the overall (statistical plus systematic) gaussian uncertainty on μ_B; and σ_N is defined as $N\sigma_A/A$, where A and σ_A are the overall acceptance (acceptance times efficiency) and the overall uncertainty on the acceptance, respectively.

Rather than perform this integral, a numerical approximation is sought using a frequentist algorithm. This algorithm is based on a toy Monte Carlo model, wherein pseudo-experiments

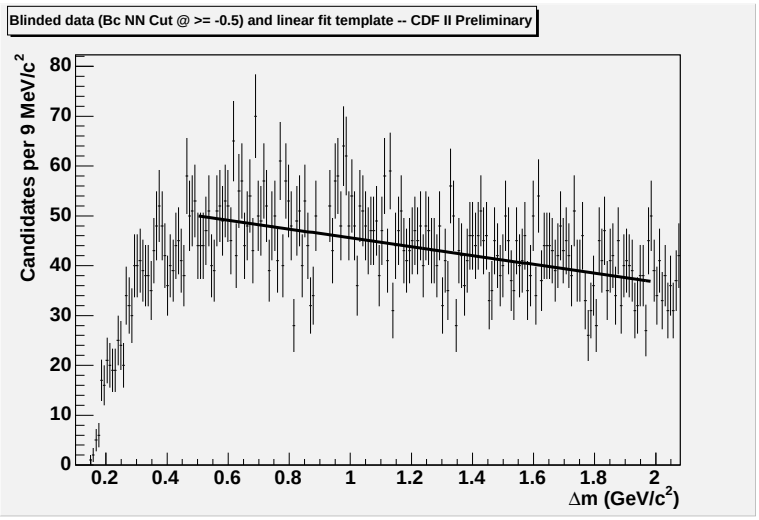

Figure 63: By loosening the B_c^+ neural network cut on data, a linear template is fitted for use in background modeling. This template is later normalized to the yield after final selection.

are performed by sampling from model distributions. The resulting distributions of outcomes are compared to the results of the actual experiment. Cases where the pseudo-experiment are inconsistent with the data of the experiment help set a limit on the range of valid hypotheses. To set a 95% confidence limit on the hypothetical number of signal events that could have been observed in this experiment, varying signal hypotheses are attempted. Comparing these results to experiment the minimal number of signal events that is inconsistent with data in 95% of cases is extrapolated from a fit. Details of this methodology follow.

First, the mean expectation of background events is extrapolated from sidebands according to a template. The template itself is produced by loosening the B_c^+ neural network cut, and fitting the resulting Δm distribution. This fit is shown in Figure 63. The fitted template is normalized by the yield seen in the sidebands after final selection to determine the value of expected background in the signal window, μ_B.

A similar template, a gaussian fitted to loosely selected Monte Carlo of signal is built, to predict the distribution of signal events. The mean expectation of signal events is set before beginning pseudo-experiments as $N_{\rm sig}$, the signal hypothesis. These mean values are then varied

(in a gaussian way) by their uncertainties due to acceptance and efficiency. (In this case, the uncertainty on signal is $\left(N_{\rm sig}\frac{\sigma_A}{A}\right)$, where, as before, A represents the combined acceptance and efficiency measurement, and σ_A the estimated uncertainty on that value.) Each pseudo-experiment, a value from the gaussian distributions for signal and background is selected. These values are then used to construct Poisson distributions for signal and background (with mean values equal to the selections from the gaussian). Values from the Poisson distribution are then selected, and labeled n_S and n_B, respectively. At this point, the pseudo-experiment is complete, and the next pseudo-experiment can begin, starting with the selection of values from the gaussian distributions of signal and background.

The 95% confidence limit is then set when a value of $N_{\rm sig}$ can be found such that, after a large number of pseudo-experiments, exactly 95% of pseudo-experiments are inconsistent with the observed data. Inconsistent, in this situation, describes the observation of a non-zero number of events in the signal window. Pseudo-experiments wherein background alone can be considered responsible for the inconsistency with observation (that is, where $n_B > n_0$) are not considered when setting this limit.

Again, we cannot exactly determine the value of $N_{\rm sig}$ for a 95% confidence limit, but numerical approximation is capable of producing a very close approximation. Numerous signal hypotheses are attempted. The resulting limit that can be set by each hypothesis is then fit with a quadratic polynomial. The limit is then extrapolated by finding the value, from the fit, for which $N_{\rm sig}$ crosses 95%. The accuracy of this method is, naturally, limited by computational resources as well as the quality of the quadratic fit to the results. The final fit from the pseudo-experiments for this analysis is shown in Figure 64. The resulting value for the 95% confidence limit on the signal hypothesis is 4.15 events.

$$95\%\ \text{C.L.}\,(N_{\text{signal events}}(\textit{observed})) \quad = \quad 4.15\ \text{events} \tag{31}$$

It is worthwhile to investigate the overall effect of systematic uncertainties on the limit produced by this method. To do so, the numerical analysis is simply repeated with only

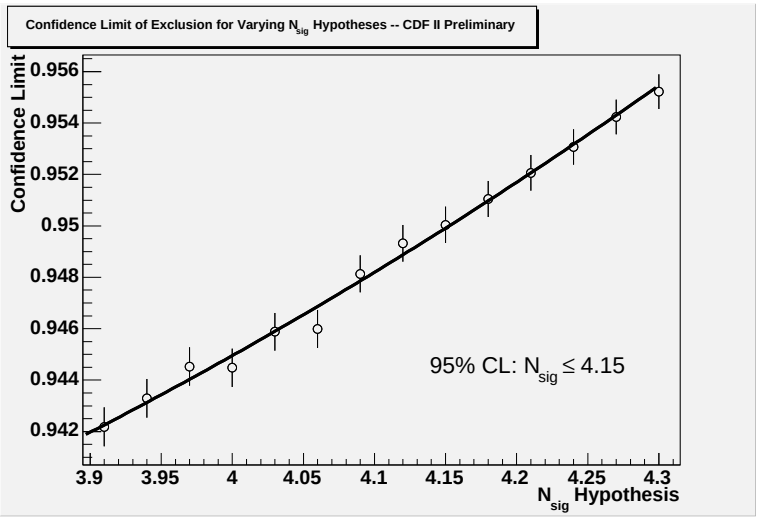

Figure 64: As the signal hypothesis is varied, the numerical estimate of the confidence limit increases. At the point where a quadratic fit to these data crosses 95%, a 95% confidence limit on signal can be set.

statistical uncertainties playing a role in the computation. Naturally, the result is a tighter limit, as can be seen in Figure 65. The 95% confidence limit on the signal hypothesis is reduced to 3.86 events, tightening the limit by 7% in the absence of systematic uncertainties. This demonstrates how systematic uncertainties weaken the 95% confidence limit on signal.

12.6 The Limit on $\frac{\sigma_{B_c}}{\sigma_{B_s}}$

From the calculations in the previous sections, the computation of a limit on $\frac{\sigma_{B_c}}{\sigma_{B_s}}$ is straightforward. From equation 24, the ratio is computed in the following way.

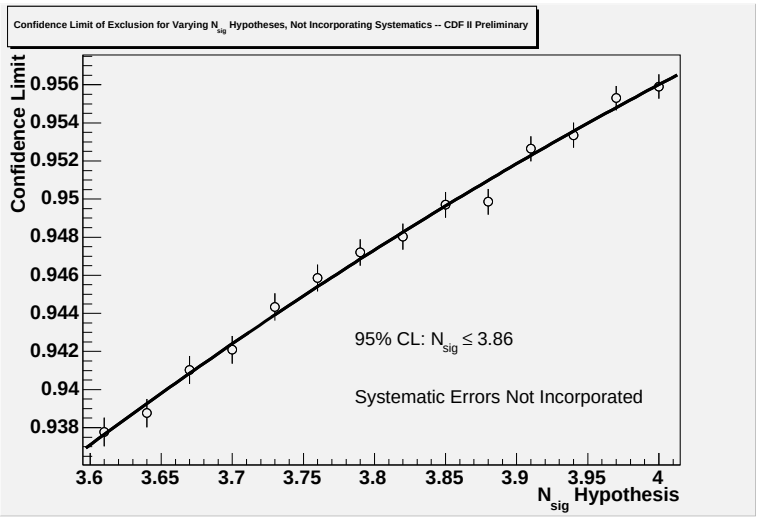

Figure 65: To estimate the effect of systematic uncertainties on the limit, the collection of pseudo-experiments is run again, setting the systematic uncertainties to zero. While artificial, this provides an understanding of the role that uncertainties play in attenuating the limit.

$$
\begin{aligned}
95\%\ \text{C.L.}\left(\frac{\sigma_{B_c}}{\sigma_{B_s}}\right) &= \frac{N_{B_c}(obs)}{N_{B_s}(obs)} \cdot \left(\frac{\mathcal{A}_{B_c} \cdot \epsilon_{B_c}}{\mathcal{A}_{B_s} \cdot \epsilon_{B_s}}\right)^{-1} \qquad (32)\\
&= \frac{4.15}{5574} \cdot (0.109)^{-1}\\
&= 0.00683\\
&= 95\%\ \text{C.L.}\left(\frac{f_c}{f_s} \cdot \mathcal{B}(B_c^+ \to B_s^0 \pi^+)\right)
\end{aligned}
$$

Assuming, for a moment, that the ratio of fragmentation fractions $\left(\frac{f_c}{f_s}\right)$ of B_c^+ to B_s^0 is exactly equal to 0.014, as estimated in Section 2.3.3, the resulting 95% upper limit on $\mathcal{B}(B_c^+ \to B_s^0\pi^+)$ (as described in equation 25) will be 48.8%. While this number would not rule out any known theoretical models, it is the first limit upon this quantity placed to date.

$$95\%\ \text{C.L.}\left(\mathcal{B}(B_c^+ \to B_s^0\pi^+)\right) \quad \leq \quad 49\% \tag{33}$$
$$\text{Assuming } \frac{f_c}{f_s} = 0.014$$

Because the assumed fragmentation fraction directly relies upon the theoretical prediction of the branching ratio of $B_c^+ \to J/\psi\ \pi^+$, which is not precisely known, the result of the calculation in equation 33 could be subject to some variation. Referring to the original prediction of the $B_c^+ \to J/\psi\ \pi^+$ branching fraction, alternate potential models are mentioned that allow for values as low as 8×10^{-4} [17]. Propagating this value through equation 14, the resulting ratio of fragmentation fractions rises to $\left(\frac{f_c}{f_s}\right) = 0.023$, allowing a tighter 95% confidence limit on $\mathcal{B}(B_c^+ \to B_s^0\pi^+) \leq 30\%$.

13 Conclusions

The limit on the ratio of cross-sections placed by this analysis is the first of its kind. While the limit is somewhat large, systematics do not play an overwhelming role in the estimation. (An estimate with systematics excluded reduces the limit by approximately 7%.) As the Tevatron and CDF II continue to operate, and continue to achieve higher instantaneous luminosities (in delivery and trigger rates, respectively), the expected increase in data available for this search (in particular, the quantity of B_s^0 events observed) can improve this limit further.

13.1 Opportunities for Further Study

The search mode chosen, $B_c^+ \to B_s^0\ \pi^+, B_s^0 \to J/\psi\ \phi$, is by no means the only available mode in which to search for $B_c^+ \to B_s^0 X$ decays. Beyond the numerous other possible decay products that could be associated with the B_c^+ daughter track (kaons, leptons, ρ, *etc.*), there are also many other fully and partially reconstructed B_s^0 decay modes found in other trigger paths in the CDF II recorded datasets. While the purity and narrow peak of $B_s^0 \to J/\psi\ \phi$ make it an obvious starting point, the high yield in hadronic peaks, such as $B_s^0 \to D_s^-\ \pi^+, D_s^- \to \phi\ \pi^-$ (shown in Figure 66), give these alternate modes the capability to further the sensitivity of this kind of study.

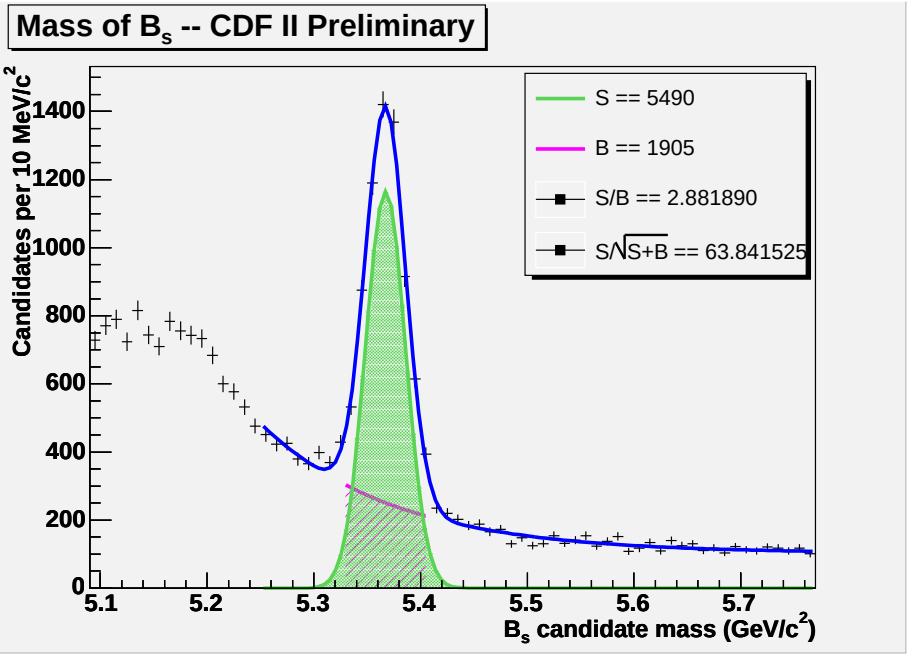

Figure 66: The yield of B_s^0 candidates in the hadronic, $B_s^0 \to D_s^- \ \pi^+, D_s^- \to \phi \ \pi^-$ decay mode. Adding decay modes such as this one is one of many ways to further the results of a search for $B_c^+ \to B_s^0 X$.

A Artificial Neural Networks

The technique of attacking problems with an artificial neural network originated with early attempts to study artificial intelligence. Research in the area continues today in the domain of machine learning. The principle behind artificial neural networks is, simply, that a single neuron is designed to take in multiple inputs, and provide a single output. The function that determines the "onto" mapping of inputs to output, generally, is a sum on the inputs after each is multiplied by a weighting coefficient.

This model derives from the functional understanding of a biological neuron. In the biological world, the neuron is a cell with a collection of dendrites on one end, which serve as inputs, and an axon (with multiple terminals) which serves as an output. Dendrites respond to electrical impulses from axon terminals in other neurons. These impulses are summed, and when the total crosses a threshold, the axon delivers a pulse of its own to the axon terminals, each of which connect to the dendrites of another neuron. The signaling of a neuron must cross a synaptic barrier which reduces the received input at the dendrites of a forward neuron. In this way, the synaptic efficiency is directly analogous to the weighting coefficient on each input described above. A diagram demonstrating the structure of a biological neuron is shown in Figure 67 [34].

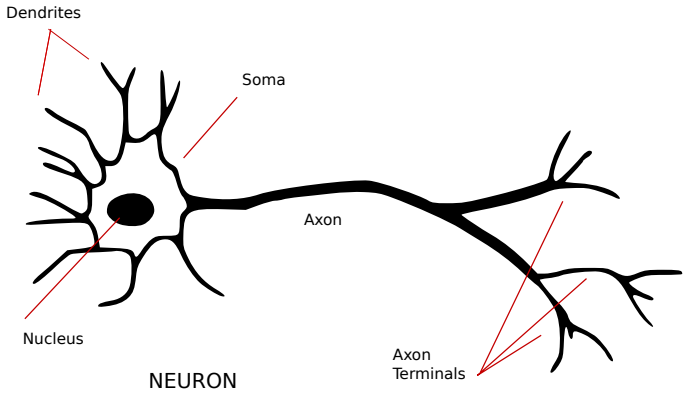

Figure 67: A biological neuron, used as the theoretical model for artificial neural networks [34].

The role of the neural network, in theory, is to vary the weighting coefficients as well as

the structure of the neural network (which inputs are connected to which outputs), until an ideal mapping of inputs to outputs is derived. This is of particular value in an analysis such as this, as well-defined, smoothly varying inputs are readily available in the form of kinematic properties of a B_c^+ candidate. Further, the desired output is precisely known for Monte Carlo simulation of signal and for a kinematically forbidden region of Δm in data. Indeed, binary classification problems such as this have been studied with artificial neural networks for some time, especially within the field of high energy physics.

Inputs, multiplied by weighting coefficients, are summed by the "neurons" of an artificial neural network. These sums are then mapped from the space of real numbers in the range of $[-\infty, \infty]$ to the range $[0, 1]$, then subtracted by a threshold bias in order to create an activation function. This activation function is typically created using a sigmoid function to perform the mapping. A common sigmoid function, the logistic function is shown in Figure 68(a). The model of a single artificial neuron, including the inputs, weights, sigmoid function and output, is shown in Figure 68(b) [34].

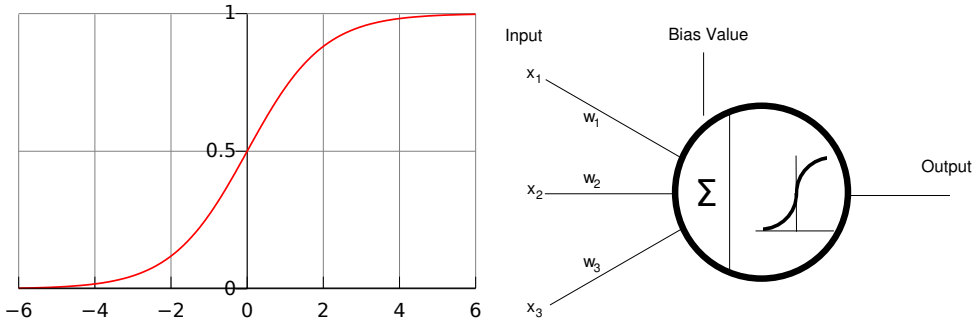

(a) The Logistic Curve

(b) Sigmoid Functionality of Neural Network

Figure 68: (a): A sigmoid function as defined by the logistic curve. **(b):** Each artificial neuron in a neural network takes inputs, modulated by weighting coefficients, and produces an output according to a sigmoid function [34].

This analysis makes use of the feed forward network structure which does not permit feedback loops during input evaluation, or "scoring." The structure of a simple, three input, feed forward neural network is shown in Figure 69. A hidden layer, where the weighting an evaluations occur, is placed between the input and output. By design, the neural networks in this

analysis have $n-1$ artificial neurons, or "nodes", available, where n is the number of inputs to the network.

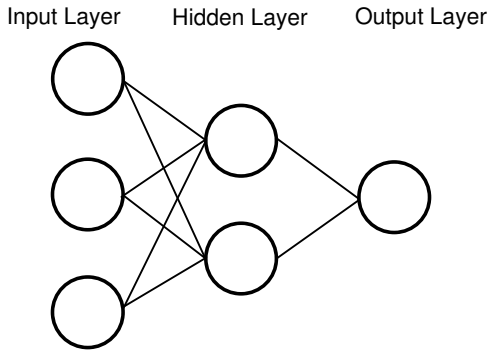

Figure 69: Arrangement of layers in a feed forward neural network. This structure prevents any feedback loops during input evaluation [34].

Training is the critical step to developing a powerful neural network. The process of training is performed by tuning the weighting coefficients of the input parameters to values that maximize the accuracy of the neural network in its classification of future inputs. To improve performance, the n-dimensional space of inputs may be rotated to diagonalize the inputs to the neural network. In the end, the neural network is designed to classify input candidates as likely signal or background. Output scores for this analysis lie in the range $[-1, 1]$, where higher scores imply a higher probability of signal for the given collection of inputs.

During training, collections of input with known (desired) outputs are provided to training software. It is critical then, that samples that simulate expected signal and background reflect realistic scenarios as much as possible. Unrealistic samples are prone to mislead the neural network, causing it to select a diagonalization and weighting coefficients that are inaccurate.

Assuming the inputs provided during training neural networks are realistic, the power of the neural network is worth examining. There are numerous ways to define "power" in a binary classification problem such as this one. A simple approach is to consider the proportion of signal to background for a given range of output scores from the neural network. This proportion of signal to background is termed "signal purity", ranging from 0 to 1. In Figure 70, the signal purity of candidates assigned a given score is shown to increase steadily as that score increases.

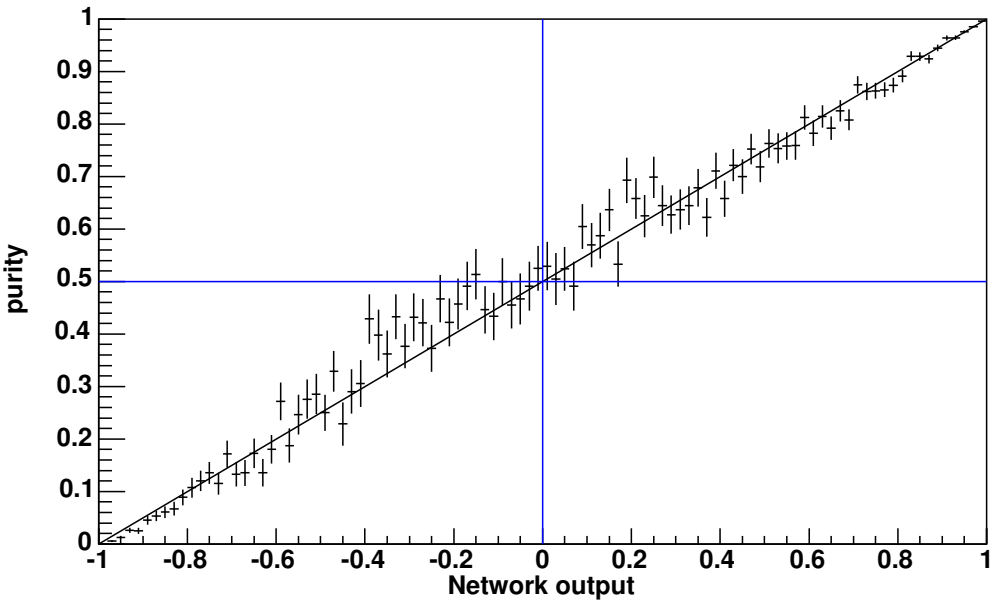

Figure 70: The signal purity of the selected sample as a binned function of neural network output. As desired, the fraction of candidates that are signal for a given neural network score increases as that neural network score increases.

The power of a neural network may also be evaluated by considered the effectiveness of applying a minimum cut on the output score in order to select signal over background. Naturally, tightening a cut will improve signal purity, as shown in Figure 70. However, tighter cuts will also lead to lower signal efficiency – the fraction of total signal inputs above the cut. A truly powerful neural network will have cuts that provide both high signal purity and high signal efficiency. In Figure 71, signal purity is plotted against signal efficiency for varying neural network cuts for the B_c^+ neural network trained in this analysis. An ideal neural network will maximize the area under the curve in this plot.

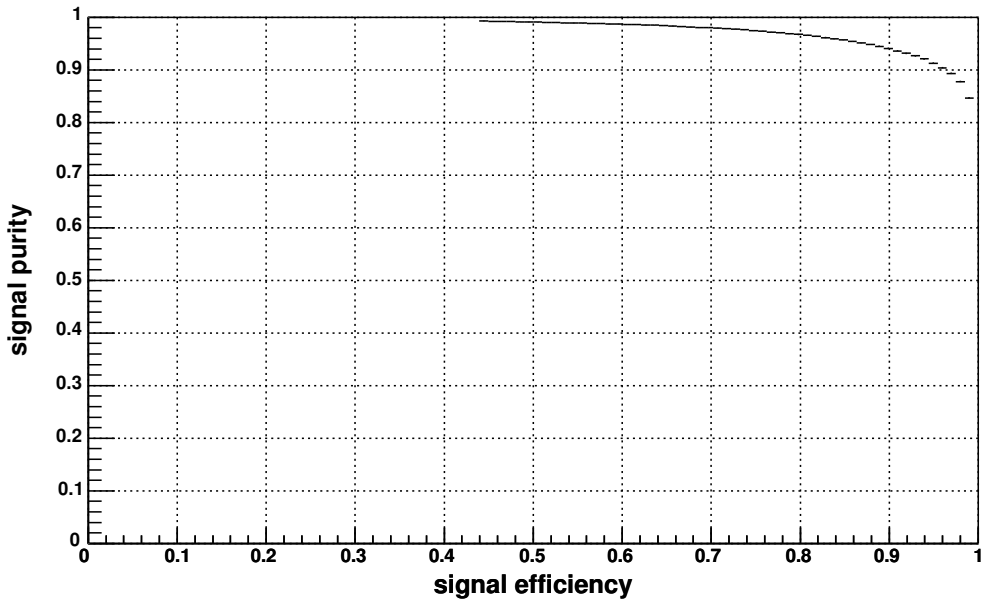

Figure 71: A plot of signal purity against signal efficiency is shown for varying neural network cuts. By one measure of neural network strength, a neural network should have a cut value able to maximize both quantities. The ideal neural network, in this measure, should maximized the area under the curve in this plot. This plot shows the notable performance of the neural network used in this analysis.

B B-Stntuple TCL Settings

B.1 bcbspi-Jpsi-stn.tcl

```
#----------------------------------------------------------------------------
# External input all here
#----------------------------------------------------------------------------
set env(SELECT_EVENTS)    disable
set env(ENV_ACTION)       off
set env(ALIGNMENT_FIX)    0
set env(ADD_STABLE_COV)   0

source $env(ENV_TCL_DIR)/init.tcl
source $env(ENV_TCL_DIR)/initBsMaker.tcl

set nRunLow  XX-NRUN_LOW-XX
set nRunHigh XX-NRUN_HIGH-XX

#----------------------------------------------------------------------------
# Get our tracks and the stable particle collections
#----------------------------------------------------------------------------
set env(ADD_L00)         true
set env(PRIMARY_VERTEX)  3
set env(POINTING_TYPE)   1
set env(TRACK_REFITTER)  KAL
set env(REJECT_NOTT)     0
set env(ELOSS_LAYER)     0.0
source $env(ENV_TCL_DIR)/stdTracks.tcl
source $env(ENV_TCL_DIR)/trigTracks.tcl
source $env(ENV_TCL_DIR)/pions.tcl
source $env(ENV_TCL_DIR)/kaons.tcl
source $env(ENV_TCL_DIR)/protons.tcl
source $env(ENV_TCL_DIR)/muons.tcl
```

```
source $env(ENV_TCL_DIR)/allMuons.tcl

#----------------------------------------------------------------------------
# Prepare some stuff for taggers
#----------------------------------------------------------------------------
source $env(ENV_TCL_DIR)/beamLine.tcl
source $env(ENV_TCL_DIR)/taggingPrep.tcl

#----------------------------------------------------------------------------
# Analysis -- Get Jpsi
#----------------------------------------------------------------------------
# only jpsi events (reject set 1)
module clone   D_SS Jpsi-MM
module enable  D_SS-Jpsi-MM
module talk    D_SS-Jpsi-MM
  source $env(ENV_TCL_DIR)/trigZero.tcl
  Cuts
    verbose     set 0
    reject      set 1
    massMin     set 2.80
    massMax     set 3.75
    chi2Max     set 30
  exit
  D_SS-Jpsi-MM
    iS1CollDesc set Muons
    iS2CollDesc set Muons
    oDCollDesc  set Jpsi-MM
    pid         set 443
  exit
exit

# Phi -> K K
```

```
module clone   D_SS Phi-KK
module enable  D_SS-Phi-KK
module talk    D_SS-Phi-KK
  source $env(ENV_TCL_DIR)/trigZero.tcl
  Cuts
    verbose     set 0
    reject      set 0
    massMin     set 1.00
    massMax     set 1.04
    chi2Max     set 30
    deltaZ0Max  set 1.5
  exit
  D_SS-Phi-KK
    iS1CollDesc set All-Kaons
    iS2CollDesc set All-Kaons
    oDCollDesc  set All-Phi-KK
    pid         set 333
  exit
exit
# Ds -> Phi Pi
module clone   D_DS Ds-PhiPi
module enable  D_DS-Ds-PhiPi
module talk    D_DS-Ds-PhiPi
  source $env(ENV_TCL_DIR)/trigZero.tcl
  Cuts
    verbose     set 0
    reject      set 0
    massMin     set 1.919
    massMax     set 2.019
    chi2Max     set 40
    dMassConst  set false
    deltaZ0Max  set 1.5
```

```
  exit
  D_DS-Ds-PhiPi
    iDCollDesc  set All-Phi-KK
    iSCollDesc  set Pions
    oDCollDesc  set Ds-PhiPi
    pid         set 431
  exit
exit
path create  LowRes   D_SS-Jpsi-MM        \
                      D_SS-Phi-KK         \
                      D_DS-Ds-PhiPi
path enable  LowRes

# Bs -> J/psi Phi   (J/psi -> Mu Mu, Phi -> K K)
module clone   D_DD Bs-JpsiPhi-MM:KK
module enable  D_DD-Bs-JpsiPhi-MM:KK
module talk    D_DD-Bs-JpsiPhi-MM:KK
  source $env(ENV_TCL_DIR)/trigZero.tcl
  Cuts
    verbose     set 0
    reject      set 0
    massMin     set 4.60
    massMax     set 6.20
    chi2Max     set 50
    dMassConst  set true
    d2MassConst set false
    deltaZ0Max  set 1.5
    source $env(ENV_TCL_DIR)/fullPrimVtx.tcl
  exit
  D_DD-Bs-JpsiPhi-MM:KK
    iD1CollDesc  set Jpsi-MM
    iD2CollDesc  set All-Phi-KK
```

```
    oDCollDesc   set Bs-JpsiPhi-MM:KK
    pid          set 531
  exit
exit
# Bc -> Bs Pi -> J/psi Phi Pi (J/psi -> Mu Mu, Phi -> K K)
module clone   D_DS Bc-BsPi-JpsiPhi-MM:KK
module enable  D_DS-Bc-BsPi-JpsiPhi-MM:KK
module talk    D_DS-Bc-BsPi-JpsiPhi-MM:KK
  source $env(ENV_TCL_DIR)/trigZero.tcl
  Cuts
    verbose     set 0
    reject      set 0
    massMin     set 5.40
    massMax     set 7.80
    chi2Max     set 50
#    massConList set 443
    dMassConst  set false
    deltaZ0Max  set 1.5
    source $env(ENV_TCL_DIR)/fullPrimVtx.tcl
  exit
  D_DS-Bc-BsPi-JpsiPhi-MM:KK
    iDCollDesc   set Bs-JpsiPhi-MM:KK
    iSCollDesc   set Pions
    oDCollDesc   set Bc-BsPi-JpsiPhi-MM:KK
    pid          set 541
  exit
exit

path create  BMesons  D_DD-Bs-JpsiPhi-MM:KK          \
                      D_DS-Bc-BsPi-JpsiPhi-MM:KK
path enable  BMesons
```

```
module clone  CandsPruner Phi-KK
module enable CandsPruner-Phi-KK
module talk   CandsPruner-Phi-KK
  CandsPruner-Phi-KK
    iDCollDesc set All-Phi-KK
    iTCollList set Ds-PhiPi Bs-JpsiPhi-MM:KK
    oDCollDesc set Phi-KK
  exit
exit

module clone  CandsPruner Kaons
module enable CandsPruner-Kaons
module talk   CandsPruner-Kaons
  CandsPruner-Kaons
    iDCollDesc set All-Kaons
    iTCollList set Phi-KK
    oDCollDesc set Kaons
  exit
exit

path create  Pruning   CandsPruner-Phi-KK      \
                       CandsPruner-AllMuons    \
                       CandsPruner-Kaons
path enable  Pruning
#--------------------------------------------------------------------------------
# We must flavor tag the Bees and other stuff
#--------------------------------------------------------------------------------
module enable BTagger
module talk   BTagger
  BTagger
    verbose       set 0
    # setting up neurobayes
```

```
    trackNetName  set dat/pbnet_cone_sa_all_l00.nb
    trackNetName2 set dat/pbnet_cone_sa_all_nol00.nb
    jetNetName    set dat/jetnet_cone_sa_all_l00.nb
    # setting up the collections
    iDCollList    set B-JpsiK-MM              \
                      B-JpsiKs-MM             \
                      Bs-JpsiPhi-MM:KK        \
                      Bc-BsPi-JpsiPhi-MM:KK
    SSTtag        set true
    OSKTtag       set false
    JQTtag        set true
    SETtag        set true
    SMTtag        set true
  exit
exit
path create  Tagging  BTagger
path enable  Tagging

#------------------------------------------------------------------------------
# Stntuple part
#------------------------------------------------------------------------------
module enable  InitStntuple FillStntuple
module enable  BsMakerModule
module talk    BsMakerModule
  # Jpsi
  DefineDecaysBlock  -name=Jpsi-MM          -s1=Muons -s2=Muons
#  # Jpsi with only one real muon leg
#  DefineDecaysBlock  -name=Bck-Jpsi-MM      -s1=Muons -s2=AllMuons
#  # K*0
#  DefineDecaysBlock  -name=KS-KPi           -s1=Kaons -s2=Pions
  # Phi
  DefineDecaysBlock  -name=Phi-KK           -s1=Kaons -s2=Kaons
```

```
#  # Kshort
#  DefineDecaysBlock  -name=Ks-PiPi          -s1=Pions   -s2=Pions
# # Lambda
#  DefineDecaysBlock  -name=Lm-PPi           -s1=Protons -s2=Pions
  # Ds
  DefineDecaysBlock  -name=Ds-PhiPi         -d1=Phi-KK  -s1=Pions
#  # Onia
#  DefineDecaysBlock  -name=Psip-JpsiK-MM       -d1=Jpsi-MM -s1=Kaons
#  DefineDecaysBlock  -name=Psip-JpsiPiPi-MM    -d1=Jpsi-MM -s1=Pions -s2=Pions
#  DefineDecaysBlock  -name=Psip-JpsiKs-MM      -d1=Jpsi-MM -d2=Ks-PiPi
#  DefineDecaysBlock  -name=Psip-JpsiLm-MM:PPi  -d1=Jpsi-MM -d2=Lm-PPi
#  DefineDecaysBlock  -name=Psip-JpsiKsPi-MM    -d1=Jpsi-MM -d2=Ks-PiPi -s1=Pions
#  DefineDecaysBlock  -name=Etab-JpsiJpsi-MM:MM -d1=Jpsi-MM -d2=Bck-Jpsi-MM
#  DefineDecaysBlock  -name=Etab-JpsiPhi-MM:KK  -d1=Jpsi-MM -d2=Phi-KK
#  # B mesons
#  DefineDecaysBlock  -name=B-JpsiK-MM          -d1=Jpsi-MM -s1=Kaons   \
#                                               -addTag -addDecayVtx -addBJet
#  DefineDecaysBlock  -name=B-JpsiKs-MM         -d1=Jpsi-MM -d2=Ks-PiPi \
#                                               -addTag -addDecayVtx -addBJet
#  DefineDecaysBlock  -name=Lb-JpsiLm-MM:PPi    -d1=Jpsi-MM -d2=Lm-PPi  \
#                                               -addTag -addDecayVtx -addBJet
#  DefineDecaysBlock  -name=B-JpsiKS-MM:KPi                  \
#                           -d1=Jpsi-MM         -d2=KS-KPi   \
#                                               -addTag -addDecayVtx -addBJet
#  DefineDecaysBlock  -name=B-PsipKS-JpsiPiPi:KPi-MM         \
#                         -d1=Psip-JpsiPiPi-MM -d2=KS-KPi   \
#                                               -addTag -addDecayVtx -addBJet
  DefineDecaysBlock  -name=Bs-JpsiPhi-MM:KK                 \
                         -d1=Jpsi-MM         -d2=Phi-KK   \
                                             -addTag -addDecayVtx -addBJet
  DefineDecaysBlock  -name=Bc-BsPi-JpsiPhi-MM:KK            \
                        -d1=Bs-JpsiPhi-MM:KK -s1=Pions    \
```

```
                                                -addTag -addDecayVtx -addBJet
#  DefineDecaysBlock  -name=Bc-JpsiDs-MM:PhiPi               \
#                          -d1=Jpsi-MM          -d2=Ds-PhiPi \
#                                                -addTag -addDecayVtx -addBJet
  # Bs** afficionados
#  DefineDecaysBlock  -name=BsS-BsPiPi-JpsiPhi-MM:KK         \
#                          -d1=Bs-JpsiPhi-MM:KK -s1=Pions    -s2=Pions
#  # B mesons for X afficionados
#  DefineDecaysBlock  -name=B-XK-JpsiPiPi-MM         \
#                           -d1=Psip-JpsiPiPi-MM -s1=Kaons
#  DefineDecaysBlock  -name=B-XKs-JpsiPiPi:PiPi-MM   \
#                           -d1=Psip-JpsiPiPi-MM -d2=Ks-PiPi
#  DefineDecaysBlock  -name=B-XKS-JpsiPiPi:KPi-MM    \
#                           -d1=Psip-JpsiPiPi-MM -d2=KS-KPi
#  DefineDecaysBlock  -name=Bs-XPhi-JpsiPiPi:KK-MM   \
#                           -d1=Psip-JpsiPiPi-MM -d2=Phi-KK
#  # Histogram file
  histfile     $env(ENV_ROOT_DIR)/$env(ENV_INPUT_FILE).root
exit
path create  NTuple   InitStntuple BsMakerModule FillStntuple
path enable  NTuple
#------------------------------------------------------------------------------
# Paths
#------------------------------------------------------------------------------
path disable AllPath
path list
#------------------------------------------------------------------------------
# Input
#------------------------------------------------------------------------------
module input   DHInput
module enable  DHInput
module talk    DHInput
```

```
  # Drop some stuff we do not need
  source $env(ENV_TCL_DIR)/dropList.tcl
  # Use dcache even if we run from root/static files (it works properly)
  cache set DCACHE
  # Appropriate inputfile(s) is read
  source input.tcl
  # Go over only 1 Run
  selectEvents set run>=$nRunLow run<$nRunHigh
  # Debugging
  report set 40
  show exclude
  show include
exit
#-------------------------------------------------------------------------------
# Do It
#-------------------------------------------------------------------------------
action on "Timer Action"
begin -nev $env(ENV_NEVENTS)
show timer
exit
```

C XTC2 Testing Software

On the following pages is the basic instruction manual for use in diagnostics and checkout of a production XTC2 for use on the CDF II detector.

Crate Operations Manual for XTC2 Diagnostics

Use PuTTY to access the crate

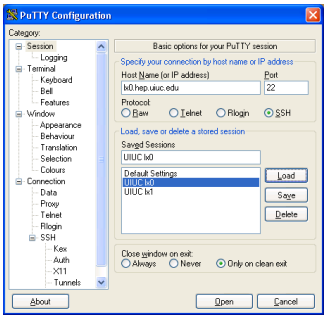

To control the crate, you must first be logged into the LX machines. Any SSH client can do this. From Windows, you'll probably find it easiest to use "PuTTY." PuTTY requires no installation.

Download PuTTY here:

http://the.earth.li/~sgtatham/putty/latest/x86/putty.exe

Changes to the default configuration:

1) Under "Window", increase the number of lines of scrollback from 200 to 200000
2) Under "Session" → "Bell", change the bell setting to "Visual Bell (flash window)" in order to promote office-mate sanity.
3) Under "Connection" → "SSH" → "X11", Enable X11 forwarding and set X display location to `localhost:0`

Add these extra aliases to .cshrc on your LX machine account

Add the following lines to the file `~/.cshrc`

```
alias cdfsoft source ~/docdfsoft2.csh
alias crate "rlogin -l vxcdf mvme2300d.hep.uiuc.edu"
set autologout = 9999
```

Note: For these changes to take effect, you will either have to restart your SSH session or type

```
source ~/.cshrc
```

Have a copy of `docdfsoft2.csh` in your home area

Your `dcodfsoft2.csh` script should setup ssh capability for later use to compile code.

```
#!/bin/csh -f

setenv USESHLIBS 1

source ~cdfsoft/cdf2.cshrc
setup cdfsoft2 6.1.2
setenv LD_LIBRARY_PATH "../shlib/Linux2-KCC_4_0:/usr/lib:$LD_LIBRARY_PATH"
setup kerberos
setup ssh
```

Log in to the crate at Loomis

In the above setup, you added an alias for the crate login command to your `.cshrc`.

```
Lx0.hep.uiuc.edu> crate
   login: vxcdf
   password: cdf347vx
```

If this doesn't successfully log you in, a few things to try include:

1) Check that the crate is powered on, with the fans running.
2) Check that the crate CPU is on and running in slot 1.
3) Check that the orange ethernet cable is plugged into the crate.
4) Ask around to see if anyone else is logged in. (It's one at a time.)
5) Power-cycle crate. Wait ~90 seconds before logging in.

AFTER TRYING ALL OF THE ABOVE…

6) Ask Dave Lesny if there is anything he needs to do to reconnect the crate to the network.

Compiled Crate Programs are put on the Windows Network

If you'd like to browse through the drive that is directly accessible to the crate, open the network folder `\\Hep-ntweb\VxUsers\VxCDF` in windows:

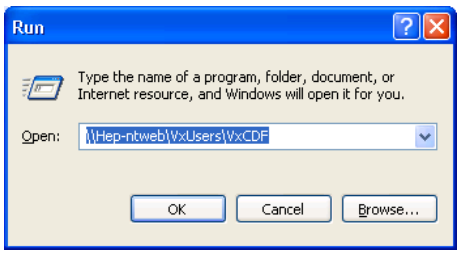

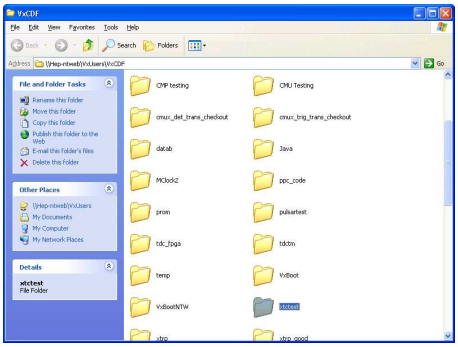

Now that you have an idea where the programs and their source code is kept, let's run this piece of code.

1) Log in to the crate, as explained above.

```
lx0.hep.uiuc.edu> crate
   login: vxcdf
   password: cdf347vx
```

2) Change to the directory with the code.

```
cd "../xtctest"
```

Note that unlike normal UNIX systems, arguments to `cd` are quoted.
Also note that the contents of "`../xtctest`" are the same as
`\\Hep-ntweb\VxUsers\VxCDF\xtctest`
on the Windows network.

3) Load a program into memory.

```
ld < xtc_comp
```

4) Run the program by typing the name of its executable function

```
run
```

To find the function name, you'll have to examine the source code.

5) Now the program is running. Go ahead and exit by typing 28

```
-> run
Checking Slot Validity
Crate configuration:
  Slot  1: Crate CPU
  Slot  2: TRACER
  Slot  3: (empty)
  Slot  4: Testclock
  Slot  5: (empty)
  Slot  6: (empty)
  Slot  7: (empty)
  Slot  8: (empty)
  Slot  9: (empty)
  Slot 10: (empty)
  Slot 11: Finder 2/4
  Slot 12: (empty)
  Slot 13: TDC
  Slot 14: (empty)
  Slot 15: (empty)
  Slot 16: (empty)
  Slot 17: (empty)
  Slot 18: (empty)
  Slot 19: (empty)
  Slot 20: (empty)
  Slot 21: (empty)
There are 2 cables:
  Cable   0: TDC 13/0 to Finder 11/4
  Cable   1: TDC 13/1 to Finder 11/3
Initializing Testclock in slot 4
Initializing TRACER in slot 2
Initializing Finder in slot 11
Initializing TDC in slot 13
xtctest: The system cannot find the file specified.
Opening Output File: XTC2_97.txt
   Opened File XTC2_97.txt
CPLD Firmware Version: 16
Data FPGA Firmware Version: 4
Kitchen Sink FPGA Firmware Version: 33
Number of Time Bins in Design: 6
================================================================================================
Kitchen Sink placed in standard operating mode

If this is a production board, its serial number is: 97

Choose:
   1)  Configure the FPGAs
   2)  Display Firmware Version Numbers
   3)  Display Current Register Contents
   13)   6-bin: Program Registers - Prototype XTC, Standard Values (Boards 1,5-10)
   14)   6-bin: Program Registers - Prototype XTC, ALT Values (Boards 2,3,4)
   15)   6-bin: Program Registers - Production XTC, Standard Values (Boards 1-131,134-
143,147-203)
   16)   6-bin: Program Registers - Production XTC, ALT Values (Boards
0,132,133,144,145,146)
   17)   6-bin: Connectivity Test
   18)   6-bin: Finder Capture Functionality Test
   19)   6-bin: Extended Finder Capture Functionality Test
   20)   6-bin: L2 Buffer Test - Old Way (Doesn't assume address incrementation)
   21)   6-bin: L2 Buffer Test - New Way (Assumes address counter is incremented by 12 each
time)
   22) Load 2-Bin Design
   23) Load ODLD Design
   24) Modify a Register Value
   25) ODLD-Finder Test (1 loop)
   26) ODLD-Finder Test (100 loops)
   27) Edgetest
   28) Exit
```

```
> 28
```

If the crate setup is incorrect, you'll see errors. The most typical error when a card is not reachable is

`FISION: S_errno_EIO (0x5): VME BERR received!`

which indicates an error on the VME Communication Bus.

Writing and Compiling Code

Edit code for use in the crate

First, start with previous code, and modify it.

```
cd ~
mkdir xtctest
cp ~erogers1/xtctest/regtest4.c ./xtctest
xemacs ./xtctest/regtest4.c &
```

(Make sure you are running XWindows and have X11 forwarding enabled.)

Go to line 439 (M-x goto-line), and insert the following print statement.

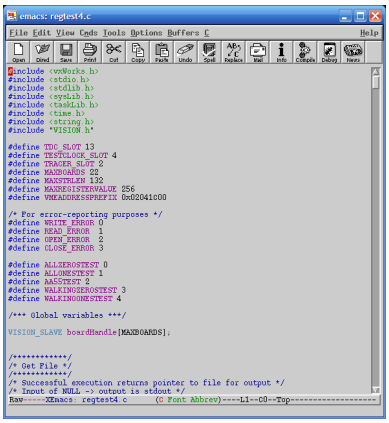

```
    /*****************************/
    /* Register Test Interface */
    /*****************************/
    printf("\n Hello World! \n");
    printf("\n\n\n");
    printf("  XTC2 Register Test\n");
```

Save your change, (C-x C-s) and you're ready to compile this code.

A few things worth noting in crate code...

- The executable function here is

```
int run(void){
```

- Many VISION commands appear in this code

```
VISIONwrite(boardHandle[tdc_slot], VMEADDRESSPREFIX + i, sizeof(my_byte), &bytes, &my_byte);
```

These commands send messages to cards in various crate slots. In particular, this command writes the byte `my_byte` to one register on the TDC card. (All XTC2 registers are accessed via the TDC.)

Compile crate code

The VISION libraries that define the crate commands are available only on B0 machines, so it will be necessary to log in to 3 different machines to edit, compile, and test this code.

• Accessible by the crate • Holds the compiled programs	• Middle man	• Has the required VISION libraries for compilation

Log in to b0doorway:

```
lx0.hep.uiuc.edu> cdfsoft
No default SAM configuration exists at this time.
lx0.hep.uiuc.edu> kinit {YOURUSERNAME}
Password for {YOURUSERNAME}@FNAL.GOV:
lx0.hep.uiuc.edu> ssh –XA {YOURUSERNAME}@b0doorway.fnal.gov
```

Add the following lines to `b0doorway.fnal.gov:~/.cshrc`

```
    alias cpc1          "setup fision"
    alias cpc2          "setup -q ppc vxworks"
    alias cpc3          '$VXCC -I${FISION_DIR}/include \!^.c'
    alias cpc4          '$VXLD -g -o \!* \!*.o'
    alias cpc           "cpc1; cpc2; cpc3 \!*; cpc4 \!*"
```

As before, the changes will not take effect until you either logout and log back in, or type the command: `source ~/.cshrc`

Copy your source code to the b0 machine, and compile it.

```
mkdir ~/xtctest
cd ~/xtctest/
scp {YOURUSERNAME}@lx0.hep.uiuc.edu:~/xtctest/regtest4.c ./
cpc regtest4
scp ./regtest4 {YOURUSERNAME}@lx0.hep.uiuc.edu:~/xtctest/
```

Copy your compiled program from `lx0.hep.uiuc.edu:~/xtctest/regtest4` to the Windows network directory using a Windows SSH utility, like "SSH Secure Shell Client"

Now, log in to the crate, and run the new version of `regtest4`. You should see the program run as usual, with your added "`Hello World!`" showing up.

```
ld < regtest4
run
```

Checkout of XTC2s

You can find plenty of information about XTC2s, including specifications, explanations of firmware versions, and register descriptions here:

http://www.hep.uiuc.edu/engin/cdf/XFT2/index.htm

Prepare an XTC2 for checkout

`ld < regtest` `run`	**Run regtest** to insure the TDC and XTC2 are communicating properly with the crate CPU.

`ld < xtc_comp`
`run`
`     ......`
`> 2 28`
	Check that CPLD version == 16 to insure that the XTC2's CPLD is properly programmed, and therefore ready to have its FlashRAM programmed. (If it's anything other than 16, see the last page of this document.)

`ld < xtc_comp`
`run`
`     ......`
`> 12 28`
	Reprogram the FlashRAM so that the FPGAs will have the most up-to-date configuration. (This takes about 2 minutes.)

After you've done these things, you're ready to "check out" an XTC2 using `xtc_comp`…

Using `xtc_comp` to check out an XTC2

To checkout an XTC2, run xtc_comp, and use each of the following commands (in order):

The procedure for running these same tests on the B0 crate is available here.
http://www-cdfonline.fnal.gov/ops/xft/nils/test2.html

```
ld < xtc_comp
run
     .......SETUP OUTPUT.......
> 15
     .....OPTION 15 OUTPUT.....
> 17
     ......TEST 17 OUTPUT......
> 18
     ......TEST 18 OUTPUT......
> 19
     ......TEST 19 OUTPUT......
> 21
     ......TEST 21 OUTPUT......
> 27
     ......TEST 27 OUTPUT......
> 28
```

NOTE: Each test output is both printed and recorded in a file in the Windows directory. You can access the last results of a particular board's tests by opening
`\\Hep-ntweb\VxUsers\VxCDF\xtctest\XTC2_{SERIAL_NUM}.txt`

What each test in the checkout does...

15) 6-Bin: Program Registers – Production XTC, Standard Values...

This option configures each of the write accessible registers with their default values. An explanation of each register is available at the website mentioned above.

17) 6-Bin: Connectivity Test

The connectivity test instructs the TDC and XTC2 to begin sending an event of all zeros. After a few such events have been sent, it inspects the Finder's RAM, and compares it to its expectation. The Finder expects to find all zeros, along with the correct formatting of B0 and Word0 signals. The test repeats using all ones, all zeros, and all ones again, for a total of 4 events worth of information being read out.

This is essentially a test of equipment between the TDC output module and the Finder input module. No XTC2 logic is used here.

18) 6-Bin: Finder Capture Functionality Test

The Finder Capture test is nearly identical to the connectivity test. The most notable difference is that random words are created in a couple of XTC2 timing windows, and the Finder RAMs are checked to insure that those words are properly formatted. This is a good test of XTC2 logic functionality, and channel-by-channel accuracy.

This test starts with a quick scan to determine approximately where the XTC2 timing windows are. Also, 100 events are tested, compared to only 4 events in the connectivity test.

19) 6-Bin: Extended Finder Capture Functionality Test

This test is exactly the same as the previous, with 100 times as many events tested.

21) 6-Bin: L2 Buffer Test – New Way ...

The L2 Buffer is a memory device on the output end of the XTC2. It stores, for testing purposes, the output of the XTC2 before it is sent on toward the Finder. If the XTC2 has shown correct functionality in the Finder Capture tests above, this can subsequently check the functionality of the L2 Buffer by comparing what it records to what the Finder receives.

The test is run in the same way as the Finder Capture functionality tests, except the inputs and outputs it compares are different. Instead of comparing XTC2 input to Finder output, it compares Finder output to XTC2 output (in the L2 buffer).

27) Edgetest

Edgetest uses pulses from the Tracer to search, channel-by-channel, for the timing of each edge of the XTC2 logical windows. On the input side of the XTC2, there are 11 windows (6 output + 5 not-sure). This test scans with variable sized pulses to find each windows beginning and end.

At the end of the test, a 12 by 96 table of timing values is displayed. Currently, there is no "failure" mode of this test, but it can be used to search for anomalous behavior on a specific channel.

Identifying error messages in `xtc_comp`

The successful output of the tests in the checkout of an XTC2 is shown below.

17) 6-Bin: Connectivity Test

Notice the 4 events captured, reading all zeros, all ones, all zeros, and all ones again. The far right column displays the XOR between what is “written” (input to the TDC) and what is “read” (read out of the Finder). This should always be zero. The last lines sum the errors over the course of the whole test. The B0 and W0 errors should be 0, and there should be no channel errors.

```
* Event      1: TDC 11/0  0000 0000 0000  0000 0000 0000  0000 0000 0000  0000 0000 0000  0000
0000 0000  0000 0000 0000
* Event      1: TDC 11/1  0000 0000 0000  0000 0000 0000  0000 0000 0000  0000 0000 0000  0000
0000 0000  0000 0000 0000
[M] Window#=3  Calib Signal=  0 Test Value=  0 Loop=   1 T:11/0 F:05/4  Word= 5:06 w=20000
r=20000 x=    0
[M] Window#=3  Calib Signal=  0 Test Value=  0 Loop=   1 T:11/0 F:05/4  Word= 6:07 w=20000
r=20000 x=    0
[M] Window#=3  Calib Signal=  0 Test Value=  0 Loop=   1 T:11/0 F:05/4  Word= 7:08 w=20000
r=20000 x=    0
[M] Window#=3  Calib Signal=  0 Test Value=  0 Loop=   1 T:11/0 F:05/4  Word=23:06 w=    0 r=
0 x=    0
[M] Window#=3  Calib Signal=  0 Test Value=  0 Loop=   1 T:11/0 F:05/4  Word=24:07 w=    0 r=
0 x=    0
[M] Window#=3  Calib Signal=  0 Test Value=  0 Loop=   1 T:11/0 F:05/4  Word=25:08 w=    0 r=
0 x=    0
[M] Window#=3  Calib Signal=  0 Test Value=  0 Loop=   1 T:11/0 F:05/4  Word=41:06 w=    0 r=
0 x=    0
[M] Window#=3  Calib Signal=  0 Test Value=  0 Loop=   1 T:11/0 F:05/4  Word=42:07 w=    0 r=
0 x=    0
[M] Window#=3  Calib Signal=  0 Test Value=  0 Loop=   1 T:11/0 F:05/4  Word=43:08 w=    0 r=
0 x=    0
[M] Window#=3  Calib Signal=  0 Test Value=  0 Loop=   1 T:11/0 F:05/4  Word=59:06 w=    0 r=
0 x=    0
[M] Window#=3  Calib Signal=  0 Test Value=  0 Loop=   1 T:11/0 F:05/4  Word=60:07 w=    0 r=
0 x=    0
[M] Window#=3  Calib Signal=  0 Test Value=  0 Loop=   1 T:11/0 F:05/4  Word=61:08 w=    0 r=
0 x=    0
[M] Window#=3  Calib Signal=  0 Test Value=  0 Loop=   1 T:11/1 F:05/3  Word= 5:06 w=20000
r=20000 x=    0
[M] Window#=3  Calib Signal=  0 Test Value=  0 Loop=   1 T:11/1 F:05/3  Word= 6:07 w=20000
r=20000 x=    0
[M] Window#=3  Calib Signal=  0 Test Value=  0 Loop=   1 T:11/1 F:05/3  Word= 7:08 w=20000
r=20000 x=    0
[M] Window#=3  Calib Signal=  0 Test Value=  0 Loop=   1 T:11/1 F:05/3  Word=23:06 w=    0 r=
0 x=    0
[M] Window#=3  Calib Signal=  0 Test Value=  0 Loop=   1 T:11/1 F:05/3  Word=24:07 w=    0 r=
0 x=    0
[M] Window#=3  Calib Signal=  0 Test Value=  0 Loop=   1 T:11/1 F:05/3  Word=25:08 w=    0 r=
0 x=    0
[M] Window#=3  Calib Signal=  0 Test Value=  0 Loop=   1 T:11/1 F:05/3  Word=41:06 w=    0 r=
0 x=    0
[M] Window#=3  Calib Signal=  0 Test Value=  0 Loop=   1 T:11/1 F:05/3  Word=42:07 w=    0 r=
0 x=    0
[M] Window#=3  Calib Signal=  0 Test Value=  0 Loop=   1 T:11/1 F:05/3  Word=43:08 w=    0 r=
0 x=    0
[M] Window#=3  Calib Signal=  0 Test Value=  0 Loop=   1 T:11/1 F:05/3  Word=59:06 w=    0 r=
0 x=    0
[M] Window#=3  Calib Signal=  0 Test Value=  0 Loop=   1 T:11/1 F:05/3  Word=60:07 w=    0 r=
0 x=    0
[M] Window#=3  Calib Signal=  0 Test Value=  0 Loop=   1 T:11/1 F:05/3  Word=61:08 w=    0 r=
0 x=    0
Test results:
  Cable   0: TDC 11/0 to Finder  5/4   Total=          64 Errors=          64
  Cable   1: TDC 11/1 to Finder  5/3   Total=          64 Errors=          64
* Event      1: TDC 11/0  FFFF FFFF FFFF  FFFF FFFF FFFF  FFFF FFFF FFFF  FFFF FFFF FFFF  FFFF
FFFF FFFF  FFFF FFFF FFFF
* Event      1: TDC 11/1  FFFF FFFF FFFF  FFFF FFFF FFFF  FFFF FFFF FFFF  FFFF FFFF FFFF  FFFF
FFFF FFFF  FFFF FFFF FFFF
[M] Window#=3  Calib Signal=  0 Test Value=  1 Loop=   1 T:11/0 F:05/4  Word= 5:06 w=2FFFF
r=2FFFF x=    0
[M] Window#=3  Calib Signal=  0 Test Value=  1 Loop=   1 T:11/0 F:05/4  Word= 6:07 w=2FFFF
r=2FFFF x=    0
[M] Window#=3  Calib Signal=  0 Test Value=  1 Loop=   1 T:11/0 F:05/4  Word= 7:08 w=2FFFF
r=2FFFF x=    0
[M] Window#=3  Calib Signal=  0 Test Value=  1 Loop=   1 T:11/0 F:05/4  Word=23:06 w= FFFF r=
FFFF x=    0
[M] Window#=3  Calib Signal=  0 Test Value=  1 Loop=   1 T:11/0 F:05/4  Word=24:07 w= FFFF r=
```

```
FFFF x=    0
[M] Window#=3  Calib Signal=  0 Test Value=  1 Loop=   1 T:11/0 F:05/4  Word=25:08 w= FFFF r=
FFFF x=    0
[M] Window#=3  Calib Signal=  0 Test Value=  1 Loop=   1 T:11/0 F:05/4  Word=41:06 w= FFFF r=
FFFF x=    0
[M] Window#=3  Calib Signal=  0 Test Value=  1 Loop=   1 T:11/0 F:05/4  Word=42:07 w= FFFF r=
FFFF x=    0
[M] Window#=3  Calib Signal=  0 Test Value=  1 Loop=   1 T:11/0 F:05/4  Word=43:08 w= FFFF r=
FFFF x=    0
[M] Window#=3  Calib Signal=  0 Test Value=  1 Loop=   1 T:11/0 F:05/4  Word=59:06 w= FFFF r=
FFFF x=    0
[M] Window#=3  Calib Signal=  0 Test Value=  1 Loop=   1 T:11/0 F:05/4  Word=60:07 w= FFFF r=
FFFF x=    0
[M] Window#=3  Calib Signal=  0 Test Value=  1 Loop=   1 T:11/0 F:05/4  Word=61:08 w= FFFF r=
FFFF x=    0
[M] Window#=3  Calib Signal=  0 Test Value=  1 Loop=   1 T:11/1 F:05/3  Word= 5:06 w=2FFFF
r=2FFFF x=    0
[M] Window#=3  Calib Signal=  0 Test Value=  1 Loop=   1 T:11/1 F:05/3  Word= 6:07 w=2FFFF
r=2FFFF x=    0
[M] Window#=3  Calib Signal=  0 Test Value=  1 Loop=   1 T:11/1 F:05/3  Word= 7:08 w=2FFFF
r=2FFFF x=    0
[M] Window#=3  Calib Signal=  0 Test Value=  1 Loop=   1 T:11/1 F:05/3  Word=23:06 w= FFFF r=
FFFF x=    0
[M] Window#=3  Calib Signal=  0 Test Value=  1 Loop=   1 T:11/1 F:05/3  Word=24:07 w= FFFF r=
FFFF x=    0
[M] Window#=3  Calib Signal=  0 Test Value=  1 Loop=   1 T:11/1 F:05/3  Word=25:08 w= FFFF r=
FFFF x=    0
[M] Window#=3  Calib Signal=  0 Test Value=  1 Loop=   1 T:11/1 F:05/3  Word=41:06 w= FFFF r=
FFFF x=    0
[M] Window#=3  Calib Signal=  0 Test Value=  1 Loop=   1 T:11/1 F:05/3  Word=42:07 w= FFFF r=
FFFF x=    0
[M] Window#=3  Calib Signal=  0 Test Value=  1 Loop=   1 T:11/1 F:05/3  Word=43:08 w= FFFF r=
FFFF x=    0
[M] Window#=3  Calib Signal=  0 Test Value=  1 Loop=   1 T:11/1 F:05/3  Word=59:06 w= FFFF r=
FFFF x=    0
[M] Window#=3  Calib Signal=  0 Test Value=  1 Loop=   1 T:11/1 F:05/3  Word=60:07 w= FFFF r=
FFFF x=    0
[M] Window#=3  Calib Signal=  0 Test Value=  1 Loop=   1 T:11/1 F:05/3  Word=61:08 w= FFFF r=
FFFF x=    0
Test results:
  Cable   0: TDC 11/0 to Finder  5/4   Total=         128 Errors=         128
  Cable   1: TDC 11/1 to Finder  5/3   Total=         128 Errors=         128
* Event      1: TDC 11/0  0000 0000 0000  0000 0000 0000  0000 0000 0000  0000 0000 0000  0000
0000 0000  0000 0000 0000
* Event      1: TDC 11/1  0000 0000 0000  0000 0000 0000  0000 0000 0000  0000 0000 0000  0000
0000 0000  0000 0000 0000
[M] Window#=3  Calib Signal=  1 Test Value=  0 Loop=   1 T:11/0 F:05/4  Word= 5:06 w=20000
r=20000 x=    0
[M] Window#=3  Calib Signal=  1 Test Value=  0 Loop=   1 T:11/0 F:05/4  Word= 6:07 w=20000
r=20000 x=    0
[M] Window#=3  Calib Signal=  1 Test Value=  0 Loop=   1 T:11/0 F:05/4  Word= 7:08 w=20000
r=20000 x=    0
[M] Window#=3  Calib Signal=  1 Test Value=  0 Loop=   1 T:11/0 F:05/4  Word=23:06 w=    0 r=
0 x=    0
[M] Window#=3  Calib Signal=  1 Test Value=  0 Loop=   1 T:11/0 F:05/4  Word=24:07 w=    0 r=
0 x=    0
[M] Window#=3  Calib Signal=  1 Test Value=  0 Loop=   1 T:11/0 F:05/4  Word=25:08 w=    0 r=
0 x=    0
[M] Window#=3  Calib Signal=  1 Test Value=  0 Loop=   1 T:11/0 F:05/4  Word=41:06 w=    0 r=
0 x=    0
[M] Window#=3  Calib Signal=  1 Test Value=  0 Loop=   1 T:11/0 F:05/4  Word=42:07 w=    0 r=
0 x=    0
[M] Window#=3  Calib Signal=  1 Test Value=  0 Loop=   1 T:11/0 F:05/4  Word=43:08 w=    0 r=
0 x=    0
[M] Window#=3  Calib Signal=  1 Test Value=  0 Loop=   1 T:11/0 F:05/4  Word=59:06 w=    0 r=
0 x=    0
[M] Window#=3  Calib Signal=  1 Test Value=  0 Loop=   1 T:11/0 F:05/4  Word=60:07 w=    0 r=
0 x=    0
```

```
[M] Window#=3  Calib Signal=  1 Test Value=  0 Loop=   1 T:11/0 F:05/4  Word=61:08 w=    0 r=
0 x=    0
[M] Window#=3  Calib Signal=  1 Test Value=  0 Loop=   1 T:11/1 F:05/3  Word= 5:06 w=20000
r=20000 x=    0
[M] Window#=3  Calib Signal=  1 Test Value=  0 Loop=   1 T:11/1 F:05/3  Word= 6:07 w=20000
r=20000 x=    0
[M] Window#=3  Calib Signal=  1 Test Value=  0 Loop=   1 T:11/1 F:05/3  Word= 7:08 w=20000
r=20000 x=    0
[M] Window#=3  Calib Signal=  1 Test Value=  0 Loop=   1 T:11/1 F:05/3  Word=23:06 w=    0 r=
0 x=    0
[M] Window#=3  Calib Signal=  1 Test Value=  0 Loop=   1 T:11/1 F:05/3  Word=24:07 w=    0 r=
0 x=    0
[M] Window#=3  Calib Signal=  1 Test Value=  0 Loop=   1 T:11/1 F:05/3  Word=25:08 w=    0 r=
0 x=    0
[M] Window#=3  Calib Signal=  1 Test Value=  0 Loop=   1 T:11/1 F:05/3  Word=41:06 w=    0 r=
0 x=    0
[M] Window#=3  Calib Signal=  1 Test Value=  0 Loop=   1 T:11/1 F:05/3  Word=42:07 w=    0 r=
0 x=    0
[M] Window#=3  Calib Signal=  1 Test Value=  0 Loop=   1 T:11/1 F:05/3  Word=43:08 w=    0 r=
0 x=    0
[M] Window#=3  Calib Signal=  1 Test Value=  0 Loop=   1 T:11/1 F:05/3  Word=59:06 w=    0 r=
0 x=    0
[M] Window#=3  Calib Signal=  1 Test Value=  0 Loop=   1 T:11/1 F:05/3  Word=60:07 w=    0 r=
0 x=    0
[M] Window#=3  Calib Signal=  1 Test Value=  0 Loop=   1 T:11/1 F:05/3  Word=61:08 w=    0 r=
0 x=    0
Test results:
  Cable   0: TDC 11/0 to Finder  5/4   Total=         192 Errors=         192
  Cable   1: TDC 11/1 to Finder  5/3   Total=         192 Errors=         192
* Event      1: TDC 11/0  FFFF FFFF FFFF  FFFF FFFF FFFF  FFFF FFFF FFFF  FFFF FFFF FFFF  FFFF
FFFF FFFF  FFFF FFFF FFFF
* Event      1: TDC 11/1  FFFF FFFF FFFF  FFFF FFFF FFFF  FFFF FFFF FFFF  FFFF FFFF FFFF  FFFF
FFFF FFFF  FFFF FFFF FFFF
[M] Window#=3  Calib Signal=  1 Test Value=  1 Loop=   1 T:11/0 F:05/4  Word= 5:06 w=2FFFF
r=2FFFF x=    0
[M] Window#=3  Calib Signal=  1 Test Value=  1 Loop=   1 T:11/0 F:05/4  Word= 6:07 w=2FFFF
r=2FFFF x=    0
[M] Window#=3  Calib Signal=  1 Test Value=  1 Loop=   1 T:11/0 F:05/4  Word= 7:08 w=2FFFF
r=2FFFF x=    0
[M] Window#=3  Calib Signal=  1 Test Value=  1 Loop=   1 T:11/0 F:05/4  Word=23:06 w= FFFF r=
FFFF x=    0
[M] Window#=3  Calib Signal=  1 Test Value=  1 Loop=   1 T:11/0 F:05/4  Word=24:07 w= FFFF r=
FFFF x=    0
[M] Window#=3  Calib Signal=  1 Test Value=  1 Loop=   1 T:11/0 F:05/4  Word=25:08 w= FFFF r=
FFFF x=    0
[M] Window#=3  Calib Signal=  1 Test Value=  1 Loop=   1 T:11/0 F:05/4  Word=41:06 w= FFFF r=
FFFF x=    0
[M] Window#=3  Calib Signal=  1 Test Value=  1 Loop=   1 T:11/0 F:05/4  Word=42:07 w= FFFF r=
FFFF x=    0
[M] Window#=3  Calib Signal=  1 Test Value=  1 Loop=   1 T:11/0 F:05/4  Word=43:08 w= FFFF r=
FFFF x=    0
[M] Window#=3  Calib Signal=  1 Test Value=  1 Loop=   1 T:11/0 F:05/4  Word=59:06 w= FFFF r=
FFFF x=    0
[M] Window#=3  Calib Signal=  1 Test Value=  1 Loop=   1 T:11/0 F:05/4  Word=60:07 w= FFFF r=
FFFF x=    0
[M] Window#=3  Calib Signal=  1 Test Value=  1 Loop=   1 T:11/0 F:05/4  Word=61:08 w= FFFF r=
FFFF x=    0
[M] Window#=3  Calib Signal=  1 Test Value=  1 Loop=   1 T:11/1 F:05/3  Word= 5:06 w=2FFFF
r=2FFFF x=    0
[M] Window#=3  Calib Signal=  1 Test Value=  1 Loop=   1 T:11/1 F:05/3  Word= 6:07 w=2FFFF
r=2FFFF x=    0
[M] Window#=3  Calib Signal=  1 Test Value=  1 Loop=   1 T:11/1 F:05/3  Word= 7:08 w=2FFFF
r=2FFFF x=    0
[M] Window#=3  Calib Signal=  1 Test Value=  1 Loop=   1 T:11/1 F:05/3  Word=23:06 w= FFFF r=
FFFF x=    0
[M] Window#=3  Calib Signal=  1 Test Value=  1 Loop=   1 T:11/1 F:05/3  Word=24:07 w= FFFF r=
FFFF x=    0
[M] Window#=3  Calib Signal=  1 Test Value=  1 Loop=   1 T:11/1 F:05/3  Word=25:08 w= FFFF r=
```

```
FFFF x=    0
[M] Window#=3  Calib Signal=  1 Test Value=  1 Loop=   1 T:11/1 F:05/3  Word=41:06 w= FFFF r=
FFFF x=    0
[M] Window#=3  Calib Signal=  1 Test Value=  1 Loop=   1 T:11/1 F:05/3  Word=42:07 w= FFFF r=
FFFF x=    0
[M] Window#=3  Calib Signal=  1 Test Value=  1 Loop=   1 T:11/1 F:05/3  Word=43:08 w= FFFF r=
FFFF x=    0
[M] Window#=3  Calib Signal=  1 Test Value=  1 Loop=   1 T:11/1 F:05/3  Word=59:06 w= FFFF r=
FFFF x=    0
[M] Window#=3  Calib Signal=  1 Test Value=  1 Loop=   1 T:11/1 F:05/3  Word=60:07 w= FFFF r=
FFFF x=    0
[M] Window#=3  Calib Signal=  1 Test Value=  1 Loop=   1 T:11/1 F:05/3  Word=61:08 w= FFFF r=
FFFF x=    0
Test results:
  Cable   0: TDC 11/0 to Finder  5/4   Total=         256 Errors=         256
  Cable   1: TDC 11/1 to Finder  5/3   Total=         256 Errors=         256

B0 Errors: 0
W0 Errors: 0
Channel Errors (out of a possible 16):
   No Channel Errors Found
```

If the highlighted section shows no errors, the XTC2 passes Test 17

18) 6-Bin: Finder Capture Functionality Test

The test starts by scanning for the 6 XTC2 output windows using the Tracer. The test then uses the results of the scan to calculate the timing of each of the 6 windows. The test then randomly selects up to 2 windows to test, and fills those windows with random bits. The first and last 2 events of this successful test are shown. According to the last line, no read-back errors occurred in this test.

```
Finding optimal TRACER fine delay value settings...

00000000000000000007accccccccccccccccccccccccccc52000000000000000000000000000000000000
00000000000000000000000000000000000000000000000000000000000000000000000000000000000000
00000000000000000000000000000000000000000000000000000000000000000000000000000000000000
0000000000000000000
Calibration Signal=0  Window=0  Min= 22  Max= 51  Chosen= 36

00000000000000000000000000000000000000000000000000000000000000000000000004accccccccccccccccccb0
00000000000000000000000000000000000000000000000000000000000000000000000000000000000000000000
00000000000000000000000000000000000000000000000000000000000000000000000000000000000000000000
0000000000000000000
Calibration Signal=0  Window=1  Min= 68  Max= 86  Chosen= 77

00000000000000000000000000000000000000000000000000000000000000000000000000000000000000000000
000000000000000ccccccccccccccccb852000000000000000000000000000000000000000000000000000000000
00000000000000000000000000000000000000000000000000000000000000000000000000000000000000000000
0000000000000000000
Calibration Signal=0  Window=2  Min=104  Max=120  Chosen=112

00000000000000000000000000000000000000000000000000000000000000000000000000000000000000000000
00000000000000000000000000000000000000000000000000007accccccccccccccccccc7610000000000000000
00000000000000000000000000000000000000000000000000000000000000000000000000000000000000000000
0000000000000000000
Calibration Signal=0  Window=3  Min=142  Max=161  Chosen=151

00000000000000000000000000000000000000000000000000000000000000000000000000000000000000000000
00000000000000000000000000000000000000000000000000000000000000000000000000000000000000000000
2accccccccccccccccccccccccccccccc665100000000000000000000
0000000000000000000
Calibration Signal=0  Window=4  Min=180  Max=211  Chosen=195

00000000000000000000000000000000000000000000000000000000000000000000000000000000000000000000
00000000000000000000000000000000000000000000000000000000000000000000000000000000000000000000
00000000000000000000000000000000000000000000000000000106ccccccc
ccccccccccc20000000
Calibration Signal=0  Window=5  Min=230  Max=247  Chosen=238

00000000000000000000047ccccccccccccccccccccccccc66600000000000000000000000000000000000000
00000000000000000000000000000000000000000000000000000000000000000000000000000000000000000000
00000000000000000000000000000000000000000000000000000000000000000000000000000000000000000000
0000000000000000000
Calibration Signal=1  Window=0  Min= 24  Max= 51  Chosen= 37

00000000000000000000000000000000000000000000000000000000000000000000000000037ccccccccccccccc
c961000000000000000000000000000000000000000000000000000000000000000000000000000000000000000000
00000000000000000000000000000000000000000000000000000000000000000000000000000000000000000000
0000000000000000000
Calibration Signal=1  Window=1  Min= 73  Max= 89  Chosen= 81

00000000000000000000000000000000000000000000000000000000000000000000000000000000000000000000
00000000000000000003ccccccccccccccccc6660000000000000000000000000000000000000000000000000000000
00000000000000000000000000000000000000000000000000000000000000000000000000000000000000000000
0000000000000000000
Calibration Signal=1  Window=2  Min=109  Max=125  Chosen=117

00000000000000000000000000000000000000000000000000000000000000000000000000000000000000000000
00000000000000000000000000000000000000000000000000001bccccccccccccccccc9660000000000000000
00000000000000000000000000000000000000000000000000000000000000000000000000000000000000000000
0000000000000000000
Calibration Signal=1  Window=3  Min=145  Max=161  Chosen=153

00000000000000000000000000000000000000000000000000000000000000000000000000000000000000000000
00000000000000000000000000000000000000000000000000000000000000000000000000000000000000000000
```

```
006ccccccccccccccccccccb66000000000000000000000000000000
0000000000000000000
Calibration Signal=1  Window=4  Min=181  Max=202  Chosen=191

000000000000000000000000000000000000000000000000000000000000000000000000000000000000000000000000000000000000000000
000000000000000000000000000000000000000000000000000000000000000000000000000000000000000000000000000000000000000000
00000000000000000000000000000000000000000017ccccccccccccccc
ccca000000000000000
Calibration Signal=1  Window=5  Min=221  Max=239  Chosen=230
Beginning random data testing...
* Event      0: TDC 11/0  0000 0000 0000  0000 0000 0000  0000 0000 0000  0000 0000 0000
0000 0000 0000  0000 0000 0000
* Event      0: TDC 11/1  0000 0000 0000  0000 0000 0000  0000 0000 0000  0000 0000 0000
0000 0000 0000  0000 0000 0000
* Event      1: TDC 11/0  1041 A828 EE21  0000 0000 0000  0000 0000 0000  0000 0000 0000
0000 0000 0000  0000 0000 0000
* Event      1: TDC 11/1  9507 904C 6A08  0000 0000 0000  0000 0000 0000  0000 0000 0000
0000 0000 0000  0000 0000 0000

                                    .....

* Event     98: TDC 11/0  0000 0000 0000  059E A0C4 4151  0000 0000 0000  0000 0000 0000
0000 0000 0000  0000 0000 0000
* Event     98: TDC 11/1  0000 0000 0000  0409 0A22 1445  0000 0000 0000  0000 0000 0000
0000 0000 0000  0000 0000 0000
* Event     99: TDC 11/0  0000 0000 0000  0000 0000 0000  4828 1614 2494  0000 0000 0000
1487 C80B 4829  0000 0000 0000
* Event     99: TDC 11/1  0000 0000 0000  0000 0000 0000  2951 1154 3081  0000 0000 0000
968A A628 C42A  0000 0000 0000
Test Results:  Events:100  Errors:0
```

19) 6-Bin: Extended Finder Capture Functionality Test

The output for this test is identical to the previous, except that the number of events is 10,000 instead of 100.

21) 6-Bin: L2 Buffer Test – New Way ...

This test has essentially the same output, though there are a few more messages printing the Bunch Count, the test has 50 events over each of the 4 L2 Buffers, and a grand-total of all four buffers is given at the end of the test. The end of the test is shown here:

```
Bunch Count: 21
* Event     48: TDC 11/0  0000 0000 0000  0000 0000 0000  0000 0000 0000  0000 0000 0000
204E 1D40 0B06  0000 0000 0000
* Event     48: TDC 11/1  0000 0000 0000  0000 0000 0000  0000 0000 0000  0000 0000 0000
00FB A416 1900  0000 0000 0000
Bunch Count: 21
* Event     49: TDC 11/0  B68C 3C45 5D2A  0871 0318 2080  0000 0000 0000  0000 0000 0000
0000 0000 0000  0000 0000 0000
* Event     49: TDC 11/1  A344 C8C2 C6D2  0CAA 041C 3900  0000 0000 0000  0000 0000 0000
0000 0000 0000  0000 0000 0000
Bunch Count: 21

Buffer 3
Test Results:  Events:50  Errors:0
               Buffer Errors:0



Beginning test of the buffer content bits...

Testing buffer 0
Testing buffer 1
Testing buffer 2
Testing buffer 3

Complete Test Results:
Level 1 pipeline length (in CDFCLK periods): 4
   Buffer 0: Events:   50     Capture Errors:     0     Buffer Errors:     0
   Buffer 1: Events:   50     Capture Errors:     0     Buffer Errors:     0
   Buffer 2: Events:   50     Capture Errors:     0     Buffer Errors:     0
   Buffer 3: Events:   50     Capture Errors:     0     Buffer Errors:     0

Buffer Content Bit Errors: 0
```

27) Edgetest

This test (as yet) does not display have a PASS/FAIL decision, and no errors are displayed. The output is a 12 by 96 list of each channel's 12 window timings as determined by the Tracer. Generally, the columns should show consistent timings, channel-to-channel, board-to-board.

Other XTC2 tests available on the Windows network drive

The following tests, while not used in the checkout of an XTC2, can help diagnose problems.

ODLD (Output Data Looping Design)

This test loads an alternate FPGA configuration into the FlashRAM. The different configuration does not perform XTC2 functionality; instead, it loops an output pattern.

xtc_kill

In a previous CPLD design, there were rare cases where an XTC2 would "die" while the FPGAs were being configured. The only remedy at the time was to reprogram the CPLDs. To help diagnose this problem, xtc_kill was built to repeatedly configure the FPGAs 5000 times an hour. CPLD v16 should be immune this whole thing.

Reprogramming CPLDs

1. Connect the computer “Tethys” to the XTC2 using the JTAG connector

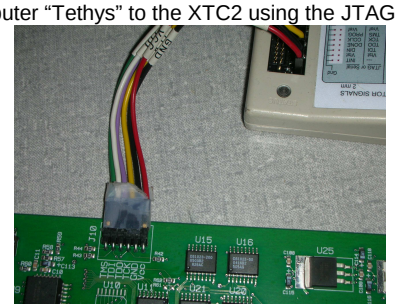

2. Power on the XTC2, by mounting it to the TDC and loading the pair into the crate.

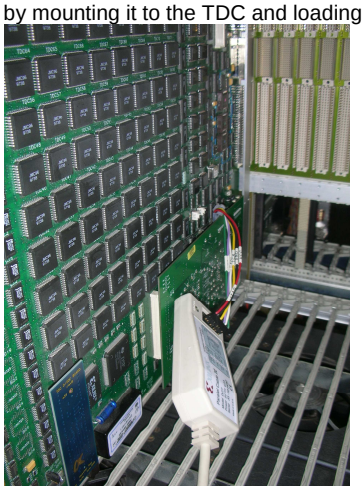

3. Load the Xilinx software on “Tethys” to Interact with the crate. There is probably a button the Desktop, or in the Programs Menu

or

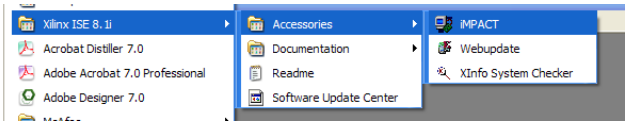

4. At the prompt, click Cancel

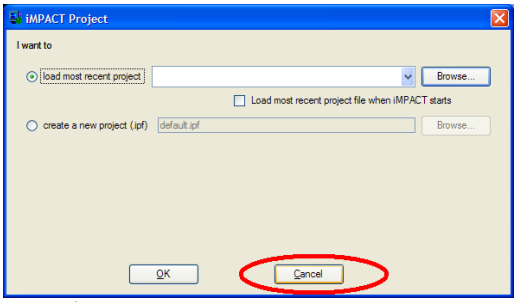

5. Double-click “Boundary Scan”

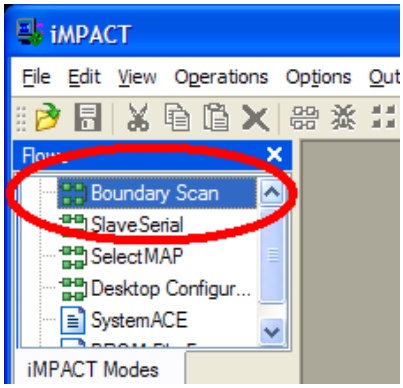

6. Click the “Initialize Chain” button

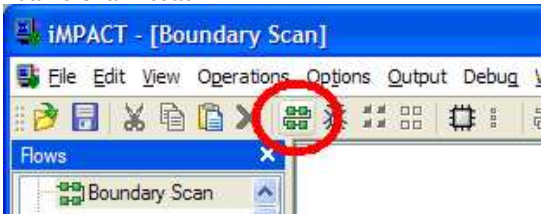

7. The program will detect four programmable chipsets, (2 CPLDs & 2 FPGAs). You’ll be programming the CPLDs only. The program will ask for 4 files.
   a. For the first file, choose
      `C:\Xilinx\xtc2\fromGregforHeather\fpga_prog_cpld v16.jed`
   b. For the second file, choose
      `C:\Xilinx\xtc2\fromGregforHeather\fpga_prog_cpld v16.jed`
   c. For the third and fourth files, choose “Bypass”

8. Last step. Program the CPLDs.
   a. Right click on the first chipset and click “Program…”

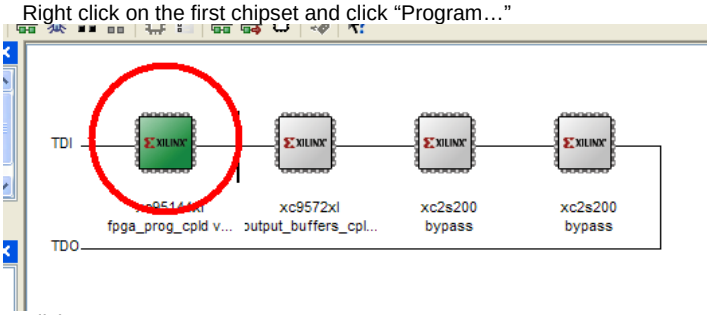

   b. Click OK
   c. Right click on the second chipset and click “Program…”

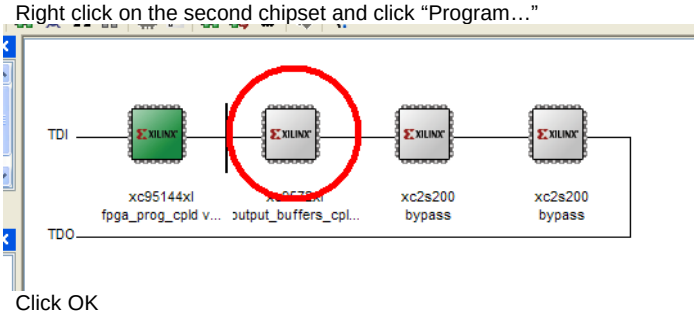

   d. Click OK
9. You’re done. Close without saving, and remove the JTAG connector. You’ve updated the CPLD version.

If you can’t find the files on the local drive required to program the CPLDs, there are backups online at:

http://www.hep.uiuc.edu/engin/cdf/XFT2/FPGA_Prog_CPLD_16.jed

http://www.hep.uiuc.edu/engin/cdf/XFT2/Output_Buffers_CPLD_1.jed

D Neurobayes© Node & Training Analysis

On the following pages is the collection of plots associated with the training of the B_c^+ neural network.

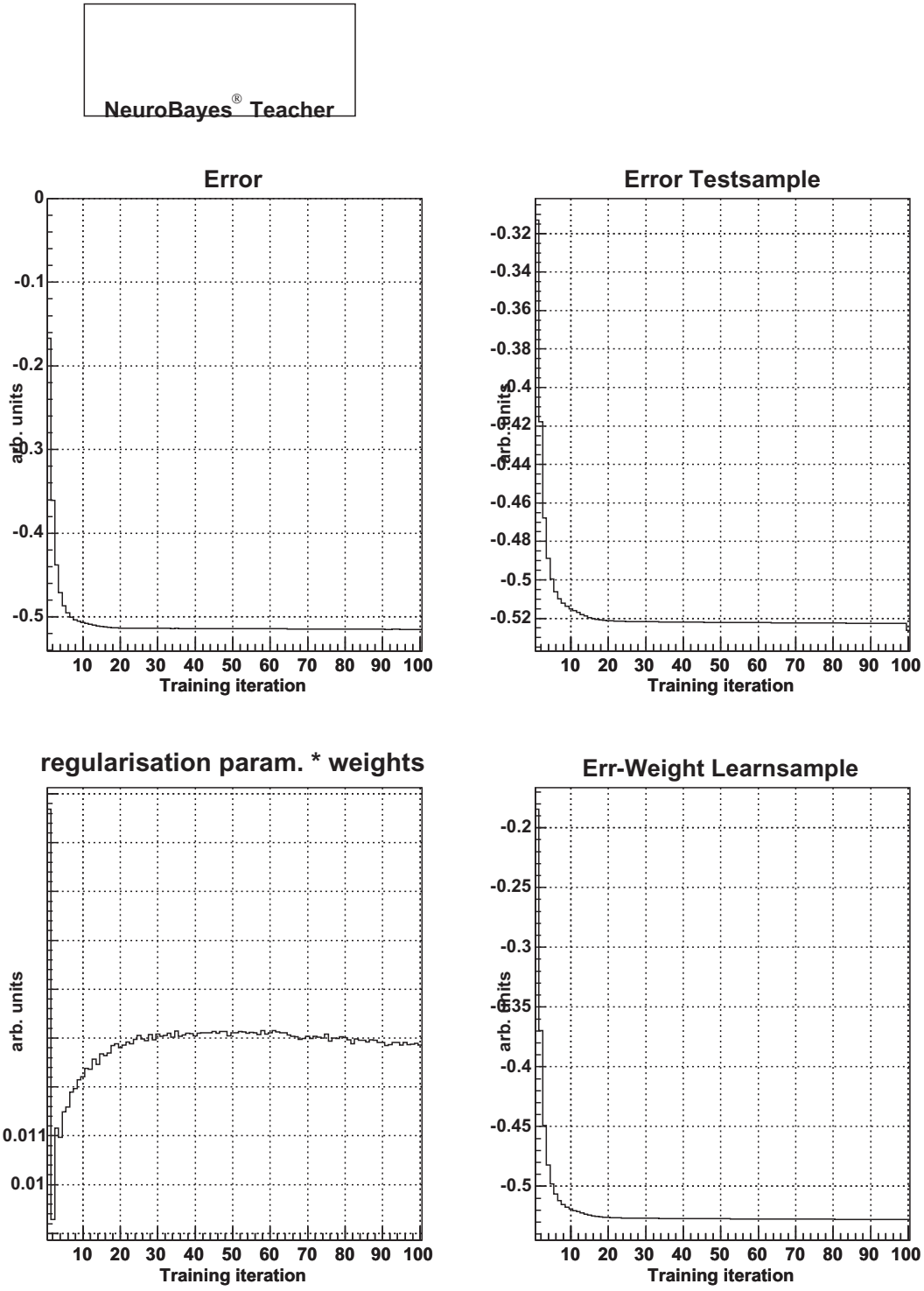
NeuroBayes® Teacher
Error
arb. units
Training iteration
Error Testsample
arb. units
Training iteration
regularisation param. * weights
arb. units
Training iteration
Err-Weight Learnsample
arb. units
Training iteration

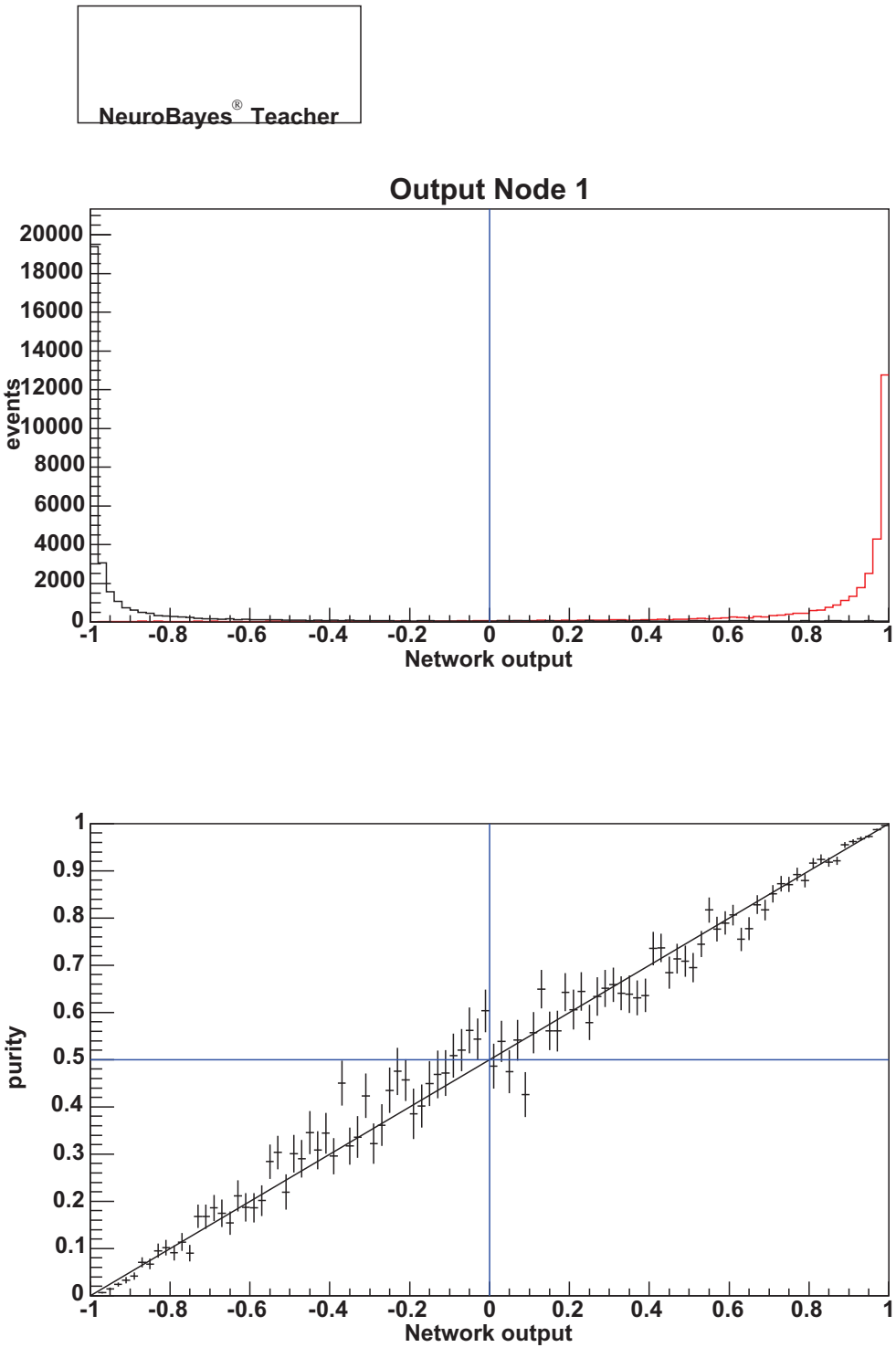
NeuroBayes® Teacher
Output Node 1
events
Network output
purity
Network output


NeuroBayes® Teacher

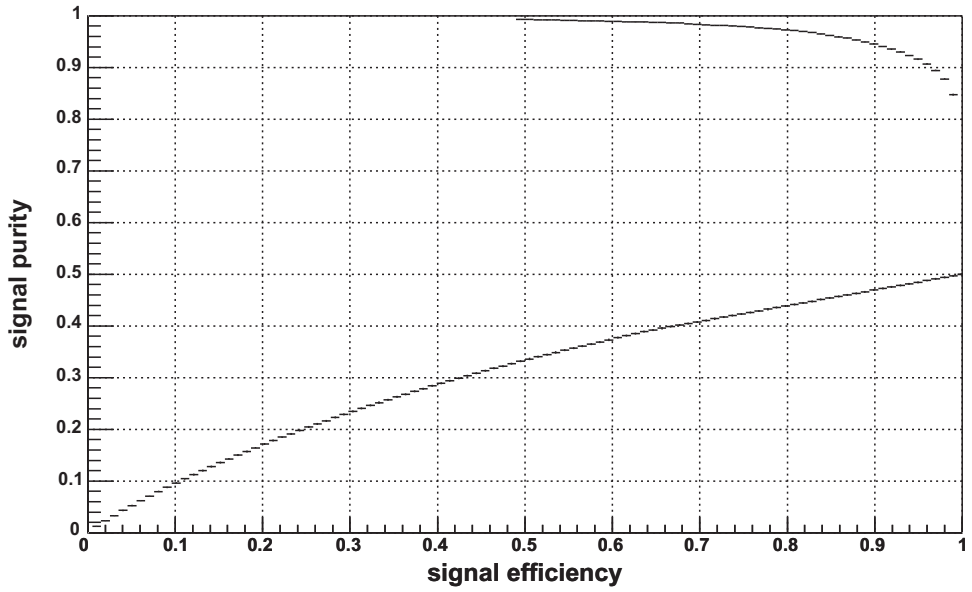
signal purity
signal efficiency
0
0.1
0.2
0.3
0.4
0.5
0.6
0.7
0.8
0.9
1

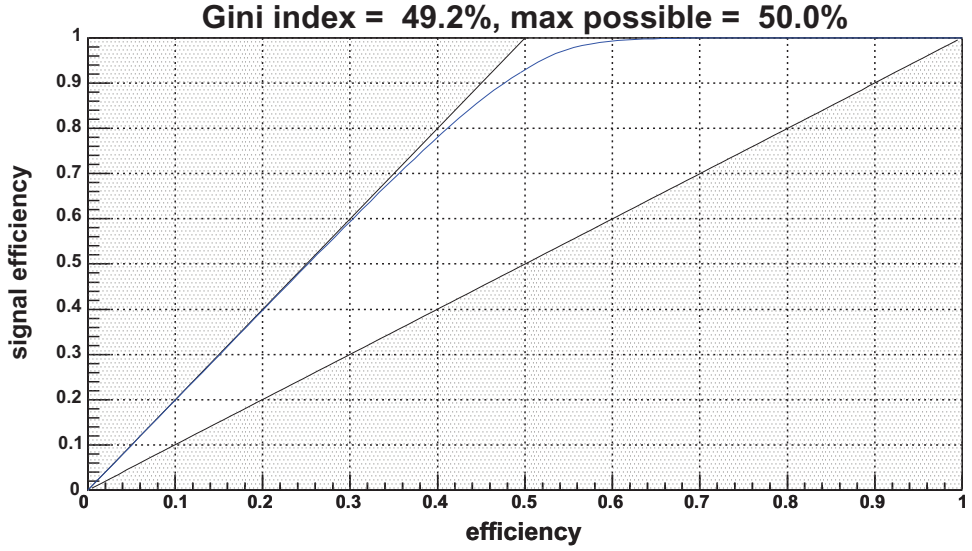
Gini index = 49.2%, max possible = 50.0%
signal efficiency
efficiency
0
0.1
0.2
0.3
0.4
0.5
0.6
0.7
0.8
0.9
1

NeuroBayes® Teacher

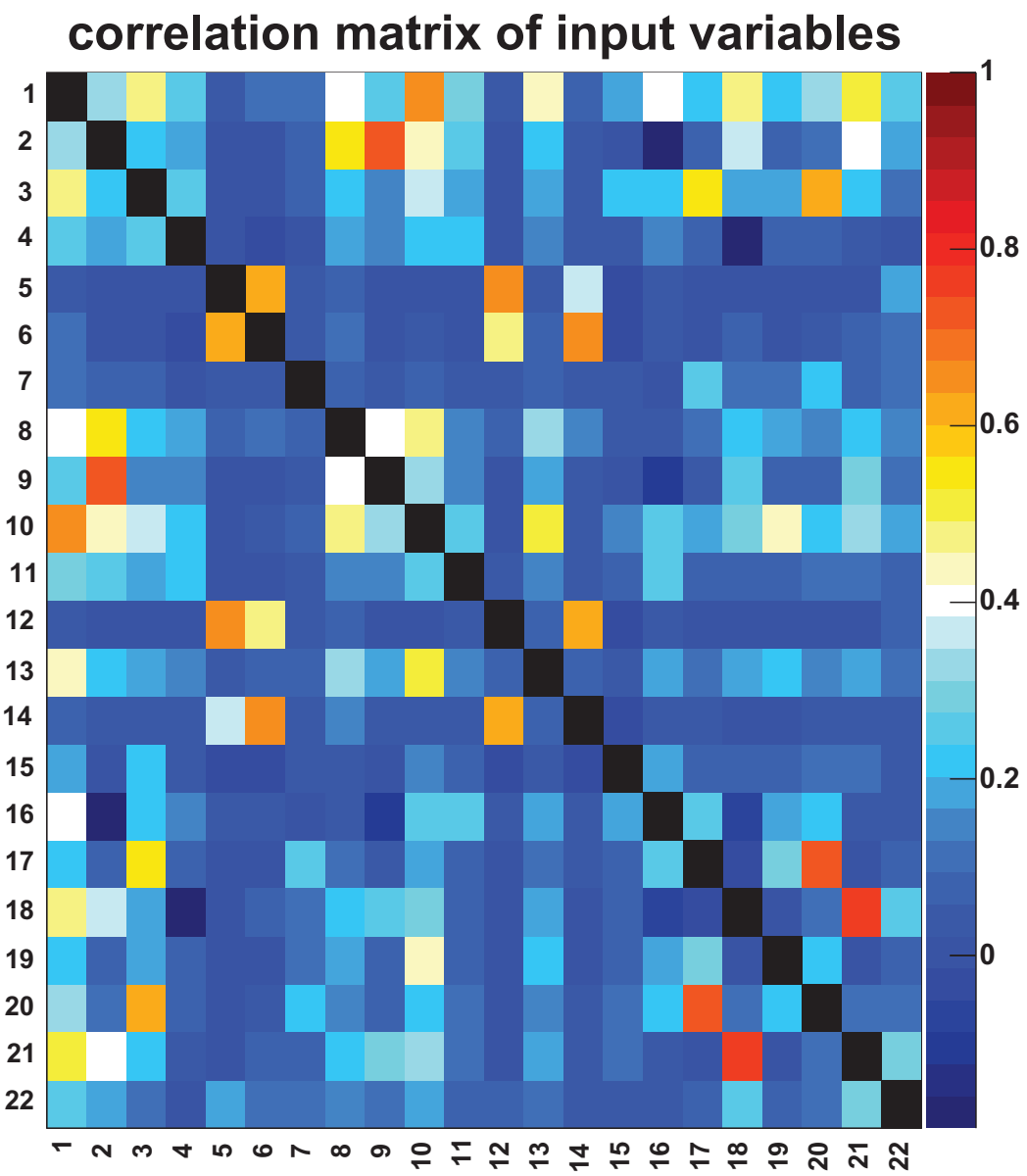

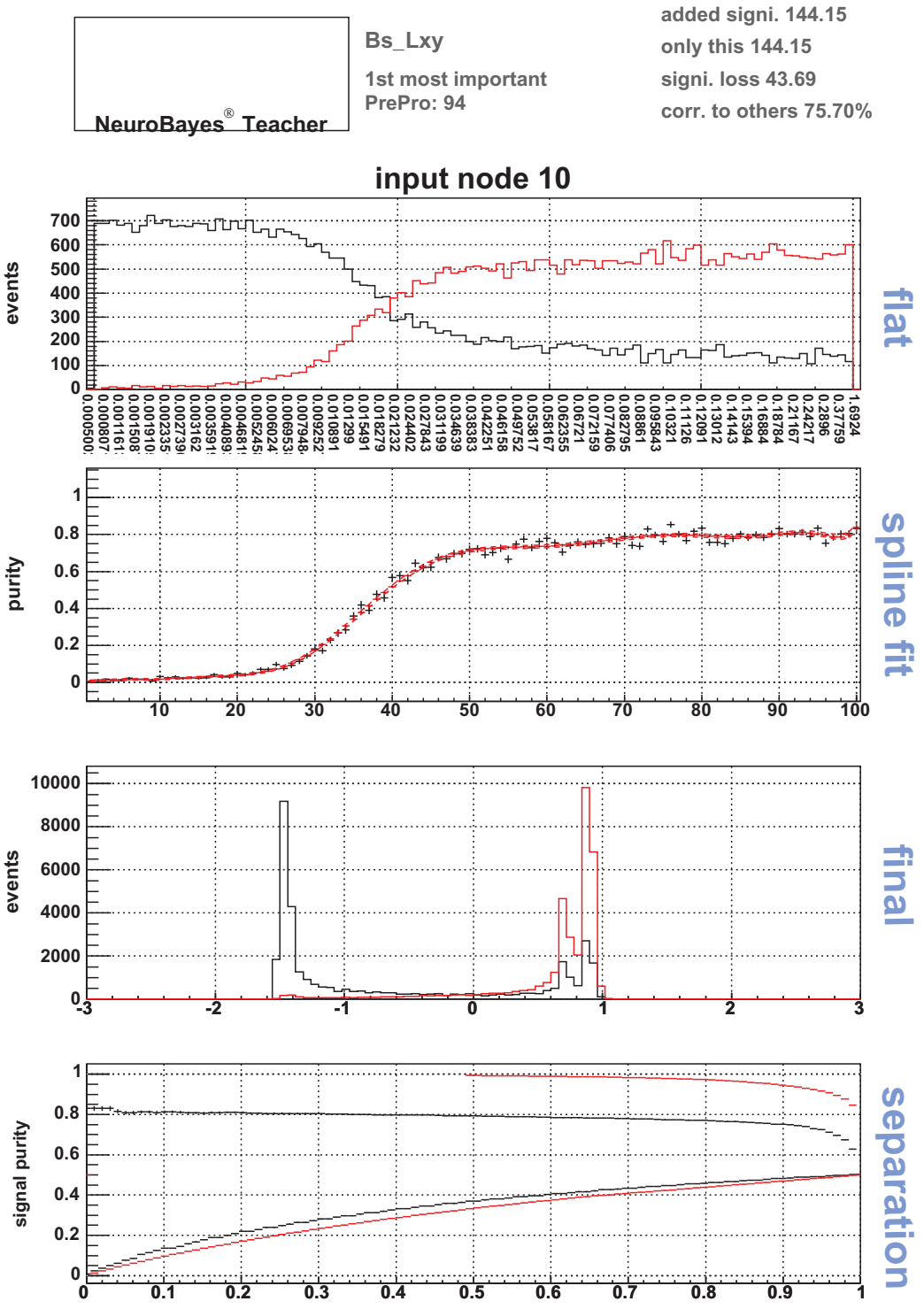
NeuroBayes® Teacher
Bs_Lxy
1st most important
PrePro: 94
added signi. 144.15
only this 144.15
signi. loss 43.69
corr. to others 75.70%
input node 10
events
flat
purity
spline fit
events
final
signal purity
separation

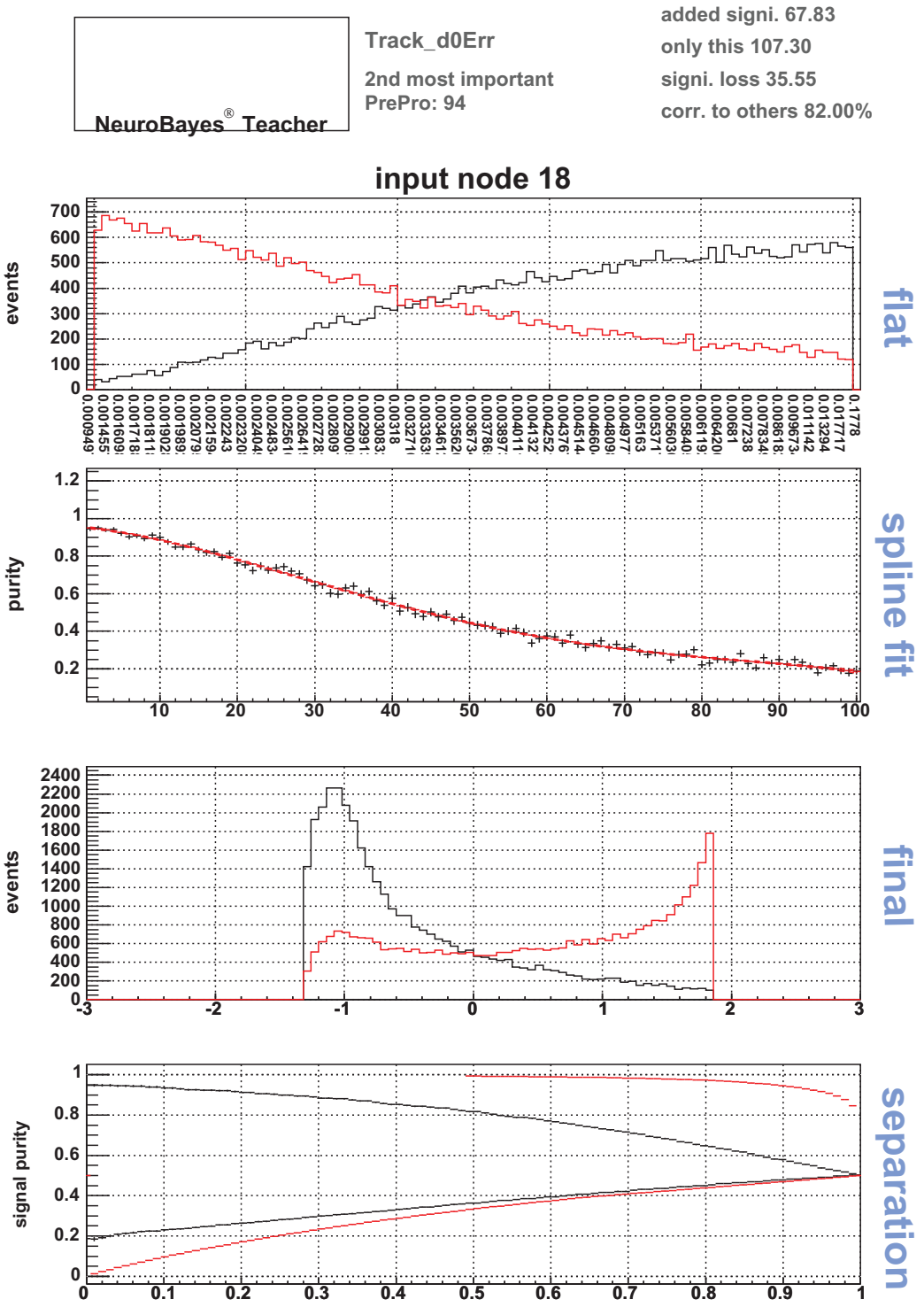
NeuroBayes® Teacher
Track_d0Err
2nd most important
PrePro: 94
added signi. 67.83
only this 107.30
signi. loss 35.55
corr. to others 82.00%
input node 18
events
flat
purity
spline fit
events
final
signal purity
separation

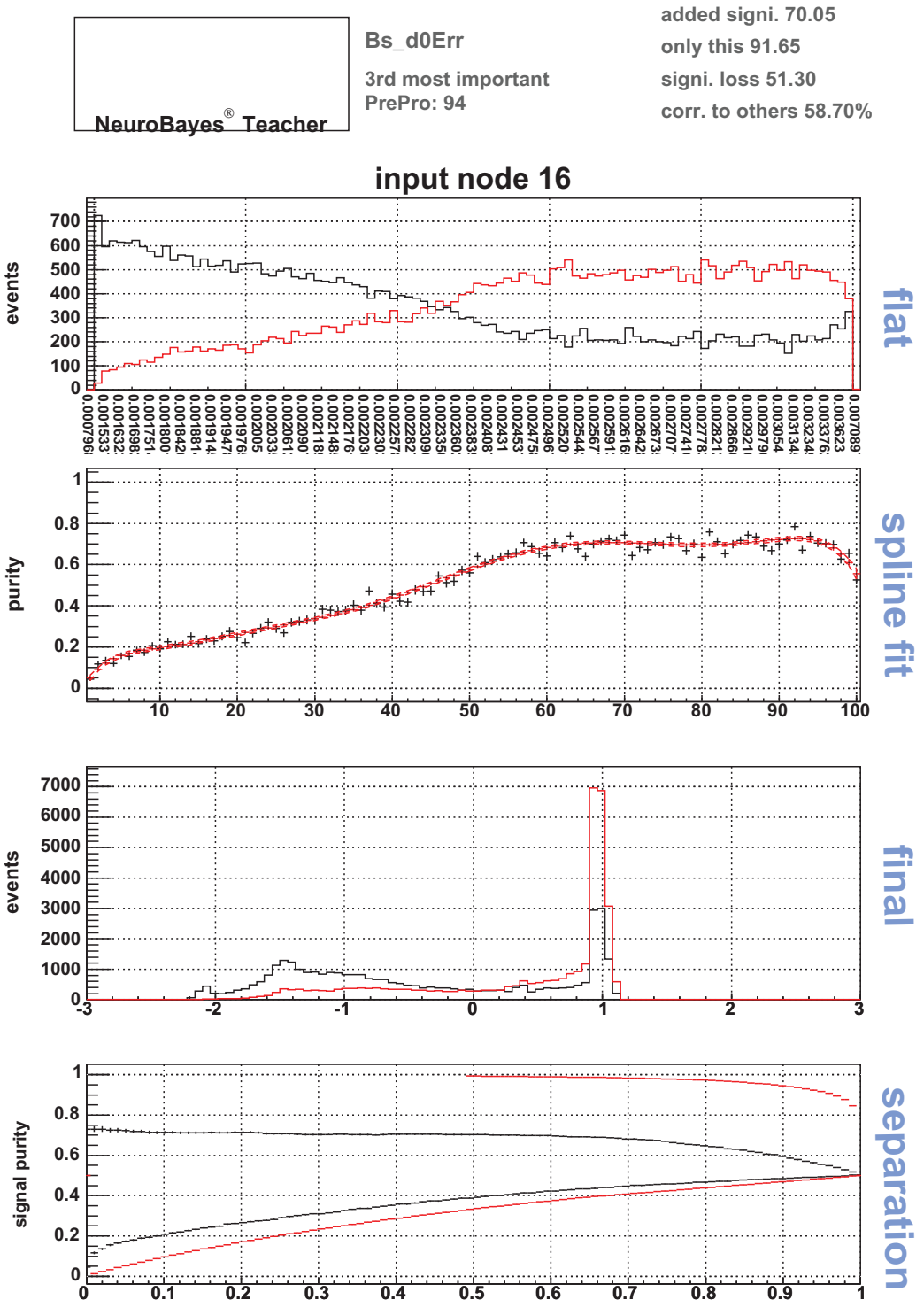
NeuroBayes® Teacher
Bs_d0Err
3rd most important
PrePro: 94
added signi. 70.05
only this 91.65
signi. loss 51.30
corr. to others 58.70%
input node 16
events
flat
purity
spline fit
events
final
signal purity
separation

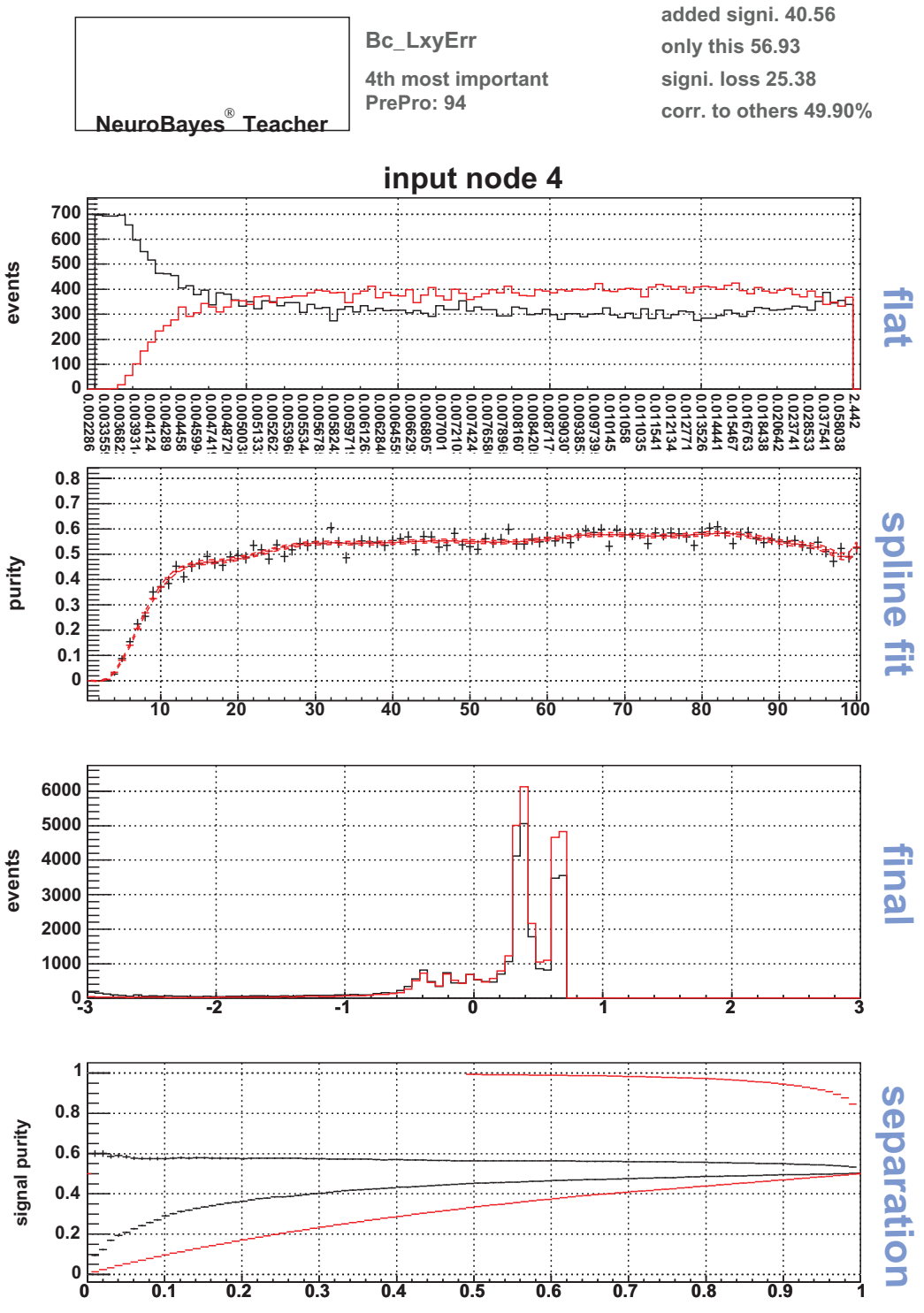
NeuroBayes® Teacher
Bc_LxyErr
4th most important
PrePro: 94
added signi. 40.56
only this 56.93
signi. loss 25.38
corr. to others 49.90%
input node 4
events
flat
purity
spline fit
events
final
signal purity
separation

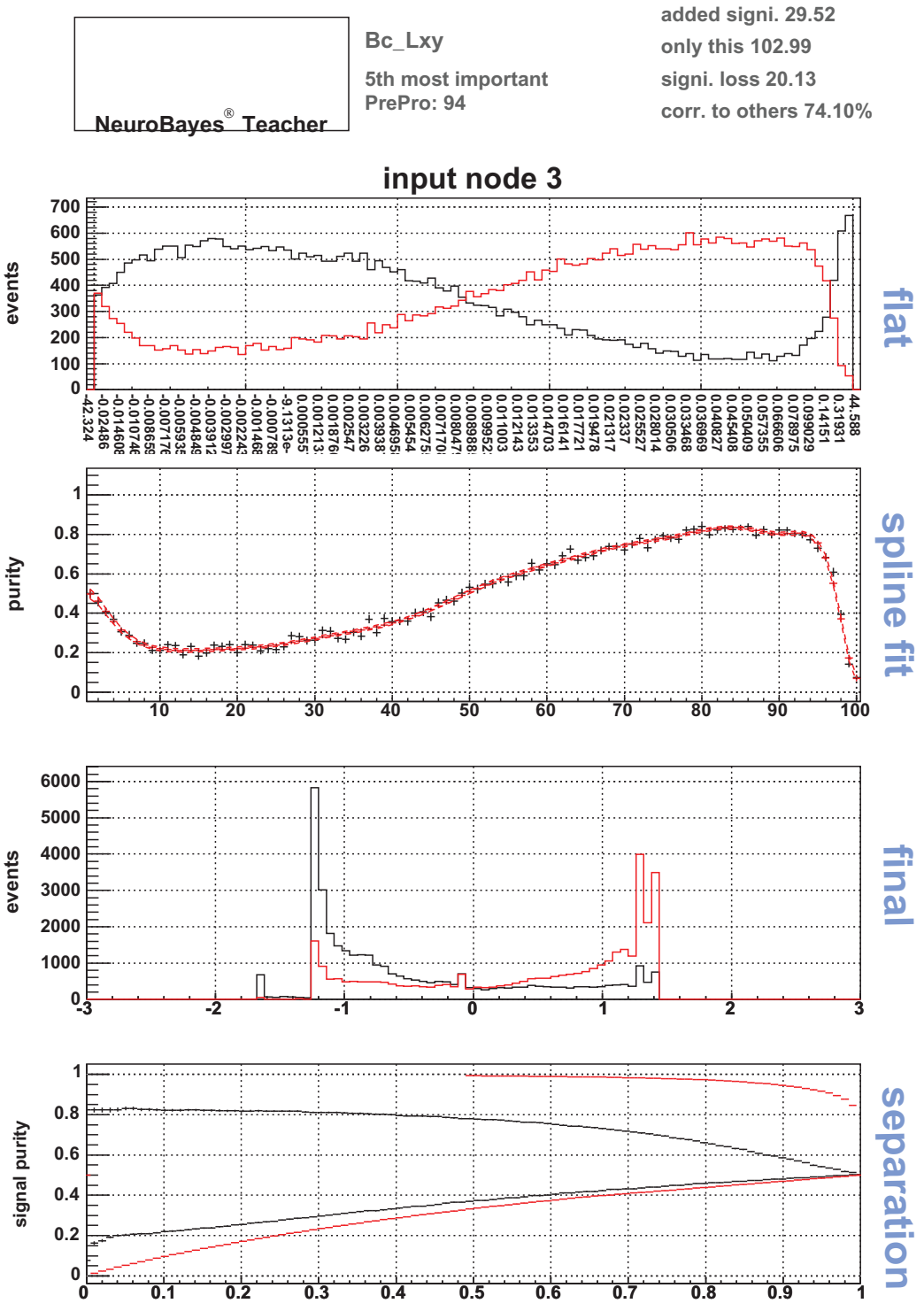
NeuroBayes® Teacher
Bc_Lxy
5th most important
PrePro: 94
added signi. 29.52
only this 102.99
signi. loss 20.13
corr. to others 74.10%
input node 3
events
flat
purity
spline fit
events
final
signal purity
separation

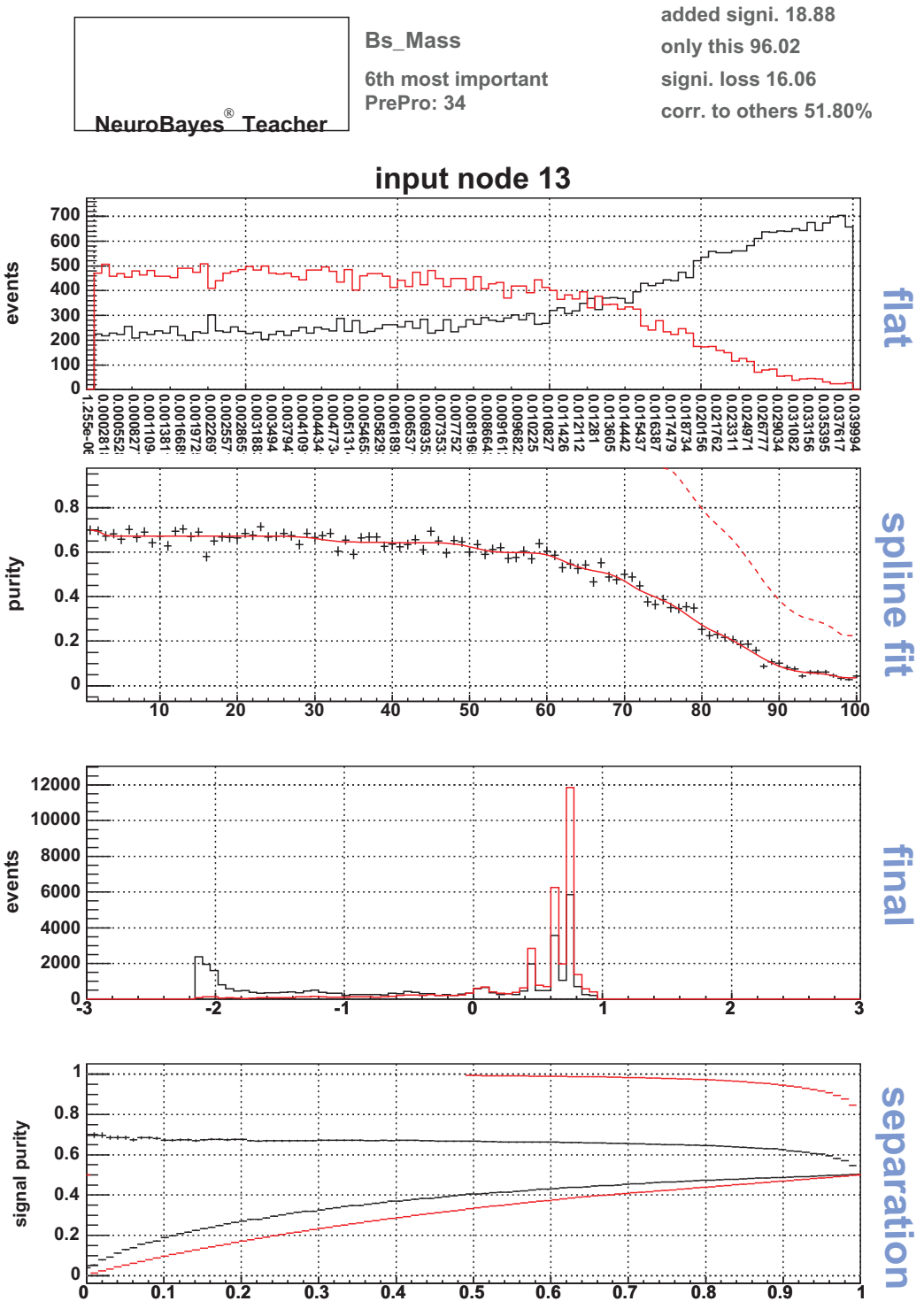
NeuroBayes® Teacher
Bs_Mass
6th most important
PrePro: 34
added signi. 18.88
only this 96.02
signi. loss 16.06
corr. to others 51.80%
input node 13
events
flat
purity
spline fit
events
final
signal purity
separation

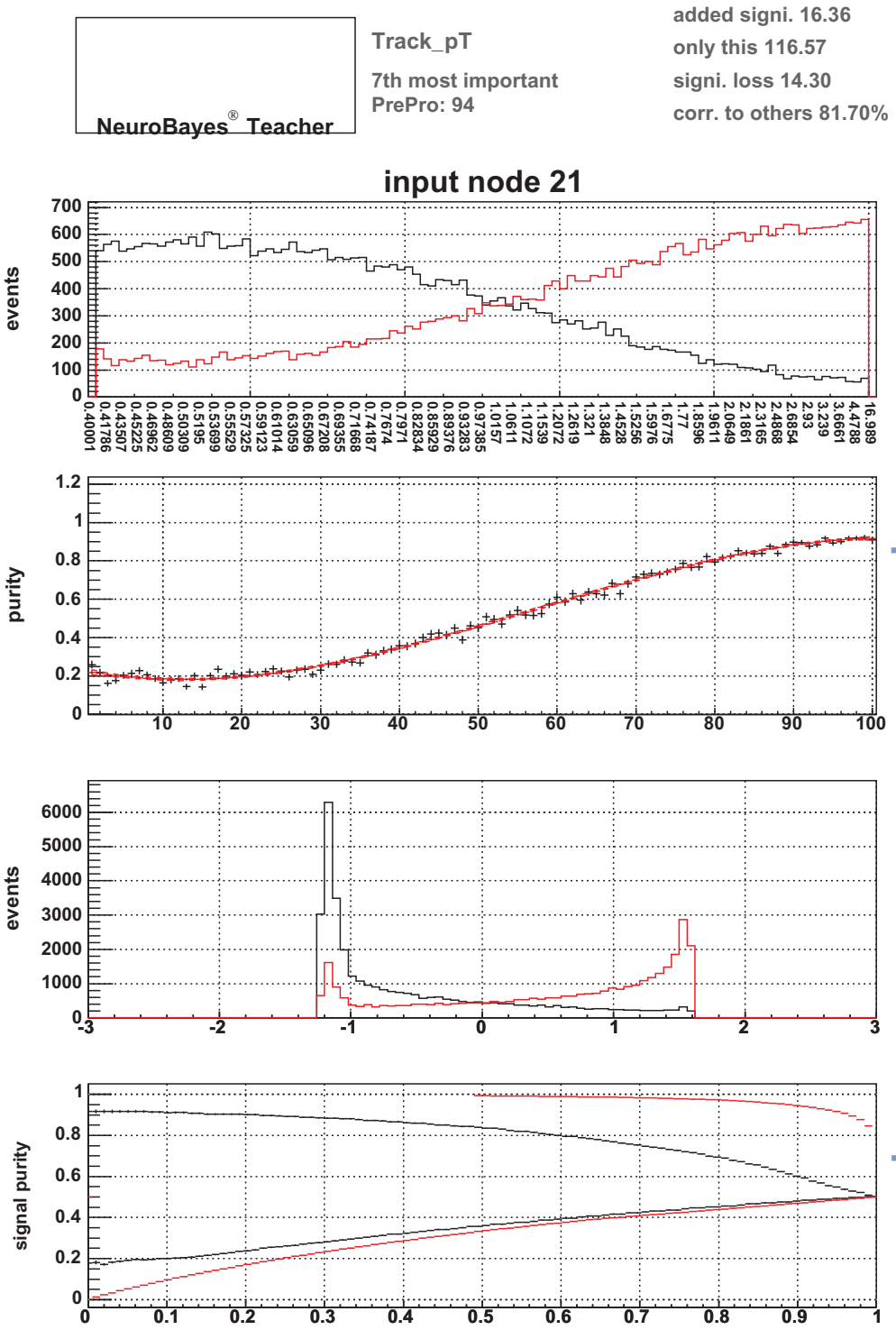
NeuroBayes® Teacher
Track_pT
7th most important
PrePro: 94
added signi. 16.36
only this 116.57
signi. loss 14.30
corr. to others 81.70%
input node 21
events
flat
purity
spline fit
events
final
signal purity
separation

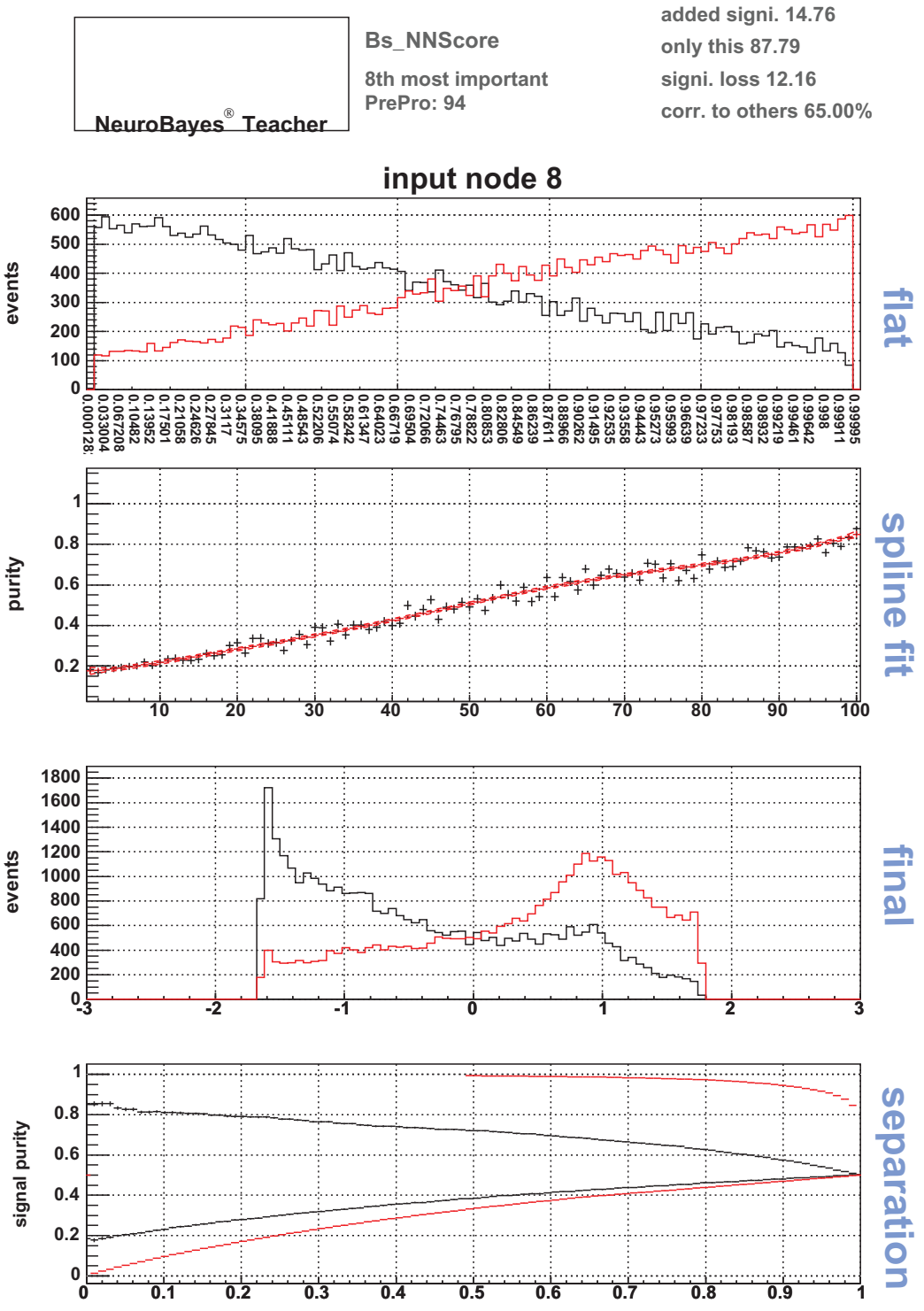
NeuroBayes® Teacher
Bs_NNScore
8th most important
PrePro: 94
added signi. 14.76
only this 87.79
signi. loss 12.16
corr. to others 65.00%
input node 8
events
flat
purity
spline fit
events
final
signal purity
separation

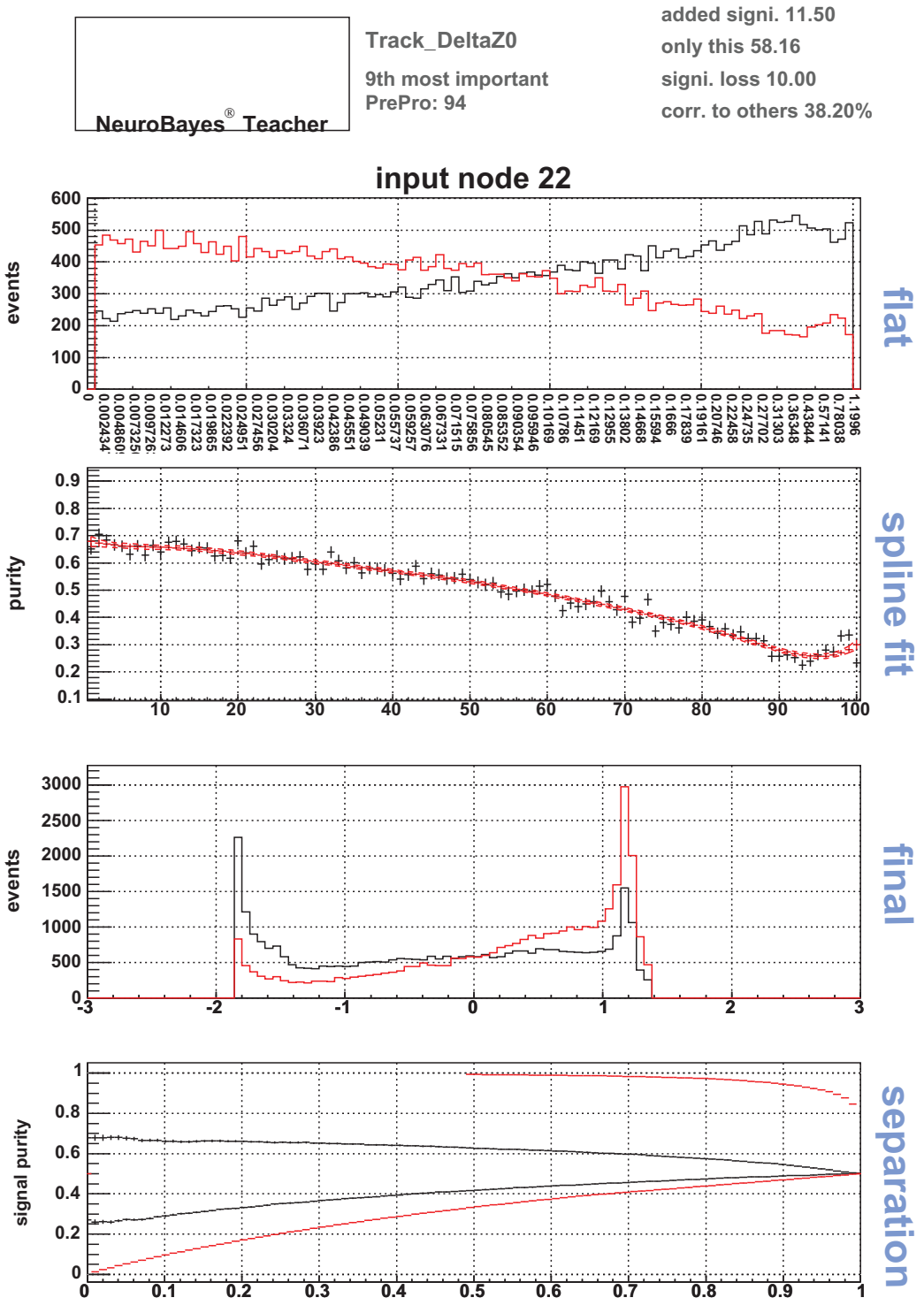
NeuroBayes® Teacher
Track_DeltaZ0
9th most important
PrePro: 94
added signi. 11.50
only this 58.16
signi. loss 10.00
corr. to others 38.20%
input node 22
events
flat
purity
spline fit
events
final
signal purity
separation

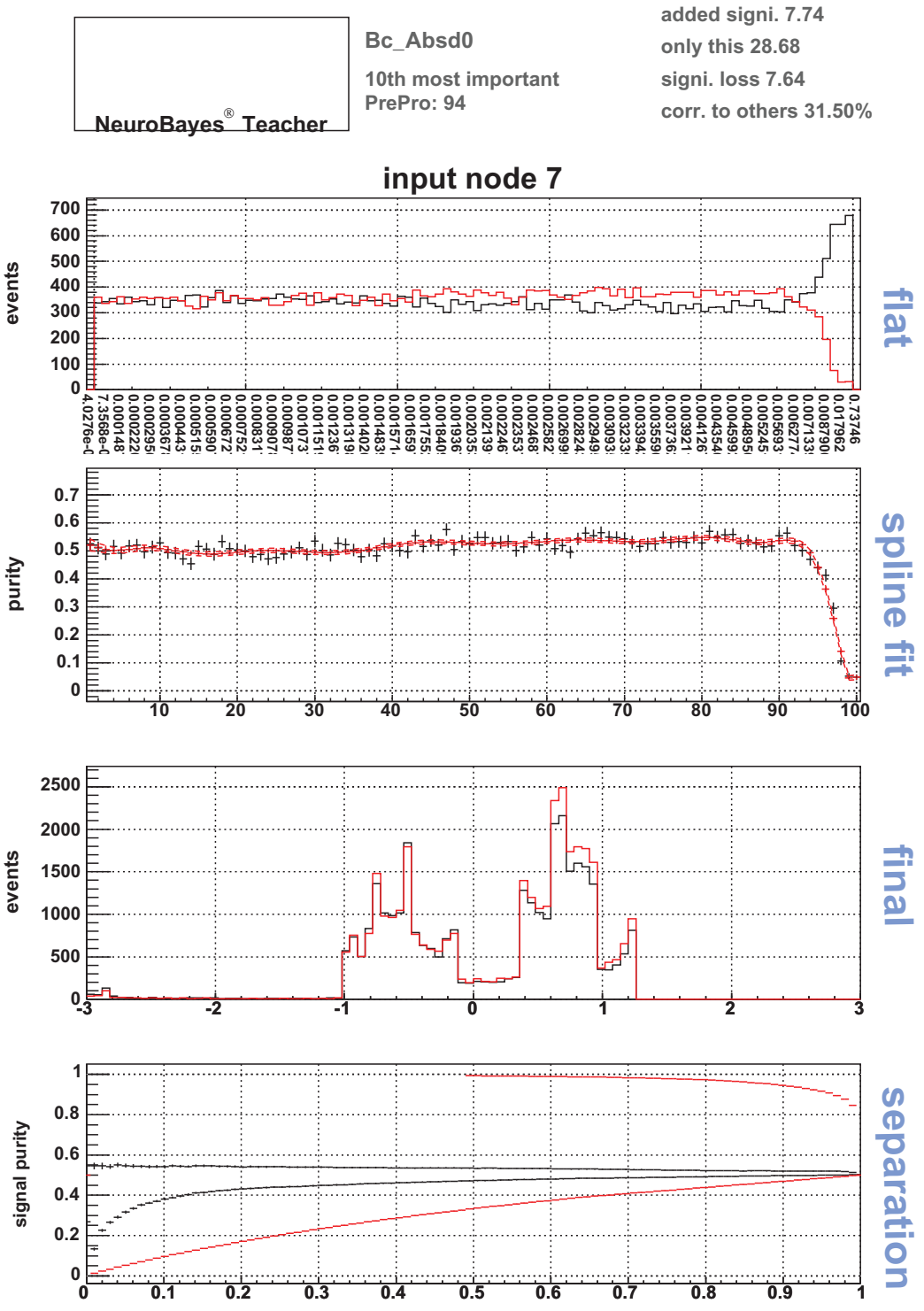
NeuroBayes® Teacher
Bc_Absd0
10th most important
PrePro: 94
added signi. 7.74
only this 28.68
signi. loss 7.64
corr. to others 31.50%
input node 7
events
flat
purity
spline fit
events
final
signal purity
separation

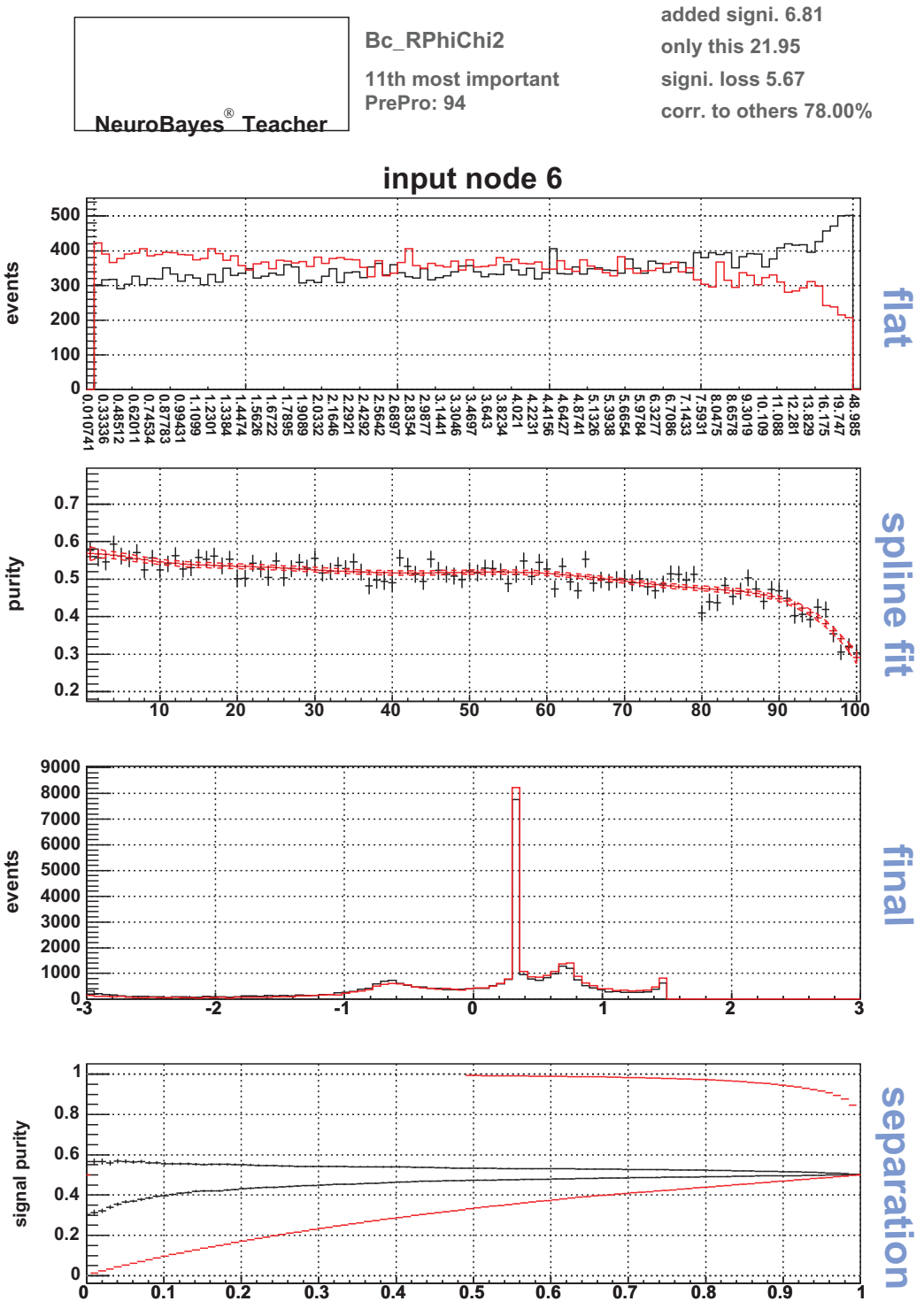
NeuroBayes® Teacher
Bc_RPhiChi2
11th most important
PrePro: 94
added signi. 6.81
only this 21.95
signi. loss 5.67
corr. to others 78.00%
input node 6
events
flat
purity
spline fit
events
final
signal purity
separation

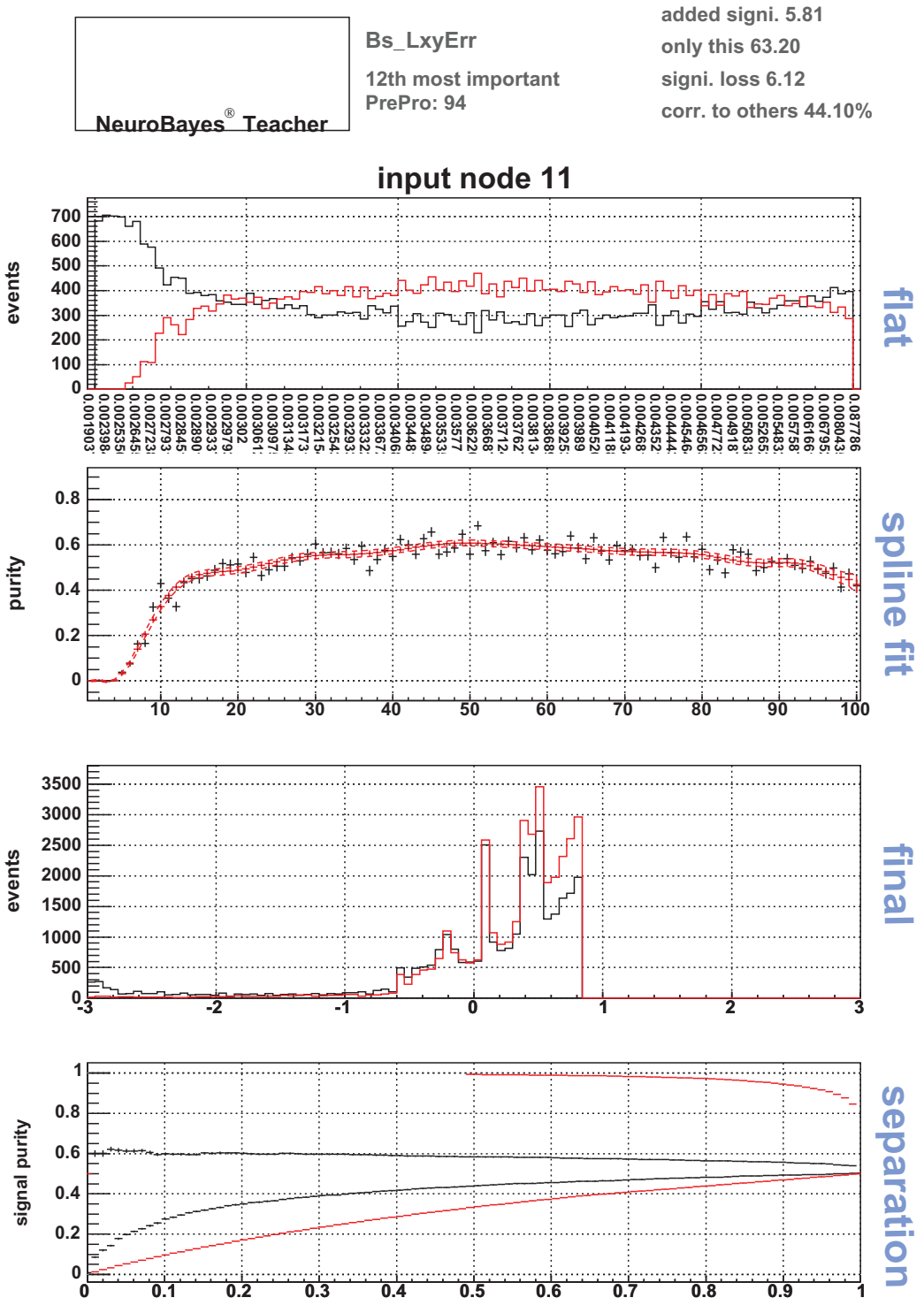
NeuroBayes® Teacher
Bs_LxyErr
12th most important
PrePro: 94
added signi. 5.81
only this 63.20
signi. loss 6.12
corr. to others 44.10%
input node 11
events
flat
purity
spline fit
events
final
signal purity
separation

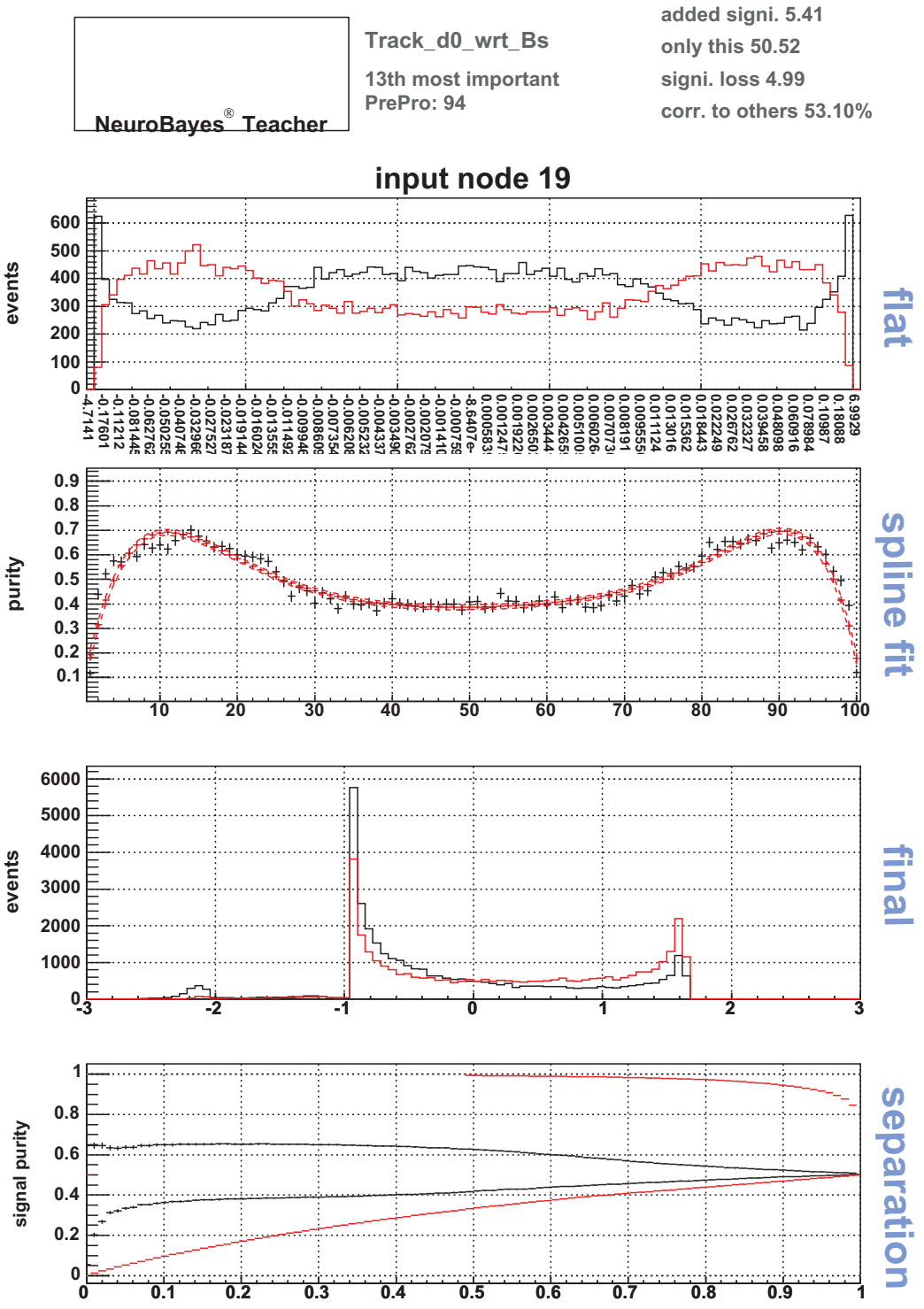
NeuroBayes® Teacher
Track_d0_wrt_Bs
13th most important
PrePro: 94
added signi. 5.41
only this 50.52
signi. loss 4.99
corr. to others 53.10%
input node 19
events
flat
purity
spline fit
events
final
signal purity
separation

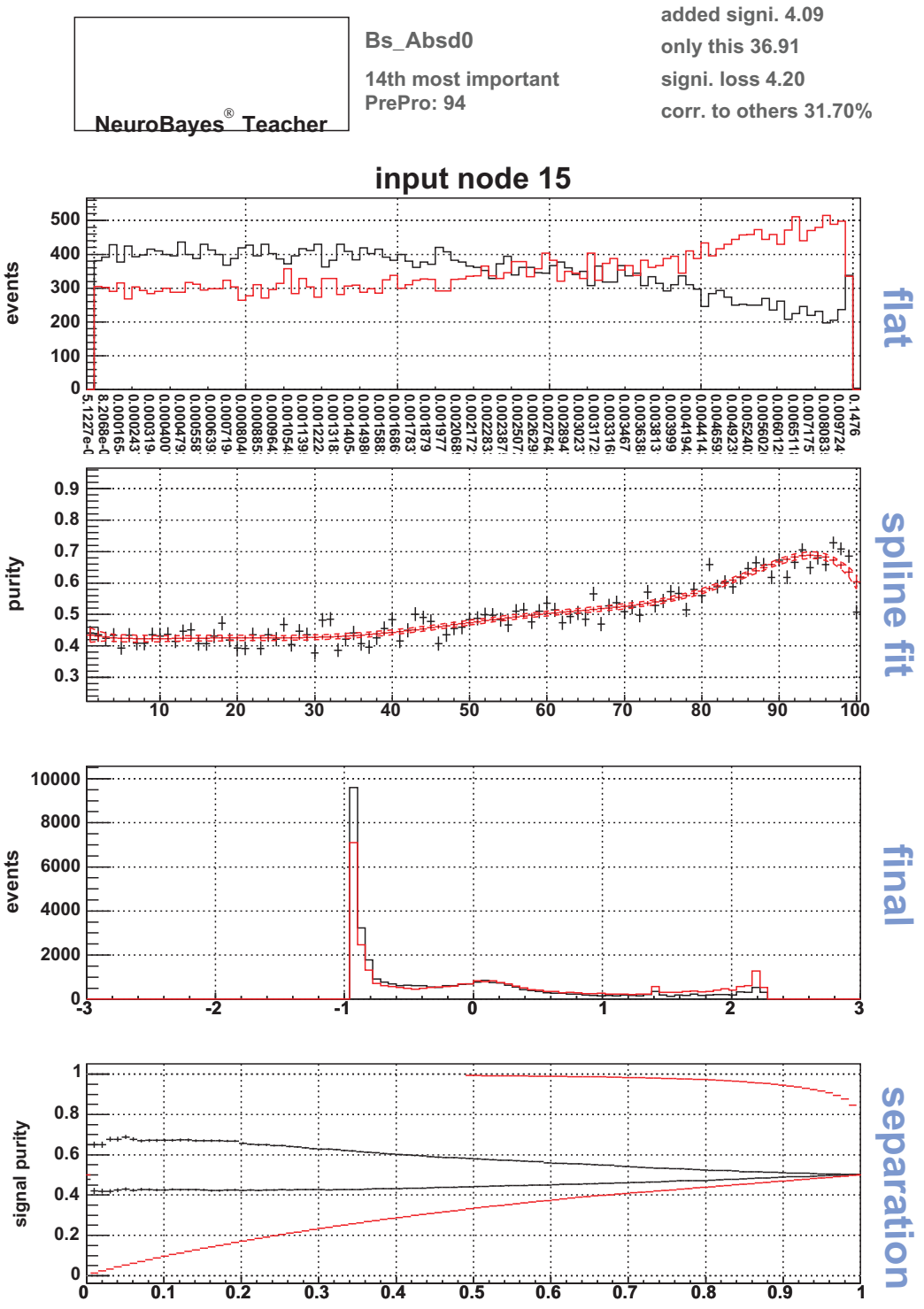
NeuroBayes® Teacher
Bs_Absd0
14th most important
PrePro: 94
added signi. 4.09
only this 36.91
signi. loss 4.20
corr. to others 31.70%
input node 15
events
flat
purity
spline fit
events
final
signal purity
separation

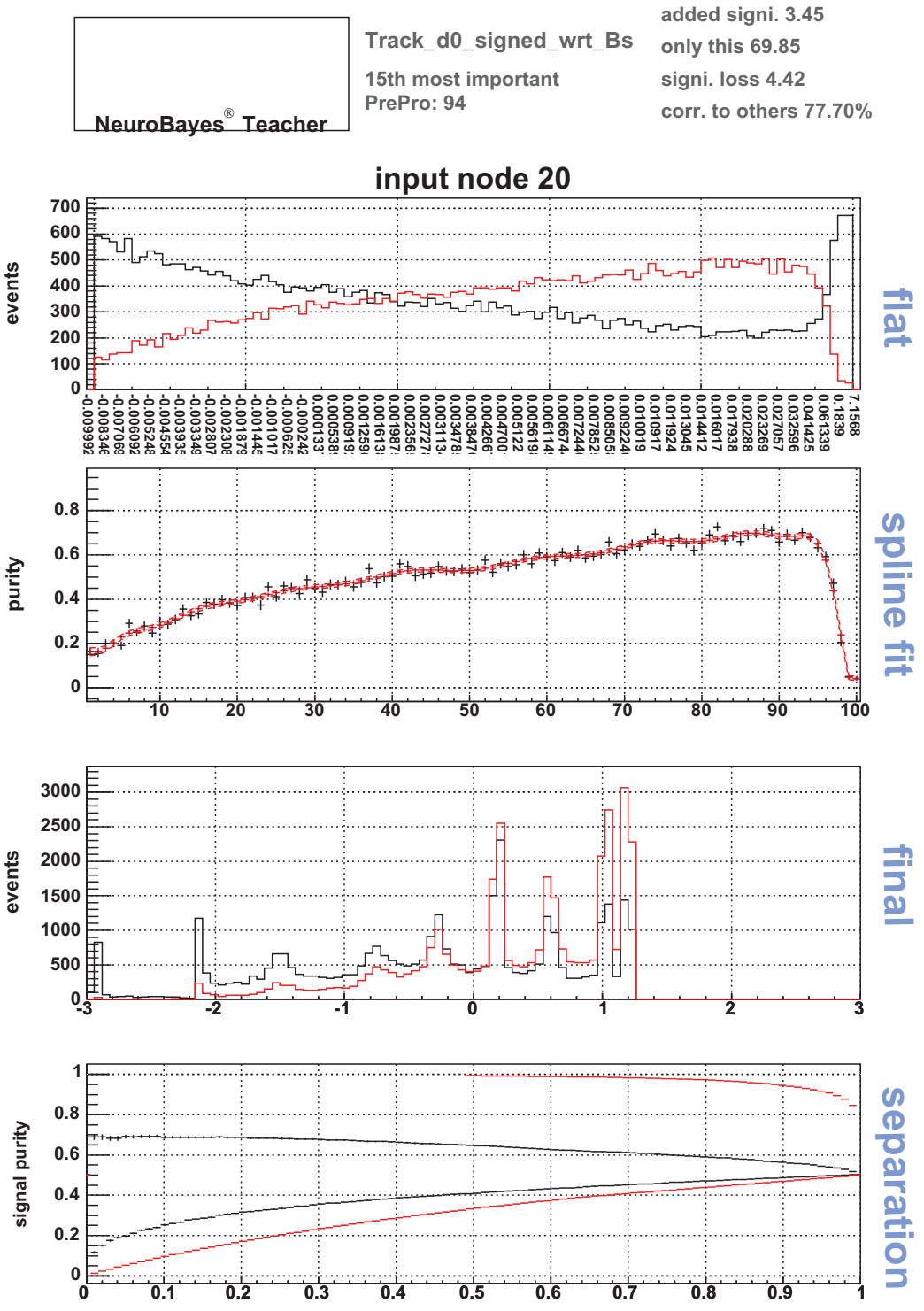
NeuroBayes® Teacher
Track_d0_signed_wrt_Bs
15th most important
PrePro: 94
added signi. 3.45
only this 69.85
signi. loss 4.42
corr. to others 77.70%
input node 20
events
flat
purity
spline fit
events
final
signal purity
separation

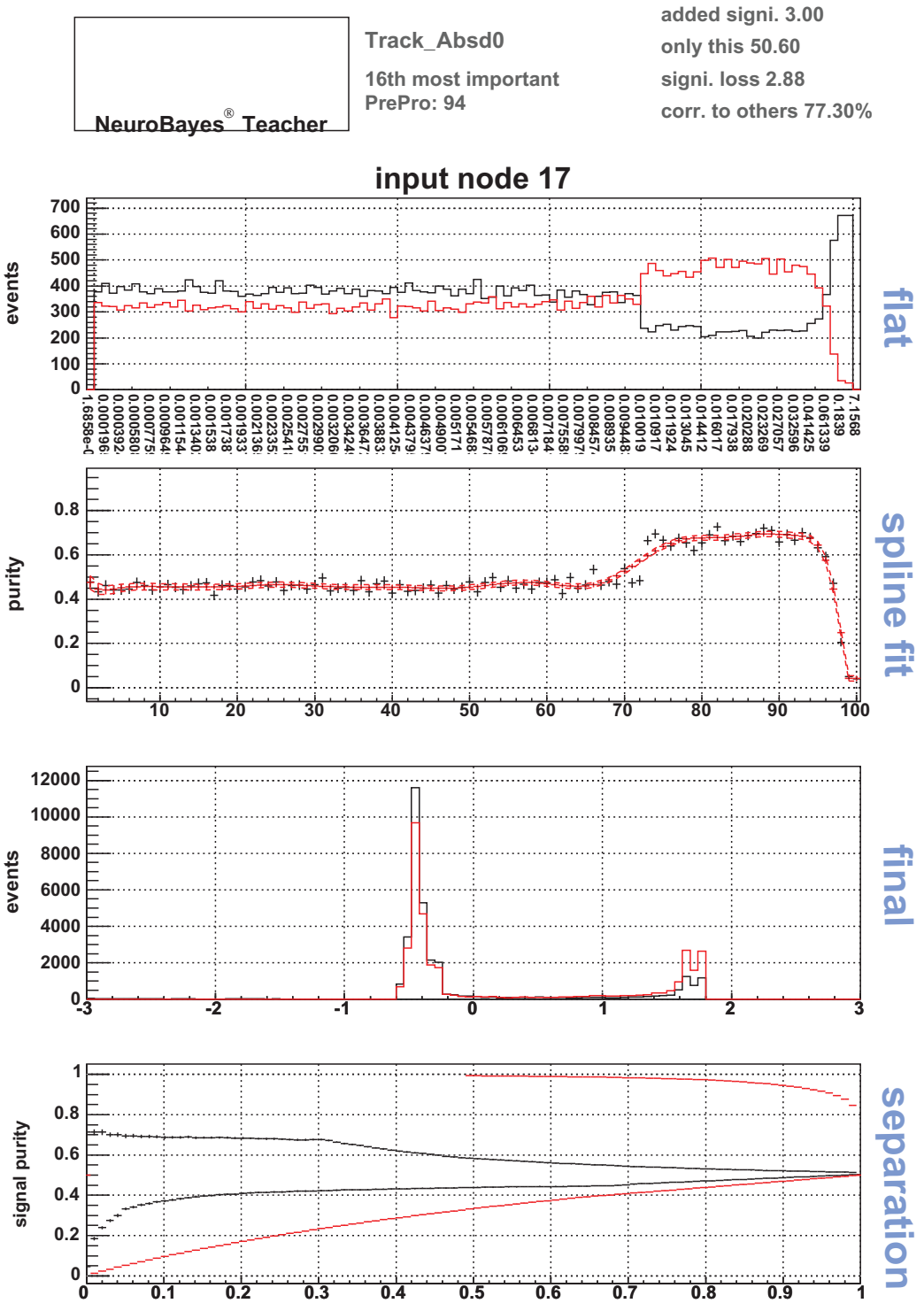
NeuroBayes® Teacher
Track_Absd0
16th most important
PrePro: 94
added signi. 3.00
only this 50.60
signi. loss 2.88
corr. to others 77.30%
input node 17
events
flat
purity
spline fit
events
final
signal purity
separation

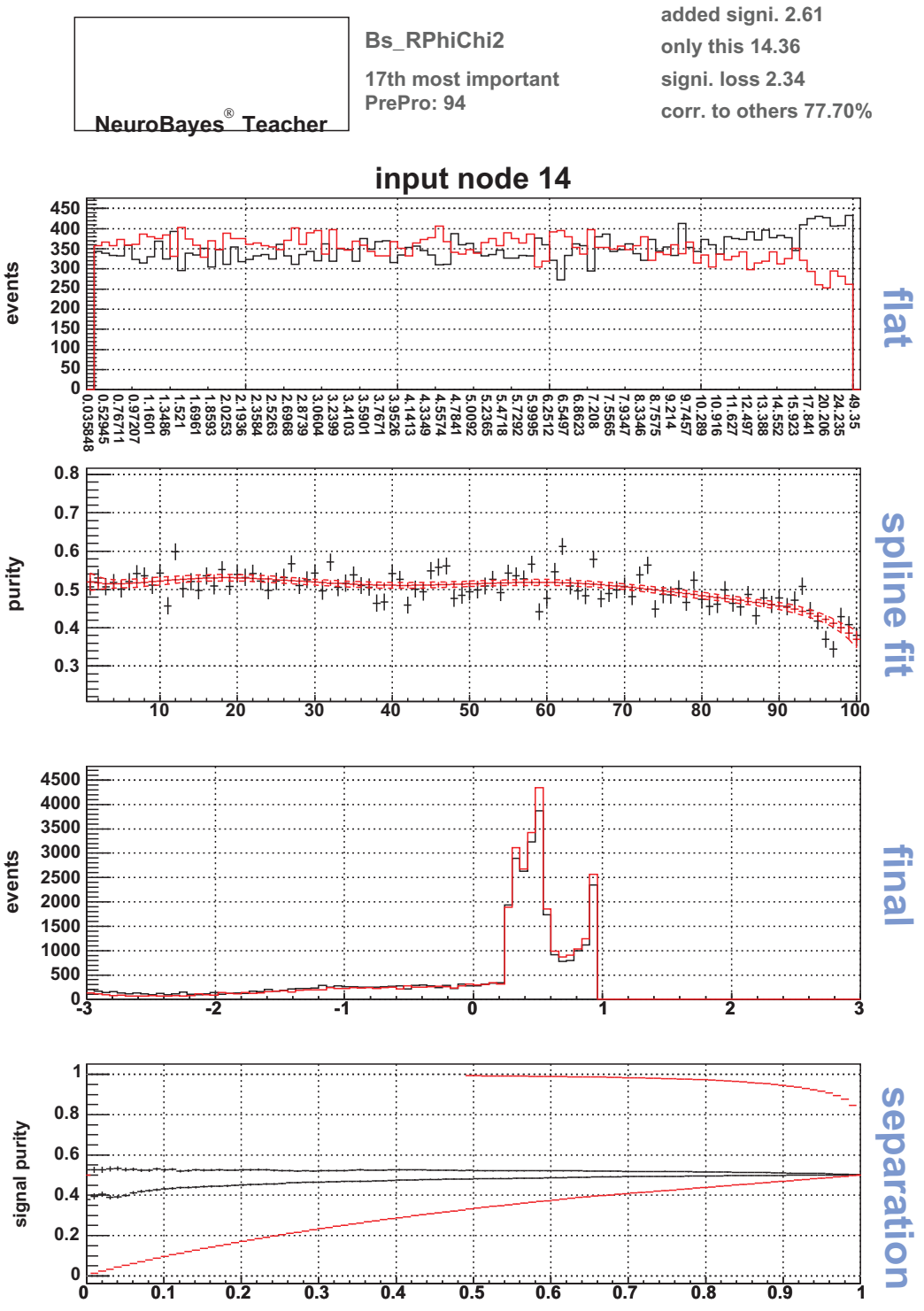
NeuroBayes® Teacher
Bs_RPhiChi2
17th most important
PrePro: 94
added signi. 2.61
only this 14.36
signi. loss 2.34
corr. to others 77.70%
input node 14
events
flat
purity
spline fit
events
final
signal purity
separation

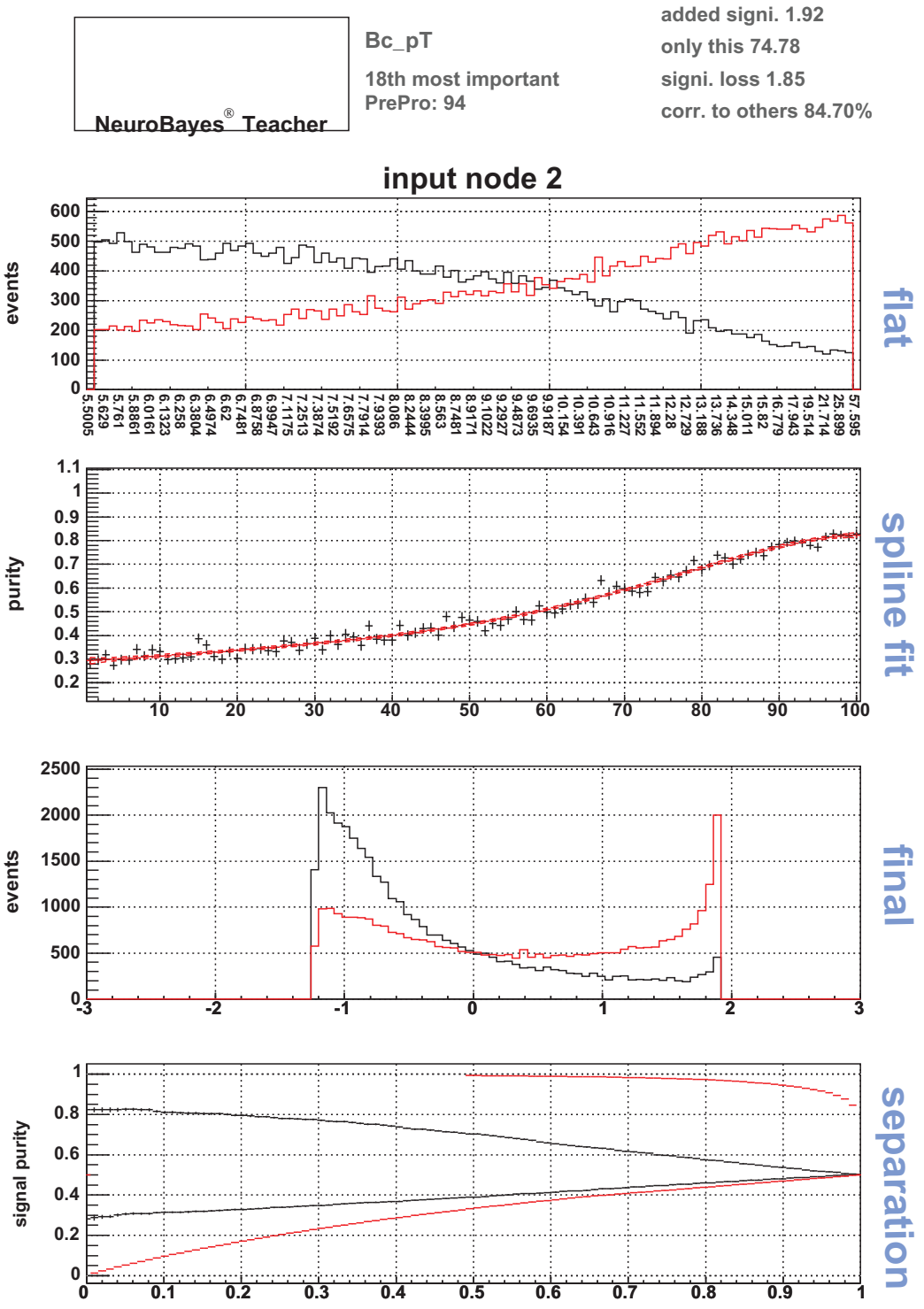
NeuroBayes® Teacher
Bc_pT
18th most important
PrePro: 94
added signi. 1.92
only this 74.78
signi. loss 1.85
corr. to others 84.70%
input node 2
events
flat
purity
spline fit
events
final
signal purity
separation

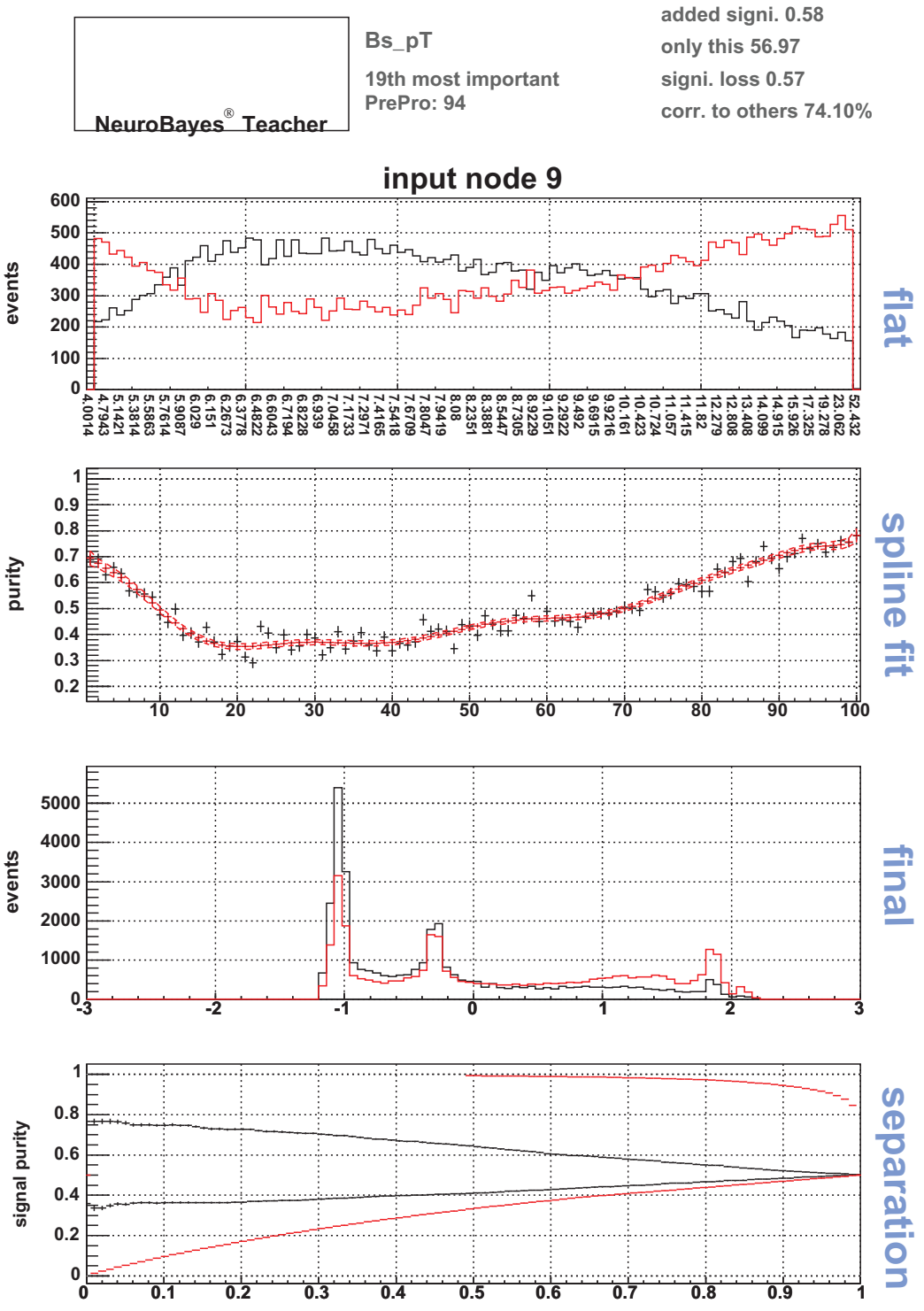
NeuroBayes® Teacher
Bs_pT
19th most important
PrePro: 94
added signi. 0.58
only this 56.97
signi. loss 0.57
corr. to others 74.10%
input node 9
events
flat
purity
spline fit
events
final
signal purity
separation

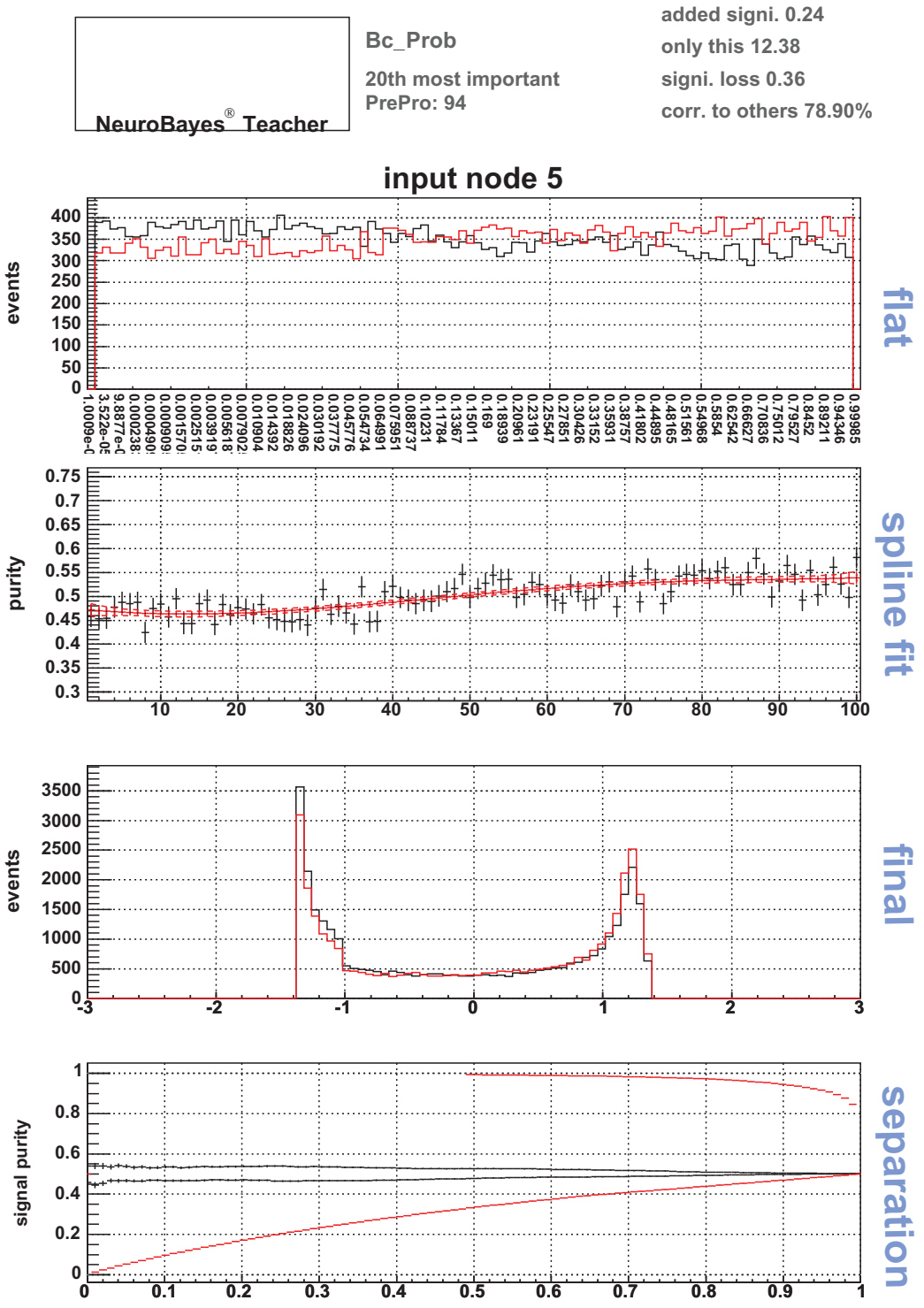
NeuroBayes® Teacher
Bc_Prob
20th most important
PrePro: 94
added signi. 0.24
only this 12.38
signi. loss 0.36
corr. to others 78.90%
input node 5
events
flat
purity
spline fit
events
final
signal purity
separation

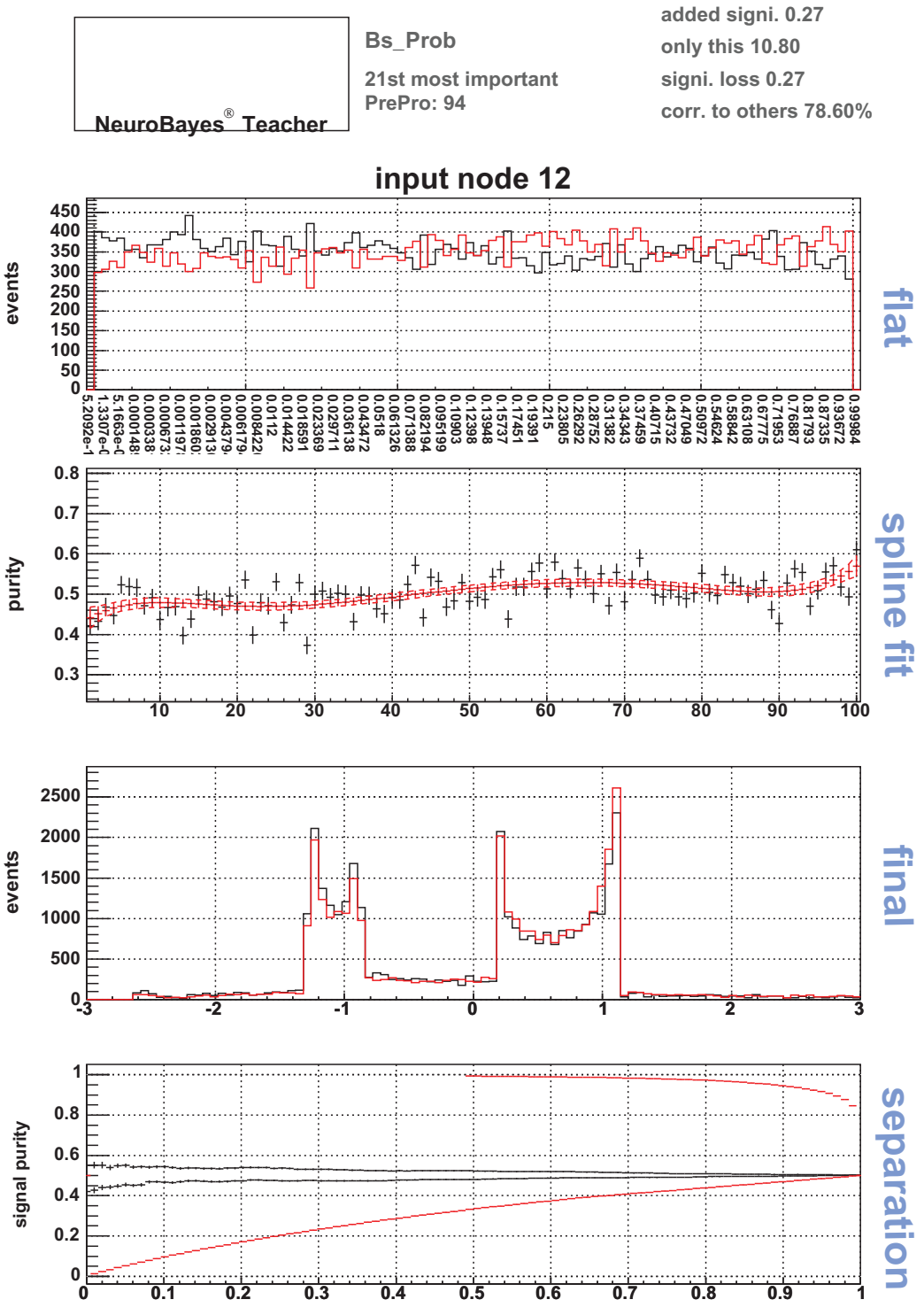
NeuroBayes® Teacher
Bs_Prob
21st most important
PrePro: 94
added signi. 0.27
only this 10.80
signi. loss 0.27
corr. to others 78.60%
input node 12
events
flat
purity
spline fit
events
final
signal purity
separation

NeuroBayes® Teacher

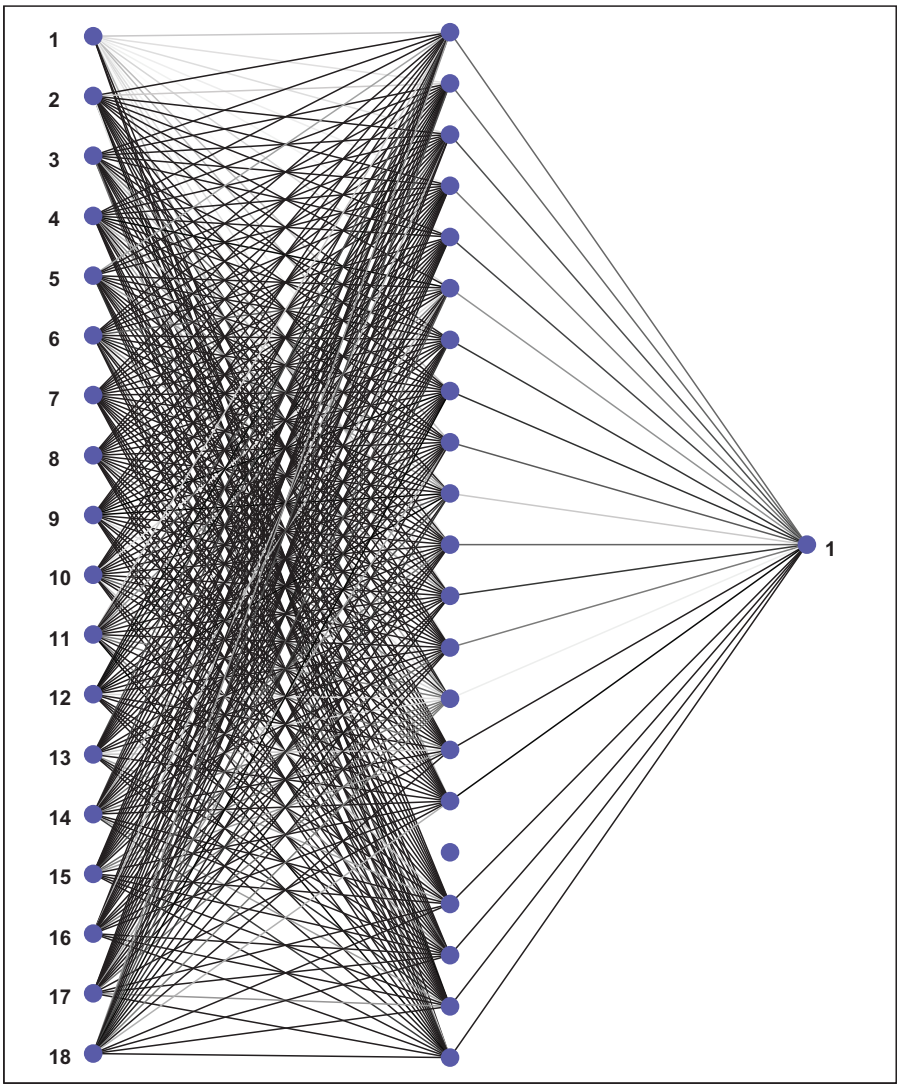

References

[1] S.W. Herb *et al.*, "Observation of a dimuon resonance at 9.5 GeV in 400-GeV proton nucleus collisions," *Phys. Rev. Lett.* **39** 252 (1977).

[2] W-M Yao *et al.*, *J. Phys. G: Nucl. Part. Phys.* **33**, 1 (2006).

[3] C. Amsler *et al.*, (Particle Data Group), *Physics Letters* **B667**, 1 (2008).

[4] N. Cabbibo, *Phys. Rev. Lett.* **10**, 531 (1963).

[5] M. Kobayashi and T. Maskawa, *Prog. Theor. Phys.* **49**, 652 (1973).

[6] F. J. Gilman *et al.*, *Phys. Lett.* **B592**, 793 (2004).

[7] L. Wolfenstein, "Parametrization of the Kobayashi-Maskawa Matrix." *Phys. Rev. Lett.*, **51**, 1945 (1983).

[8] D. Silverman and H. Yao, "Relativistic treatment of light quarks in D and B mesons and W-exchange weak decays." *Phys. Rev. D* **38** *pgs. 214-232* (1988).

[9] I. I. Bigi, "The QCD perspective on lifetimes of heavy flavor hadrons." arXiv:hep-ph/9508408. (1995).

[10] I. I. Bigi, "The Lifetimes of Heavy Flavour Hadrons: A Case Study in Quark Hadron Duality." arXiv:hep-ph/0001003. (1999).

[11] E. Franco *et al.*, "Lifetime ratios of beauty hadrons at the next-to-leading order in QCD." *Nucl. Phys. B.*, **633** 212. (2002).

[12] A. Abulencia, *et al.*, "Measurement of the B_c^+ Meson Lifetime Using the Decay Mode $B_c^+ \rightarrow J/\psi\, e^+\nu_e$." *Phys. Lett. D* **97**, 012002 (2006).

[13] I. F. Allison *et al.*, "Mass of the B_c Meson in Three-Flavor Lattice QCD." *Phys. Rev. Lett.* **94**, 172001 (2005).

[14] N. Brambilla *et al.*, "Quarkonium spectroscopy and perturbative QCD: Massive quark-loop effects." *Phys. Lett. D* **65**, 034001 (2002).

[15] E. J. Eichten and C. Quigg, "Mesons with beauty and charm: Spectroscopy." *Phys. Lett. D* **49**, 5845 (1994).

[16] C. Quigg, "Proceedings of the Workshop on B Physics at Hadron Accelerators." Report No SSCL-SR-1225/FERMILAB-CONF-93/267. *pgs. 439-441* (1993) http://lss.fnal.gov/archive/1993/conf/Conf-93-267.pdf (visited 04 Oct., 2010).

[17] V. V. Kiselev, "Decays of the B_c meson", arXiv:hep-ph/0308214. (2003).

[18] M. Mangano, "The saga of bottom production in $p\bar{p}$ collisions." arXiv:hep-ph/0411020v1. (2004).

[19] B. Abbott, *et al.*, "Small-Angle Muon and Bottom-Quark Production in $p\bar{p}$ Collisions at $\sqrt{s} = 1.8$ TeV." *Phys. Rev. Lett.* **84** *pgs. 54785483* (2000).

[20] J. Kraus, "Measurements of the B Production Cross Section in $p\bar{p}$ Collisions at $\sqrt{s} =$ 1.96 TeV Using Semileptonic Decays of B Hadrons." *Ph.D. Thesis* University of Illinois Urbana Champaign. (2006).

[21] F. Abe, *et al.*, "Observation of B_c mesons in $p\bar{p}$ collisions at $sqrts = 1.8$ TeV." *Phys. Lett. D* **58**, 112004 (1998).

[22] T. Aaltonen, *et al.*, "Observation of the Decay $B_c^{\pm} \to J/\psi\pi^{\pm}$ and Measurement of the $B_c^{\pm}$ Mass." *Phys. Rev. Lett.* **100**, 182002 (2008).

[23] P. Abreu, *et al.*, "Search for the B_c Meson." *Phys. Lett. B* **398** *pgs. 207-222* [CERN-PPE-96-194] (1997).

[24] K. Ackerstaff, *et al.*, "Search for the B_c meson in hadronic Z_0 decays." *Phys. Lett. B* **420** *pgs. 157-168* [CERN-PPE-97-137] (1998).

[25] R. Barate, *et al.*, "Search for the B_c meson in hadronic Z decays." *Phys. Lett. B* **402** *pgs. 213-226* [CERN-PPE-97-026] (1997).

[26] B. Casal, *et al.*, "First Look into the Search for $B_c^+ \to B_s^0 X$ Decays." 13 Oct., 2006. CDF Note **8537**.

[27] The CDF Collaboration, "$B_c^- \to J/\psi\ \pi^-$ at CDF with 1.1 fb^{-1}." 7 Sep., 2006. CDF Note **8004**.

[28] Fermi National Accelerator Laboratory, "Accelerator – Fermilab's Tevatron." 23 Apr., 2009. http://www.fnal.gov/pub/science/accelerator/ (visited 9 Jan., 2010).

[29] Fermi National Accelerator Laboratory, "Press Room." 27 Sep., 2004. http://www.fnal.gov/pub/presspass/vismedia/gallery/accelerator.html (visited 9 Jan., 2010).

[30] R. Wisniewski, "Universities Help to Upgrade Booster." *Fermilab Today* (21 Oct., 2004).

[31] Fermi National Accelerator Laboratory, "Tevatron Luminosity." 23 Nov., 2009. http://www.fnal.gov/pub/now/tevlum.html (visited 9 Jan., 2010).

[32] Collider Detector at Fermilab, "CDF Summary of Stores." 9 Jan., 2010. http://www-cdfonline.fnal.gov/ops/opshelp/stores/ (visited 9 Jan., 2010).

[33] The CDF IIb Collaboration, "The CDF IIb Detector Technical Design Report." 2 Sep., 2002. CDF Note **6261**.

[34] M. Milnik, "Measurement of the lifetime difference and cp-violating phase in $B_s \to J/\psi\phi$ decays." 30 Nov., 2007. http://www.slac.stanford.edu/spires/find/hep?key=7554591 (visited 25 Mar., 2010).

[35] M. Jones, "TOF Design Draft Page." 10 Mar., 2002. http://www-cdf.fnal.gov/upgrades/TOF/pr_plots/TOF_PR_plots.html (visited 31 Mar., 2010).

[36] S. Bertolucci, *et. al.*, "The CDF central and endwall hadron calorimeter." 1 May, 1988. *Nucl. Instr. & Meth.*, **A267**:301.

[37] M. Herndon, "Tracking at CDF." Mar., 2003. http://www.slac.stanford.edu/econf/C0303241/proc/pres/360.PS (visited 30 Mar., 2010).

[38] The CDF II Collaboration, "The CDF II Detector Technical Design Report." 13 Jul., 2001. http://www-cdf.fnal.gov/upgrades/tdr/tdr.html (visited 30 Mar., 2010).

[39] R. Downing, *et al.*, "Track Extrapolation and Distribution for the CDF-II Trigger System." *Nucl. Instr. & Meth.*, **A570**:36-50 (2007).

[40] J. D. Lewis, "CDF Trigger and DAQ Overview." CDF New Ace Training, 15 Jun., 2010. http://www-cdf.fnal.gov/internal/WebTalks/Archive/1006/100615_ace_training_at_3pm/ (visited 16 Sep., 2010).

[41] C.-J. Lin, "Introduction to CDF L1/L2 Triggers." CDF New Ace Training, 18 Nov., 2004. http://www-cdf.fnal.gov/internal/WebTalks/Archive/0411/041118_detector_lecture_cdf_trigger/ (visited 20 Sep., 2010).

[42] A. Abulencia, *et al.*, "The CDF II eXtremely Fast Tracker Upgrade." Published Proceedings 10th Pisa Meeting on Advanced Detectors: Frontier Detectors for Frontier Physics. 17 Aug., 2006.

[43] A. Abulencia, *et al.*, "The CDF II 3D-Track Level 2 Trigger Upgrade." Published Proceedings, 15th IEEE NPSS Real Time Conference 2007 (RT 07)

[44] R. Hughes, "Upgrade of the CDF Track Trigger for High Luminosity Running." Director's Review: CDF Run IIb Upgrade. 18 Jan., 2005. http://www-cdf.fnal.gov/upgrades/run2b/DIR_Jan05/Talks/ (visited 17 Sep., 2010).

[45] S. Holm, *et al.*, "Specifications for the Stereo Linker Association Module" 22 Sep., 2004. CDF Note **7073**.

[46] M. Paulini and B. Wicklund, "Summary of Proposals for B Physics Triggers in Run II." 18 Dec., 2000. CDF Note **5483**.

[47] E. Rogers, "Crate Operations Manual for XTC2 Diagnostics." Jan. 30, 2008. https://netfiles.uiuc.edu/erogers1/www/files/CrateTutorial.pdf (visited 28 Jun., 2010).

[48] R. Mokos, "XTC 2 Memory Space." Mar. 13, 2006. http://www.hep.uiuc.edu/engin/cdf/XFT2/index.htm (visited 28 Jun., 2010).

[49] F. Azfar, *et al.* (B_s Mixing Group), "Signal Optimization for $B_d \to D\pi, D \to K\pi\pi$ using a Neural Network." CDF Note: 8123, 16 Mar., 2006.

[50] A. Ryd and D. Lange, "The EvtGen Package." 26 Mar., 1999. http://charm.physics.ucsb.edu/people/lange/EvtGen/ (visited 21 Sep., 2010).

[51] R. J. Tesarek, "Getting Started with CDF B Monte Carlo." 29 Aug., 2010. http://www-cdf.fnal.gov/internal/mcProduction/cdf_bmc/ (visited 21 Sep., 2010).

[52] C. H. Chang and Y. Q. Chen, "Hadronic production of the B_c meson at TeV energies." 1 Nov., 1993. *Physical Review D*, **48** 4086.

[53] C. H. Chang, *et al.*, "Comparative study of the hadronic production of B_c mesons." 1 Oct., 1996. *Physical Review D*, **54** 4344.

[54] G. Giurgiu, *et al.*, "Muon B Flavor Tagging - A Likelihood Approach" CDF Note: 7043, 21 Jul., 2004.

[55] G. Punzi, "Sensitivity of searches for new signals and its optimization." arXiv:physics/0308063. (2003).

[56] T. Aaltonen, *et al.*, "Measurement of the b-hadron production cross section using decays to $\mu^- D^0 X$ final states in $p\bar{p}$ collisions at $\sqrt{s} = 1.96$ TeV" *Phys. Lett. D* **79**, 092003 (2009).

[57] J. Conway and K. Maeshima, "Upper Limits on Poisson Processes Incorporating Uncertainties in Acceptance and Background." CDF Note: 4476, 13 Mar., 1998.